

Air Force Institute of Technology

AFIT Scholar

[Theses and Dissertations](#)

[Student Graduate Works](#)

9-1-2008

Range Precision of LADAR Systems

Steven E. Johnson

Follow this and additional works at: <https://scholar.afit.edu/etd>



Part of the [Electrical and Electronics Commons](#)

Recommended Citation

Johnson, Steven E., "Range Precision of LADAR Systems" (2008). *Theses and Dissertations*. 2638.
<https://scholar.afit.edu/etd/2638>

This Dissertation is brought to you for free and open access by the Student Graduate Works at AFIT Scholar. It has been accepted for inclusion in Theses and Dissertations by an authorized administrator of AFIT Scholar. For more information, please contact richard.mansfield@afit.edu.



RANGE PRECISION
OF LADAR SYSTEMS

DISSERTATION

Steven Johnson,

AFIT/DEE/ENG/08-15

DEPARTMENT OF THE AIR FORCE
AIR UNIVERSITY

AIR FORCE INSTITUTE OF TECHNOLOGY

Wright-Patterson Air Force Base, Ohio

APPROVED FOR PUBLIC RELEASE; DISTRIBUTION UNLIMITED.

The views expressed in this dissertation are those of the author and do not reflect the official policy or position of the United States Air Force, Department of Defense, or the United States Government

AFIT/DEE/ENG/08-15

RANGE PRECISION
OF LADAR SYSTEMS

DISSERTATION

Presented to the Faculty
Department of Electrical and Computer Engineering
Graduate School of Engineering and Management
Air Force Institute of Technology
Air University
Air Education and Training Command
In Partial Fulfillment of the Requirements for the
Degree of Doctor of Philosophy in Electrical Engineering

Steven Johnson, B.S. Physics, M.S.E.E.

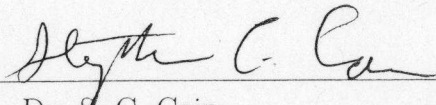
September 2008

APPROVED FOR PUBLIC RELEASE; DISTRIBUTION UNLIMITED.

RANGE PRECISION
OF LADAR SYSTEMS

Steven Johnson, B.S. Physics, M.S.E.E.

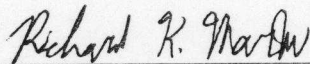
Approved:



Dr. S. C. Cain
Dissertation Advisor

24 July 2008

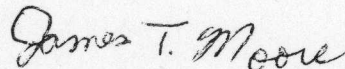
date



Dr. R. K. Martin
Committee Member

14 Aug 2008


date



Dr. J. T. Moore
Dean's Representative

24 July 2008

date

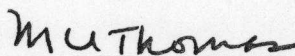


Lt. Col. R. E. Neher Ph.D.
Committee Member

20 Jun 08

date

Accepted:



M. U. Thomas

18 Aug 08

Date

Dean, Graduate School of Engineering and Management

Abstract

A key application of Laser Detection and Ranging (LADAR) systems is measurement of range to a target. Many modern LADAR systems are capable of transmitting laser pulses that are less than a few nanoseconds in duration. These short-duration pulses provide excellent range precision. However, randomness in the detected laser signals places limits on the precision.

The goal of this dissertation is to quantify the range precision limits of LADAR systems. The randomness in the time between photon arrivals, which is called shot noise, is discussed in depth. System-dependent noise sources such as dark current and detector gain variation are considered. The effect of scene-dependent parameters including background light, target obscuration, and target orientation is also discussed. Finally, noise mitigation strategies such as pulse averaging and gain equalization are described and tested on simulated and real LADAR data.

Table of Contents

	Page
Abstract	iv
List of Figures	viii
List of Tables	x
List of Symbols	xi
List of Abbreviations	xv
I. Introduction	1
1.1 LADAR Systems	2
1.1.1 LADAR System Diagram	2
1.1.2 Pulsed LADAR Systems	3
1.1.3 Imaging LADAR Systems	4
1.1.4 Airborne LADAR Systems	4
1.2 LADAR Signals	5
1.2.1 LADAR Receivers	5
1.2.2 LADAR Signals	6
1.2.3 Signal Parameter Estimation	7
II. Problem Background	9
2.1 Laser Beam Propagation	10
2.1.1 Beam Quality	10
2.1.2 Fresnel Propagation of Gaussian Beams	13
2.1.3 Gaussian Beam Size	14
2.1.4 Beam Divergence Angle	15
2.1.5 Propagation Examples	16
2.1.6 Temporal Laser Pulse Shape	17
2.2 LADAR Detectors and Signals	18
2.2.1 Photodetectors and their Output Signals	18
2.2.2 LADAR Signal Model	20
2.2.3 Photoelectron Probability Density Functions	21
2.2.4 Single Detector LADAR Signal Model	23
2.3 LADAR Range Precision	25
2.3.1 Cramer-Rao Lower Bounds	25
2.4 Gain Variation in APD Arrays	29
2.5 Overview of Dissertation	31
2.6 Chapter Summary	32

	Page
III. Poisson-Distributed LADAR Signal Models	34
3.1 Parabolic Pulse LADAR Signal Model	35
3.1.1 Fisher Information Matrix	36
3.1.2 Cramer-Rao Lower Bounds	51
3.1.3 Maximum Likelihood Estimation of Parameters	53
3.1.4 Range Estimation Methods	56
3.1.5 Gain and Bias Estimation	62
3.2 Obscured Target LADAR Signal Model	65
3.2.1 LADAR Signal Model with Obscuration	65
3.2.2 Fisher Information Matrix Elements	68
3.2.3 Cramer-Rao Lower Bounds	70
3.2.4 Parameter Estimation	72
3.2.5 Simulations	76
3.3 Variable Pulse Width LADAR Signals	78
3.3.1 Variable Pulse Width LADAR Signal Model	80
3.3.2 Log-Likelihood Function and its Derivatives	80
3.3.3 Fisher Information Matrix	82
3.3.4 Cramer-Rao Lower Bounds	86
3.3.5 Simulations	87
3.4 Chapter Summary	94
IV. Range Precision of LADAR Systems	95
4.1 Target Range Estimation	95
4.1.1 Comparison to Gaussian-Noise Signals	96
4.1.2 Simulations	99
4.1.3 Multiple Pulses and Range Precision	101
4.2 Surface Orientation and Range Estimation	104
4.2.1 Scenario and Assumptions	105
4.2.2 Scenario Geometry	106
4.2.3 Propagation and Reflection	107
4.2.4 Gaussian Pulses	111
4.2.5 Parabolic Pulses	114
4.2.6 Range Precision and the CRLB	116
4.2.7 Gaussian Pulse CRLB	119
4.3 Chapter Summary	122

	Page
V. Gain Variation in APD Arrays	124
5.1 FLASH LADAR Data	124
5.2 Gauss-Newton Method for Gain Estimation	127
5.2.1 Detector Array Signal Model	128
5.2.2 Iterative Gain Estimation	130
5.2.3 Simulations	136
5.2.4 Gain Estimation with LADAR Data	139
5.3 Gain Equalization using Background Data	143
5.3.1 Gain Variation in Flash LADAR Data	144
5.3.2 Gain Variation Equalization	145
5.3.3 Range Measurements	147
5.4 Chapter Summary	152
VI. Conclusion	153
6.1 Poisson-Distributed LADAR Signal Models	153
6.2 Range Precision of LADAR Systems	154
6.3 Gain Variation in APD Arrays	155
6.4 Summary	156
Appendix A. Photoelectron Statistics	157
A.1 Integration of Intensity	157
A.2 Photon Arrival Statistics	158
A.3 Poisson Approximation to Negative Binomial Distribution	160
A.4 Photon Arrivals and Quantum Efficiency	161
Appendix B. Parabolic and Gaussian Pulse Properties	163
B.1 Parabolic Pulse Properties	163
B.2 Gaussian Pulse Properties	166
B.3 Parabolic and Gaussian Pulse Comparison	168
B.4 Power Full-Width Half-Maximum	170
B.5 Time-Bandwidth Products	170
Appendix C. Lower Bound on Estimator Variance	174
C.1 Decomposition of the Fisher Information Matrix	174
C.2 Relationship Between CRLB and FIM Diagonal Elements	175
Bibliography	178

List of Figures

Figure		Page
1.1.	LADAR system block diagram.	3
1.2.	LADAR signal block diagram.	5
2.1.	Fresnel propagation of a Gaussian beam.	16
2.2.	Gaussian plane wave beam divergence.	17
2.3.	Round-trip range parabolic pulse LADAR signal model.	22
2.4.	Fisher information matrix functions.	30
3.1.	Parabolic pulse LADAR signal model.	37
3.2.	Fisher information matrix functions.	43
3.3.	Test of range estimation algorithms.	60
3.4.	Simulation of range estimation.	61
3.5.	Simulation of gain estimation.	63
3.6.	Simulation of gain estimation.	65
3.7.	Obscured target LADAR signal model.	67
3.8.	Obscured target model FIM function.	71
3.9.	Range estimation with obscured target.	77
3.10.	Gain estimation with obscured target.	77
3.11.	Bias estimation with obscured target.	78
3.12.	FIM functions for variable pulse width model.	84
3.13.	Range estimation with variable width model.	89
3.14.	Pulse width estimation simulations.	92
4.1.	Range estimation with Gaussian and Poisson noise.	99
4.2.	Bias in range estimates.	101
4.3.	Range CRLB for fixed total energy LADAR.	104
4.4.	Laser beams and surface orientation.	107
4.5.	Reflected laser pulse.	108

Figure		Page
4.6.	Shape of pulses reflected off tilted surfaces.	114
4.7.	Convolution of parabolic and Gaussian pulses.	116
4.8.	Range CRLBs for tilted targets.	121
4.9.	System parameter trades and ilted target CRLBs.	122
5.1.	LADAR image of target panel.	126
5.2.	Range-resolved LADAR signals.	127
5.3.	Array Signal Model Simulation.	137
5.4.	Iterative range and amplitude estimation.	140
5.5.	Estimation of gain and signals.	140
5.6.	Gain variation estimation with LADAR data.	141
5.7.	Range and amplitude estimation with LADAR data.	142
5.8.	Range resolved LADAR data.	145
5.9.	LADAR data from target-free pixels.	146
5.10.	Gain equalized LADAR data.	147
5.11.	Illustration of range estimation algorithm.	148
5.12.	Raw and equalized range estimates.	150
A.1.	Poisson approximation as count degeneracy decreases.	160
A.2.	Poisson approximation as diversity increases.	161
B.1.	Parabolic pulse Fourier transform.	164
B.2.	Parabolic pulse energy spectrum.	167
B.3.	Gaussian pulse Fourier transform.	169
B.4.	Gaussian pulse energy spectrum.	169
B.5.	Parabolic and Gaussian pulse comparison.	170
B.6.	Parabolic and Gaussian pulse power.	171

List of Tables

Table		Page
3.1.	Parabolic Pulse Signal Model CRLBs.	53
3.2.	Obscured Target Model Fisher Information Matrix Elements.	73
3.3.	Obscured Target Model Cramer-Rao Lower Bounds.	73
3.4.	Variable Width Model Fisher Information Matrix Elements.	88
3.5.	Variable Width Model Cramer-Rao Lower Bounds.	88
5.1.	Range Error in APD Array LADAR Data.	151

List of Symbols

Symbol		Page
M_x^2	Beam quality	10
σ_x^2	Normalized spatial variance	11
I_0	Irradiance	11
U_0	Optical field	11
\bar{x}	Beam irradiance centroid	11
$\sigma_{s_x}^2$	Normalized spatial frequency variance	11
\hat{I}_0	Spatial frequency distribution	12
\bar{s}_x	Beam spatial frequency distribution centroid	12
z	Propagation distance	13
W_0	Beam size at aperture	13
F_0	Focus distance	13
k	Wave number	13
P	Power	13
W_z	Beam size after propagation	14
θ_d	Gaussian beam divergence angle	15
D_a	Aperture diameter	15
θ_p	Plane wave divergence angle	15
i	Photocurrent	19
A_d	Binary detector area function	19
\mathfrak{R}	Detector responsivity	19
G	Gain	19
η	Quantum efficiency	19
h	Planck's constant	19
ν	Optical frequency	19
P_r	Received power	19

Symbol		Page
P_t	Transmitted power	20
η_s	LADAR system efficiency	20
ρ	Target reflectivity	20
A_r	Receiver area	20
R	Range to target	20
c	Speed of light	20
I	Mean photoelectrons per sample	20
R_{rt}	Round-trip range	20
t_k	Sample time	20
p_w	Parabolic pulse width	20
B	Bias or background	20
q_s	Stochastic noise term	21
D	Photocount random variable	21
\mathcal{M}	Diversity	23
d	Photocount realization	23
J	Fisher information matrix	25
l	Log-likelihood function	26
L	Likelihood function	26
t_d	Sampling duration	28
f_s	Sampling frequency	28
Δt	Sample time spacing	28
V_{bias}	Bias voltage	29
V_{bd}	Breakdown voltage	29
p	Gain model constant	29
p_p	Parabolic pulse	56
t_{rt}	Round-trip time	58
$f_n = f_s/2$	Nyquist frequency	61
θ	Unknown signal parameter	90

Symbol		Page
ϕ	Surface orientation angle	106
P_{tilt}	Received power from tilted surface	110
p_g	Gaussian pulse	111
w	Gaussian pulse width	111
τ_g	Gaussian pulse full-width half-maximum	111
w_t	Received pulse width from tilted surface	113
τ_p	Parabolic pulse full-width half-maximum	114
E_e	Electrical energy	117
r	Received signal	117
N_0	Height of White Noise PSD	117
σ^2	Gaussian noise variance	117
A_m	Signal amplitude	128
D	Set of photocount random variables	129
d	Set of photocount realizations	129
g	Set of unknown gain values	129
a	Set of unknown amplitude values	129
r	Set of unknown range values	129
θ	Vector of unknown signal parameters	130
Λ	Gauss-Newton iteration matrix	130
λ	Gauss-Newton iteration vector	130
P_b	Background power	143
i_b	Background photocurrent	145
W	Energy incident on receive aperture	157
A_r	Binary receiver aperture function	157
\bar{W}	Mean energy	157
\bar{N}	Mean number of photons	159
h	Planck's constant	159
ν	Optical frequency	159

Symbol		Page
δ_c	Count degeneracy parameter	160
G_p	Parabolic pulse energy spectral density	165
E_p	Parabolic pulse energy	166
G_g	Gaussian pulse energy spectral density	167
E_g	Gaussian pulse energy	167
σ_t	Mean square duration	170
σ_f	Mean square bandwidth	170

List of Abbreviations

Abbreviation		Page
LADAR	Laser Detection and Ranging	1
PMT	Photomultiplier Tube	5
APD	Avalanche Photodiode	5
MLE	Maximum Likelihood Estimate	7
CRLB	Cramer-Rao Lower Bound	8
TOF	Time of Flight	9
LOS	Line of Sight	9
FIM	Fisher Information Matrix	25
ZZLB	Ziv-Zakai Lower Bound	59
SNR	Signal-to-Noise Ratio	59
AWGN	Additive White Gaussian Noise	96
TR	Transmit-Receive	106
FWHM	Full-Width Half-Maximum	111
PSD	Power Spectral Density	117
ROIC	Readout Integrated Circuit	125
IFOV	Instantaneous Field of View	125
IID	Independent and Identically Distributed	128
ESD	Energy Spectral Density	165
TBP	Time-Bandwidth Product	170

RANGE PRECISION OF LADAR SYSTEMS

I. Introduction

Laser detection and ranging or LADAR systems have developed rapidly in recent years. LADAR is analogous to radar, but is done at optical wavelengths rather than radio frequencies. The use of optical wavelengths, which are roughly one-thousandth the length of the shortest radar wavelengths, yields many benefits and challenges.

LADAR systems are used for many remote sensing applications. They are used to measure wind speeds in clear air [19]. LADAR systems with two or more wavelengths are used to detect and measure concentrations of certain gasses in the atmosphere [28]. Some LADARs interfere received laser light with a local laser in order to measure Doppler shift [8]. These coherent LADARs are sensitive enough to measure surface vibrations on remote objects [17]. However, a primary application of LADAR has always been the measurement of range to a target.

Different LADAR technologies are used to measure target range with a laser. Amplitude and frequency modulation of continuous-wave lasers has been used to measure range [44]. But the most commonly-used technique is to transmit a short-duration laser pulse and measure its time of flight. Multiple range measurements taken along different lines of sight can be combined to create a three-dimensional image of a scene. These three-dimensional images are valuable in applications such as mapping and target recognition.

The precision of range measurements made with a LADAR system is limited by noise. The fundamental source of noise in a laser signal is the random time between photon arrivals. This phenomenon, called shot-noise, can be modeled as a Poisson random process [21]. Other noise sources in LADAR systems can also be modeled as Poisson processes [31].

Noise in LADAR systems is not always modeled using the Poisson distribution. The noise in systems with high levels of electronic noise can be accurately characterized with a Gaussian distribution [22]. The various noise models (Poisson or Gaussian) can be used to derive limits on the precision of range measurements.

This dissertation examines several different signal and noise models for LADAR systems transmitting short pulses of laser light. Limits on range precision are derived for different scenarios such as calculating range to a target that is partially obscured or is tilted at an oblique angle when the LADAR observes it. Electronic effects in systems can distort the data recorded by a LADAR. This distortion can affect range measurements. Thus, methods of correction are developed and tested. In all cases, the goal of this dissertation is to characterize the precision of LADAR range measurements and to develop new methods that improve the process of range estimation.

1.1 LADAR Systems

1.1.1 LADAR System Diagram. All LADAR systems include a laser transmitter and a receiver designed to detect laser light reflected from a target. A LADAR system block diagram is shown in Fig. 1.1. The transmitter emits laser light toward the target. In an imaging system the target is the solid object in the scene. However, some LADAR systems are designed to observe laser light scattered from aerosols. A fraction of the light hitting the target is reflected into the LADAR's receiver. That light is detected and processed by the system.

A wide variety of lasers have been used as LADAR transmitters. Wavelengths between the ultraviolet and the long wave infrared have been employed. However, it is most common to use lasers that operate in the near infrared when building a LADAR system. The near infrared band of wavelengths offers reasonably good eye-safety. Because most optical telecommunication equipment operates in the near infrared, optical components designed to operate at those wavelengths are plentiful and relatively inexpensive.

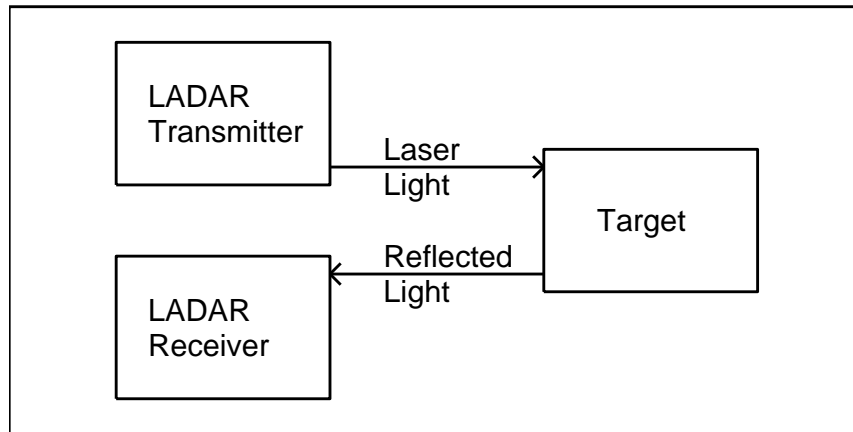


Figure 1.1: Block diagram used to model a LADAR system.

LADAR systems also need receivers to detect reflected laser light. The receiver consists of a lens that focuses reflected laser light onto a photodetector. The photodetector converts the received light into an electrical signal. That signal is processed in order to measure information about the target such as range, reflectivity, and velocity.

Some LADAR systems use the same aperture to transmit and receive laser light. Such systems are called monostatic. Systems with separate transmit and receive apertures are referred to as bistatic. Bistatic systems usually have transmit and receive apertures that are located very near each other.

1.1.2 Pulsed LADAR Systems. Laser detection and ranging systems can be used to measure range to targets. In order to measure range, typical LADAR systems transmit short pulses of laser light. There are alternative methods of measuring target range such as with a chirped waveform and coherent processing. But the most common method of range estimation involves measuring the time of flight for a short duration laser pulse.

Typical LADAR systems transmit short laser pulses using a process called Q-switching. The Q-switching process allows relatively large amounts of energy to build within the laser cavity before being released over a very short period of time. The energy is released from the laser cavity using a device such as a rotating mirror or

a Pockels cell crystal [38]. Laser pulses created by Q-switched systems can have durations measured in nanoseconds.

Given a fixed pulse energy, shorter pulses provide better range precision. However, shorter pulses require optical components and photodetectors that can tolerate higher peak powers. Shorter pulses also demand faster sampling. Generation of laser pulses is often accomplished using a component within the laser cavity called a Q-switch. Shorter pulses necessitate the use of more sophisticated and expensive Q-switches. These engineering issues place practical limits on how short a laser pulse can be made. Current LADAR systems typically transmit pulses that are a few nanoseconds long and sample those pulses at a rate around one Gigahertz.

The short pulses created by the Q-switching process yield excellent range precision. LADAR range precision of less than 3 cm has been claimed [2]. However, short pulses place demands on the detection and digitization hardware in LADAR systems since nanosecond-class pulses have bandwidths on the order of a Gigahertz.

1.1.3 Imaging LADAR Systems. Development of LADAR imaging systems is advancing rapidly. Early LADAR imaging systems used few detectors and usually relied on mechanical scanning systems to produce images with large numbers of pixels. Newer systems use arrays of photodetectors and can produce images with large numbers of pixels without the use of mechanical scanning. Imaging LADARs with more than ten thousand pixels are commercially available. However, it has been shown that the photodetector arrays in these compact imaging systems can have undesirable electronic effects that degrade range precision. A key undesirable effect that has been observed in photodetector arrays is the phenomenon of gain variation.

1.1.4 Airborne LADAR Systems. Airborne LADAR systems are used for three-dimensional mapping and applications such as target recognition. Typical systems transmit beams through apertures that are several inches wide and use pulses that are a few nanoseconds in duration. If the pulse reflects off a target that is tilted

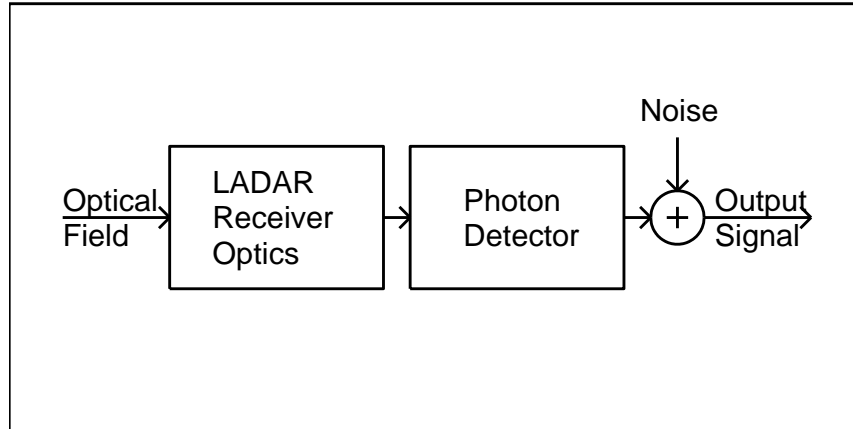


Figure 1.2: Block diagram describing a LADAR system’s receiver and output signal.

with respect to the line-of-sight, then the reflection process will elongate the received signal as compared to transmitted pulse. If the range is more than a few kilometers and the target is tilted more than about forty-five degrees, the increase in the width of the received pulse produces a significant drop in range precision. The loss in precision due to target tilt is quantified in this dissertation.

1.2 LADAR Signals

1.2.1 LADAR Receivers. A LADAR system makes measurements of target parameters by processing the laser signal detected by its receiver. A LADAR receiver block diagram is shown in Fig. 1.2. Transmitted laser light reflects off of objects in the scene. Some of the reflected laser light is intercepted by receiver optics. Those optics focus the light onto a photodetector, which is small compared to the receiver aperture. The photodetector converts the focused optical field into an electrical signal. Typical detectors are photomultiplier tubes (PMT)s, p-i-n diodes, and avalanche photodiodes (APD)s.

There is noise in the received signal. One source of noise is background light detected by the photodetector. The background light level is roughly constant over the time it takes to record a laser pulse. Thus, it interferes with detection of that pulse and degrades measurements of signal parameters such as time of flight. There

are also electronic noise sources in the system. Photodetectors generate false signals called dark current. The signal quantization process (analog-to-digital conversion) also introduces error. These processes are all sources of noise in the received signal [30].

A LADAR must make multiple target range measurements to create a three-dimensional image. Arrays of avalanche photodiodes are used in LADAR receivers to create three-dimensional images. Avalanche photodiodes convert laser light into an electrical signal called the photocurrent. The photocurrent is related to the irradiance of the received light by a parameter called the gain. Ideally, the gain would remain constant over time. However, it has been demonstrated experimentally that the gain varies in some situations due to limitations in photodiode array design. It has also been shown that gain equalization techniques can reduce some of the gain variation in the data.

In order to characterize gain variation in LADAR detector arrays, nonlinear models are also being used to describe received LADAR signals. The nonlinear models trade simplicity for realism. It has been shown in a real LADAR that the nonlinear effects are significant and that attempts should be made to correct for these effects [37]. Correction methods were proposed, but little work was done to determine range precision in the nonlinear signal model.

1.2.2 LADAR Signals. The time between photon arrivals at the detector varies. The fluctuating number of photons arriving in a time interval is called shot noise. Shot noise is a source of error in LADAR measurements. Goodman has shown that when measuring coherent or partially coherent light, the number of signal photocounts observed in a time interval is a negative binomial random variable [11, 13]. Negative binomial random variables have Fano factors (the ratio of the variance to the mean [7]) greater than one. A high Fano factor indicates that the signal fluctuation is large compared to the signal energy. LADAR systems are often designed to reduce the Fano factor through the use of diversity. Spatial averaging of statistically independent laser speckle cells and the detection of multiple polarizations are common

methods used to increase diversity. As diversity increases, the Fano factor approaches one, and the negative binomial distribution converges to the Poisson distribution. Regardless of the diversity, the Poisson distribution is also an accurate approximation to the negative binomial distribution whenever the mean number of photocounts is low [13]. Because the Poisson distribution can accurately approximate the negative binomial distribution, it is used in this dissertation to model the number of observed photocounts in a LADAR signal.

In addition to the received laser pulse, signals are produced by noise sources. Noise sources include background photons, dark current, and thermal noise [21]. These sources of noise corrupt the LADAR signal and degrade the precision of range measurements. Arrivals of background photons, dark counts, and thermal noise counts are random. In [21] and [31], it is assumed that these noise sources are Poisson processes. This model is reasonable since it only requires independent exponentially-distributed times between noise incidents. The number of counts produced by a Poisson process within a specified time interval is a Poisson random variable. Sums of statistically independent Poisson random variables are Poisson with mean equal to the sum of the means of the constituent random variables. Thus, the entire observed LADAR signal (laser pulse and noise) can be modeled as a sequence of Poisson random variables.

The Poisson distribution accurately characterizes the signals recorded by shot-noise limited LADAR systems. However, the noise in a LADAR signal is sometimes dominated by electronic noise sources [9]. In that case, the stochastic component of the LADAR signal can be modeled with a Gaussian distribution [22]. The Gaussian distribution is often easier to work with than the Poisson distribution.

1.2.3 Signal Parameter Estimation. LADAR signal processing involves estimating parameters such as range, amplitude, and background level. Methods of parameter estimation include maximum likelihood estimation (MLE) and least squares.

In some cases, the parameter estimates are derived empirically because there are often simple and nearly-optimal estimators of signal parameters available.

Though many different parameters can be estimated, the key parameter is usually range to target. In order to make a precise measurement of target range, the received laser pulse is usually match-filtered. After filtering, a peak-fitting routine is used to calculate a range estimate to the target. However, randomness in the signal creates fluctuations in the output of the peak-fitting algorithm. These fluctuations cause error in the range estimates. The distribution of the observed signal is assumed known. However, the combination of matched-filtering and peak-fitting makes it difficult, if not impossible, to derive the distribution of the actual range estimate. Instead, the range precision is analyzed using the Cramer-Rao Lower Bound (CRLB). The CRLB provides a lower limit on the variance of any unbiased estimate of a parameter such as range. The CRLB is valid regardless of the exact filtering and fitting algorithms used, as long as those algorithms produce unbiased range estimates.

II. Problem Background

Typical imaging LADAR systems transmit short pulses of laser light. Modern systems use pulses that are only a few nanoseconds in duration. The pulses scatter off of objects in a scene. The backscattered laser light is detected by the LADAR's receiver. The received signal is digitized and converted to an estimate of range to the target based on the laser pulse's time of flight (TOF). Multiple estimates of target range can be combined into a three-dimensional image of a scene.

Range precision is limited by the length of the transmitted laser pulse, the pulse's shape, and noise sources in the LADAR system. In order to predict limits on LADAR range precision, mathematical models of the shape of the laser pulse are needed. Statistical methods are employed to simulate the noise sources present in the LADAR system. In this chapter, laser beam models used in the literature and in this dissertation are described. The stochastic methods used to simulate noise sources are also presented.

Laser beams transmitted by LADAR systems are characterized by their shape transverse to the line of sight (LOS) and their shape along the line of sight. The transverse shape describes the beam's irradiance pattern. As the beam propagates, its transverse shape varies due to diffraction. The beam is also described by a shape along the LADAR LOS. This shape models the instantaneous power in the beam and can be thought of as a temporal function. The beam's shape along the LOS varies little as the beam propagates. However, the pulse shape received by the system can be very different from the transmitted pulse shape because of the reflection process.

Throughout this dissertation, it is assumed that the transverse beam shape is Gaussian. The reasons for this assumption and its consequences are discussed in Sec. 2.1. Several different transmitted temporal (along line of sight) pulse shape models are used in the literature. In this dissertation, either a truncated parabola or a Gaussian function is used to describe the temporal shape of a laser pulse. The parabola accurately models the steep leading edge of real laser pulses. It also proves easier to work with than other temporal pulse shape models when deriving bounds

on range precision in the presence of Poisson-distributed noise. The parabolic pulse model is discussed in Sec. 2.1.6. The Gaussian shape does a good job of modeling the smooth trailing edge of a laser pulse. The Gaussian model is described in Chapter IV.

2.1 Laser Beam Propagation

The irradiance pattern of the laser beam transmitted by a LADAR system can be many different shapes. The most common shape is a Gaussian pattern. However, top-hat beams, which have a flat irradiance pattern as they exit the LADAR transmitter aperture, can also be used. There are also higher-order modes described by Hermite-Gaussian functions in rectangular coordinates [42] and by Laguerre-Gaussian functions in cylindrical coordinates [3]. The fundamental mode created by a laser resonator is the called the zero-order transverse electromagnetic or TEM00 mode. Typical systems transmit TEM00 Gaussian beams.

Zero-order transverse electromagnetic Gaussian beams are usually used in LADAR systems because they produce the best-quality diffraction patterns in the far field. Beam quality is described in detail in the following section.

2.1.1 Beam Quality. In [39–41], Siegman developed a beam quality metric. The metric is denoted M_x^2 . This metric is the product of the beam’s normalized irradiance standard deviation and the beam’s normalized spatial frequency standard deviation along an axis transverse to the LADAR line of sight. A laser beam actually has two beam quality measurements. There is one measurement along each axis perpendicular to the LOS (the x -axis and the y -axis). The following equations used to calculate beam quality show it being computed along the x -axis. It is straightforward to modify them to calculate beam quality along the y -axis in case that measurement (M_y^2) is desired.

Beam quality along the x -axis is [39]

$$M_x^2 = 4\pi\sigma_x\sigma_{s_x}. \quad (2.1)$$

The normalized spatial variance σ_x^2 is a function of the beam's irradiance pattern $I_0(x, y)$. Irradiance has units of power per area. Irradiance is the magnitude squared of optical field $U_0(x, y)$.

$$I_0(x, y) = |U_0(x, y)|^2. \quad (2.2)$$

The terms irradiance and intensity are often used interchangeably in the optics literature [3]. However, in the field of radiometry, intensity has units of power per area per solid angle [56]. Therefore, intensity could also be defined as irradiance per solid angle. To avoid confusion, only the term irradiance is used in this dissertation when referring to the optical field $U_0(x, y)$.

The normalized spatial variance σ_x^2 is

$$\sigma_x^2 = \frac{\int_{-\infty}^{\infty} \int_{-\infty}^{\infty} (x - \bar{x})^2 I_0(x, y) dx dy}{\int_{-\infty}^{\infty} \int_{-\infty}^{\infty} I_0(x, y) dx dy}. \quad (2.3)$$

The variable \bar{x} in Eq. 2.3 is the beam's irradiance centroid in the x -direction. The beam centroid, which is the beam's center of gravity, is (see p. 662 of [38])

$$\bar{x} = \frac{\int_{-\infty}^{\infty} \int_{-\infty}^{\infty} x I_0(x, y) dx dy}{\int_{-\infty}^{\infty} \int_{-\infty}^{\infty} I_0(x, y) dx dy}. \quad (2.4)$$

Calculation of the normalized spatial frequency variance $\sigma_{s_x}^2$ begins with computation of the two-dimensional Fourier transform of the optical field $U_0(x, y)$. This

function is denoted $\widehat{U}_0(s_x, s_y)$. This Fourier transform is

$$\widehat{U}_0(s_x, s_y) = \int_{-\infty}^{\infty} \int_{-\infty}^{\infty} U_0(x, y) \exp[-i2\pi(s_x x + s_y y)] dx dy \quad (2.5)$$

where $i = \sqrt{-1}$. The spatial frequency distribution $\widehat{I}_0(s_x, s_y)$ is the magnitude squared of this Fourier transform.

$$\widehat{I}_0(s_x, s_y) = \left| \widehat{U}_0(s_x, s_y) \right|^2. \quad (2.6)$$

The normalized variance of the spatial frequency distribution is

$$\sigma_{s_x}^2 = \frac{\int_{-\infty}^{\infty} \int_{-\infty}^{\infty} (s_x - \bar{s}_x)^2 \widehat{I}_0(s_x, s_y) ds_x ds_y}{\int_{-\infty}^{\infty} \int_{-\infty}^{\infty} \widehat{I}_0(s_x, s_y) ds_x ds_y}. \quad (2.7)$$

where \bar{s}_x is the centroid of the spatial frequency distribution. This variable is computed in the same way the irradiance centroid was calculated in Eq. 2.4.

$$\bar{s}_x = \frac{\int_{-\infty}^{\infty} \int_{-\infty}^{\infty} s_x \widehat{I}_0(s_x, s_y) ds_x ds_y}{\int_{-\infty}^{\infty} \int_{-\infty}^{\infty} \widehat{I}_0(s_x, s_y) ds_x ds_y}. \quad (2.8)$$

Siegman showed in [39] that for any arbitrary laser beam

$$M_x^2 \geq 1 \quad (2.9)$$

with equality if and only if the irradiance pattern has a Gaussian shape. Thus, the beams with the best quality have Gaussian irradiance patterns and Gaussian beams are almost always used in LADAR systems.

Combining Eqs. 2.1 and 2.9 shows that

$$\sigma_x \sigma_{s_x} \geq \frac{1}{4\pi}. \quad (2.10)$$

This bound on the product of space and spatial frequency bandwidths is equivalent to the bound on time and frequency that appears in literature on radar and signal processing [51].

2.1.2 Fresnel Propagation of Gaussian Beams. The optical field after propagating distance z is denoted $U_0(r, z)$. The field for a Gaussian beam at the aperture ($z = 0$) is given by Eq. 8 of [3].

$$U_0(r, 0) = \left(\frac{2P}{\pi W_0^2} \right)^{1/2} \exp \left(-\frac{1}{2} \alpha k r^2 \right) \quad (2.11)$$

where

$$\alpha = \frac{2}{kW_0^2} + \frac{i}{F_0}. \quad (2.12)$$

In Eq. 2.12, W_0 is the beam size, F_0 is the focus distance, and $k = 2\pi/\lambda$ is the wave number. The beam size (W_0) is the e^{-1} radius of the magnitude of the field at the aperture. In other words, it is the e^{-1} radius of $|U_0(r, 0)|$. The power in this beam is denoted P .

$$P = \int_0^{2\pi} \int_0^\infty |U_0(r, 0)|^2 r dr d\theta = 2\pi \int_0^\infty |U_0(r, 0)|^2 r dr \quad (2.13)$$

where the radial symmetry in the field has been exploited. The power in Eq. 2.13 is measured at an instant. In LADAR systems transmitting laser pulses, the power varies with time.

The Fresnel propagation of the field from Eq. 2.11 is

$$U_0(r, z) = \left(\frac{2P}{\pi W_0^2} \right)^{1/2} \frac{1}{1 + i\alpha z} \exp \left[ikz - \frac{\alpha k r^2}{2(1 + i\alpha z)} \right]. \quad (2.14)$$

This is Eq. 24 of [3]. The irradiance after propagating distance z is

$$I_0(r, z) = \frac{2P/\pi W_0^2}{(1 - z/F_0)^2 + (\lambda z/\pi W_0^2)^2} \exp \left[-\frac{2(r/W_0)^2}{(1 - z/F_0)^2 + (\lambda z/\pi W_0^2)^2} \right]. \quad (2.15)$$

When the beam is collimated ($F_0 \rightarrow \infty$), the propagated irradiance is

$$I_0(r, z)|_{F_0 \rightarrow \infty} = \frac{2P/\pi W_0^2}{1 + (\lambda z/\pi W_0^2)^2} \exp \left[-\frac{2(r/W_0)^2}{1 + (\lambda z/\pi W_0^2)^2} \right]. \quad (2.16)$$

When the beam is at the focus distance ($z = F_0$), the propagated irradiance is

$$\begin{aligned} I_0(r, F_0) &= \frac{2P}{\pi W_0^2} \left(\frac{\pi W_0^2}{\lambda F_0} \right)^2 \exp \left[-2 \left(\frac{\pi W_0 r}{\lambda F_0} \right)^2 \right] \\ &= \frac{2\pi P W_0^2}{\lambda^2 F_0^2} \exp \left[-2 \left(\frac{\pi W_0 r}{\lambda F_0} \right)^2 \right] \end{aligned} \quad (2.17)$$

2.1.3 Gaussian Beam Size. The beam size W_0 is measured at the LADAR system's transmitter aperture. As the beam propagates, its size varies. The size as a function of range is calculated from the field magnitude equation, which is the square root of the beam's irradiance. The Fresnel propagated field magnitude is

$$|U_0(r, z)| = \left[\frac{2P/\pi W_0^2}{(1 - z/F_0)^2 + (\lambda z/\pi W_0^2)^2} \right]^{1/2} \exp \left[-\frac{(r/W_0)^2}{(1 - z/F_0)^2 + (\lambda z/\pi W_0^2)^2} \right]. \quad (2.18)$$

The beam size at range z , which is denoted W_z , is

$$W_z = W_0 \left[\left(1 - \frac{z}{F_0} \right)^2 + \left(\frac{\lambda z}{\pi W_0^2} \right)^2 \right]^{1/2}. \quad (2.19)$$

This is the radius at which the field magnitude is below the peak magnitude by a factor of e^{-1} .

The beam size at range z when the beam has been focused is

$$W_{F_0} = \frac{\lambda F_0}{\pi W_0}. \quad (2.20)$$

When the beam is collimated ($F_0 \rightarrow \infty$), the beam size at range z is (see also Eq. 5.85 of [28])

$$W_z|_{F_0 \rightarrow \infty} = W_0 \left[1 + \left(\frac{\lambda z}{\pi W_0^2} \right)^2 \right]^{1/2}. \quad (2.21)$$

The equation for the propagated beam size W_z (Eq. 2.19) can be used to write the field magnitude and irradiance equations in simpler forms. The field magnitude from Eq. 2.18 can be written

$$|U_0(r, z)| = \left(\frac{2P}{\pi W_z^2} \right)^{1/2} \exp \left(-\frac{r^2}{W_z^2} \right). \quad (2.22)$$

The propagated irradiance from Eq. 2.17 can be expressed

$$I_0(r, z) = \frac{2P}{\pi W_z^2} \exp \left(-2\frac{r^2}{W_z^2} \right). \quad (2.23)$$

2.1.4 Beam Divergence Angle. In the far field, the beam's size is approximately proportional to the distance of propagation. Because of this linear dependence, the beam's size is often measured in terms of the angle between the axis of propagation and the e^{-1} field magnitude. The TEM00 Gaussian beam divergence angle θ_d is (Eq. 5.86 of [28])

$$\theta_d = \frac{\lambda}{\pi W_0}. \quad (2.24)$$

The Gaussian beam divergence angle can be compared to the divergence angle for a plane wave truncated by an aperture with diameter D_a . The plane wave divergence angle θ_p is (Eq. 5.87 of [28])

$$\theta_p = 1.22 \frac{\lambda}{D_a}. \quad (2.25)$$

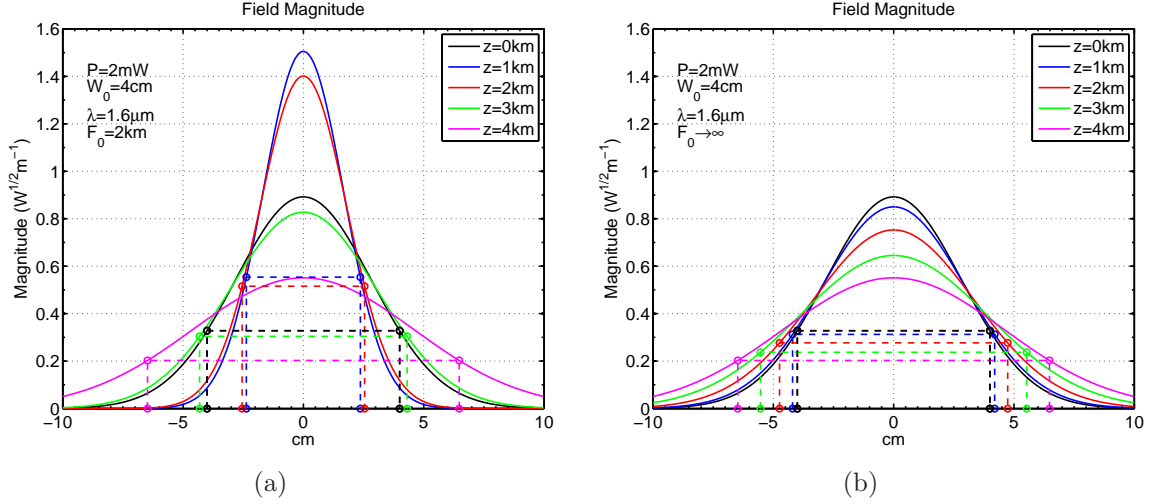


Figure 2.1: (a) Propagation of a 4 cm beam that's focused at 2 km. (b) Propagation of a 4 cm beam that is focused at infinity (collimated).

The scaling of 1.22 in the previous equation is the first zero of $J_1(\pi x)$ where J_1 is the modified Bessel function of the first kind of order one. (See Table 4.1 of [13].)

2.1.5 Propagation Examples. Examples of propagated TEM00 Gaussian beams are shown in Fig. 2.1. In Fig. 2.1a, the beam is focused at 2 km. The beam size is 4 cm and the wavelength is $1.6\mu\text{m}$. Notice that the beam is narrower after 1 km of propagation than at the 2 km focus distance. A beam focused at a particular distance has the narrowest possible value at that distance. But it could be even narrower at a shorter distance than the focus. In Fig. 2.1b, propagated collimated Gaussian beams are shown. In the collimated case, the beam's size increases monotonically with range.

The Gaussian beam size as a function of range is shown in Fig. 2.2a. Beams focused at 2, 5, and 10 km are shown, along with a collimated beam. The divergence angle from Eq. 2.24 is shown for comparison. Notice that the beam focused at short range (2 km) begins to diverge faster than the collimated beam at longer ranges. If the beams propagate far enough, any Gaussian beam not collimated will eventually begin to diverge faster than the Eq. 2.24 divergence angle.

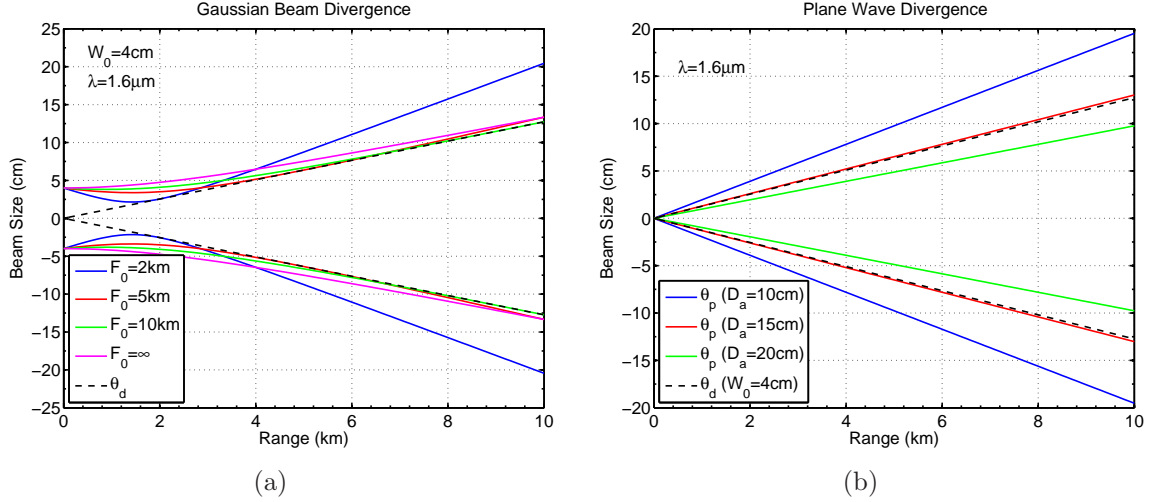


Figure 2.2: (a) Beam divergence for Gaussian beams.
(b) Beam divergence for plane wave beams.

The plane wave divergence angle from Eq. 2.25 is shown in Fig. 2.2b. The angle for 10, 15, and 20 cm apertures is illustrated. Note that the 15 cm plane wave divergence angle is nearly equal to the Gaussian beam divergence angle for a transmitted beam size of 4 cm.

2.1.6 Temporal Laser Pulse Shape. Derivation of the Cramer-Rao lower bound on range precision requires a mathematical model of the received laser pulse's temporal shape. Several different LADAR pulse shape models are used in the literature. Both a Gaussian shape [22] and heavy-tailed (asymmetric) [15, 45] models have been previously employed. In this dissertation, parabolas and Gaussian shapes are used to describe the temporal shape of the transmitted laser pulse.

The Gaussian model does not work well when it is assumed that the noise is Poisson. In that case, CRLBs are very difficult to calculate. A very similar problem was considered by Winick [55]. That author considered the problem of calculating the CRLB on position of a Poisson-distributed Gaussian shape in two-dimensions. A CRLB was presented, but the author did not show a closed-form solution. However,

it is straightforward to calculate the range CRLB for a Gaussian pulse using the same sort of numeric expressions that are in [4, 55].

A solution for the shape of a pulse created by a Q-switched laser is presented by Siegman in [38]. However, that solution is expressed as an integral that must be evaluated numerically. Cramer-Rao lower bound analysis on such a signal would be difficult. Even if an exact solution for the shape of the transmitted laser pulse was used, the reflection process can distort the shape of that pulse, causing the received pulse to have a different shape. The truncated parabola used in this dissertation is not meant to be an exact representation of the true received signal. Rather, it is an adequate approximation of received pulse shape and it produces a relatively simple range CRLB in the Poisson noise case.

The various laser pulse shape models each have advantages and disadvantages. The asymmetric models from [15, 45] accurately simulate the relatively fast rise of a laser pulse. However, those models can overestimate the amount of pulse energy in the tail. The asymmetry also makes analytic analysis of range precision more difficult.

The parabolic shape generally models the fast rise of a real laser pulse better than the Gaussian model. However, the Gaussian model approximates the tail of the laser pulse better than the parabolic model. The parabolic model is truncated and does not have the tail that is present in a laser pulse. But since only a small fraction of the pulse energy is present in the tail of a real laser pulse, the inverted parabola is a reasonable approximation.

2.2 LADAR Detectors and Signals

2.2.1 Photodetectors and their Output Signals. A portion of the propagated field is reflected off the target. Some of the reflected field is intercepted by the LADAR system's receiver optics, which focus that field onto a photodetector. A LADAR's detector converts the received optical power to a photocurrent.

The photocurrent is denoted $i(t)$. It is a function of the optical field and the detector's responsivity.

$$i(t) = \int_{-\infty}^{\infty} \int_{-\infty}^{\infty} A_d(x, y) \mathfrak{R}(x, y) |U_0(x, y)|^2 dx dy \quad (2.26)$$

where $A_d(x, y)$, written as a function of spatial coordinates x and y , is the binary detector area function. This function represents the detector's active region. In this case, the optical field $U_0(x, y)$ is evaluated in the detector plane.

The variable $\mathfrak{R}(x, y)$ in Eq. 2.26 is detector responsivity. The responsivity is given by [13]

$$\mathfrak{R}(x, y) = \frac{Gq\eta(x, y)}{h\nu} \quad (2.27)$$

where G is the detector gain, q is the electron charge (1.602×10^{-19} Coulombs), $\eta(x, y)$ is the photodetector's quantum efficiency, h is Planck's constant (6.626×10^{-34} Joule-seconds), and ν is the optical frequency of the laser. The units of responsivity are electric charge per unit of energy (e.g., Coulombs per Joule), or equivalently, current per power (e.g., Amps per Watt). The spatial coordinates are frequently dropped from the responsivity and quantum efficiency terms because these values are often nearly uniform over the photodetector.

Targets observed by imaging systems are usually extended. That is, they are large compared to the size of the laser beam. When extended targets are observed, none of the transmitted laser power misses the target. However, some laser power is absorbed by the target materials. The materials illuminated by LADAR systems are often assumed to be Lambertian. This means that reflected laser light scatters equally in all directions.

The power received $P_r(t)$ by a LADAR system illuminating an extended Lambertian target can be approximated as [21, 31]

$$P_r(t) = \frac{\eta_s \rho A_r}{4R^2} P_t(t - 2R/c) \quad (2.28)$$

where $P_t(t)$ is the power transmitted at time t , η_s is the system efficiency, ρ is the target's reflectivity, A_r is the area of the receiver, R is the range to the target, and c is the speed of light. The system efficiency η_s is the product of the various loss factors such as atmospheric transmission and optical transmission. In a system using detector arrays, the received power is divided between the pixels in the array.

2.2.2 LADAR Signal Model. The following model was used in “*Flash light detection and ranging precision limits for returns from single opaque surfaces via Cramer-Rao bounds*” by Cain, et al. [4] to represent the mean number of photoelectrons per sample $I(t_k, x_n, y_m)$ in an imaging LADAR system. The model describes the received laser pulse as an upside-down parabola. This LADAR signal model is

$$\begin{aligned}
 I(t_k, x_n, y_m) & \qquad \qquad \qquad (2.29) \\
 = G(x_n, y_m) & \left\{ 1 - \frac{[R_{rt}(x_n, y_m) - t_k c]^2}{(c p_w)^2} \right\} \text{rect} \left[\frac{R_{rt}(x_n, y_m) - t_k c}{2 c p_w} \right] \\
 & + B(x_n, y_m) + q_s(t_k, x_n, y_m)
 \end{aligned}$$

where gain term $G(x_n, y_m)$ is the peak mean number of photoelectrons per sample from the target, $R_{rt}(x_n, y_m)$ is the round-trip range to the target, t_k is the time at which the k -th sample is collected, p_w is the pulse width, c is the speed of light, and $B(x_n, y_m)$ represents a bias level on each pixel in the LADAR's detector array.

The variables m and n in Eq. 2.29 are the spatial indices in the LADAR image. These indices specify the coordinate of the detector in the receiver's detector array. They index x_m and y_n , which are the spatial coordinates. Since much analysis in this dissertation (e.g., CRLB derivations) is done on only the data from one pixel at a time, the spatial coordinates indexed by these variables are sometimes dropped in equations. However, it has been noted that a large signal incident on one detector can effect adjacent detectors in an imaging LADAR's focal plane array [37]. In such a case, it is not valid to ignore data from the other detectors in the array, and the spatial coordinates must be included in any analysis.

The bias term is the mean number of noise photoelectrons per sample observed by the detectors in the LADAR system. It represents the mean number of noise counts due to noise sources such as background light and dark current. The term $q_s(t_k, x_n, y_m)$ is a stochastic noise component in each voxel of the three-dimensional image. Inclusion of this term allows the noise level to vary for different samples from a particular pixel. The units of $q_s(t_k, x_n, y_m)$ are photoelectrons per sample. The stochastic noise term $q_s(t_k, x_n, y_m)$ is sometimes dropped from this equation since the gain and bias terms may accurately model the signal by themselves.

The $\text{rect}(x)$ function in Eq. 2.29 is the standard rectangle function from the optics and signal processing literature. It is defined in [13].

$$\text{rect}(x) = \begin{cases} 1 & \text{when } |x| < 1/2 \\ \frac{1}{2} & \text{when } |x| = 1/2 \\ 0 & \text{when } |x| > 1/2 \end{cases} . \quad (2.30)$$

The parabolic pulse shape used in the signal model from Eq. 2.29 is illustrated in Fig. 2.3. This illustration shows that the pulse width p_w in the parabolic signal model is the distance between the points that are three-quarters of the maximum pulse height. The entire pulse width is actually $2p_w$. The bias illustrated in Fig. 2.3 is one ($B = 1$) and the gain is three ($G = 3$). The round-trip range is ten meters ($R_{rt} = 10$ m). It has been assumed that the stochastic noise term is zero, i.e., $q_s(t_k, x_n, y_m) = 0$, in this figure.

2.2.3 Photoelectron Probability Density Functions. The photocurrent is proportional to the number of photoelectrons observed by the LADAR photodetector. The observed number of photoelectrons is denoted $D(t_k, x_n, y_m)$. The process of converting a photon to a photoelectron is called a photoevent. The number of photoevents that occur in some time duration is called the number of photocounts. These terms photoevent and photocounts are described in detail in Sec. 9.1 of *Statistical Optics* by Goodman [12].

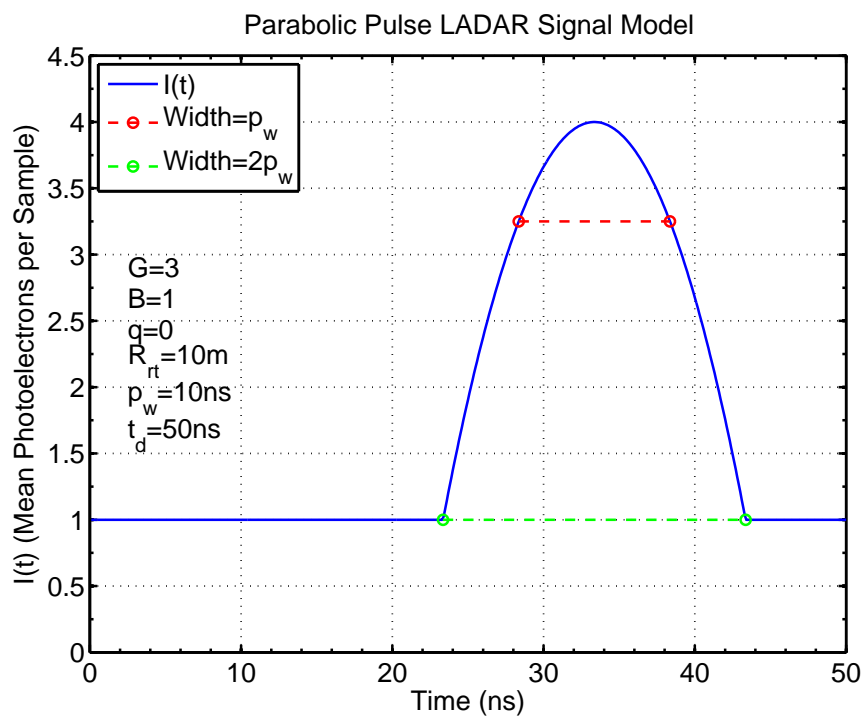


Figure 2.3: Illustration of the parabolic pulse LADAR signal model. This model is used for estimator derivations and for CRLB calculations.

Through much of this dissertation, it is assumed that the number of photocounts $D(t_k, x_n, y_m)$ has a Poisson distribution with mean $I(t_k, x_n, y_m)$ given by Eq. 2.29. It has been shown that the integrated irradiance of coherent light reflected off of a diffuse surface actually has a negative binomial distribution (see Sec. A.2). The number of photoelectrons observed by a LADAR system's receiver $D(t_k, x_n, y_m)$ is proportional to this integrated irradiance (see Sec. 9.2.3 of [12]). They are related by the gain and the quantum efficiency of the detector (often a photodiode or PMT) in the LADAR's receiver. The negative binomial distribution is parameterized by the mean number of photoelectrons and the diversity parameter \mathcal{M} . If the mean number of photoelectrons is fixed and the diversity \mathcal{M} becomes large in the negative binomial distribution, then that distribution converges to the Poisson distribution [12]. It has also been shown that as the mean number of photoelectrons approaches zero, that the negative binomial distribution is approximately equal to the Poisson distribution (see Sec. A.3).

Typical direct detection LADAR systems have a relatively high diversity. Thus, the Poisson distribution is often used as an accurate approximation to the true negative binomial distribution that describes the number of photoelectrons in the LADAR signal. For example, the system discussed in [4] had a diversity of about nine hundred ($\mathcal{M} \approx 900$). The Poisson distribution, used to model the number of photoelectrons counted in some time interval, is

$$\text{Prob} [D(t_k, x_n, y_m) = d(t_k, x_n, y_m)] = \frac{I(t_k, x_n, y_m)^{d(t_k, x_n, y_m)}}{d(t_k, x_n, y_m)!} e^{-I(t_k, x_n, y_m)}$$

where (2.31)

$$d(t_k, x_n, y_m) = 0, 1, 2, \dots$$

The variable $d(t_k, x_n, y_m)$ is a realization of photocurrent random variable $D(t_k, x_n, y_m)$. Variable $I(t_k, x_n, y_m)$ is the mean value for each sample.

2.2.4 Single Detector LADAR Signal Model. At this point, the mean photocurrent Eq. 2.29 is simplified. First, it is assumed that only one pixel in the LADAR

detector array is being analyzed. Thus, the spatial indexing coordinates (x_m, y_n) from Eq. 2.29 have been dropped in order to simplify the notation. Second, it is assumed that the stochastic noise term $q_s(t_k, x_n, y_m)$ is zero.

The parabolic pulse LADAR signal model without spatial dependence is

$$I(t_k) = G \left[1 - \frac{(R_{rt} - t_k c)^2}{(cp_w)^2} \right] \text{rect} \left(\frac{R_{rt} - t_k c}{2cp_w} \right) + B. \quad (2.32)$$

This equation is a simplification of the model from [4] (which is also shown in Eq. 2.29 of this dissertation). The more general model includes spatial dependence (denoted by variables x_n and y_m) and a stochastic noise term $q_s(t_k, x_n, y_m)$ for each voxel in the three-dimensional image.

In this chapter, it is assumed that each signal received by the LADAR system is statistically independent from all others. Therefore, the each pulse can be treated individually for purposes for parameter estimation and CRLB derivations. The fact that each pulse's signal is independent justifies the dropping of the spatial variables when going from Eq. 2.29 to Eq. 2.32.

The number of temporal samples recorded by the (m, n) -th detector is denoted K . If it is further assumed that the samples are statistically independent of each other, then the joint PDF of the photoelectrons observed at each sample is simply the product of the K PDFs for each individual sample. The assumption of statistical independence between samples comes from the fact that the photocurrent is assumed to be a Poisson process. Poisson processes are memoryless. Therefore, any sample

has no dependence on all previous samples. The joint PDF is

$$\begin{aligned}
& \text{Prob} [D(t_1) = d(t_1), D(t_2) = d(t_2), \dots, D(t_K) = d(t_K)] \\
&= p [d(t_1), d(t_2), \dots, d(t_K)] \\
&= \prod_{k=1}^K \frac{I(t_k)^{d(t_k)} e^{-I(t_k)}}{d(t_k)!} \\
&= \frac{\exp \left[- \sum_{k=1}^K I(t_k) \right] \prod_{k=1}^K I(t_k)^{d(t_k)}}{\prod_{k=1}^K d(t_k)!} \tag{2.33}
\end{aligned}$$

where $d(t_k)$ is the observed realization of the Poisson process and $I(t_k)$ is the mean number of photons from Eq. 2.32.

2.3 LADAR Range Precision

The precision of range estimates in LADAR systems has been studied in previous publications. This precision is bounded using Cramer-Rao analysis. Derivation of the CRLB requires a statistical model for the received signal. That model includes the noise terms present in the received signal. Unknown parameters in the model, such as amplitude of the received signal and range to target, must be estimated from the noisy data. The model is used in the Cramer-Rao lower bound to determine precision limits on unbiased estimates of the unknown parameters.

2.3.1 Cramer-Rao Lower Bounds. At this point, the Cramer-Rao lower bounds for Eq. 2.32 are calculated using the distribution from Eq. 2.33. In the K sample LADAR signal, there are three unknown parameters that can be estimated. The round-trip range to target R_{rt} , the gain G , and the bias B are all unknown parameters. The precision of estimates of the unknown parameters can be analyzed using the Cramer-Rao lower bound. The CRLB is found by first evaluating the Fisher information matrix (FIM). The Fisher information matrix $\mathbf{J}(R_{rt}, G, B)$ for

this problem is

$$\mathbf{J}(R_{rt}, G, B) = - \begin{bmatrix} \mathbb{E} \left[\frac{\partial^2 l(R_{rt}, G, B)}{\partial R_{rt}^2} \right] & \mathbb{E} \left[\frac{\partial^2 l(R_{rt}, G, B)}{\partial R_{rt} \partial G} \right] & \mathbb{E} \left[\frac{\partial^2 l(R_{rt}, G, B)}{\partial R_{rt} \partial B} \right] \\ \mathbb{E} \left[\frac{\partial^2 l(R_{rt}, G, B)}{\partial R_{rt} \partial G} \right] & \mathbb{E} \left[\frac{\partial^2 l(R_{rt}, G, B)}{\partial G^2} \right] & \mathbb{E} \left[\frac{\partial^2 l(R_{rt}, G, B)}{\partial G \partial B} \right] \\ \mathbb{E} \left[\frac{\partial^2 l(R_{rt}, G, B)}{\partial R_{rt} \partial B} \right] & \mathbb{E} \left[\frac{\partial^2 l(R_{rt}, G, B)}{\partial G \partial B} \right] & \mathbb{E} \left[\frac{\partial^2 l(R_{rt}, G, B)}{\partial B^2} \right] \end{bmatrix} \quad (2.34)$$

where $l(R_{rt}, G, B)$ is the log-likelihood function.

The likelihood function, which is denoted $L(R_{rt}, G, B)$, is closely related to the PDF of the data. It is the PDF written as a function of the unknown parameters. The PDF, on the other hand, is a function of the data realization. The likelihood function derived from Eq. 2.33 is a function of the round-trip range, gain, and bias in the signal. Specifically, the likelihood function associated with the distribution from Eq. 2.31 is

$$L [R_{rt}, G, B | d(t_1), d(t_2), \dots, d(t_K)] = \frac{\exp \left[- \sum_{k=1}^K I(t_k) \right] \prod_{k=1}^K I(t_k)^{d(t_k)}}{\prod_{k=1}^K d(t_k)!}. \quad (2.35)$$

The log-likelihood function, which is denoted $l(R_{rt}, G, B)$, is simply the natural logarithm of the likelihood function. The log-likelihood function for Eq. 2.31 is

$$\begin{aligned} l [R_{rt}, G, B | d(t_1), d(t_2), \dots, d(t_K)] & \quad (2.36) \\ &= \log \{ L [R_{rt}, G, B | d(t_1), d(t_2), \dots, d(t_K)] \} \\ &= \log \left\{ \frac{\exp \left[- \sum_{k=1}^K I(t_k) \right] \prod_{k=1}^K I(t_k)^{d(t_k)}}{\prod_{k=1}^K d(t_k)!} \right\} \\ &= \sum_{k=1}^K d(t_k) \log [I(t_k)] - \sum_{k=1}^K I(t_k) - \sum_{k=1}^K \log [d(t_k)!]. \end{aligned}$$

The second derivatives of the log-likelihood function with respect to unknown parameters R_{rt} , G , and B are

$$\begin{aligned} & \frac{\partial^2 l(R_{rt}, G, B)}{\partial R_{rt}^2} \\ &= - \left[\frac{2G}{(cp_w)^2} \right]^2 \sum_{k=1}^K \left[(R_{rt} - t_k c)^2 \frac{d(t_k)}{I^2(t_k)} + \frac{d(t_k)}{I(t_k)} - 1 \right] \text{rect} \left(\frac{R_{rt} - t_k c}{2cp_w} \right), \end{aligned} \quad (2.37)$$

$$\begin{aligned} & \frac{\partial^2 l(R_{rt}, G, B)}{\partial R_{rt} \partial G} \\ &= \frac{2G}{(cp_w)^2} \sum_{k=1}^K (R_{rt} - t_k c) \left[1 - \frac{(R_{rt} - t_k c)^2}{(cp_w)^2} \right] \frac{d(t_k)}{I^2(t_k)} \text{rect} \left(\frac{R_{rt} - t_k c}{2cp_w} \right), \end{aligned} \quad (2.38)$$

$$\frac{\partial^2 l(R_{rt}, G, B)}{\partial R_{rt} \partial B} = \frac{2G}{(cp_w)^2} \sum_{k=1}^K (R_{rt} - t_k c) \frac{d(t_k)}{I^2(t_k)} \text{rect} \left(\frac{R_{rt} - t_k c}{2cp_w} \right), \quad (2.39)$$

$$\frac{\partial^2 l(R_{rt}, G, B)}{\partial G^2} = - \sum_{k=1}^K \left[1 - \frac{(R_{rt} - t_k c)^2}{(cp_w)^2} \right]^2 \frac{d(t_k)}{I^2(t_k)} \text{rect} \left(\frac{R_{rt} - t_k c}{2cp_w} \right), \quad (2.40)$$

$$\frac{\partial^2 l(R_{rt}, G, B)}{\partial G \partial B} = - \sum_{k=1}^K \left[1 - \frac{(R_{rt} - t_k c)^2}{(cp_w)^2} \right] \frac{d(t_k)}{I^2(t_k)} \text{rect} \left(\frac{R_{rt} - t_k c}{2cp_w} \right), \quad (2.41)$$

and

$$\frac{\partial^2 l(R_{rt}, G, B)}{\partial B^2} = - \sum_{k=1}^K \frac{d(t_k)}{I^2(t_k)}. \quad (2.42)$$

The elements of the Fisher information matrix are the negative expectations of these second derivatives

$$-\mathbb{E} \left[\frac{\partial^2 l(R_{rt}, G, B)}{\partial R_{rt}^2} \right] = \left[\frac{2G}{(cp_w)^2} \right]^2 \sum_{k=1}^K (R_{rt} - t_k c)^2 \frac{1}{I(t_k)} \text{rect} \left(\frac{R_{rt} - t_k c}{2cp_w} \right), \quad (2.43)$$

$$\begin{aligned}
& -\mathbb{E} \left[\frac{\partial^2 l(R_{rt}, G, B)}{\partial R_{rt} \partial G} \right] \\
& = -\frac{2G}{(cp_w)^2} \sum_{k=1}^K (R_{rt} - t_k c) \left[1 - \frac{(R_{rt} - t_k c)^2}{(cp_w)^2} \right] \frac{1}{I(t_k)} \text{rect} \left(\frac{R_{rt} - t_k c}{2cp_w} \right),
\end{aligned} \tag{2.44}$$

$$-\mathbb{E} \left[\frac{\partial^2 l(R_{rt}, G, B)}{\partial R_{rt} \partial B} \right] = -\frac{2G}{(cp_w)^2} \sum_{k=1}^K (R_{rt} - t_k c) \frac{1}{I(t_k)} \text{rect} \left(\frac{R_{rt} - t_k c}{2cp_w} \right), \tag{2.45}$$

$$-\mathbb{E} \left[\frac{\partial^2 l(R_{rt}, G, B)}{\partial G^2} \right] = \sum_{k=1}^K \left[1 - \frac{(R_{rt} - t_k c)^2}{(cp_w)^2} \right]^2 \frac{1}{I(t_k)} \text{rect} \left(\frac{R_{rt} - t_k c}{2cp_w} \right), \tag{2.46}$$

$$-\mathbb{E} \left[\frac{\partial^2 l(R_{rt}, G, B)}{\partial G \partial B} \right] = \sum_{k=1}^K \left[1 - \frac{(R_{rt} - t_k c)^2}{(cp_w)^2} \right] \frac{1}{I(t_k)} \text{rect} \left(\frac{R_{rt} - t_k c}{2cp_w} \right), \tag{2.47}$$

and

$$-\mathbb{E} \left[\frac{\partial^2 l(R_{rt}, G, B)}{\partial B^2} \right] = \sum_{k=1}^K \frac{1}{I(t_k)}. \tag{2.48}$$

The derivations of the previous equations made use of the fact that the mean of a Poisson random variable $D(t_k)$ is $I(t_k)$. That is, $\mathbb{E}[D(t_k)] = I(t_k)$. Eqs. 2.43 - 2.48 were first derived in [4].

The functions being summed in Eqs. 2.43 - 2.48 are illustrated in Fig. 2.4. The round-trip range, gain, and bias values used to create these plots are the same as are used in Fig. 2.3. It is shown in Chapter III that the summations in these equations can be approximated using integrals. The functions in Eqs. 2.44 and 2.45 have odd symmetry around the center of the pulse. Therefore, those equations are approximately zero.

The duration of the pulse is $2p_w$. The sampling duration, which is denoted t_d , is

$$t_d = K/f_s = K\Delta t \tag{2.49}$$

where f_s is the sampling frequency. The sampling frequency is the reciprocal of the time between samples in the system ($f_s = 1/\Delta t$) where Δt denotes the time between samples.

The pulse in Eq. 2.32 is centered at time $t_k = R_{rt}/c$. Since we have assumed that the entire pulse is sampled, it is required that $p_w < R_{rt}/c < t_d - p_w$. If this requirement is not satisfied, then the pulse is not completely sampled and some received signal energy is missed.

2.4 Gain Variation in APD Arrays

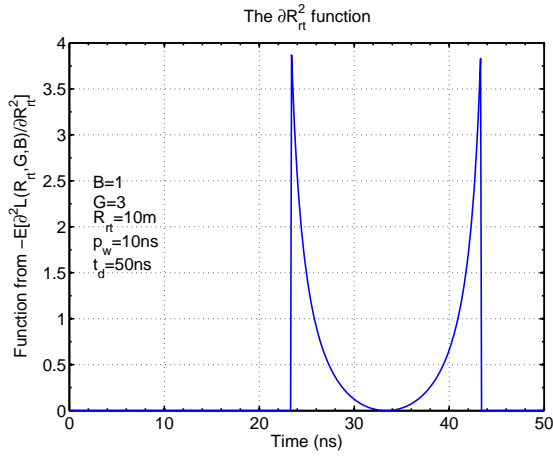
In Sec. 2.3, a model was presented to describe the received signal in the photodetector array of an imaging LADAR. The model from Eq. 2.29 assumes that the gain term G is constant across the entire detector array. That model also assumes that the gain is fixed for each pixel over its range record. Fixed detector gain was also assumed in [4].

However, recent research has demonstrated that there can be gain variations in LADAR detector arrays [37]. Gain can vary for a particular detector within an array over that detector's sampling time. Gain can also fluctuate across an array of photodetectors at any particular sample. These fluctuations in gain were observed in the Advanced Scientific Concepts LADAR owned by AFRL Sensors Directorate. The detector used in that system is an array of avalanche photodiodes.

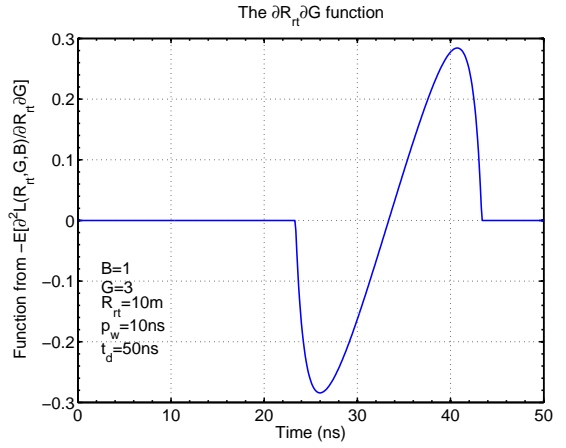
An empirical model for the gain in an avalanche diode was developed by Miller [29]. Miller's model is

$$G = \frac{1}{1 - \left(\frac{V_{bias}}{V_{bd}}\right)^p} \quad (2.50)$$

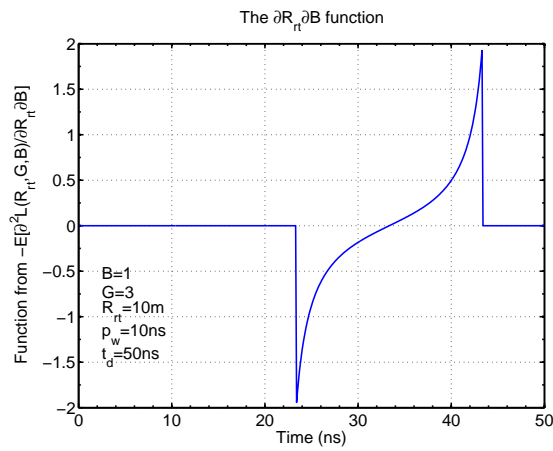
where V_{bias} is the bias voltage, V_{bd} is the breakdown voltage, and p is an empirical constant used to model the device. Some imaging LADARs use detector arrays that share a common voltage regulator, which is the component that sets the bias voltage V_{bias} . Sharing the voltage regulator saves on weight and power in the system. However, when a signal is received, the regulator's bias voltage drifts. Fluctuations in the bias voltage cause variations in the gain equation (Eq. 2.50). And if the same regulator is used by all detectors in the system, then the gain will vary in all pixels.



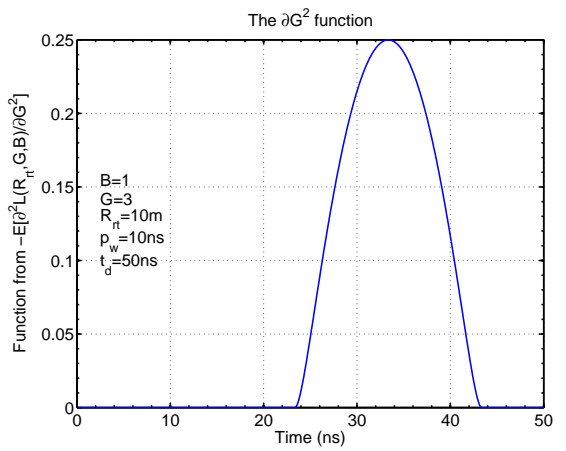
(a)



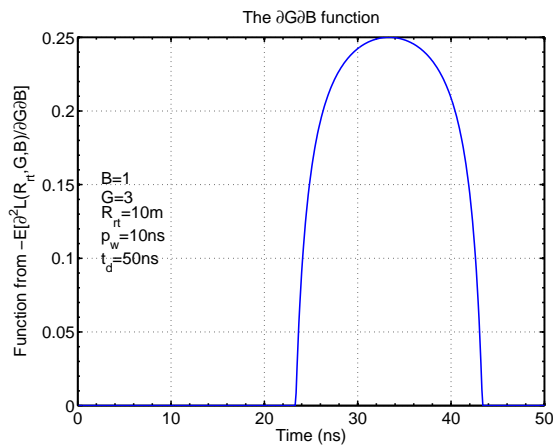
(b)



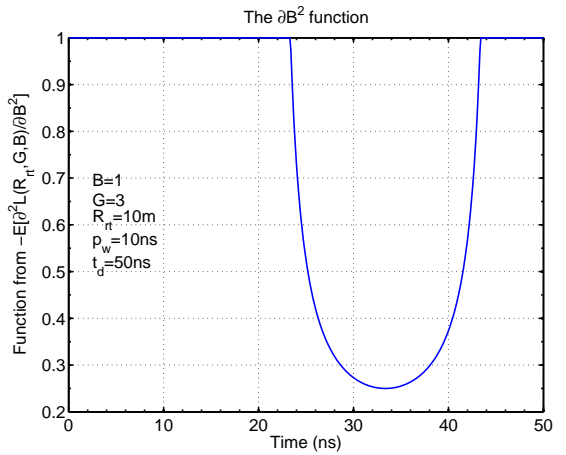
(c)



(d)



(e)



(f)

Figure 2.4: (a) The round-trip range second derivative. (b) The range-gain derivative. (c) The range-bias derivative. (d) The gain second derivative. (e) The gain-bias derivative. (f) The bias second derivative.

Methods for compensation of gain variation were proposed and tested in [37], but further work was also recommended. In this dissertation, more LADAR data collected with an ASC system is analyzed. The gain variation is observed and its effect on range measurements is demonstrated. Different methods of gain equalization are proposed and tested in an attempt to correct for the gain variation in the avalanche photodiode array.

2.5 Overview of Dissertation

The research in this dissertation begins in Chapter III with a Poisson-distributed signal model that simulates a laser pulse received by a shot-noise limited LADAR system. This signal model was previously analyzed by Cain et al. in [4]. In this dissertation, the Cramer-Rao lower bound analysis work from that paper is extended. Numerical solutions for range, gain, and background level CRLBs were formerly published in that paper. In this dissertation, new closed-form analytic expressions are derived for those Cramer-Rao lower bounds.

The shot-noise limited signal model from [4] is also extended to cases where there are multiple received signals. These cases simulate the signal in a LADAR observing a target partially obscured by forest canopy. Earlier work with this signal model assumed that the received pulse width was known. However, when a target has depth that is significant compared to the laser pulse width, the received pulse width is larger than the transmitted width. In this case, the known width assumption is not realistic. In Chapter III, the effect of an unknown pulse width is analyzed and the effect on signal parameter CRLBs is calculated.

In Chapter IV of this dissertation, the range CRLB for a Poisson-distributed signal is compared to the CRLB for a signal mixed with Gaussian noise. The comparison assumes the background Poisson and Gaussian noise variances are equal. Proof that the Gaussian noise range CRLB is a lower bound for the Poisson noise CRLB is presented. Also, the effect of using multiple pulses on range precision of a shot-noise limited LADAR is studied. It is shown that for a laser capable of dividing a fixed

amount of energy into multiple pulses, the best range precision is achieved when all energy is transmitted in a single pulse. Equivalently, distributing a fixed amount of energy into multiple pulses increases the range CRLB, which indicates that there is a decrease in precision.

It is also noted in Chapter IV that there are cases where the effect of target surface orientation on range precision can not be ignored. These cases usually involve systems with modest aperture sizes (a few inches in diameter) and target ranges of at least several kilometers. However, such scenarios are common for airborne LADAR systems. If the target surface is tilted with respect to the LADAR line of sight, then there is a drop in range precision. The drop in precision is quantified in this dissertation.

In Chapter V, it is noted that detector arrays composed of avalanche photodiodes (APDs) are being used in current imaging LADAR systems. Current arrays have tens of thousands of APDs. The compact size and high numbers of pixels makes the use of APD arrays desirable in imaging LADARs. However, gain variation in APD arrays can produce undesirable effects. Gain variation distorts the shape of received signals and introduces bias into range measurements.

In Chapter V, methods of gain variation correction (gain equalization) are proposed and tested. It is shown that background data collected by an APD array can be used to decrease the gain variation and improve the range precision in three-dimensional LADAR images.

2.6 Chapter Summary

Understanding of LADAR systems requires knowledge of several key subjects. The propagation of laser light was described in Sec. 2.1 of this chapter. Photodetectors are used to convert a received optical field to an electrical signal. That signal is inevitably noisy. The stochastic models used to characterize the noisy signals were covered in Sec. 2.2 of this chapter. Received LADAR signals are often used to calculate

the range to a target. This process, and the limitations on range precision due to noise, were covered in Sec. 2.3. It has been noted that the constant of proportionality relating the mean energy in the optical field and the mean electrical signal (the gain) produced by an avalanche photodiode can vary. This APD gain variation problem was discussed in Sec. 2.4.

This dissertation covers several different topics associated with the problem of range estimation using a LADAR system. These items were described in Sec. 2.5 of this chapter.

III. Poisson-Distributed LADAR Signal Models

The subject of this chapter is LADAR signal modeling using the Poisson distribution. These models represent the signals detected by LADAR systems as series of statistically independent Poisson random variables. The validity of the Poisson assumption is discussed in detail in Sec. 2.2.3. The mean values of these Poisson random variables are the sum of a fixed bias level and possibly a signal component. The bias level represents the noise sources in the system such as background light entering the LADAR's receiver aperture and dark current in the present in the photodetector. The signals are modeled as finite duration (truncated) parabolas. The parabolic pulse shape model is not used universally in the literature, but is a reasonable approximation to the true shape of a laser pulse. Various laser pulse shape models used in the literature are compared in Sec. 2.1.6. The parabolic model is used because it is simple and reasonably realistic.

The LADAR signal models are parameterized by range to target, gain, bias, and pulse width. In some cases, more than one range or gain term is present in the signal model. When multiple parameters of the same type are used, it is to simulate the signal observed when the LADAR transmits one pulse but observes received signals from more than one target. It is usually assumed that the received laser pulse width is known. However, received pulse width can be treated as an unknown parameter to be estimated.

The LADAR signal models are used to derive parameter estimates and to calculate the bounds on precision of those estimates. The use of established parameter estimation techniques such as maximum likelihood estimation is discussed. The signal models are also used to find the Cramer-Rao lower bounds for unbiased estimates of unknown parameters.

Three different LADAR signal models are discussed in this chapter. The first model considered is the single parabolic pulse model with known width. This model was studied in a previous publication [4] and is discussed in Sec. 2.2.4. It is revisited

in order to present analytic expressions for the Cramer-Rao lower bounds on the parameter estimates in that model.

The second model in this chapter is a generalization of the parabolic pulse model that includes obscuration. This obscured target model is used to approximate the observed LADAR signal when the target of interest is partially occluded by clutter. In military remote sensing scenarios, the obscurant is typically camouflage netting or some sort of foliage. The obscuration is simulated by adding a second parabolic pulse to the simulated signal with its own range and gain values.

The final model is equivalent to the single laser pulse parabolic signal model. However, this version treats the pulse width as an unknown parameter that must be estimated instead of a known constant. Estimation algorithms for the pulse width are proposed. The effect of unknown pulse width on the Cramer-Rao lower bounds is also discussed.

3.1 Parabolic Pulse LADAR Signal Model

All three LADAR signal models in this chapter are generalizations of the model published by Cain, et al. [4] in “*Flash light detection and ranging accuracy limits for returns from single opaque surfaces via Cramer-Rao bounds.*” The CRLBs for the parabolic pulse model are derived in that paper. However, they are expressed in terms of summations of various sampled functions.

Because parabolic pulse models are used extensively in this dissertation, it proves useful to derive analytic approximations to the summations from [4]. These analytic approximations are used to find simpler expressions for various Cramer-Rao lower bounds. In this section, the original parabolic pulse model from [4] is revisited in order to derive analytic CRLB expressions.

In this dissertation, the round-trip range from Eq. 2.32 is replaced by range to target R . Round-trip range R_{rt} is double the one-way range to the target.

$$R_{rt} = 2R. \quad (3.1)$$

The parabolic pulse model in terms of range to target is

$$I(t_k) = G \left[1 - \left(\frac{t_k - 2R/c}{p_w} \right)^2 \right] \text{rect} \left(\frac{t_k - 2R/c}{2p_w} \right) + B. \quad (3.2)$$

The pulse is sampled in its entirety as long as $p_w < 2R/c < t_d - p_w$.

The parabolic pulse model from Eq. 3.2 is equal to Eq. 2.32 with the substitution from Eq. 3.1. An example of the parabolic pulse model from Eq. 3.2 is shown in Fig. 3.1. The signal shapes shown in Figs. 2.3 and 3.1 appear equal because the range to target is the same in both. In Fig. 2.3, the round-trip range is $R_{rt} = 10$ m and in Fig. 3.1, the range is $R = 5$ m.

3.1.1 Fisher Information Matrix. The Fisher information matrix is used to calculate the Cramer-Rao lower bounds on unbiased estimates of signal parameters. The unknown parameters in Eq. 3.2 are range, gain, and bias (denoted R , G , and B). The FIM associated with the parabolic pulse model from Eq. 3.2 is

$$\mathbf{J}(R, G, B) = - \begin{bmatrix} \mathbb{E} \left[\frac{\partial^2 l(R, G, B)}{\partial R^2} \right] & \mathbb{E} \left[\frac{\partial^2 l(R, G, B)}{\partial R \partial G} \right] & \mathbb{E} \left[\frac{\partial^2 l(R, G, B)}{\partial R \partial B} \right] \\ \mathbb{E} \left[\frac{\partial^2 l(R, G, B)}{\partial R \partial G} \right] & \mathbb{E} \left[\frac{\partial^2 l(R, G, B)}{\partial G^2} \right] & \mathbb{E} \left[\frac{\partial^2 l(R, G, B)}{\partial G \partial B} \right] \\ \mathbb{E} \left[\frac{\partial^2 l(R, G, B)}{\partial R \partial B} \right] & \mathbb{E} \left[\frac{\partial^2 l(R, G, B)}{\partial G \partial B} \right] & \mathbb{E} \left[\frac{\partial^2 l(R, G, B)}{\partial B^2} \right] \end{bmatrix} \quad (3.3)$$

The FIM elements are calculated from the expectations of the second derivatives of the log-likelihood function $l(R, G, B)$. The signal is modeled as a sequence of independent Poisson random variables, each with mean $I(t_k)$. The log-likelihood function from (see

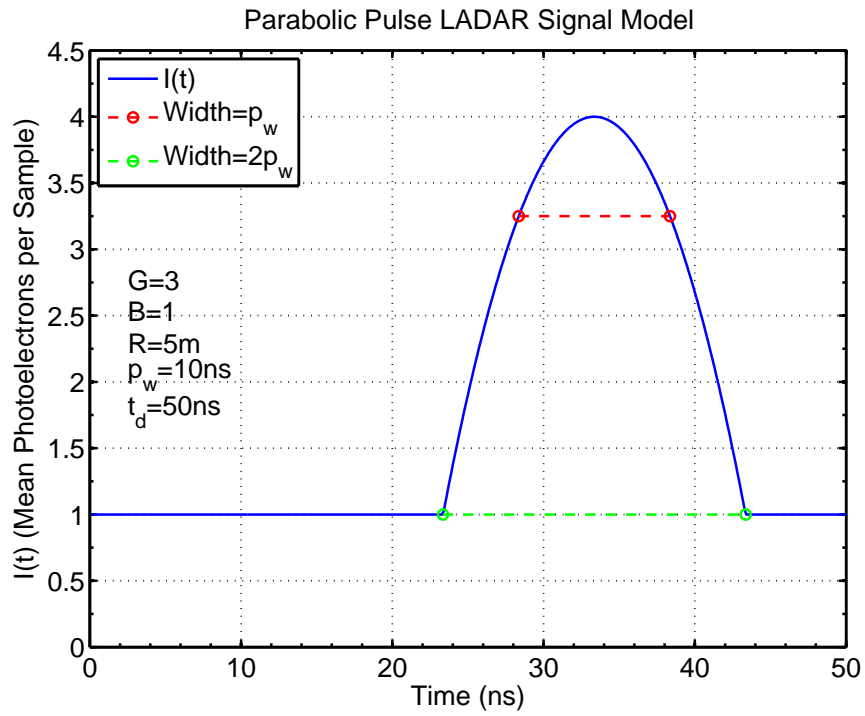


Figure 3.1: Illustration of the parabolic pulse LADAR signal model from Eq. 3.2. This signal model differs from the one shown in Fig 2.3 because it is defined in terms of range to target (R) rather than round-trip range (R_{rt}).

Eqs. 2.35 and 2.36) for the parabolic pulse from Eq. 3.2 is

$$l(R, G, B) = \sum_{k=1}^K d(t_k) \log [I(t_k)] - \sum_{k=1}^K I(t_k) - \sum_{k=1}^K \log [d(t_k)!]. \quad (3.4)$$

Derivatives of the log-likelihood function are needed to calculate the FIM. The first derivatives of the log-likelihood function for the parabolic pulse signal model (Eq. 3.2) with respect to the unknown parameters are

$$\frac{\partial l(R, G, B)}{\partial R} = \sum_{k=1}^K \frac{\partial I(t_k)}{\partial R} \left[\frac{d(t_k)}{I(t_k)} - 1 \right], \quad (3.5)$$

$$\frac{\partial l(R, G, B)}{\partial G} = \sum_{k=1}^K \frac{\partial I(t_k)}{\partial G} \left[\frac{d(t_k)}{I(t_k)} - 1 \right], \quad (3.6)$$

and

$$\frac{\partial l(R, G, B)}{\partial B} = \sum_{k=1}^K \left[\frac{d(t_k)}{I(t_k)} - 1 \right]. \quad (3.7)$$

Eq. 3.7 was evaluated using the fact that

$$\frac{\partial I(t_k)}{\partial B} = 1. \quad (3.8)$$

For the CRLB to exist, the expectations of the first derivatives of the log-likelihood function must be zero. This requirement is called the regularity condition [23]. The fact that the mean of Poisson random variable $D(t_k)$ is $I(t_k)$ is used to find these expectations.

$$\mathbb{E} \left[\frac{D(t_k)}{I(t_k)} - 1 \right] = \frac{\mathbb{E} [D(t_k)]}{I(t_k)} - 1 = 0. \quad (3.9)$$

Eq. 3.9 can be used to show that the first derivatives of the log-likelihood (Eqs. 3.5 - 3.7) all have an expected value of zero. Thus, the regularity condition is satisfied.

The second derivatives needed for the diagonal elements of the Fisher information matrix are

$$\frac{\partial^2 l(R, G, B)}{\partial R^2} = \sum_{k=1}^K \left\{ \frac{\partial^2 I(t_k)}{\partial R^2} \left[\frac{d(t_k)}{I(t_k)} - 1 \right] - \left[\frac{\partial I(t_k)}{\partial R} \right]^2 \frac{d(t_k)}{I^2(t_k)} \right\}, \quad (3.10)$$

$$\frac{\partial^2 l(R, G, B)}{\partial G^2} = \sum_{k=1}^K \left\{ \frac{\partial^2 I(t_k)}{\partial G^2} \left[\frac{d(t_k)}{I(t_k)} - 1 \right] - \left[\frac{\partial I(t_k)}{\partial G} \right]^2 \frac{d(t_k)}{I^2(t_k)} \right\}, \quad (3.11)$$

and

$$\frac{\partial^2 l(R, G, B)}{\partial B^2} = - \sum_{k=1}^K \frac{d(t_k)}{I^2(t_k)}. \quad (3.12)$$

The second derivatives needed for the off-diagonal elements of the FIM are

$$\frac{\partial^2 l(R, G, B)}{\partial R \partial G} = \sum_{k=1}^K \left\{ \frac{\partial^2 I(t_k)}{\partial R \partial G} \left[\frac{d(t_k)}{I(t_k)} - 1 \right] - \frac{\partial I(t_k)}{\partial R} \frac{\partial I(t_k)}{\partial G} \frac{d(t_k)}{I^2(t_k)} \right\}, \quad (3.13)$$

$$\frac{\partial^2 l(R, G, B)}{\partial R \partial B} = - \sum_{k=1}^K \frac{\partial I(t_k)}{\partial R} \frac{d(t_k)}{I^2(t_k)}, \quad (3.14)$$

and

$$\frac{\partial^2 l(R, G, B)}{\partial G \partial B} = - \sum_{k=1}^K \frac{\partial I(t_k)}{\partial G} \frac{d(t_k)}{I^2(t_k)} \quad (3.15)$$

where Eq. 3.8 was used to evaluate Eqs. 3.14 and 3.15.

The expectations of the log-likelihood function derivatives must be calculated to find the FIM. Eq. 3.9 is used to find the FIM element expectations. The FIM diagonal elements are

$$-\mathbb{E} \left[\frac{\partial^2 l(R, G, B)}{\partial R^2} \right] = \sum_{k=1}^K \frac{1}{I(t_k)} \left[\frac{\partial I(t_k)}{\partial R} \right]^2, \quad (3.16)$$

$$-\mathbb{E} \left[\frac{\partial^2 l(R, G, B)}{\partial G^2} \right] = \sum_{k=1}^K \frac{1}{I(t_k)} \left[\frac{\partial I(t_k)}{\partial G} \right]^2, \quad (3.17)$$

and

$$-\mathbb{E} \left[\frac{\partial^2 l(R, G, B)}{\partial B^2} \right] = \sum_{k=1}^K \frac{1}{I(t_k)}. \quad (3.18)$$

The off-diagonal FIM elements are

$$-\mathbb{E} \left[\frac{\partial^2 l(R, G, B)}{\partial R \partial G} \right] = \sum_{k=1}^K \frac{1}{I(t_k)} \frac{\partial I(t_k)}{\partial R} \frac{\partial I(t_k)}{\partial G}, \quad (3.19)$$

$$-\mathbb{E} \left[\frac{\partial^2 l(R, G, B)}{\partial R \partial B} \right] = \sum_{k=1}^K \frac{1}{I(t_k)} \frac{\partial I(t_k)}{\partial R}, \quad (3.20)$$

and

$$-\mathbb{E} \left[\frac{\partial^2 l(R, G, B)}{\partial G \partial B} \right] = \sum_{k=1}^K \frac{1}{I(t_k)} \frac{\partial I(t_k)}{\partial G}. \quad (3.21)$$

The derivatives of the parabolic pulse are needed to evaluate Eqs. 3.16 - 3.21. The derivative of Eq. 3.2 with respect to range is

$$\frac{\partial I(t_k)}{\partial R} = \frac{4G}{cp_w} \left(\frac{t_k - 2R/c}{p_w} \right) \text{rect} \left(\frac{t_k - 2R/c}{2p_w} \right). \quad (3.22)$$

The derivative with respect to gain is

$$\frac{\partial I(t_k)}{\partial G} = \left[1 - \left(\frac{t_k - 2R/c}{p_w} \right)^2 \right] \text{rect} \left(\frac{t_k - 2R/c}{2p_w} \right). \quad (3.23)$$

In these two derivative equations (Eqs. 3.22 and 3.23), the effect of the discontinuity in $I(t_k)$ due to the rectangle function has been ignored.

Using Eq. 3.22, the FIM element from Eq. 3.16 can be written

$$\begin{aligned} & -\mathbb{E} \left[\frac{\partial^2 l(R, G, B)}{\partial R^2} \right] \\ &= \sum_{k=1}^K \frac{1}{G \left[1 - \left(\frac{t_k - 2R/c}{p_w} \right)^2 \right] + B} \left[\frac{4G}{cp_w} \left(\frac{t_k - 2R/c}{p_w} \right) \right]^2 \text{rect} \left(\frac{t_k - 2R/c}{2p_w} \right). \end{aligned} \quad (3.24)$$

The Fisher information matrix element in Eq. 3.24 includes a summation. Summations such as this one can be approximated using integrals. The integral approximation to Eq. 3.24 is

$$\begin{aligned}
& -\mathbb{E} \left[\frac{\partial^2 l(R, G, B)}{\partial R^2} \right] \\
& \approx f_s \left(\frac{4G}{cp_w} \right)^2 \int_{2R/c-p_w}^{2R/c+p_w} \frac{1}{G \left[1 - \left(\frac{t-2R/c}{p_w} \right)^2 \right] + B} \left(\frac{t-2R/c}{p_w} \right)^2 dt.
\end{aligned} \tag{3.25}$$

This approximation assumes that the data was sampled at rate f_s . The integral in Eq. 3.25 is evaluated using the following change of variable.

$$u = \sqrt{\frac{G}{B+G}} \frac{t-2R/c}{p_w}. \tag{3.26}$$

Using this change of variable in the integral from Eq. 3.25 yields

$$\begin{aligned}
& -\mathbb{E} \left[\frac{\partial^2 l(R, G, B)}{\partial R^2} \right] \\
& \approx f_s \left(\frac{4G}{cp_w} \right)^2 \int_{-\sqrt{\frac{G}{B+G}}}^{\sqrt{\frac{G}{B+G}}} \frac{1}{G \left(1 - \frac{B+G}{G} u^2 \right) + B} \frac{B+G}{G} u^2 p_w \sqrt{\frac{B+G}{G}} du \\
& = \frac{16f_s G}{c^2 p_w} \sqrt{\frac{B+G}{G}} \int_{-\sqrt{\frac{G}{B+G}}}^{\sqrt{\frac{G}{B+G}}} \frac{u^2}{1-u^2} du.
\end{aligned} \tag{3.27}$$

Eq. 2.147.5 of *Table of Integrals, Series, and Products* by Gradshteyn and Ryzhik [14] is

$$\int \frac{x^m}{1-x^2} dx = -\frac{x^{m-1}}{m-1} + \int \frac{x^{m-2}}{1-x^2} dx. \tag{3.28}$$

Letting $m = 2$ in the previous equation produces

$$\int \frac{x^2}{1-x^2} dx = -x + \int \frac{1}{1-x^2} dx. \tag{3.29}$$

Eq. 2.143.2 of [14] is

$$\int \frac{1}{1-x^2} dx = \operatorname{atanh}(x) \quad (3.30)$$

if $|x| < 1$ where $\operatorname{atanh}(x)$ is the inverse hyperbolic tangent function. Combining Eqs. 3.25, 3.29, and 3.30 produces

$$-\mathbb{E} \left[\frac{\partial^2 l(R, G, B)}{\partial R^2} \right] \approx \frac{32Gf_s}{c^2 p_w} \left[\sqrt{\frac{B+G}{G}} \operatorname{atanh} \left(\sqrt{\frac{G}{B+G}} \right) - 1 \right]. \quad (3.31)$$

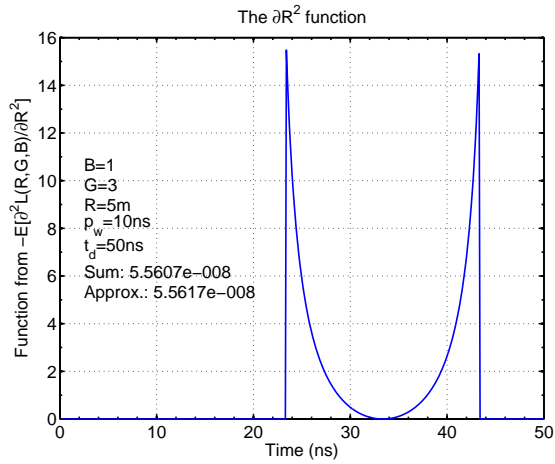
The following variable a is defined to simplify the Fisher information matrix elements and later CRLB equations.

$$a = \sqrt{\frac{B+G}{G}} \operatorname{atanh} \left(\sqrt{\frac{G}{B+G}} \right). \quad (3.32)$$

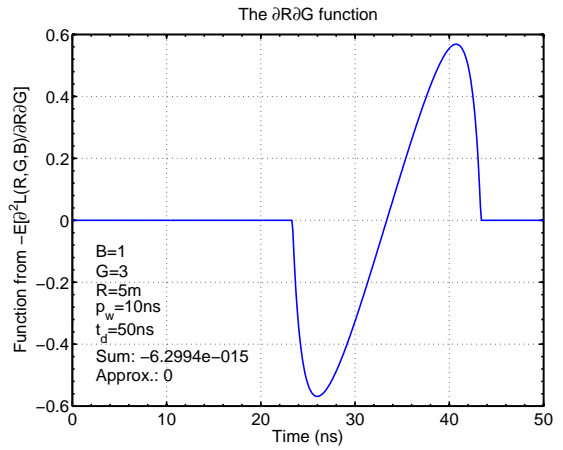
Using this variable allows Eq. 3.31 to be written

$$-\mathbb{E} \left[\frac{\partial^2 l(R, G, B)}{\partial R^2} \right] \approx \frac{32Gf_s}{c^2 p_w} (a - 1). \quad (3.33)$$

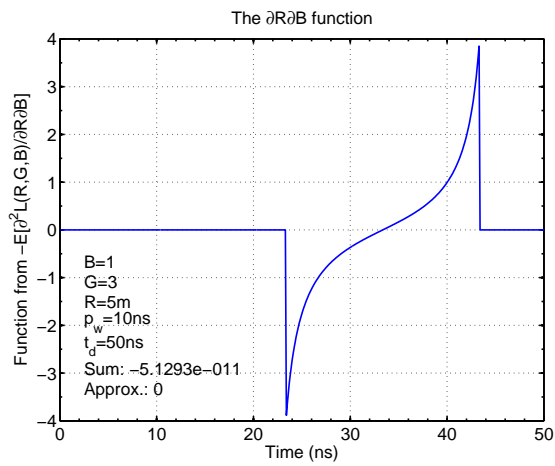
This integral approximation for the FIM element was validated by comparing it to an actual summation. The results are shown in Fig. 3.2a. There is good agreement between the integral approximation and the numeric result.



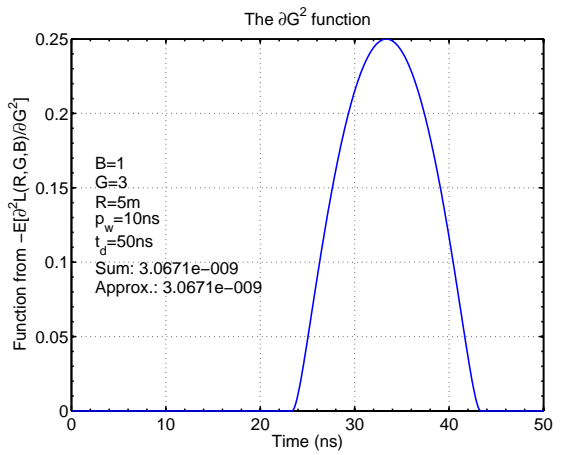
(a)



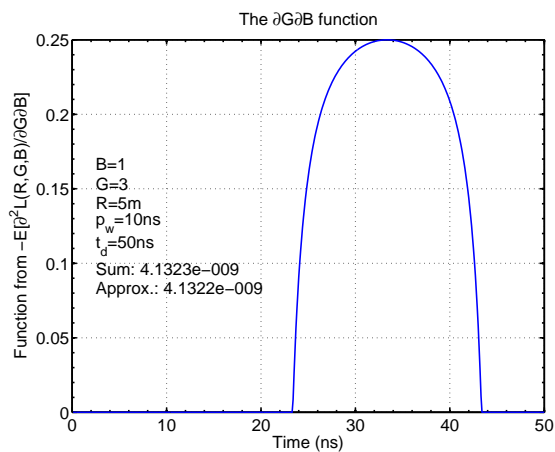
(b)



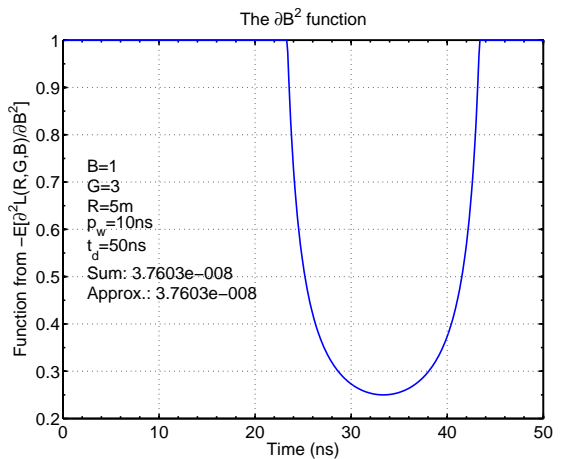
(c)



(d)



(e)



(f)

Figure 3.2: (a) The range second derivative. (b) The range-gain derivative. (c) The range-bias derivative. (d) The gain second derivative. (e) The gain-bias derivative. (f) The bias second derivative.

Using Eqs. 3.22 and 3.23, the FIM element from Eq. 3.19 can be approximated by an integral.

$$\begin{aligned}
& -\mathbb{E} \left[\frac{\partial^2 l(R, G, B)}{\partial R \partial G} \right] \\
&= \frac{4G}{cp_w} \sum_{k=1}^K \frac{\left(\frac{t_k - 2R/c}{p_w} \right) \left[1 - \left(\frac{t_k - 2R/c}{p_w} \right)^2 \right]}{G \left[1 - \left(\frac{t_k - 2R/c}{p_w} \right)^2 \right] + B} \text{rect} \left(\frac{t_k - 2R/c}{2p_w} \right) \\
&\approx f_s \frac{4G}{cp_w} \int_{2R/c - p_w}^{2R/c + p_w} \frac{\left(\frac{t - 2R/c}{p_w} \right) \left[1 - \left(\frac{t - 2R/c}{p_w} \right)^2 \right]}{G \left[1 - \left(\frac{t - 2R/c}{p_w} \right)^2 \right] + B} dt \\
&= f_s \frac{4G}{cp_w} \int_{-1}^1 \frac{v(1 - v^2)}{G(1 - v^2) + B} p_w dv.
\end{aligned} \tag{3.34}$$

The following change of variable was used in the above equation.

$$v = \frac{t - 2R/c}{p_w}. \tag{3.35}$$

Inspection of the integrand of Eq. 3.34 shows that it is an odd function (i.e., $f(x) = -f(-x)$). Since the integrand is odd and the range of integration is centered around the origin, the integral is zero. Therefore, this FIM element is approximately zero.

$$-\mathbb{E} \left[\frac{\partial^2 l(R, G, B)}{\partial R \partial G} \right] \approx 0. \tag{3.36}$$

This approximation was compared to a summation in Fig. 3.2b. The summation was very close to zero, but not exactly zero. The numeric result is not exactly zero because the samples are not aligned exactly with the pulse center. If they were, then the summation would be exactly zero. However, the magnitude of the summation is very small and can be accurately approximated by a zero.

The FIM element from Eq. 3.20 is approximately

$$\begin{aligned}
& -\mathbb{E} \left[\frac{\partial^2 l(R, G, B)}{\partial R \partial B} \right] \tag{3.37} \\
&= \frac{4G}{cp_w} \sum_{k=1}^K \frac{1}{G \left[1 - \left(\frac{t_k - 2R/c}{p_w} \right)^2 \right] + B} \left(\frac{t_k - 2R/c}{p_w} \right) \text{rect} \left(\frac{t_k - 2R/c}{2p_w} \right) \\
&\approx f_s \frac{4G}{cp_w} \int_{2R/c - p_w}^{2R/c + p_w} \frac{1}{G \left[1 - \left(\frac{t - 2R/c}{p_w} \right)^2 \right] + B} \left(\frac{t - 2R/c}{p_w} \right) dt \\
&= f_s \frac{4G}{cp_w} \int_{-1}^1 \frac{v}{G(1 - v^2) + B} p_w dv.
\end{aligned}$$

where the change of variable from Eq. 3.35 is used. The integrand of Eq. 3.37 is an odd function and the range of integration is centered around the origin. Thus, the integral is zero and the FIM element is approximately zero.

$$-\mathbb{E} \left[\frac{\partial^2 l(R, G, B)}{\partial R \partial B} \right] \approx 0. \tag{3.38}$$

The integrand being approximated is shown in Fig. 3.2c. In that figure, the approximation was compared to a summation. The summation result was small, but not as small as in the previous case. The discrepancy is likely caused by the sharp discontinuities in the function near the edges of the parabolic pulse. The other FIM element with an integral approximation that is approximately zero (Eq. 3.36) is shown in Fig. 3.2b. In that case, the function did not have sharp discontinuities and the summation was about 10^4 times smaller than the output in this case. However, the analytic approximation error is still small compared to the other terms in the Fisher information matrix. Thus, the approximations are accurate and the CRLBs they generate are precise.

By using the change of variable from Eq. 3.26, the FIM element from Eq. 3.17 can be approximated by

$$\begin{aligned}
& -\mathbb{E} \left[\frac{\partial^2 l(R, G, B)}{\partial G^2} \right] \tag{3.39} \\
&= \sum_{k=1}^K \frac{1}{G \left[1 - \left(\frac{t_k - 2R/c}{p_w} \right)^2 \right] + B} \left[1 - \left(\frac{t_k - 2R/c}{p_w} \right)^2 \right]^2 \text{rect} \left(\frac{t_k - 2R/c}{2p_w} \right) \\
&\approx f_s \int_{2R/c - p_w}^{2R/c + p_w} \frac{1}{G \left[1 - \left(\frac{t - 2R/c}{p_w} \right)^2 \right] + B} \left[1 - \left(\frac{t - 2R/c}{p_w} \right)^2 \right]^2 dt \\
&= f_s \int_{-\sqrt{\frac{G}{B+G}}}^{\sqrt{\frac{G}{B+G}}} \frac{1}{G \left(1 - \frac{B+G}{G} u^2 \right) + B} \left(1 - \frac{B+G}{G} u^2 \right)^2 p_w \sqrt{\frac{B+G}{G}} du \\
&= \frac{p_w f_s}{\sqrt{G} \sqrt{B+G}} \int_{-\sqrt{\frac{G}{B+G}}}^{\sqrt{\frac{G}{B+G}}} \frac{1}{1 - u^2} du \\
&\quad - 2 \frac{B+G}{G} \frac{p_w f_s}{\sqrt{G} \sqrt{B+G}} \int_{-\sqrt{\frac{G}{B+G}}}^{\sqrt{\frac{G}{B+G}}} \frac{u^2}{1 - u^2} du \\
&\quad + \frac{(B+G)^2}{G^2} \frac{p_w f_s}{\sqrt{G} \sqrt{B+G}} \int_{-\sqrt{\frac{G}{B+G}}}^{\sqrt{\frac{G}{B+G}}} \frac{u^4}{1 - u^2} du.
\end{aligned}$$

Eq. 3.39 is the sum of three integrals. The first and second integrals in this equation can be evaluated using Eqs. 3.29 and 3.30. In order to evaluate the third integral in Eq. 3.39, start by letting $m = 4$ in Eq. 3.28.

$$\int \frac{x^4}{1 - x^2} dx = -\frac{x^3}{3} + \int \frac{x^2}{1 - x^2} dx = -\frac{x^3}{3} - x + \text{atanh}(x) \tag{3.40}$$

where $|x| < 1$ and Eq. 3.30 is used. The first integral from Eq. 3.39 is evaluated using Eq. 3.30.

$$\begin{aligned} & \frac{p_w f_s}{\sqrt{G}\sqrt{B+G}} \int_{-\sqrt{\frac{G}{B+G}}}^{\sqrt{\frac{G}{B+G}}} \frac{1}{1-u^2} du \\ &= \frac{2p_w f_s}{\sqrt{G}\sqrt{B+G}} \operatorname{atanh} \left(\sqrt{\frac{G}{B+G}} \right). \end{aligned} \quad (3.41)$$

The second integral from Eq. 3.39 is evaluated using Eqs. 3.29 and 3.30.

$$\begin{aligned} & -2 \frac{B+G}{G} \frac{p_w f_s}{\sqrt{G}\sqrt{B+G}} \int_{-\sqrt{\frac{G}{B+G}}}^{\sqrt{\frac{G}{B+G}}} \frac{u^2}{1-u^2} du \\ &= \frac{2p_w f_s}{\sqrt{G}\sqrt{B+G}} \left[\frac{2\sqrt{B+G}}{\sqrt{G}} - \frac{2(B+G)}{G} \operatorname{atanh} \left(\sqrt{\frac{G}{B+G}} \right) \right]. \end{aligned} \quad (3.42)$$

The third integral from Eq. 3.39 is evaluated using Eq. 3.40.

$$\begin{aligned} & \frac{(B+G)^2}{G^2} \frac{p_w f_s}{\sqrt{G}\sqrt{B+G}} \int_{-\sqrt{\frac{G}{B+G}}}^{\sqrt{\frac{G}{B+G}}} \frac{u^4}{1-u^2} du \\ &= \frac{2p_w f_s}{\sqrt{G}\sqrt{B+G}} \\ & \quad \times \left[\frac{(B+G)^2}{G^2} \operatorname{atanh} \left(\sqrt{\frac{G}{B+G}} \right) - \frac{(B+G)^{3/2}}{G^{3/2}} - \frac{\sqrt{B+G}}{3\sqrt{G}} \right]. \end{aligned} \quad (3.43)$$

Eqs. 3.41, 3.42, and 3.43 can be combined to create an analytic approximation for the Fisher information matrix term from Eq. 3.17.

$$\begin{aligned} & -\mathbb{E} \left[\frac{\partial^2 l(R, G, B)}{\partial G^2} \right] \\ & \approx 2p_w f_s \left[\frac{B^2}{G^{5/2}\sqrt{B+G}} \operatorname{atanh} \left(\sqrt{\frac{G}{B+G}} \right) + \frac{2}{3G} - \frac{B}{G^2} \right]. \end{aligned} \quad (3.44)$$

Using the variable a , which was defined in Eq. 3.32, this can be written

$$-\text{E} \left[\frac{\partial^2 l(R, G, B)}{\partial G^2} \right] \approx \frac{2p_w f_s}{G} \left[\frac{2}{3} - \frac{B}{G} \left(1 - \frac{aB}{B+G} \right) \right]. \quad (3.45)$$

This integral approximation is compared to a summation in Fig. 3.2d. The numeric and analytic results are exactly the same.

The FIM element from Eq. 3.21 can be approximated with an integral.

$$\begin{aligned} & -\text{E} \left[\frac{\partial^2 l(R, G, B)}{\partial G \partial B} \right] \quad (3.46) \\ &= \sum_{k=1}^K \frac{1}{G \left[1 - \left(\frac{t_k - 2R/c}{p_w} \right)^2 \right] + B} \left[1 - \left(\frac{t_k - 2R/c}{p_w} \right)^2 \right] \text{rect} \left(\frac{t_k - 2R/c}{2p_w} \right) \\ &\approx f_s \int_{2R/c - p_w}^{2R/c + p_w} \frac{1}{G \left[1 - \left(\frac{t - 2R/c}{p_w} \right)^2 \right] + B} \left[1 - \left(\frac{t - 2R/c}{p_w} \right)^2 \right] dt \\ &= f_s \int_{-\sqrt{\frac{G}{B+G}}}^{\sqrt{\frac{G}{B+G}}} \frac{1}{G \left(1 - \frac{B+G}{G} u^2 \right) + B} \left(1 - \frac{B+G}{G} u^2 \right) p_w \sqrt{\frac{B+G}{G}} du \\ &= \frac{p_w f_s}{\sqrt{G} \sqrt{B+G}} \int_{-\sqrt{\frac{G}{B+G}}}^{\sqrt{\frac{G}{B+G}}} \frac{1}{1-u^2} \left(1 - \frac{B+G}{G} u^2 \right) du \\ &= \frac{p_w f_s}{\sqrt{G} \sqrt{B+G}} \left[\int_{-\sqrt{\frac{G}{B+G}}}^{\sqrt{\frac{G}{B+G}}} \frac{1}{1-u^2} du - \frac{B+G}{G} \int_{-\sqrt{\frac{G}{B+G}}}^{\sqrt{\frac{G}{B+G}}} \frac{u^2}{1-u^2} du \right]. \end{aligned}$$

There are two integrals in Eq. 3.46. These integrals can be evaluated using Eqs. 3.28 and 3.29. Therefore, the FIM element from Eq. 3.21 is approximately

$$\begin{aligned}
& -\mathbb{E} \left[\frac{\partial^2 l(R, G, B)}{\partial G \partial B} \right] \\
& \approx 2p_w f_s \left[\frac{1}{G} - \frac{B}{G^{3/2} \sqrt{B+G}} \operatorname{atanh} \left(\sqrt{\frac{G}{B+G}} \right) \right] \\
& = \frac{2p_w f_s}{G} \left(1 - \frac{aB}{B+G} \right).
\end{aligned} \tag{3.47}$$

where the variable a from Eq. 3.32 was used. It is shown in Fig. 3.2e that this result is nearly equal to the summation over the actual function.

The final FIM element to be evaluated (Eq. 3.18) can be approximated with an integral.

$$\begin{aligned}
& -\mathbb{E} \left[\frac{\partial^2 l(R, G, B)}{\partial B^2} \right] \\
& = \sum_{k=1}^K \frac{1}{G \left[1 - \left(\frac{t_k - 2R/c}{p_w} \right)^2 \right] \operatorname{rect} \left(\frac{t_k - 2R/c}{2p_w} \right) + B} \\
& \approx f_s \int_0^{t_d} \frac{1}{G \left[1 - \left(\frac{t - 2R/c}{p_w} \right)^2 \right] \operatorname{rect} \left(\frac{t - 2R/c}{2p_w} \right) + B} dt.
\end{aligned} \tag{3.48}$$

This integral approximation differs from the integral approximations of all the other FIM terms because the integrand is nonzero over the entire data collection region ($0 \leq t \leq t_d$). This integral can be computed by splitting it into three different

regions.

$$\begin{aligned}
& f_s \int_0^{t_d} \frac{1}{G \left[1 - \left(\frac{t-2R/c}{p_w} \right)^2 \right] \text{rect} \left(\frac{t-2R/c}{2p_w} \right) + B} dt \quad (3.49) \\
&= f_s \int_0^{2R/c-p_w} \frac{1}{B} dt + f_s \int_{2R/c-p_w}^{2R/c+p_w} \frac{1}{G \left[1 - \left(\frac{t-2R/c}{p_w} \right)^2 \right]} dt + f_s \int_{2R/c+p_w}^{t_d} \frac{1}{B} dt \\
&= f_s \frac{t_d - 2p_w}{B} + \frac{p_w f_s}{\sqrt{G} \sqrt{B+G}} \int_{-\sqrt{\frac{G}{B+G}}}^{\sqrt{\frac{G}{B+G}}} \frac{1}{1-u^2} du
\end{aligned}$$

where the change of variable from Eq. 3.26 is used. It can be shown using Eq. 3.30 that Eq. 3.49 is

$$\begin{aligned}
& f_s \frac{t_d - 2p_w}{B} + \frac{p_w f_s}{\sqrt{G} \sqrt{B+G}} \int_{-\sqrt{\frac{G}{B+G}}}^{\sqrt{\frac{G}{B+G}}} \frac{1}{1-u^2} du \quad (3.50) \\
&= f_s \frac{t_d - 2p_w}{B} + \frac{2p_w f_s}{\sqrt{G} \sqrt{B+G}} \text{atanh} \left(\sqrt{\frac{G}{B+G}} \right).
\end{aligned}$$

Therefore, the FIM element from Eq. 3.18 can be approximated by the following formula.

$$\begin{aligned}
& -\text{E} \left[\frac{\partial^2 l(R, G, B)}{\partial B^2} \right] \quad (3.51) \\
&\approx 2p_w f_s \left[\frac{t_d}{2p_w B} - \frac{1}{B} + \frac{1}{\sqrt{G} \sqrt{B+G}} \text{atanh} \left(\sqrt{\frac{G}{B+G}} \right) \right] \\
&= 2p_w f_s \left(\frac{t_d - 2p_w}{2p_w B} + \frac{a}{B+G} \right).
\end{aligned}$$

where Eq. 3.32 was used. This integral approximation to the FIM term is compared to the output of a summation in 3.2f. The results are nearly identical.

3.1.2 *Cramer-Rao Lower Bounds.* The Cramer-Rao lower bounds are the lower limits on the variance of any unbiased estimate of an unknown parameter. The CRLBs are obtained by inverting the Fisher information matrix. The FIM for the parabolic pulse signal model from Eq. 3.2 is

$$\mathbf{J}(R, G, B) \approx \begin{bmatrix} J_{RR} & 0 & 0 \\ 0 & J_{GG} & J_{GB} \\ 0 & J_{GB} & J_{BB} \end{bmatrix}. \quad (3.52)$$

There are matrix elements approximately equal to zero because Eqs. 3.36 and 3.38 are about zero. The J_{RR} term in the Fisher information matrix is Eq. 3.33.

$$J_{RR} = \frac{32Gf_s}{p_w c^2} (a - 1). \quad (3.53)$$

where a was defined in Eq. 3.32. The J_{GG} term in the FIM is Eq. 3.45.

$$J_{GG} = \frac{2p_w f_s}{G} \left[\frac{2}{3} - \frac{B}{G} \left(1 - \frac{aB}{B+G} \right) \right]. \quad (3.54)$$

The J_{GB} term is Eq. 3.47.

$$J_{GB} = \frac{2p_w f_s}{G} \left(1 - \frac{aB}{B+G} \right). \quad (3.55)$$

Finally, the J_{BB} term is Eq. 3.51.

$$J_{BB} = 2p_w f_s \left(\frac{t_d - 2p_w}{2p_w B} + \frac{a}{B+G} \right) = \frac{2p_w f_s}{B} \left[\frac{t_d}{2p_w} - \left(1 - \frac{aB}{B+G} \right) \right]. \quad (3.56)$$

The Fisher information matrix (Eq. 3.52) for the parabolic pulse LADAR signal model from Eq. 3.2 has a block diagonal form. The inverse of a block diagonal matrix is

$$\begin{bmatrix} \mathbf{A} & \mathbf{0} \\ \mathbf{0} & \mathbf{B} \end{bmatrix}^{-1} = \begin{bmatrix} \mathbf{A}^{-1} & \mathbf{0} \\ \mathbf{0} & \mathbf{B}^{-1} \end{bmatrix}. \quad (3.57)$$

Since the FIM (Eq. 3.52) for the parabolic LADAR pulse signal model from Eq. 3.2 is block diagonal, Eq. 3.57 can be used to find the FIM inverse.

$$\mathbf{J}^{-1}(R, G, B) \approx \begin{bmatrix} 1/J_{RR} & 0 & 0 \\ 0 & J_{BB}/d & -J_{GB}/d \\ 0 & -J_{GB}/d & J_{GG}/d \end{bmatrix} \quad (3.58)$$

where d is the determinant of the 2×2 matrix in the lower right corner of the 3×3 FIM matrix in Eq. 3.52. The determinant of the 2×2 matrix is

$$d = \left| \begin{bmatrix} J_{GG} & J_{GB} \\ J_{GB} & J_{BB} \end{bmatrix} \right| = J_{GG}J_{BB} - J_{GB}^2. \quad (3.59)$$

Eqs. 3.45, 3.47, and 3.51 are used to calculate this determinant.

$$d = \frac{4p_w^2 f_s^2}{BG} \left[\frac{t_d}{3p_w} - \left(\frac{t_d B}{2p_w G} + \frac{2}{3} \right) \left(1 - \frac{aB}{B+G} \right) \right]. \quad (3.60)$$

The CRLBs for estimates of range, gain, and bias are the diagonal elements of the inverse of the Fisher information matrix. The CRLB for range estimates is the reciprocal of J_{RR} . This variable is used in Eq. 3.53 to calculate the bound.

$$\text{Var} \left[\widehat{R} \right] \geq \frac{1}{J_{RR}} = \frac{p_w c^2}{32G f_s (a-1)}. \quad (3.61)$$

The CRLB for estimates of the gain is J_{BB} (Eq. 3.56) divided by the determinant d from Eq. 3.60.

$$\text{Var} \left[\widehat{G} \right] \geq \frac{J_{BB}}{d} = \frac{G}{2p_w f_s} \frac{\frac{t_d}{2p_w} - \left(1 - \frac{aB}{B+G} \right)}{\frac{t_d}{3p_w} - \left(\frac{t_d B}{2p_w G} + \frac{2}{3} \right) \left(1 - \frac{aB}{B+G} \right)}. \quad (3.62)$$

Table 3.1: Parabolic Pulse Signal Model CRLBs.

Parameter	Cramer-Rao Lower Bounds
Range	$\frac{p_w c^2}{32Gf_s \left[\sqrt{\frac{B+G}{G}} \operatorname{atanh}\left(\sqrt{\frac{G}{B+G}}\right) - 1 \right]}$
Gain	$\frac{G}{2p_w f_s} \frac{\frac{t_d}{3p_w} - \left[1 - \frac{B}{\sqrt{G}\sqrt{B+G}} \operatorname{atanh}\left(\sqrt{\frac{G}{B+G}}\right) \right]}{\frac{t_d}{3p_w} - \left(\frac{t_d B}{2p_w G} + \frac{2}{3} \right) \left[1 - \frac{B}{\sqrt{G}\sqrt{B+G}} \operatorname{atanh}\left(\sqrt{\frac{G}{B+G}}\right) \right]}$
Bias	$\frac{B}{2p_w f_s} \frac{\frac{2}{3} - \frac{B}{G} \left[1 - \frac{B}{\sqrt{G}\sqrt{B+G}} \operatorname{atanh}\left(\sqrt{\frac{G}{B+G}}\right) \right]}{\frac{t_d}{3p_w} - \left(\frac{t_d B}{2p_w G} + \frac{2}{3} \right) \left[1 - \frac{B}{\sqrt{G}\sqrt{B+G}} \operatorname{atanh}\left(\sqrt{\frac{G}{B+G}}\right) \right]}$

The bias estimate CRLB is J_{GG} (Eq. 3.54) divided by the determinant d from Eq. 3.60.

$$\operatorname{Var} \left[\hat{B} \right] \geq \frac{J_{GG}}{d} = \frac{B}{2p_w f_s} \frac{\frac{2}{3} - \frac{B}{G} \left(1 - \frac{aB}{B+G} \right)}{\frac{t_d}{3p_w} - \left(\frac{t_d B}{2p_w G} + \frac{2}{3} \right) \left(1 - \frac{aB}{B+G} \right)}. \quad (3.63)$$

The following term appears in the gain and bias CRLBs (Eqs. 3.62 and 3.63) and can be expressed in terms of the hyperbolic arctangent function.

$$1 - \frac{aB}{B+G} = 1 - \frac{B}{\sqrt{G}\sqrt{B+G}} \operatorname{atanh} \left(\sqrt{\frac{G}{B+G}} \right) \quad (3.64)$$

The Cramer-Rao lower bounds for the parabolic pulse LADAR signal model from Eq. 3.2 are summarized in Table 3.1.

3.1.3 Maximum Likelihood Estimation of Parameters. Maximum likelihood estimation is one of the most popular parameter estimation techniques. The MLEs for the range, gain, and bias in the parabolic pulse signal model from Eq. 3.2 are calculated from the joint PDF for the samples (Eq. 2.33).

The likelihood function is maximized with respect to the unknown values. Maximization of the likelihood function is equivalent to maximization of the log-likelihood function from Eq. 3.4. Since the log-likelihood function is easier to work with with respect to range, it is used to find the MLEs. The derivative of the log-likelihood

function with respect to range is (see Eqs. 3.5 and 3.22)

$$\begin{aligned} \frac{\partial l(R, G, B)}{\partial R} &= \frac{4G}{cp_w} \sum_{k=1}^K \frac{d(t_k)}{G \left[1 - \left(\frac{t_k - 2R/c}{p_w} \right)^2 \right] + B} \left(\frac{t_k - 2R/c}{p_w} \right) \text{rect} \left(\frac{t_k - 2R/c}{2p_w} \right) \\ &\quad - \frac{4G}{cp_w} \sum_{k=1}^K \left(\frac{t_k - 2R/c}{p_w} \right) \text{rect} \left(\frac{t_k - 2R/c}{2p_w} \right). \end{aligned} \quad (3.65)$$

The second term has odd symmetry about the center of the rectangle function. Therefore, it goes to zero. The MLE is found by setting Eq. 3.65 to zero. The range MLE is the value of \hat{R} that satisfies the following equation.

$$\sum_{k=1}^K \frac{d(t_k)}{G \left[1 - \left(\frac{t_k - 2\hat{R}/c}{p_w} \right)^2 \right] + B} \left(\frac{t_k - 2\hat{R}/c}{p_w} \right) \text{rect} \left(\frac{t_k - 2\hat{R}/c}{2p_w} \right) = 0. \quad (3.66)$$

Evaluation of Eq. 3.66 requires knowledge of the gain and bias. In real LADAR data, the gain and bias are usually unknowns. Thus, the range, gain, and bias usually have to be estimated simultaneously in order to calculate the range MLE.

The derivative of the log-likelihood function with respect to gain is (see Eqs. 3.6 and 3.23)

$$\begin{aligned} \frac{\partial l(R, G, B)}{\partial G} &= \sum_{k=1}^K \frac{d(t_k)}{G \left[1 - \left(\frac{t_k - 2R/c}{p_w} \right)^2 \right] + B} \left[1 - \left(\frac{t_k - 2R/c}{p_w} \right)^2 \right] \text{rect} \left(\frac{t_k - 2R/c}{2p_w} \right) \\ &\quad - \sum_{k=1}^K \left[1 - \left(\frac{t_k - 2R/c}{p_w} \right)^2 \right] \text{rect} \left(\frac{t_k - 2R/c}{2p_w} \right). \end{aligned} \quad (3.67)$$

By using the change of variable from Eq. 3.35, the second summation in Eq. 3.67 can be written

$$\begin{aligned} \sum_{k=1}^K \left[1 - \left(\frac{t_k - 2R/c}{p_w} \right)^2 \right] \text{rect} \left(\frac{t_k - 2R/c}{2p_w} \right) &\approx f_s p_w \int_{-1}^1 (1 - v^2) dv \\ &= \frac{4}{3} f_s p_w. \end{aligned} \quad (3.68)$$

Therefore, the gain MLE is the value of \hat{G} satisfying

$$\sum_{k=1}^K \frac{d(t_k) \left[1 - \left(\frac{t_k - 2R/c}{p_w} \right)^2 \right] \text{rect} \left(\frac{t_k - 2R/c}{2p_w} \right)}{\hat{G} \left[1 - \left(\frac{t_k - 2R/c}{p_w} \right)^2 \right] + B} = \frac{4}{3} f_s p_w. \quad (3.69)$$

The derivative of the log-likelihood function with respect to bias is

$$\frac{\partial l(R, G, B)}{\partial B} = -K + \sum_{k=1}^K \frac{d(t_k)}{G \left[1 - \left(\frac{t_k - 2R/c}{p_w} \right)^2 \right] \text{rect} \left(\frac{t_k - 2R/c}{2p_w} \right) + B}. \quad (3.70)$$

Therefore, the MLE of the bias is the value \hat{B} that satisfies

$$\sum_{k=1}^K \frac{d(t_k)}{G \left[1 - \left(\frac{t_k - 2R/c}{p_w} \right)^2 \right] \text{rect} \left(\frac{t_k - 2R/c}{2p_w} \right) + \hat{B}} = K. \quad (3.71)$$

All three of the MLEs derived (Eqs. 3.66, 3.69, and 3.71) require knowledge of the other unknown parameters in the model. In practice all three MLEs must be solved simultaneously. Additionally, there is no analytic solution for any of these MLEs. All must be solved using iterative numeric methods. Iterative numeric estimation of multiple parameters is often complicated and can be time consuming. Therefore, in Sec. 3.1.4 alternate methods of estimation are considered.

3.1.4 Range Estimation Methods. It is noted in Sec. 3.1.3 that the maximum likelihood estimates of range, gain, and bias in the parabolic pulse model are difficult to calculate. Calculation is complicated because the MLEs must be evaluated using iterative numeric methods implemented simultaneously on all three parameters. This complexity leads to consideration of simpler parameter estimates.

It is proposed that range estimation can be done using a combination of matched filtering and peak fitting. The problem of range estimation for a signal that has been mixed with zero-mean white Gaussian noise was considered in *Fundamentals of Statistical Signal Processing: Estimation Theory* by Kay [23]. It was determined that for a signal mixed with zero-mean Gaussian noise, that the range MLE can be calculated by filtering the noisy signal with a noiseless copy of the signal. The range MLE is the range at which the filtered output is at its maximum.

Range estimation in LADAR systems differs from the zero-mean Gaussian noise case because the received signal is Poisson-distributed and never has nonnegative values. Also, while it is assumed that each sample in the received signal is statistically independent from every other sample, the variance is changes from sample to sample. In fact, the variance is equal to the mean value for Poisson noise.

The range estimate is based on the Gaussian noise MLE from [23]. The estimate is the range at which the output of the data $d(t)$, convolved with filter $h(t)$, is at its maximum. The range estimate R can be written

$$\hat{R} = \arg \max_R h(t) * d(t). \quad (3.72)$$

Because the Poisson-distributed noise is not white, the matched filter is not necessarily the optimal filter for range estimation. Thus, alternative filters are tested in the range estimation process. Four different filters were tested in Eq. 3.72. In the first case, the filter is equal to the shape of the parabolic pulse $p_p(t)$. That is,

$$h_1(t) = p_p(t) \quad (3.73)$$

where the pulse is

$$p_p(t) = \left[1 - \left(\frac{t_k - 2R/c}{p_w} \right)^2 \right] \text{rect} \left(\frac{t_k - 2R/c}{2p_w} \right). \quad (3.74)$$

This is a true matched filter where $h_1(t)$ is equal to the noiseless pulse. The next filter tested was the square root of the noiseless pulse. The reason for trying this variation on the true matched filter is that in the Poisson noise case, the samples with the highest mean also have the greatest variance. Using the square root of the noiseless pulse will put slightly less weight on the highest variance samples than the standard matched filter does. The filter is,

$$h_2(t) = [p_p(t)]^{1/2}. \quad (3.75)$$

The third filter tested uses the true mean value of the received signal. Because the noise (the bias) is not zero-mean, the bias value is added to the filter. This filter is

$$h_3(t) = Gp_p(t) + B. \quad (3.76)$$

The final filter tested was the square root of the true mean value. The motivation for using this filter is the same as for filter $h_2(t)$ (Eq. 3.75). That is, the square root operation puts slightly less weight on the highest variance values in the received signal than the filter without the square root (Eq. 3.76) does. This filter is,

$$h_4(t) = [Gp_p(t) + B]^{1/2}. \quad (3.77)$$

There is a fundamental difference between the first two and the last two filters. The first two filters (Eqs. 3.73 and 3.75) do not require any knowledge of the unknown parameters in the system. The second two filters (Eqs. 3.76 and 3.77) assumed exact knowledge of the gain and bias in the system. In practice, the gain and bias may not be known exactly and may need to be replaced with estimates in order to implement the

second two filters. Filters that assume knowledge of system parameters that could be unknowns are sometimes called clairvoyant filters [10]. Because the second two filters assume knowledge of the gain and bias in the system, they are called clairvoyant.

The four filters were tested using Monte Carlo simulations. The results are shown in Fig. 3.3. Simulated Poisson noise signals were generated. A simulated ten nanosecond pulse ($p_w = 10$ ns) was centered within a one hundred nanosecond ($t_d = 100$ ns) sampling interval. This signal was sampled at a rate of one Gigahertz ($f_s = 1$ GHz). Therefore, there were one hundred samples in each simulated received signal ($K = 100$). The bias in the signal was fixed at five ($B = 5$) and the gain was varied from one-tenth to one thousand ($0.1 \leq G \leq 1000$). The Monte Carlo simulation was run many times in order to obtain multiple range estimates for each gain value simulated. The precision of the range estimate was measured by calculating the sample mean over the set of range estimates for each of the four filters.

The simulated received signals were processed using each of the four filters (Eqs. 3.73 - 3.77). The simulated signal was convolved with each of the filters, then the edges of the output were trimmed so that the width of the sampling interval was not increased. The range estimate was obtained by finding the peak sample and then doing a three-point parabolic fit to the peak output point and the two adjacent points. The exact parabolic fit algorithm used was the one presented in Eqs. 1 and 2 of [20]. The parabolic fit was used to get precision better than a bin width from the range estimate. If the range estimate had been set to the center of the peak bin, then the precision could never be better than the standard deviation of a uniform random variable over one bin width.

The sampling duration is t_d . The measured round-trip time t_{rt} is related to the round-trip range R_{rt} by

$$R_{rt} = t_{rt}c \quad (3.78)$$

where c is the speed of light. The variance of a uniform random variable is the width of that random variable's support squared divided by twelve. Therefore, the variance

of a range estimate that is uniformly distributed over a sampling duration of t_d is

$$\sigma_R^2 = \frac{t_d^2 c^2}{48}. \quad (3.79)$$

Inspection of the results shown in Fig. 3.3 shows that none of the filters tested achieved the Cramer-Rao lower bound. However, for gain values between about three and one thousand, the best precision was at worst about double the CRLB. As the gain values dropped below the level of the bias, the range precision decreased rapidly. For gains around one and two, the range estimate standard deviation is nearly ten times the CRLB. When the gain is low enough (less than about one), the range estimate precision is equal to the precision of a uniform random estimate over the search interval (see Eq. 3.79). A uniform random error is effectively the worst case scenario. Therefore, the filtering operation is providing no benefit for gain values below one.

The Ziv-Zakai lower bound (ZZLB) is sometimes used to characterize limits on parameter precision. The ZZLB was originally derived in [57] and was improved in [6]. In [24], it was applied to estimation of pulse time-of-flight. The ZZLB has the advantage of being valid in the low signal-to-noise (SNR) regime. However, it is more complicated to evaluate than the CRLB [24]. Also, the ZZLB is not as tight as the CRLB at high SNRs [6]. Thus, it was not used in this dissertation.

The estimate variances in Fig. 3.3 drop below the variance predicted by the CRLB because at very low gain values, they are biased. Unbiased parameter estimates can not have variances lower than what is predicted by their Cramer-Rao lower bounds. However, it is possible for a biased estimate to have a variance lower than the CRLB.

The best filter overall is the square root filter (Eq. 3.75). However, the standard matched filter (Eq. 3.73) did perform slightly better than the square root filter for a small range of gain values. The standard matched filter worked the best for gains from about three to ten. The clairvoyant filters (the filters that assumed exact knowledge of

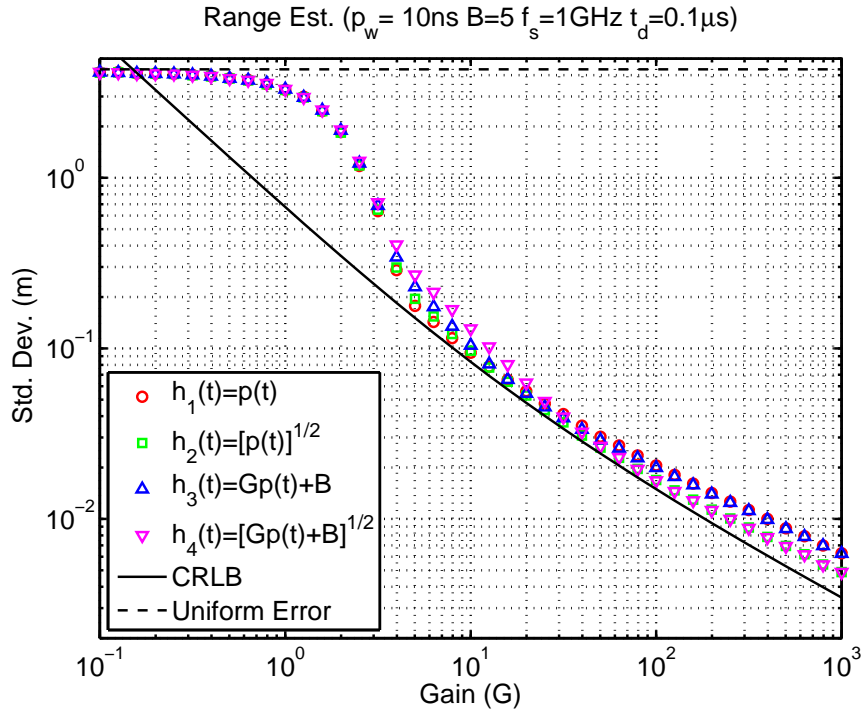


Figure 3.3: Illustration shows range precision produced by four different filters. The Cramer-Rao lower bound is also shown.

the gain and bias) did not work better than the standard matched filter and the square root matched filter. In general, the precision of parameter estimation improves when more of the other parameters are known. But in this case, knowledge of the gain and bias did not help. However, it is possible that a different filter that incorporated the gain and bias values in a different way could achieve performance closer to the Cramer-Rao lower bound. The clairvoyant filters performed worse than their counterparts. This performance convergence was expected since as G/B approaches infinity, the filters themselves converge to the non-clairvoyant versions.

Several more Monte Carlo simulations of range estimation are shown in Fig. 3.4. Since the results in Fig. 3.3 showed that the square root filter had the best overall performance, it was the only filter used in these simulations. In these simulations, the sampling duration was $t_d = 100$ ns and the sampling rate was $f_s = 1$ GHz.

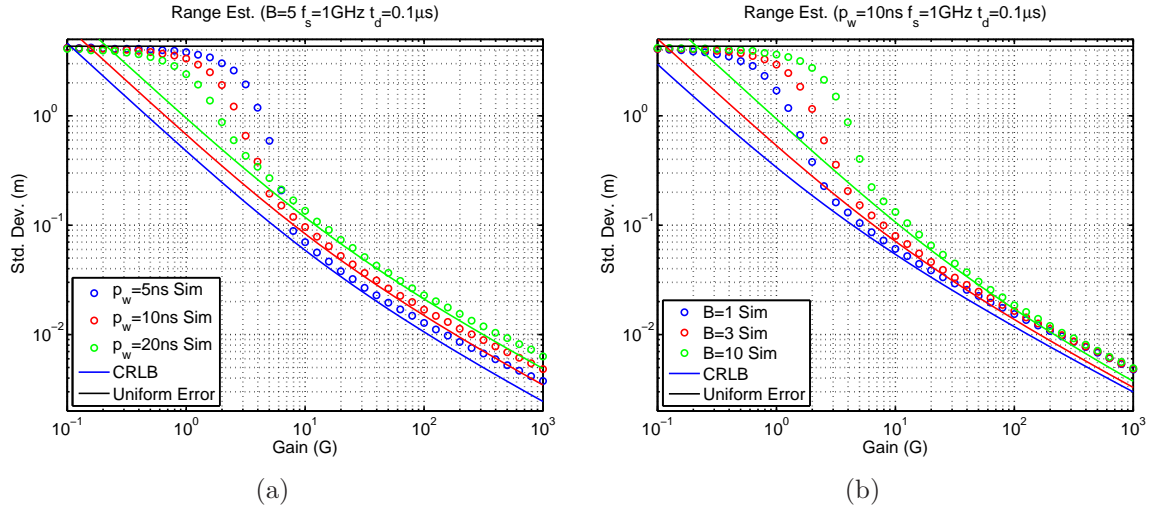


Figure 3.4: (a) Range estimation with bias $B = 5$.
(b) Range estimation with pulse width $p_w = 10$ ns.

In Fig. 3.4a, the bias is $B = 5$ and the plot is parametric in pulse width. The narrowest pulse ($p_w = 5$ ns) had the best performance over most of the gain values. With all else being equal, short pulses are better than long pulses for range estimation since the received signal energy is focused within a shorter duration. When a long pulse is used, the energy is spread over a longer duration and it is more difficult to obtain an precise measurement of the peak value (the range estimate). However, the longest pulse ($p_w = 20$ ns) shows performance closest to the CRLB and showed the best performance at certain low gain values (below about five). It is possible that the longer pulse is closer to the CRLB than the shorter pulses because the shorter pulses have more energy at higher frequencies and are not being sampled quickly enough. The Nyquist frequency ($f_n = f_s/2$) was 500 MHz in these simulations. The 5 ns pulse has four times the bandwidth of the 20 ns pulse, so it is possible that the 20 ns pulse is being sampled at an adequate rate while the 5 ns pulse is experiencing aliasing when sampled.

The bandwidth of a parabolic pulse was derived in Appendix B. It is shown in Fig. B.2 that only about two parts in ten thousand of the total energy is outside the Nyquist frequency for the 5 ns pulse. The energy outside the Nyquist frequency is

aliased and will interfere with parameter estimates. The fraction of parabolic pulse energy aliased for the 10 and 20 ns pulses is nearly one-tenth, and one one-hundredth, lower than for the 5 ns pulse, respectively. The lower amount of aliased energy is a possible explanation for why the longer pulses were closer to the range estimate CRLB in Fig. 3.4a.

In Fig. 3.4b, the pulse width is $p_w = 10$ ns and the plot is parametric in bias. It is not surprising that the best range estimate precision was observed when the bias was lowest ($B = 1$). For bias $B = 1$, the range estimate was nearly at the CRLB for gain values over about three. For the highest bias case ($B = 10$), the precision was significantly over the CRLB until the gain was greater than about six. Once the gain was over about one hundred, the range precision was roughly equal for all three bias values simulated because at those levels, the bias was much smaller than the gain in each case.

3.1.5 Gain and Bias Estimation. In Sec. 3.1.3, the maximum likelihood estimates for gain (Eq. 3.69) and bias (Eq. 3.71) are derived. However, the MLEs for both of these parameters are difficult to evaluate. In this section, simple clairvoyant estimates of gain and bias are proposed and tested. The estimates are clairvoyant because they assume knowledge of the range to the target. These clairvoyant estimates are not useful with real data since they assume knowledge of a parameter that is unknown (the range). The purpose of these estimates is to validate the Cramer-Rao lower bound formulas derived in Sec. 3.1.2.

The bias estimate used throws out the points in the received data that contain any part of the parabolic pulse. The estimator then averages the remaining points to obtain the bias estimate. Mathematically, the bias estimate is

$$\hat{B} = \frac{\sum_{k=1}^K d(t_k) \left[1 - \text{rect} \left(\frac{t_k - 2R/c}{2p_w} \right) \right]}{\sum_{k=1}^K \left[1 - \text{rect} \left(\frac{t_k - 2R/c}{2p_w} \right) \right]}. \quad (3.80)$$

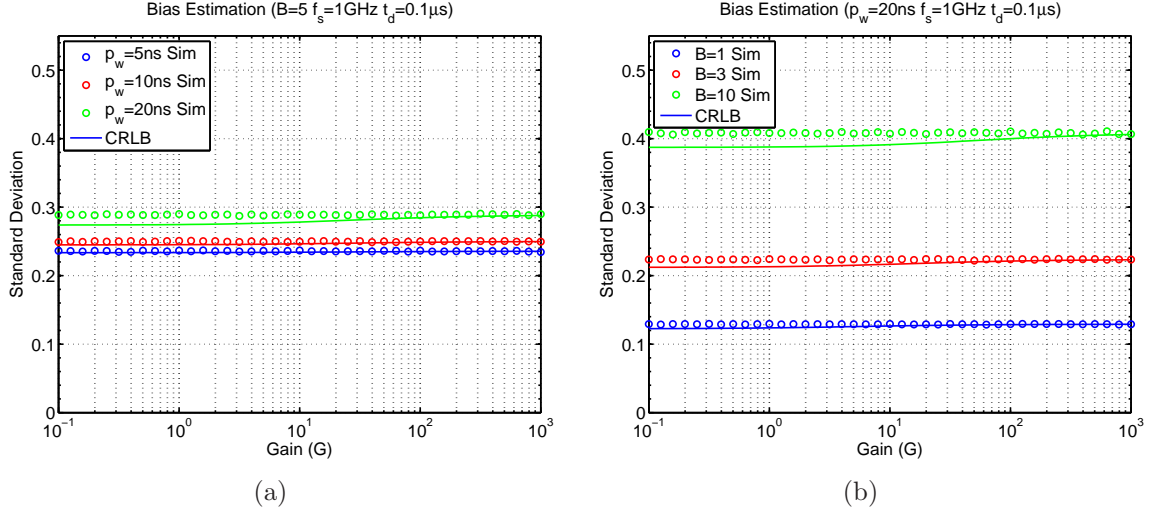


Figure 3.5: (a) Bias estimation with bias $B = 5$.
(b) Bias estimation with pulse width $p_w = 10$ ns.

The same estimate was used in [4]. Eq. 3.80 is equal to Eq. 3 from that reference. This estimator is simply an average of the data points that are separate from the pulse. The $\text{rect}(x)$ term in the numerator and denominator zero the points that are part of the parabolic pulse in the received signal.

Monte Carlo simulations of gain estimation are shown in Fig. 3.6. As in the range estimation simulations (Figs. 3.3, 3.4), the sampling duration is $t_d = 100$ ns and the sampling rate is $f_s = 1$ GHz. In Fig. 3.6a, the bias is fixed at $B = 5$ and the plot is parametric in pulse width. In Fig. 3.6b, the pulse width is fixed at $p_w = 10$ ns and the plot is parametric in bias. In both Fig. 3.6a and 3.6b, the precision of the bias estimate (Eq. 3.80) meets the CRLB unless the pulse duration is long and the gain is low. If the pulse duration is short, then very little data is omitted by the $\text{rect}(x)$ function in the estimator. If the gain is high, then the data in the pulse is of little use for bias estimation regardless of the pulse duration.

A relatively simple gain estimate can be derived by first examining the expectation of the sum of the data points from the pulse.

$$\begin{aligned}
& \mathbb{E} \left[\sum_{k=1}^K D(t_k) \text{rect} \left(\frac{t_k - 2R/c}{2p_w} \right) \right] & (3.81) \\
& = \sum_{k=1}^K \left\{ G \left[1 - \left(\frac{t_k - 2R/c}{p_w} \right)^2 \right] + B \right\} \text{rect} \left(\frac{t_k - 2R/c}{2p_w} \right) \\
& \approx f_s \int_{2R/c-p_w}^{2R/c+p_w} \left\{ G \left[1 - \left(\frac{t - 2R/c}{p_w} \right)^2 \right] + B \right\} dt \\
& = 2f_s p_w B + f_s G p_w \int_{-1}^1 (1 - v^2) dv \\
& = 2f_s p_w \left(B + \frac{2}{3} G \right)
\end{aligned}$$

where the change of variable from Eq. 3.35 was used. Therefore, the following equation is an unbiased gain estimate.

$$\hat{G} = \frac{3}{4f_s p_w} \left[\sum_{k=1}^K d(t_k) \text{rect} \left(\frac{t_k - 2R/c}{2p_w} \right) \right] - \frac{3\hat{B}}{2} \quad (3.82)$$

where the bias estimate from Eq. 3.80 was used. The $\text{rect}(x)$ function in this estimate omits the points that are outside the parabolic pulse. This estimator was tested using Monte Carlo simulations and the results are shown in Fig. 3.6. In Fig. 3.6a, the bias is fixed at $B = 5$ and the plot is parametric in pulse width. The precision of the estimate improves as the pulse width increases since an increase in pulse width provides more samples to use in the estimator. In Fig. 3.6b, the pulse width is fixed at $p_w = 10$ ns and the bias is varied. The precision of the gain estimator improves as the bias drops since a decrease in bias decreases the variance in the samples used in the estimator.

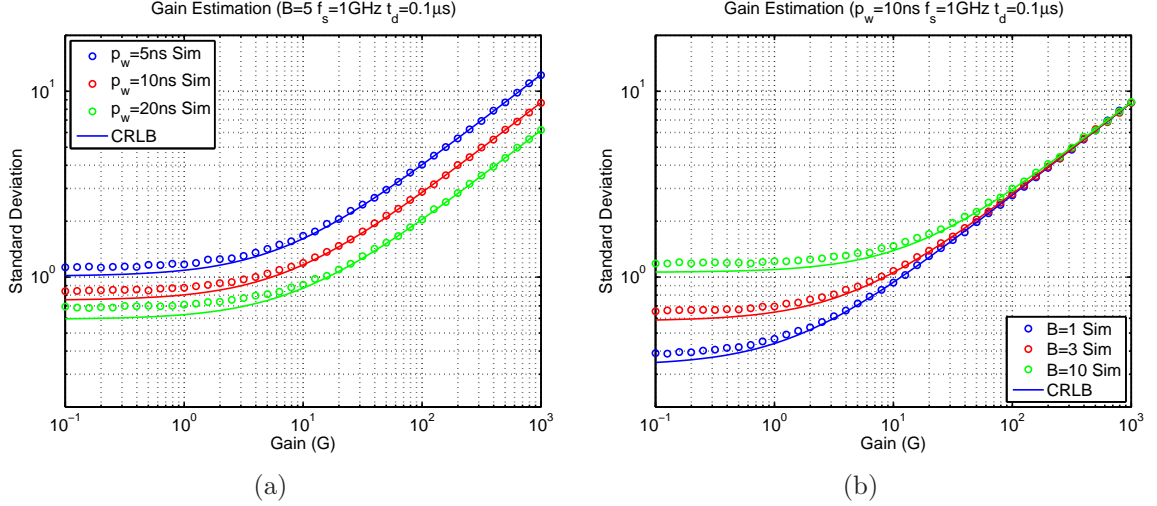


Figure 3.6: (a) Gain estimation with bias $B = 5$.
(b) Gain estimation with pulse width $p_w = 10$ ns.

3.2 Obscured Target LADAR Signal Model

The LADAR signal model published in [4] is a representation of a received signal from a target in the open. However, imaging LADARs are often used to create images of targets that are behind vegetation or beneath tree canopy [26, 27]. In this section, a new signal model is developed that includes the target and the obscuration. This new model is used to derive estimators for parameters including the target range. The model is also used to derive CRLBs for the signal parameters.

3.2.1 LADAR Signal Model with Obscuration. In order to develop efficient obscured target detection algorithms, a signal model is needed that includes the obscuration and the target. The model in [4] can be modified to include two returns, one from the obscuration and one from the target behind the obscurant. There are different range (R) and gain (G) values for both of the returns. As with the single return model, the bias is assumed to be at a constant level over all samples. The

following modification of the parabolic pulse model from Eq. 3.2 is proposed.

$$\begin{aligned}
I(t_k) = & G_1 \left[1 - \left(\frac{t_k - 2R_1/c}{p_w} \right)^2 \right] \text{rect} \left(\frac{t_k - 2R_1/c}{2p_w} \right) \\
& + G_2 \left[1 - \left(\frac{t_k - 2R_2/c}{p_w} \right)^2 \right] \text{rect} \left(\frac{t_k - 2R_2/c}{2p_w} \right) + B.
\end{aligned} \tag{3.83}$$

This equation is similar to the single return parabolic pulse model from Eq. 3.2. However, it has separate gain and range values for the obscuration (G_1 and R_1) and for the target (G_2 and R_2). It is assumed that R_1 is the range to the object closer to the sensor and that R_2 is the range to the farther object ($R_1 < R_2$).

It is assumed that the two pulses do not overlap and that both pulses are completely sampled. In order for the pulses to not overlap, it is required that $R_2 - R_1 > p_w c$. The requirements that must be satisfied for the pulses to be completely sampled are $2R_1/c > p_w$ and $2R_2/c < t_d - p_w$. At the speed of light, every nanosecond of pulse width corresponds to about one foot of distance. Pulses that are only a few nanoseconds are able to resolve multiple targets that are separated by a few feet.

The obscured target signal model from Eq. 3.83 is illustrated in Fig. 3.7. As in the original parabolic pulse signal model from Eq. 3.2, p_w is the three-quarter width of the maximum pulse height. The entire pulse width is $2p_w$. The bias illustrated in Fig. 3.7 is one-half ($B = 0.5$). There are two signals. One represents the signal received from the obscuration. The other signal is from the target. The obscuration range and gain illustrated in Fig. 3.7 are $R_1 = 5$ m and $G_1 = 2$. The target range and gain are $R_2 = 10$ m and $G_2 = 0.25$.

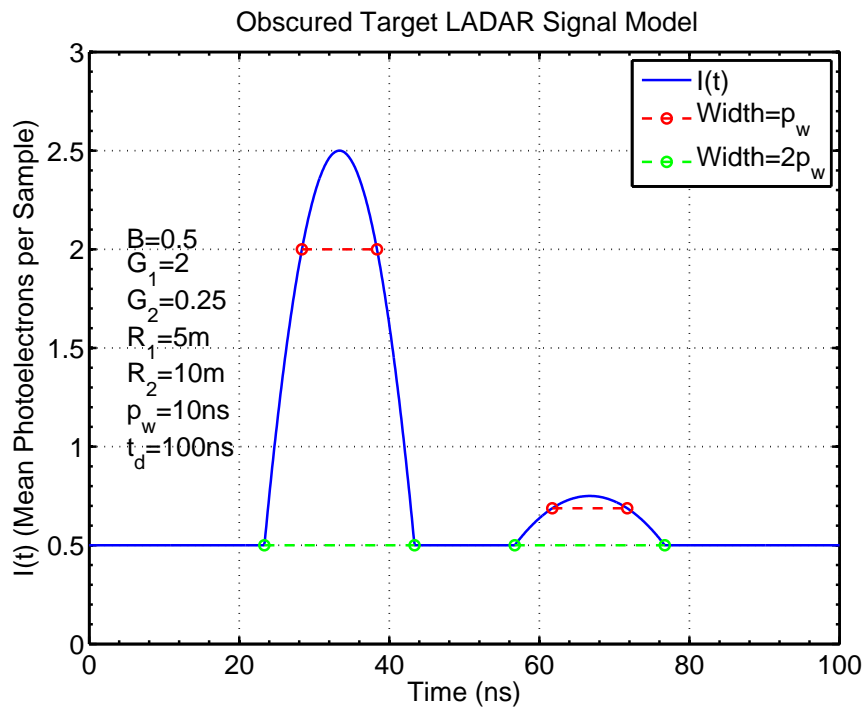


Figure 3.7: Illustration of the obscured target LADAR signal model with parabolic pulses. This model can be used for CRLB derivations and to calculate parameter estimates.

3.2.2 *Fisher Information Matrix Elements.* The Fisher information matrix for the variable pulse width model from Eq. 3.83 is

$$\mathbf{J}(R_1, R_2, G_1, G_2, B) \quad (3.84)$$

$$= - \begin{bmatrix} \mathbb{E} \left[\frac{\partial^2 l}{\partial R_1^2} \right] & \mathbb{E} \left[\frac{\partial^2 l}{\partial R_1 \partial R_2} \right] & \mathbb{E} \left[\frac{\partial^2 l}{\partial R_1 \partial G_1} \right] & \mathbb{E} \left[\frac{\partial^2 l}{\partial R_1 \partial G_2} \right] & \mathbb{E} \left[\frac{\partial^2 l}{\partial R_1 \partial B} \right] \\ \mathbb{E} \left[\frac{\partial^2 l}{\partial R_1 \partial R_2} \right] & \mathbb{E} \left[\frac{\partial^2 l}{\partial R_2^2} \right] & \mathbb{E} \left[\frac{\partial^2 l}{\partial R_2 \partial G_1} \right] & \mathbb{E} \left[\frac{\partial^2 l}{\partial R_2 \partial G_2} \right] & \mathbb{E} \left[\frac{\partial^2 l}{\partial R_2 \partial B} \right] \\ \mathbb{E} \left[\frac{\partial^2 l}{\partial R_1 \partial G_1} \right] & \mathbb{E} \left[\frac{\partial^2 l}{\partial R_2 \partial G_1} \right] & \mathbb{E} \left[\frac{\partial^2 l}{\partial G_1^2} \right] & \mathbb{E} \left[\frac{\partial^2 l}{\partial G_1 \partial G_2} \right] & \mathbb{E} \left[\frac{\partial^2 l}{\partial G_1 \partial B} \right] \\ \mathbb{E} \left[\frac{\partial^2 l}{\partial R_1 \partial G_2} \right] & \mathbb{E} \left[\frac{\partial^2 l}{\partial R_2 \partial G_2} \right] & \mathbb{E} \left[\frac{\partial^2 l}{\partial G_1 \partial G_2} \right] & \mathbb{E} \left[\frac{\partial^2 l}{\partial G_2^2} \right] & \mathbb{E} \left[\frac{\partial^2 l}{\partial G_2 \partial B} \right] \\ \mathbb{E} \left[\frac{\partial^2 l}{\partial R_1 \partial B} \right] & \mathbb{E} \left[\frac{\partial^2 l}{\partial R_2 \partial B} \right] & \mathbb{E} \left[\frac{\partial^2 l}{\partial G_1 \partial B} \right] & \mathbb{E} \left[\frac{\partial^2 l}{\partial G_2 \partial B} \right] & \mathbb{E} \left[\frac{\partial^2 l}{\partial B^2} \right] \end{bmatrix}.$$

The log-likelihood derivatives with respect to R_i and G_i are equal to zero outside the range $|t - 2R_i/c| < p_w$ (see Eqs. 3.22 and 3.23). Therefore, the second derivatives from the FIM (Eq. 3.84) are zero for any pair of parameters that characterizes the obscuration and the target. Thus, there are several FIM terms with expected value zero.

$$\mathbb{E} \left[\frac{\partial^2 l}{\partial R_1 \partial R_2} \right] \approx \mathbb{E} \left[\frac{\partial^2 l}{\partial R_1 \partial G_2} \right] \approx \mathbb{E} \left[\frac{\partial^2 l}{\partial G_1 \partial R_2} \right] \approx \mathbb{E} \left[\frac{\partial^2 l}{\partial G_1 \partial G_2} \right] \approx 0. \quad (3.85)$$

The range and gain second derivatives for the signal from the obscuration and target will also be about zero as they were for the single parabolic pulse case (see Eq. 3.36).

$$\mathbb{E} \left[\frac{\partial^2 l}{\partial R_1 \partial G_1} \right] \approx \mathbb{E} \left[\frac{\partial^2 l}{\partial R_2 \partial G_2} \right] \approx 0. \quad (3.86)$$

The range and bias second derivatives are also about zero (see Eq. 3.38).

$$\mathbb{E} \left[\frac{\partial^2 l}{\partial R_1 \partial B} \right] \approx \mathbb{E} \left[\frac{\partial^2 l}{\partial R_2 \partial B} \right] \approx 0. \quad (3.87)$$

Therefore, the only nonzero off-diagonal terms in the Fisher information matrix are the second derivative pairs corresponding to the two gain variables and the bias.

The diagonal elements for range and gain are identical to the ones derived for the parabolic pulse model in Sec. 3.1. The obscured target model FIM (Eq. 3.84) can be populated using Eqs. 3.33 and 3.45. The range terms are

$$\begin{aligned} -\mathbb{E} \left[\frac{\partial^2 l}{\partial R_i^2} \right] &\approx \frac{32G_i f_s}{p_w c^2} \left[\sqrt{\frac{B+G_i}{G_i}} \operatorname{atanh} \left(\sqrt{\frac{G_i}{B+G_i}} \right) - 1 \right] \\ &= \frac{32G_i f_s}{p_w c^2} (a_i - 1) \end{aligned} \quad (3.88)$$

where

$$a_i = \sqrt{\frac{B+G_i}{G_i}} \operatorname{atanh} \left(\sqrt{\frac{G_i}{B+G_i}} \right). \quad (3.89)$$

The gain terms are

$$-\mathbb{E} \left[\frac{\partial^2 l}{\partial G_i^2} \right] \approx \frac{2p_w f_s}{G_i} \left[\frac{2}{3} - \frac{B}{G_i} \left(1 - \frac{a_i B}{B+G_i} \right) \right]. \quad (3.90)$$

The approximation to the FIM bias element is not the same as the one in the parabolic pulse model because of the multiple pulses present in the received signal. However, it is evaluated in the same way as was done in Eqs. 3.48 - 3.51. Combining Eqs. 3.18 and 3.83 yields

$$\begin{aligned} -\mathbb{E} \left[\frac{\partial^2 l}{\partial B^2} \right] &= \sum_{k=1}^K \frac{1}{I(t_k)} \\ &\approx f_s \frac{t_d - 4p_w}{B} \\ &\quad + f_s \int_{2R_1/c-p_w}^{2R_1/c+p_w} \frac{dt}{G_1 \left[1 - \left(\frac{t-2R_1/c}{p_w} \right)^2 \right] \operatorname{rect} \left(\frac{t-2R_1/c}{2p_w} \right) + B} \\ &\quad + f_s \int_{2R_2/c-p_w}^{2R_2/c+p_w} \frac{dt}{G_2 \left[1 - \left(\frac{t-2R_2/c}{p_w} \right)^2 \right] \operatorname{rect} \left(\frac{t-2R_2/c}{2p_w} \right) + B}. \end{aligned} \quad (3.91)$$

Through the change of variable from Eq. 3.26, this equation can be written

$$\begin{aligned}
-\mathbb{E} \left[\frac{\partial^2 l}{\partial B^2} \right] &\approx f_s \frac{t_d - 4p_w}{B} + \frac{p_w f_s}{\sqrt{G_1} \sqrt{B + G_1}} \int_{-\sqrt{\frac{G_1}{B+G_1}}}^{\sqrt{\frac{G_1}{B+G_1}}} \frac{du}{1 - u^2} \\
&\quad + \frac{p_w f_s}{\sqrt{G_2} \sqrt{B + G_2}} \int_{-\sqrt{\frac{G_2}{B+G_2}}}^{\sqrt{\frac{G_2}{B+G_2}}} \frac{du}{1 - u^2}. \tag{3.92}
\end{aligned}$$

The integrals in the previous equation are equivalent to the integral that appears in Eq. 3.50. Using the result from that equation, the FIM term can be written

$$\begin{aligned}
-\mathbb{E} \left[\frac{\partial^2 l}{\partial B^2} \right] &\approx f_s \frac{t_d - 4p_w}{B} + \frac{2p_w f_s}{\sqrt{G_1} \sqrt{B + G_1}} \operatorname{atanh} \left(\sqrt{\frac{G_1}{B + G_1}} \right) \\
&\quad + \frac{2p_w f_s}{\sqrt{G_2} \sqrt{B + G_2}} \operatorname{atanh} \left(\sqrt{\frac{G_2}{B + G_2}} \right) \\
&= 2p_w f_s \left[\frac{t_d - 4p_w}{2p_w B} + \frac{a_1}{B + G_1} + \frac{a_2}{B + G_2} \right]. \tag{3.93}
\end{aligned}$$

This analytic approximation is compared to the output of a numeric integration in Fig. 3.8b and the results are nearly identical.

The only nonzero off-diagonal FIM term is the one that corresponds to the gain and the bias. This term is identical to the one from the parabolic pulse model. It is (see Eq. 3.47)

$$-\mathbb{E} \left[\frac{\partial^2 l}{\partial G_i \partial B} \right] \approx \frac{2p_w f_s}{G_i} \left(1 - \frac{a_i B}{B + G_i} \right). \tag{3.94}$$

3.2.3 Cramer-Rao Lower Bounds. The Cramer-Rao lower bounds are the lower limits on the variance of any unbiased estimate of an unknown parameter. The CRLBs are obtained by inverting the Fisher information matrix. The FIM for the

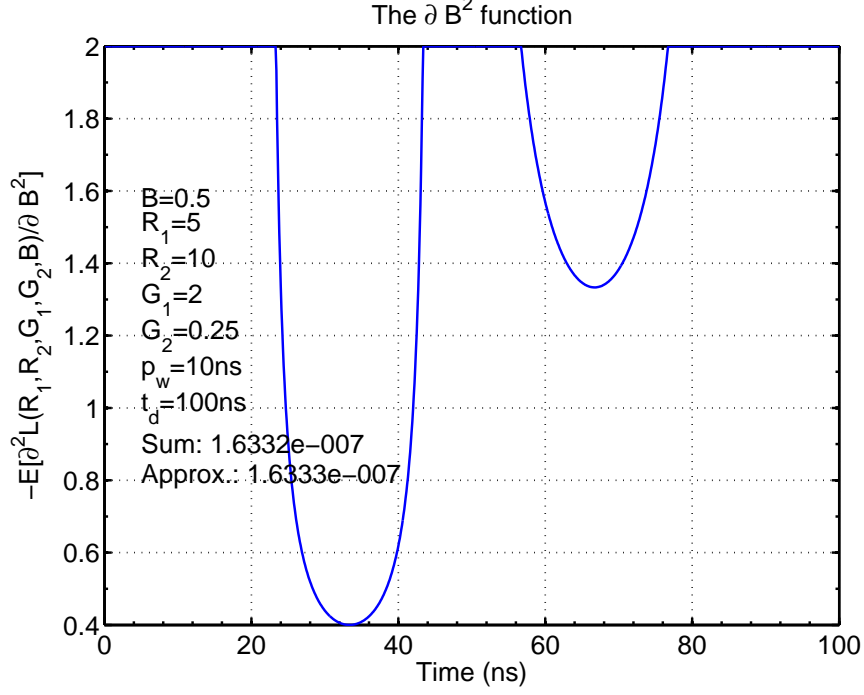


Figure 3.8: The bias second derivative.

parabolic pulse signal model from Eq. 3.83 is

$$\mathbf{J}(R_1, R_2, G_1, G_2, B) \approx \begin{bmatrix} J_{R_1 R_1} & 0 & 0 & 0 & 0 \\ 0 & J_{R_2 R_2} & 0 & 0 & 0 \\ 0 & 0 & J_{G_1 G_1} & 0 & J_{G_1 B} \\ 0 & 0 & 0 & J_{G_2 G_2} & J_{G_2 B} \\ 0 & 0 & J_{G_1 B} & J_{G_2 B} & J_{BB} \end{bmatrix}. \quad (3.95)$$

Several matrix elements approximately equal to zero because the FIM elements shown in Eqs. 3.85, 3.86, and 3.87 are about zero. The nonzero elements of the approximate FIM from Eq. 3.95 are

$$J_{R_i R_i} = \frac{32G_i f_s}{p_w c^2} (a_i - 1), \quad (3.96)$$

$$J_{G_i G_i} = \frac{2p_w f_s}{G_i} \left[\frac{2}{3} - \frac{B}{G_i} \left(1 - \frac{a_i B}{B + G_i} \right) \right], \quad (3.97)$$

$$J_{BB} = 2p_w f_s \left[\frac{t_d - 4p_w}{2p_w B} + \frac{a_1}{B + G_1} + \frac{a_2}{B + G_2} \right], \quad (3.98)$$

and

$$J_{G_i B} = \frac{2p_w f_s}{G_i} \left(1 - \frac{a_i B}{B + G_i} \right) \quad (3.99)$$

where the variable a_i was defined in Eq. 3.89.

The Cramer-Rao lower bounds for the unknown parameters in the obscured target signal model (Eq. 3.83) are the diagonal elements of the inverse of the matrix in Eq. 3.95. The FIM is block diagonal, so it is inverted using Eq. 3.57. The range CRLBs are the reciprocals of the corresponding FIM elements. The CRLB for estimates of range is

$$\text{Var} \left[\widehat{R}_i \right] \geq \frac{p_w c^2}{32G_i f_s (a_i - 1)}. \quad (3.100)$$

The CRLBs for gain and bias are more complicated than the range CRLB since there are off-diagonal elements that complicate the matrix inverse. The gain CRLBs are

$$\text{Var} \left[\widehat{G}_1 \right] \geq \frac{J_{G_2 G_2} J_{BB} - J_{G_2 B}^2}{J_{G_1 G_1} (J_{G_2 G_2} J_{BB} - J_{G_2 B}^2) - J_{G_2 G_2} J_{G_1 B}^2} \quad (3.101)$$

and

$$\text{Var} \left[\widehat{G}_2 \right] \geq \frac{J_{G_1 G_1} J_{BB} - J_{G_1 B}^2}{J_{G_2 G_2} (J_{G_1 G_1} J_{BB} - J_{G_1 B}^2) - J_{G_1 G_1} J_{G_2 B}^2}. \quad (3.102)$$

Finally, the bias CRLB is

$$\text{Var} \left[\widehat{B} \right] \geq \frac{1}{J_{BB} - J_{G_1 B}^2 / J_{G_1 G_1} - J_{G_2 B}^2 / J_{G_2 G_2}}. \quad (3.103)$$

The CRLBs for the obscured target LADAR signal model from Eq. 3.83 are summarized in Tables 3.2 and 3.3. The actual CRLBs are shown in Table 3.3. The Fisher information matrix elements needed to calculate those CRLBs are shown in Table 3.2.

3.2.4 Parameter Estimation. Estimation of the five parameters in the obscured target model from Eq. 3.83 is difficult. It is straightforward to express the likelihood function associated with Eq. 3.83. However, there are no simple analytic

Table 3.2: Obscured Target Model
Fisher Information Matrix Elements.

FIM Element	Value
$J_{G_1G_1}$	$\frac{2p_w f_s}{G_1} \left\{ \frac{2}{3} - \frac{B}{G_1} \left[1 - \frac{B}{\sqrt{G_1}\sqrt{B+G_1}} \operatorname{atanh} \left(\sqrt{\frac{G_1}{B+G_1}} \right) \right] \right\}$
$J_{G_2G_2}$	$\frac{2p_w f_s}{G_2} \left\{ \frac{2}{3} - \frac{B}{G_2} \left[1 - \frac{B}{\sqrt{G_2}\sqrt{B+G_2}} \operatorname{atanh} \left(\sqrt{\frac{G_2}{B+G_2}} \right) \right] \right\}$
J_{G_1B}	$\frac{2p_w f_s}{G_1} \left[1 - \frac{B}{\sqrt{G_1}\sqrt{B+G_1}} \operatorname{atanh} \left(\sqrt{\frac{G_1}{B+G_1}} \right) \right]$
J_{G_2B}	$\frac{2p_w f_s}{G_2} \left[1 - \frac{B}{\sqrt{G_2}\sqrt{B+G_2}} \operatorname{atanh} \left(\sqrt{\frac{G_2}{B+G_2}} \right) \right]$
J_{BB}	$2p_w f_s \left[\frac{t_d - 4p_w}{2p_w B} + \frac{\operatorname{atanh} \left(\sqrt{\frac{G_1}{B+G_1}} \right)}{\sqrt{G_1}\sqrt{B+G_1}} + \frac{\operatorname{atanh} \left(\sqrt{\frac{G_2}{B+G_2}} \right)}{\sqrt{G_2}\sqrt{B+G_2}} \right]$

Table 3.3: Obscured Target Model
Cramer-Rao Lower Bounds.

Parameter	Cramer-Rao Lower Bounds
Range to near target	$\frac{p_w c^2}{32G_1 f_s \left[\sqrt{\frac{B+G_1}{G_1}} \operatorname{atanh} \left(\sqrt{\frac{G_1}{B+G_1}} \right) - 1 \right]}$
Range to far target	$\frac{p_w c^2}{32G_2 f_s \left[\sqrt{\frac{B+G_2}{G_2}} \operatorname{atanh} \left(\sqrt{\frac{G_2}{B+G_2}} \right) - 1 \right]}$
Gain for near target	$\frac{1}{J_{G_1G_1} - J_{G_2G_2} J_{G_1B}^2 / (J_{G_2G_2} J_{BB} - J_{G_2B}^2)}$
Gain for far target	$\frac{1}{J_{G_2G_2} - J_{G_1G_1} J_{G_2B}^2 / (J_{G_1G_1} J_{BB} - J_{G_1B}^2)}$
Bias	$\frac{1}{J_{BB} - J_{G_1B}^2 / J_{G_1G_1} - J_{G_2B}^2 / J_{G_2G_2}}$

solutions that simultaneously maximize the unknowns in that likelihood function. A numeric search algorithm such as a gradient descent based search would be necessary to calculate the MLEs.

It is desirable to test the CRLBs from Sec. 3.2.3 using Monte Carlo methods. Instead of relying on numeric methods, simple suboptimal estimators were used on simulated data following the obscured target model. These estimators are similar to the ones presented in Sec. 3.1.4 and Sec. 3.1.5, but are more complicated because the received signal now contains two different signals.

Four different range estimator filters were tested using Monte Carlo simulations in Sec. 3.1.4. The filter with the best overall performance was $h_2(t)$ (see Eq. 3.75). This filter is used to estimate the range to the largest gain signal. The estimate is

$$\widehat{R}_{large} = \arg \max_R h_2(t) * d(t) \quad (3.104)$$

where filter $h_2(t)$ is the square root of the parabolic pulse from the obscured target model (Eq. 3.83). This filter is

$$h_2(t) = [p_p(t)]^{1/2} = \left[1 - \left(\frac{t - 2R/c}{p_w} \right)^2 \right]^{1/2} \text{rect} \left(\frac{t - 2R/c}{2p_w} \right). \quad (3.105)$$

The estimate above is the range to the peak gain signal. However, there are two signals in the obscured target model. The range to the other signal is calculated using the same filter as in Eq. 3.104. However, the large gain pulse centered at range \widehat{R}_{large} is removed from the data before the filter is employed. The range estimate for the smaller gain pulse can be expressed

$$\widehat{R}_{small} = \arg \max_R h_2(t) * \left\{ d(t) \left[1 - \text{rect} \left(\frac{t - 2\widehat{R}_{large}/c}{2p_w} \right) \right] \right\}. \quad (3.106)$$

The obscured target signal illustrated in Fig. 3.7 shows gain being larger for the closest pulse ($G_1 > G_2$). However, it was not assumed that that the closest

pulse's gain is always larger. Therefore, the range estimate to the closest pulse is the minimum of the estimates from Eq. 3.104 and Eq. 3.106.

$$\widehat{R}_1 = \min \left\{ \widehat{R}_{large}, \widehat{R}_{small} \right\}. \quad (3.107)$$

The range estimate to the pulse that is farther away is

$$\widehat{R}_2 = \max \left\{ \widehat{R}_{large}, \widehat{R}_{small} \right\}. \quad (3.108)$$

As in Sec. 3.1.5, simple clairvoyant gain and bias estimates are used in order to validate the CRLBs derived in Sec. 3.2.3. The estimates are clairvoyant because they assume exact knowledge of the target ranges R_1 and R_2 . The bias estimate is a generalization of the one shown in Eq. 3.80. It is

$$\widehat{B} = \frac{\sum_{k=1}^K d(t_k) \left[1 - \text{rect} \left(\frac{t_k - 2R_1/c}{2p_w} \right) - \text{rect} \left(\frac{t_k - 2R_2/c}{2p_w} \right) \right]}{\sum_{k=1}^K \left[1 - \text{rect} \left(\frac{t_k - 2R_1/c}{2p_w} \right) - \text{rect} \left(\frac{t_k - 2R_2/c}{2p_w} \right) \right]}. \quad (3.109)$$

This bias estimate is similar to the one in Eq. 3.80, but in this case, there are two rectangle functions. Two rectangle functions are needed to remove the two signals in the obscured target model.

The clairvoyant gain estimates are based on the one shown in Eq. 3.82. Like the bias estimate from Eq. 3.109, they assume exact knowledge of the target ranges R_1 and R_2 . They are

$$\widehat{G}_1 = \frac{3}{4f_s p_w} \left[\sum_{k=1}^K d(t_k) \text{rect} \left(\frac{t_k - 2R_1/c}{2p_w} \right) \right] - \frac{3\widehat{B}}{2} \quad (3.110)$$

and

$$\widehat{G}_2 = \frac{3}{4f_s p_w} \left[\sum_{k=1}^K d(t_k) \text{rect} \left(\frac{t_k - 2R_2/c}{2p_w} \right) \right] - \frac{3\widehat{B}}{2}. \quad (3.111)$$

3.2.5 Simulations. Range estimation for an obscured target was simulated using Monte Carlo methods. Many realizations of Poisson-distributed signals with mean values given by Eq. 3.83 were generated. Using the randomly generated data, the ranges to the near and far targets were estimated using Eqs. 3.107 and 3.108. These range estimate equations do not require knowledge of the gain or bias in the data. Thus, they are not clairvoyant estimators. The results of the simulation are shown in Fig. 3.9.

This obscured target range estimation simulation is similar to the range estimation simulation from the previous section (Figs. 3.3 and 3.4). However, there are some differences between the range estimation simulations in the different sections. As the gain drops, the range standard deviation in the simulation shown in Fig. 3.9 settles to value that is less than the uniformly-distributed error from Eq. 3.79. This uniformly-distributed error is not achieved because the range estimation equations (Eqs. 3.107 and 3.108) bias the estimates toward the beginning and end of the interval, respectively. At high gain values, the CRLB is nearly achieved.

Monte Carlo simulations of gain estimation are shown in Fig. 3.10. In Fig. 3.10a, the gain of the first pulse (G_1) is estimated while the gain of the second (G_2) is varied. These simulations, and the CRLBs illustrated in the figure, show that the precision of estimates of one gain value are independent of the other gain value. In Fig. 3.10b, the gain of the second pulse, G_2 , is estimated for different values of that gain. As G_2 increases, the variance of its estimate also increases. This occurs since the data is Poisson-distributed and the variance increases with increases in gain or bias. However, given a particular value of B , the CRLB only drops so far because the variance of the bias remains to interfere with the precision of the estimate.

Monte Carlo simulations of bias estimation are illustrated in Fig. 3.11. In Fig. 3.11a, the gain of the second pulse, G_2 , is varied and the simulations are run for three different bias values ($B = 1, 3, \text{ and } 10$). The bias estimate variance is dominated by the actual bias level. The CRLB does show a slight dependence on the gain level.

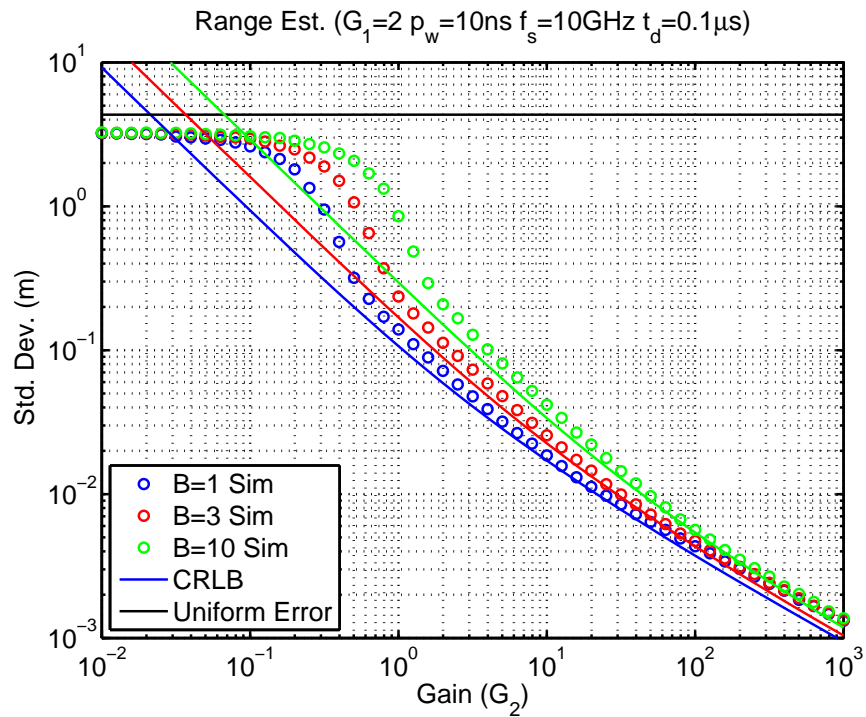


Figure 3.9: Precision of range estimate is shown. Cramer-Rao lower bounds are also illustrated.

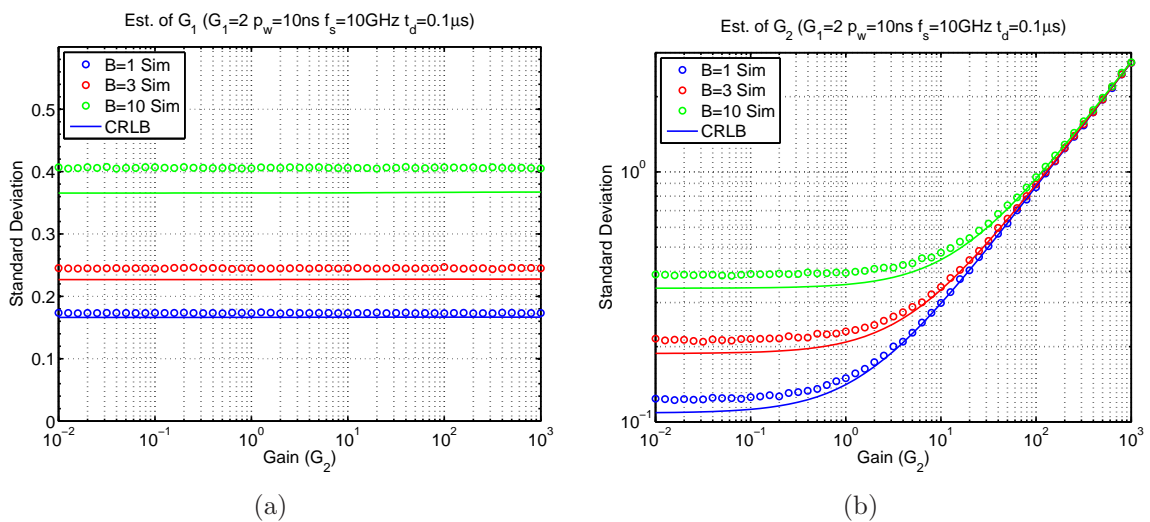


Figure 3.10: (a) Estimation of G_1 as G_2 varies parametric in bias. (b) Estimation of G_2 as G_2 varies parametric in bias.

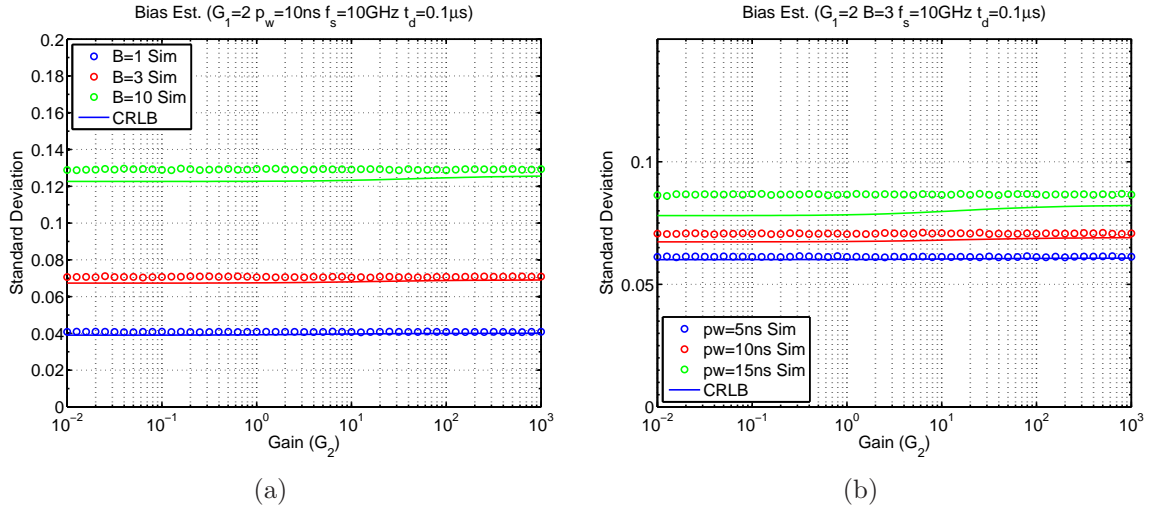


Figure 3.11: (a) Bias estimation with bias $p_w = 10$ ns parametric in bias. (b) Bias estimation with pulse width $B = 3$ parametric in pulse width.

However, the bias estimate used in this simulation, Eq. 3.109, omits laser pulse data. Therefore, the sample variance of the bias estimates in Fig. 3.11a do not depend on G_2 .

In Fig. 3.11b, bias estimation is simulated for different values of G_2 and pulse width (p_w). The bias is fixed at $B = 3$ in all simulations. As in Fig. 3.11a, the CRLB is a function of more than just the bias. In this case, it drops as pulse width decreases because there is more background-only data from which to measure the bias. And as with the Fig. 3.11a case, the CRLB varies with G_2 . The simulations, on the other hand, do not use the laser pulse data and have roughly the same sample variance for all levels of gain.

3.3 Variable Pulse Width LADAR Signals

The single parabolic pulse model from [4] (discussed in Sec. 3.1) and the obscured target model from Sec. 3.2 assume that the pulse width in the received signal is a known constant. This assumption is valid in some cases. The width of the transmitted pulse in a LADAR system is almost always known to a high degree of precision.

Therefore, if the reflection process does not alter the pulse width by a significant amount, then the received pulse width is the same as the transmitted width.

There are scenarios where the reflection process does not make a significant change to the pulse width. When the transmitted laser pulse hits a surface that is perpendicular to the LADAR line of sight, the width of the received pulse is equal to the width of the transmitted pulse. Depending on the transmitted pulse width and the size of the beam after propagation, small perturbations from perpendicular in surface orientation may not change the pulse length by a significant amount. When the beam hits a surface that has depth in range, there is always an increase in the width of the pulse that is received. But if the target's range depth is small compared to the length of the pulse, then the increase in received pulse width will be negligible.

While there are situations where the received laser pulse has the same width as the transmitted pulse, there are also many real world scenarios where the received LADAR signal is wider than that pulse that was transmitted. The laser pulse can hit a flat surface that is not perpendicular to the line of sight. In that case, the received pulse is stretched. Objects being imaged such as buildings, vehicles, and vegetation usually have range depth that will increase the width of the received pulse. In general, the amount of pulse width distortion increases with range since the width of a focused laser beam increases with distance. The problem is also exacerbated as laser pulse width decreases. Short pulses are desirable for good range precision, but are more easily distorted by targets with range depth.

In this section, a single parabolic pulse model is used to simulate the received signal. That finite duration parabola, plus a bias level used to simulate noise sources, models the mean value of the received signal. As in previous sections, the received signal is a sequence of statistically independent Poisson random variables. But in this case, the pulse width is treated as an unknown parameter that must be estimated. However, it is shown through Cramer-Rao lower bound analysis that when the pulse width is unknown, that the range precision of the system does not necessarily decrease.

3.3.1 Variable Pulse Width LADAR Signal Model. The signal model used for the variable pulse width case is equal to the parabolic pulse model from Eq. 3.2. The model is

$$I(t_k) = G \left[1 - \left(\frac{t_k - 2R/c}{p_w} \right)^2 \right] \text{rect} \left(\frac{t_k - 2R/c}{2p_w} \right) + B. \quad (3.112)$$

Mathematically, this model is equivalent to the one presented in Sec. 3.1. But in this case, the pulse width (p_w) is an unknown that must be estimated from the data. The unknown pulse width will increase the size of the Fisher information matrix.

3.3.2 Log-Likelihood Function and its Derivatives. Because the model in Eq. 3.112 has an unknown parameter that is not present in previous models, the CRLBs derived for those models can not be used. The Fisher information matrix for this model contains elements that relate to the unknown pulse width p_w .

The log-likelihood function for the variable pulse width LADAR signal model is

$$l(R, G, B, p_w) = \sum_{k=1}^K d(t_k) \log [I(t_k)] - \sum_{k=1}^K I(t_k) - \sum_{k=1}^K \log [d(t_k)!]. \quad (3.113)$$

Derivatives of the log-likelihood function are used to calculate the CRLBs. However, many of the needed derivatives were already calculated in Sec. 3.1.

The first derivatives of the log-likelihood function with respect to range, gain, and bias have already been computed. The derivative with respect to pulse width is

$$\frac{\partial l(R, G, B, p_w)}{\partial p_w} = \sum_{k=1}^K \frac{\partial I(t_k)}{\partial p_w} \left[\frac{d(t_k)}{I(t_k)} - 1 \right]. \quad (3.114)$$

The only second derivative diagonal element from the FIM that has not been computed previously is

$$\frac{\partial^2 l(R, G, B, p_w)}{\partial p_w^2} = \sum_{k=1}^K \left\{ \frac{\partial^2 I(t_k)}{\partial p_w^2} \left[\frac{d(t_k)}{I(t_k)} - 1 \right] - \frac{d(t_k)}{I^2(t_k)} \left[\frac{\partial I(t_k)}{\partial p_w} \right]^2 \right\}. \quad (3.115)$$

The off-diagonal elements of the FIM associated with pulse width are

$$\frac{\partial^2 l(R, G, B, p_w)}{\partial R \partial p_w} = \sum_{k=1}^K \left\{ \frac{\partial^2 I(t_k)}{\partial R \partial p_w} \left[\frac{d(t_k)}{I(t_k)} - 1 \right] - \frac{d(t_k)}{I^2(t_k)} \frac{\partial I(t_k)}{\partial R} \frac{\partial I(t_k)}{\partial p_w} \right\}, \quad (3.116)$$

$$\frac{\partial^2 l(R, G, B, p_w)}{\partial G \partial p_w} = \sum_{k=1}^K \left\{ \frac{\partial^2 I(t_k)}{\partial G \partial p_w} \left[\frac{d(t_k)}{I(t_k)} - 1 \right] - \frac{d(t_k)}{I^2(t_k)} \frac{\partial I(t_k)}{\partial G} \frac{\partial I(t_k)}{\partial p_w} \right\}, \quad (3.117)$$

and

$$\frac{\partial^2 l(R, G, B, p_w)}{\partial B \partial p_w} = - \sum_{k=1}^K \frac{d(t_k)}{I^2(t_k)} \frac{\partial I(t_k)}{\partial p_w}. \quad (3.118)$$

The derivatives of Eq. 3.112 with respect to pulse width is needed to calculate the Fisher information matrix elements for the variable pulse width model. This derivative is

$$\frac{\partial I(t_k)}{\partial p_w} = \frac{2G}{p_w^3} (t_k - 2R/c)^2 \text{rect} \left(\frac{t_k - 2R/c}{2p_w} \right). \quad (3.119)$$

The elements of the Fisher information matrix are the negatives of the expectations of the second derivatives of the log-likelihood function. Many of these have already been calculated in Sec. 3.1. The FIM terms that are needed for the variable width model are

$$-E \left[\frac{\partial^2 l(R, G, B, p_w)}{\partial p_w^2} \right] = \sum_{k=1}^K \frac{1}{I(t_k)} \left[\frac{\partial I(t_k)}{\partial p_w} \right]^2, \quad (3.120)$$

$$-E \left[\frac{\partial^2 l(R, G, B, p_w)}{\partial R \partial p_w} \right] = \sum_{k=1}^K \frac{1}{I(t_k)} \frac{\partial I(t_k)}{\partial R} \frac{\partial I(t_k)}{\partial p_w}, \quad (3.121)$$

$$-E \left[\frac{\partial^2 l(R, G, B, p_w)}{\partial G \partial p_w} \right] = \sum_{k=1}^K \frac{1}{I(t_k)} \frac{\partial I(t_k)}{\partial G} \frac{\partial I(t_k)}{\partial p_w}, \quad (3.122)$$

and

$$-E \left[\frac{\partial^2 l(R, G, B, p_w)}{\partial B \partial p_w} \right] = \sum_{k=1}^K \frac{1}{I(t_k)} \frac{\partial I(t_k)}{\partial p_w}. \quad (3.123)$$

3.3.3 *Fisher Information Matrix.* The Fisher information matrix for the variable pulse width model from Eq. 3.112 is

$$\mathbf{J}(R, G, B, p_w) \quad (3.124)$$

$$= - \begin{bmatrix} \mathbb{E} \left[\frac{\partial^2 l(R, G, B, p_w)}{\partial R^2} \right] & \mathbb{E} \left[\frac{\partial^2 l(R, G, B, p_w)}{\partial R \partial G} \right] & \mathbb{E} \left[\frac{\partial^2 l(R, G, B, p_w)}{\partial R \partial B} \right] & \mathbb{E} \left[\frac{\partial^2 l(R, G, B, p_w)}{\partial R \partial p_w} \right] \\ \mathbb{E} \left[\frac{\partial^2 l(R, G, B, p_w)}{\partial R \partial G} \right] & \mathbb{E} \left[\frac{\partial^2 l(R, G, B, p_w)}{\partial G^2} \right] & \mathbb{E} \left[\frac{\partial^2 l(R, G, B, p_w)}{\partial G \partial B} \right] & \mathbb{E} \left[\frac{\partial^2 l(R, G, B, p_w)}{\partial G \partial p_w} \right] \\ \mathbb{E} \left[\frac{\partial^2 l(R, G, B, p_w)}{\partial R \partial B} \right] & \mathbb{E} \left[\frac{\partial^2 l(R, G, B, p_w)}{\partial G \partial B} \right] & \mathbb{E} \left[\frac{\partial^2 l(R, G, B, p_w)}{\partial B^2} \right] & \mathbb{E} \left[\frac{\partial^2 l(R, G, B, p_w)}{\partial B \partial p_w} \right] \\ \mathbb{E} \left[\frac{\partial^2 l(R, G, B, p_w)}{\partial R \partial p_w} \right] & \mathbb{E} \left[\frac{\partial^2 l(R, G, B, p_w)}{\partial G \partial p_w} \right] & \mathbb{E} \left[\frac{\partial^2 l(R, G, B, p_w)}{\partial B \partial p_w} \right] & \mathbb{E} \left[\frac{\partial^2 l(R, G, B, p_w)}{\partial p_w^2} \right] \end{bmatrix}.$$

First, the diagonal elements from the FIM are evaluated. The range, gain, and bias were already derived in Sec. 3.1.

$$-\mathbb{E} \left[\frac{\partial^2 l(R, G, B, p_w)}{\partial R^2} \right] \approx \frac{32Gf_s}{p_w c^2} (a - 1). \quad (3.125)$$

$$-\mathbb{E} \left[\frac{\partial^2 l(R, G, B, p_w)}{\partial G^2} \right] \approx \frac{2p_w f_s}{G} \left[\frac{2}{3} - \frac{B}{G} \left(1 - \frac{aB}{B+G} \right) \right]. \quad (3.126)$$

$$-\mathbb{E} \left[\frac{\partial^2 l(R, G, B, p_w)}{\partial B^2} \right] \approx 2p_w f_s \left(\frac{t_d - 2p_w}{2p_w B} + \frac{a}{B+G} \right). \quad (3.127)$$

The final FIM diagonal element is the one associated with pulse width. Eqs. 3.120 and 3.119 are combined to obtain the following integral approximation.

$$-\mathbb{E} \left[\frac{\partial^2 l(R, G, B, p_w)}{\partial p_w^2} \right] \approx \frac{4f_s (B+G)^{3/2}}{p_w \sqrt{G}} \int_{-\sqrt{\frac{G}{B+G}}}^{\sqrt{\frac{G}{B+G}}} \frac{u^4}{1-u^2} du. \quad (3.128)$$

where the change of variable from Eq. 3.26 was used. This equation can be evaluated using the integral from Eq. 3.40.

$$\begin{aligned}
& -\mathbb{E} \left[\frac{\partial^2 l(R, G, B, p_w)}{\partial p_w^2} \right] \tag{3.129} \\
& \approx \frac{4f_s (B + G)^{3/2}}{p_w \sqrt{G}} \left[-\frac{2}{3} \left(\frac{G}{B + G} \right)^{3/2} - 2\sqrt{\frac{G}{B + G}} + 2\text{atanh} \left(\sqrt{\frac{G}{B + G}} \right) \right] \\
& = \frac{8f_s}{p_w} \left[(B + G)(a - 1) - \frac{G}{3} \right]
\end{aligned}$$

where a is defined in Eq. 3.32. This analytic approximation is compared to a summation in Fig. 3.12a. Both numbers are large and they are almost identical.

As in previous cases, odd symmetry causes several FIM elements to be approximately zero. Inspection of the first derivative equations shows that the range derivative is odd about the pulse center, but that all other derivatives are even about the pulse center. When the terms are multiplied, range and all others produce odd functions that are about zero after integration. Therefore,

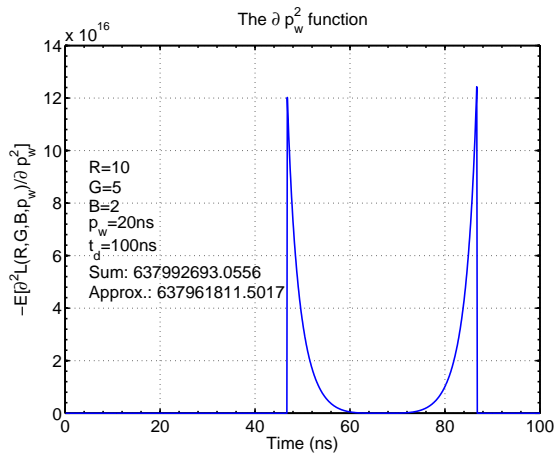
$$\mathbb{E} \left[\frac{\partial^2 l(R, G, B, p_w)}{\partial R \partial G} \right] \approx \mathbb{E} \left[\frac{\partial^2 l(R, G, B, p_w)}{\partial R \partial B} \right] \approx \mathbb{E} \left[\frac{\partial^2 l(R, G, B, p_w)}{\partial R \partial p_w} \right] \approx 0. \tag{3.130}$$

The odd symmetry of the function associated with range and pulse width is illustrated in Fig. 3.12b. The functions for the other two terms were present in previous signal models and are illustrated in Fig. 2.4. This range and pulse width function was summed. The numeric result is small (0.06), but not exactly zero since the sampling was not aligned exactly with the pulse center.

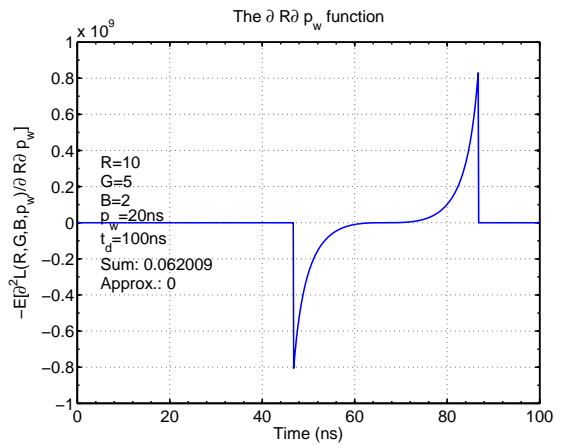
The off-diagonal FIM element relating gain and bias was evaluated earlier (see Eq. 3.47).

$$-\mathbb{E} \left[\frac{\partial^2 l(R, G, B, p_w)}{\partial G \partial B} \right] \approx \frac{2p_w f_s}{G} \left(1 - \frac{aB}{B + G} \right). \tag{3.131}$$

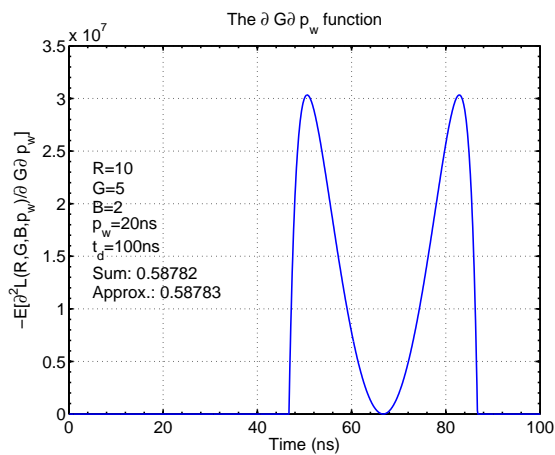
The FIM element relating gain and pulse width must be calculated. Eqs. 3.23, 3.119, and 3.122 can be combined with the change of variable from Eq. 3.26 to produce the



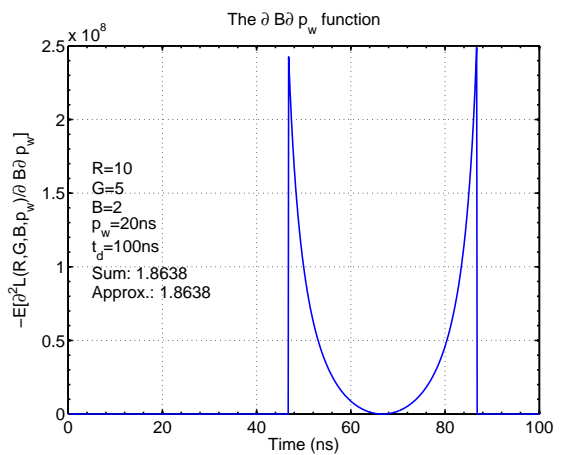
(a)



(b)



(c)



(d)

Figure 3.12: (a) The pulse width second derivative. (b) The range-width derivative. (c) The gain-width derivative. (d) The bias-width derivative.

following integral approximation,

$$\begin{aligned}
& -\mathbb{E} \left[\frac{\partial^2 l(R, G, B, p_w)}{\partial G \partial p_w} \right] \\
& \approx 2f_s \sqrt{\frac{B+G}{G}} \left[\int_{-\sqrt{\frac{G}{B+G}}}^{\sqrt{\frac{G}{B+G}}} \frac{u^2}{1-u^2} du - \frac{B+G}{G} \int_{-\sqrt{\frac{G}{B+G}}}^{\sqrt{\frac{G}{B+G}}} \frac{u^4}{1-u^2} du \right].
\end{aligned} \tag{3.132}$$

Using Eqs. 3.29 and 3.40, the approximation becomes

$$-\mathbb{E} \left[\frac{\partial^2 l(R, G, B, p_w)}{\partial G \partial p_w} \right] \approx 4f_s \left[\frac{1}{3} - \frac{B}{G}(a-1) \right]. \tag{3.133}$$

This approximation is compared to a numeric integration in Fig. 3.12c. The results are nearly equal. The final FIM term in the variable pulse width model is a combination of Eqs. 3.123 and 3.119.

$$\begin{aligned}
& -\mathbb{E} \left[\frac{\partial^2 l(R, G, B, p_w)}{\partial B \partial p_w} \right] \\
& \approx \frac{2Gf_s}{p_w} \int_{2R/c-p_w}^{2R/c+p_w} \frac{1}{G \left[1 - \left(\frac{t-2R/c}{p_w} \right)^2 \right] + B} \left(\frac{t-2R/c}{p_w} \right)^2 dt.
\end{aligned} \tag{3.134}$$

This integral is proportional to the one that was evaluated to find the range diagonal element of the Fisher information matrix (Eq. 3.25). Therefore,

$$\begin{aligned}
& -\mathbb{E} \left[\frac{\partial^2 l(R, G, B, p_w)}{\partial B \partial p_w} \right] \\
& \approx \frac{2Gf_s}{p_w} \frac{1}{f_s} \left(\frac{cp_w}{4G} \right)^2 \left(-\mathbb{E} \left[\frac{\partial^2 l(R, G, B, p_w)}{\partial R^2} \right] \right) \\
& = 4f_s(a-1)
\end{aligned} \tag{3.135}$$

where Eq. 3.88 was used. This approximation is compared to a numeric integration in Fig. 3.12d. The results are equal.

3.3.4 *Cramer-Rao Lower Bounds.* Using the results from Sec. 3.3.3, the Fisher information matrix can be written

$$\mathbf{J}(R, G, B, p_w) \approx \begin{bmatrix} J_{RR} & 0 & 0 \\ 0 & J_{GG} & J_{GB} & J_{Gp_w} \\ 0 & J_{GB} & J_{BB} & J_{Bp_w} \\ 0 & J_{Gp_w} & J_{Bp_w} & J_{p_w p_w} \end{bmatrix}. \quad (3.136)$$

This is a block diagonal matrix. It can be inverted using Eq. 3.57. The Cramer-Rao lower bound for range is the reciprocal of the upper-left element of Eq. 3.136.

$$\text{Var} \left[\hat{R} \right] \geq \frac{p_w c^2}{32Gf_s(a-1)}. \quad (3.137)$$

The range CRLB is identical to the one derived for the original parabolic pulse model (Eq. 3.61) in spite of the fact that pulse width was known in that model but is unknown in this case. However, range estimation is more difficult when the width is unknown.

The non-zero 3×3 sub-matrix in the FIM makes the CRLBs for gain, bias, and pulse width complicated. Instead of presenting complicated expressions for those CRLBs, they are listed in terms of Fisher information matrix elements. All three CRLBs calculations use the determinant of the sub-matrix from Eq. 3.136.

$$\begin{aligned} & \left| \begin{bmatrix} J_{GG} & J_{GB} & J_{Gp_w} \\ J_{GB} & J_{BB} & J_{Bp_w} \\ J_{Gp_w} & J_{Bp_w} & J_{p_w p_w} \end{bmatrix} \right| \\ &= J_{GG}J_{BB}J_{p_w p_w} + 2J_{GB}J_{Gp_w}J_{Bp_w} - J_{GG}J_{Bp_w}^2 - J_{BB}J_{Gp_w}^2 - J_{p_w p_w}J_{GB}^2. \end{aligned} \quad (3.138)$$

Using this result, the CRLBs are

$$\begin{aligned}
\text{Var} \left[\widehat{G} \right] & \tag{3.139} \\
& \geq \frac{J_{BB}J_{p_w p_w} - J_{B p_w}^2}{J_{GG}J_{BB}J_{p_w p_w} + 2J_{GB}J_{G p_w}J_{B p_w} - J_{GG}J_{B p_w}^2 - J_{BB}J_{G p_w}^2 - J_{p_w p_w}J_{GB}^2} \\
& = \frac{1}{J_{GG} + (2J_{GB}J_{G p_w}J_{B p_w} - J_{BB}J_{G p_w}^2 - J_{p_w p_w}J_{GB}^2) / (J_{BB}J_{p_w p_w} - J_{B p_w}^2)},
\end{aligned}$$

$$\begin{aligned}
\text{Var} \left[\widehat{B} \right] & \tag{3.140} \\
& \geq \frac{1}{J_{BB} + (2J_{GB}J_{G p_w}J_{B p_w} - J_{GG}J_{B p_w}^2 - J_{p_w p_w}J_{GB}^2) / (J_{GG}J_{p_w p_w} - J_{G p_w}^2)},
\end{aligned}$$

and

$$\begin{aligned}
\text{Var} \left[\widehat{p_w} \right] & \tag{3.141} \\
& \geq \frac{1}{J_{p_w p_w} + (2J_{GB}J_{G p_w}J_{B p_w} - J_{GG}J_{B p_w}^2 - J_{BB}J_{G p_w}^2) / (J_{GG}J_{BB} - J_{GB}^2)}.
\end{aligned}$$

The Fisher information matrix elements for the variable pulse width model from Eq. 3.112 are summarized in Table 3.4. The CRLBs, written in terms of the FIM elements are shown in Table 3.5.

3.3.5 Simulations. Estimates of range, gain, and bias have been discussed and tested in Secs. 3.1 and 3.2. Though the range CRLB is the same for all three signal models, the actual process of range estimation differs depending on the model. In this section, estimation of range and pulse width are simulated. Parameter estimation for the variable pulse width model from Eq. 3.112 is difficult because there are four unknown parameters that must be estimated. A relatively complicated algorithm to estimate multiple signal parameters is derived in Sec. 5.2.2 and tested on real LADAR data. In this section, a simpler clairvoyant pulse width estimation algorithm is developed for the purpose of validating the width CRLB. The process of range estimation is also simulated and compared to the range CRLB.

Table 3.4: Variable Width Model
Fisher Information Matrix Elements.

FIM Element	Value
J_{GG}	$\frac{2p_w f_s}{G} \left[\frac{2}{3} - \frac{B}{G} \left(1 - \frac{aB}{B+G} \right) \right]$
J_{BB}	$2p_w f_s \left(\frac{t_d - 2p_w}{2p_w B} + \frac{a}{B+G} \right)$
$J_{p_w p_w}$	$\frac{8f_s}{p_w} \left[(B+G)(a-1) - \frac{G}{3} \right]$
J_{GB}	$\frac{2p_w f_s}{G} \left(1 - \frac{aB}{B+G} \right)$
$J_{G p_w}$	$4f_s \left[\frac{1}{3} - \frac{B}{G}(a-1) \right]$
$J_{B p_w}$	$4f_s(a-1)$

Table 3.5: Variable Width Model
Cramer-Rao Lower Bounds.

Parameter	Cramer-Rao Lower Bounds
Range	$\frac{p_w c^2}{32Gf_s(a-1)}$
Gain	$\frac{1}{J_{GG} + \frac{2J_{GB}J_{Gp_w}J_{Bp_w} - J_{BB}J_{Gp_w}^2 - J_{p_w p_w}J_{GB}^2}{J_{BB}J_{p_w p_w} - J_{Bp_w}^2}}$
Bias	$\frac{1}{J_{BB} + \frac{2J_{GB}J_{Gp_w}J_{Bp_w} - J_{GG}J_{Bp_w}^2 - J_{p_w p_w}J_{GB}^2}{J_{GG}J_{p_w p_w} - J_{Gp_w}^2}}$
Pulse Width	$\frac{1}{J_{p_w p_w} + \frac{2J_{GB}J_{Gp_w}J_{Bp_w} - J_{GG}J_{Bp_w}^2 - J_{BB}J_{Gp_w}^2}{J_{GG}J_{BB} - J_{GB}^2}}$

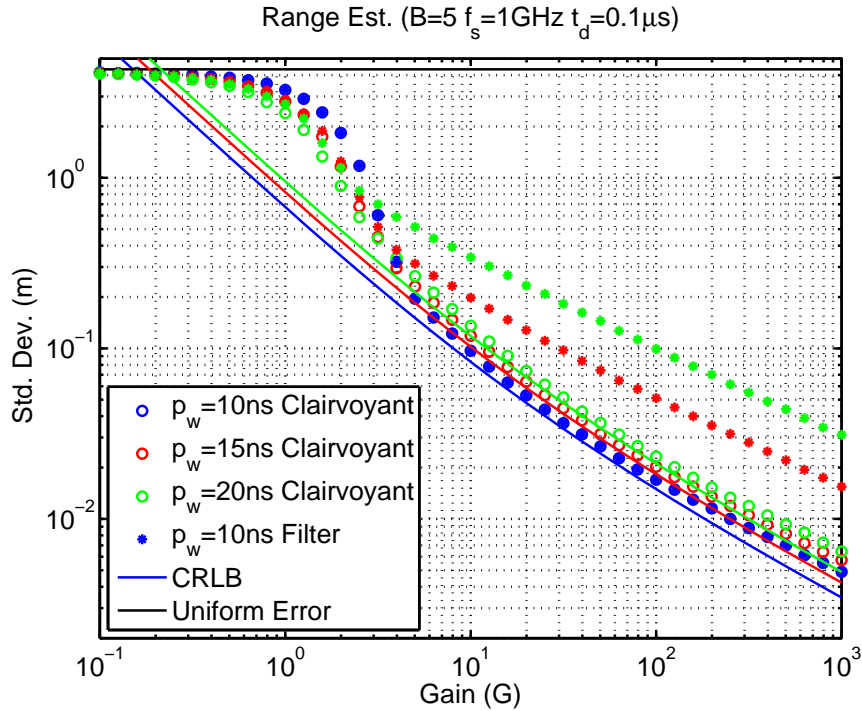


Figure 3.13: Range estimation using a clairvoyant (known received pulse width) filter and a filter with a fixed 10 ns filter.

The range estimation simulations from Secs. 3.1 and 3.2 assumed that the pulse width in the received signal is known. In practice, the width may be unknown. The simulation in Fig. 3.13 shows the precision of range estimation with knowledge of the received pulse width (clairvoyant) and without knowledge of the pulse width.

In the simulations in Fig. 3.13, the range estimation method from Sec. 3.1.4 was used. Pulse widths between 10 and 20 ns were simulated. In the clairvoyant case, the width was known during estimation. In the other case, the pulse width used by the filter was fixed at 10 ns regardless of actual pulse width. The results show that using the wrong pulse width in the filter will decrease the precision of range estimates.

The problem of pulse width estimation is now addressed. The Gauss-Newton method of parameter estimation is described in [23]. This process assumes knowledge of the probability distribution of the data. It requires an initial estimate of the unknown parameter. That initial estimate is updated through multiple iterations

until it converges to the parameter estimate. The iteration is a function of the data's log-likelihood function.

The unknown signal parameter is denoted θ . The initial estimate is $\widehat{\theta}_0$. The Gauss-Newton iterative estimate is

$$\widehat{\theta}_n = \widehat{\theta}_{n-1} - \left[\frac{\partial^2 l(\widehat{\theta}_{n-1})}{\partial \theta^2} \right]^{-1} \frac{\partial l(\widehat{\theta}_{n-1})}{\partial \theta}. \quad (3.142)$$

The Gauss-Newton algorithm must be initialized with a coarse estimate of the pulse width. A clairvoyant width estimate, that is an estimate that assumes knowledge of the gain, range, and bias of the signal, can be derived using the expectation of the sum of the data. The expectation of the sum of the data is

$$\begin{aligned} \mathbb{E} \left[\sum_{k=1}^K d(t_k) \right] &= \sum_{k=1}^K I(t_k) \quad (3.143) \\ &\approx f_s \int_{R_{rt}/c-p_w}^{R_{rt}/c+p_w} \left\{ G \left[1 - \left(\frac{t-2R/c}{p_w} \right)^2 \right] \text{rect} \left(\frac{t-2R/c}{2p_w} \right) + B \right\} dt \\ &= f_s t_d B + f_s G \int_{2R/c-p_w}^{2R/c+p_w} \left[1 - \left(\frac{t-2R/c}{p_w} \right)^2 \right] dt \\ &= f_s t_d B + f_s G \int_{-p_w}^{p_w} \left(1 - \frac{u^2}{p_w^2} \right) dt \\ &= f_s t_d B + \frac{4}{3} f_s G p_w \end{aligned}$$

where the change of variable $u = tc - R_{rt}$ was used. Thus, the following equation is an unbiased pulse width estimate.

$$\widehat{p}_w = \frac{3}{4f_s G} \left[\sum_{k=1}^K d(t_k) - f_s t_d B \right]. \quad (3.144)$$

This becomes the initial estimate for the Gauss-Newton iteration.

$$\hat{\theta}_0 = \frac{3}{4f_s G} \left[\sum_{k=1}^K d(t_k) - f_s t_d B \right]. \quad (3.145)$$

The Gauss-Newton iteration is derived using the log-likelihood function associated with the model from Eq. 3.112. The first and second derivatives of the log-likelihood with respect to pulse width were already computed. They are shown in Eqs. 3.114 and 3.115. The derivatives of the mean photocurrent with respect to pulse width are

$$\frac{\partial I(t_k)}{\partial p_w} = \frac{2G}{p_w^3} (t_k - 2R/c)^2 \text{rect} \left(\frac{t - 2R/c}{2p_w} \right) \quad (3.146)$$

and

$$\frac{\partial^2 I(t_k)}{\partial p_w^2} = -\frac{6G}{p_w^4} (t_k - 2R/c)^2 \text{rect} \left(\frac{t - 2R/c}{2p_w} \right) = -\frac{3}{p_w} \frac{\partial I(t_k)}{\partial p_w}. \quad (3.147)$$

Therefore, the terms from the Gauss-Newton iteration (Eq. 3.142) are

$$\frac{\partial(R, G, B, p_w)}{\partial p_w} = \frac{2G}{p_w^3} \sum_{k=1}^K (t_k - 2R/c)^2 \text{rect} \left(\frac{t_k - 2R/c}{2p_w} \right) \left[\frac{d(t_k)}{I(t_k)} - 1 \right] \quad (3.148)$$

and

$$\frac{\partial^2(R, G, B, p_w)}{\partial p_w^2} = \sum_{k=1}^K \frac{\partial I(t_k)}{\partial p_w} \left\{ \frac{3}{p_w} \left[1 - \frac{d(t_k)}{I(t_k)} \right] - \frac{\partial I(t_k)}{\partial p_w} \frac{d(t_k)}{I^2(t_k)} \right\}. \quad (3.149)$$

When evaluating Eqs. 3.148 and 3.149, the current pulse width estimate is used to calculate the mean photocurrent $I(t_k)$. These two equations are used to compute the Gauss-Newton iteration from Eq. 3.142. The iteration is done repeatedly until the pulse width estimate converges to a stable value.

The Gauss-Newton iteration for pulse width estimation was simulated using Monte Carlo methods. Many realizations of Poisson-distributed signals were generated for different gain, bias, and pulse width values. The algorithm was initialized

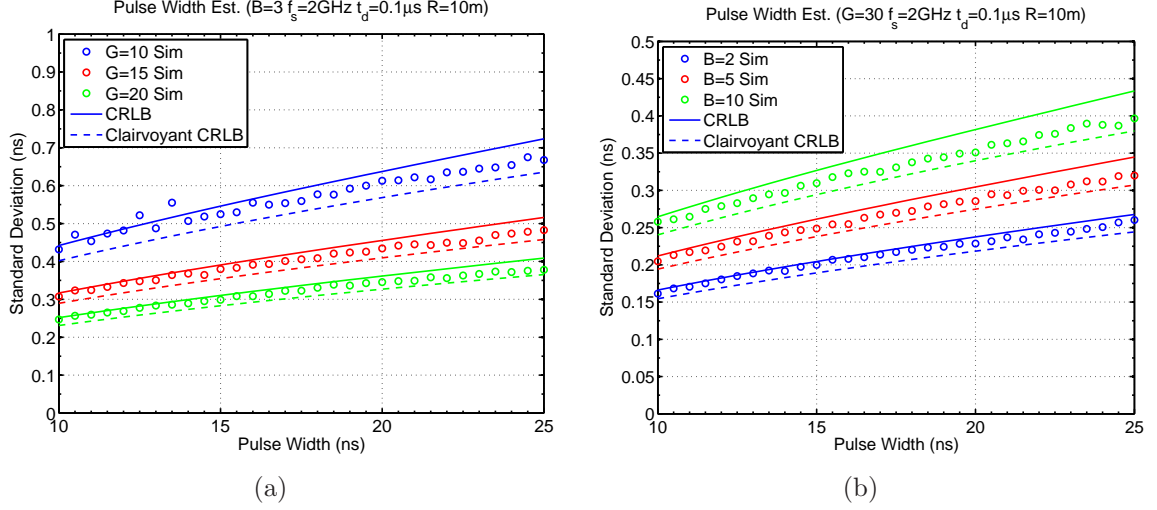


Figure 3.14: (a) Pulse width estimation as width and gain vary. (b) Pulse width estimation as width and bias vary.

using Eq. 3.145. Twenty iterations of the algorithm were implemented per realization because tests showed that it consistently converged after that number.

The results of the Monte Carlo simulations are shown in Fig. 3.14. In Fig. 3.14a, the bias is fixed and different values of gain are simulated. In Fig. 3.14b, the gain is constant and the bias is varied. Pulse width values between 10 and 25 ns are tested.

Two different CRLBs are shown in Fig. 3.14. The solid lines describe the CRLB from Eq. 3.141. This CRLB does not assume that the other signals parameters (range, gain, and bias) are known. The simulations, on the other hand, assumed that those parameters were known. The simulations used that information to improve the precision of the pulse width estimate. Because the clairvoyant pulse width estimate knew the gain and bias, that estimate was more precise than predicted by the CRLB from Eq. 3.141.

The second CRLB shown in Fig. 3.14 is the clairvoyant pulse width estimate CRLB. This bound assumes knowledge of the signal's gain and bias. It is lower than the CRLB from Eq. 3.141. That CRLB assumes that the gain and bias must be estimated from the data, and therefore, will not be as precise as the clairvoyant

estimate that knows the gain and bias. The clairvoyant CRLB is

$$\text{Var} [\widehat{p}_w]_{clairvoyant} \geq \frac{1}{J_{p_w p_w}} = \frac{p_w}{8f_s [(B + G)(a - 1) - G/3]}. \quad (3.150)$$

This CRLB has an interesting characteristic. This bound increases as the pulse width increases. Equivalently, the CRLB is increasing as the mean pulse energy increases. In most cases, an increase in pulse energy implies an improvement in the precision of signal parameter estimates. But in this case, if the pulse energy increase is due to an increase in pulse width while the gain is fixed, the pulse energy estimate becomes less precise.

The clairvoyant pulse width CRLB from Eq. 3.150 is always less than or equal to the pulse width CRLB from Eq. 3.141.

$$\text{Var} [\widehat{p}_w] \geq \text{Var} [\widehat{p}_w]_{clairvoyant}. \quad (3.151)$$

This is because the CRLB for any parameter is always greater than or equal to the reciprocal of its Fisher information matrix element. That is,

$$\text{Var} [\widehat{p}_w] \geq \frac{1}{J_{p_w p_w}}. \quad (3.152)$$

See Appendix C for proof of this property. Thus the clairvoyant CRLB from Eq. 3.150 is a lower bound for the variance of unbiased pulse width estimates. However, it is not as tight as the CRLB from Eq. 3.141.

The simulated clairvoyant estimates shown in Fig. 3.14 of pulse width are less precise than the clairvoyant estimate CRLB says they could be. Gauss-Newton estimates are generally not efficient [54]. That is, Gauss-Newton estimates generally have a variance greater than the Cramer-Rao lower bound. However, the simulated clairvoyant estimates have variance lower than the CRLB from Eq. 3.141. That CRLB assumes the estimator does not know the gain and bias and is higher than the clairvoyant bound from Eq. 3.150.

3.4 Chapter Summary

In this chapter, three different models for Poisson-distributed LADAR signals were presented. The process of parameter estimation was discussed for each of these models. Cramer-Rao lower bounds were derived for all parameters present in these models such as range to target, gain, and bias.

In Sec. 3.1, a LADAR signal model that describes a laser pulse as a truncated parabolic shape was discussed. It was shown that a relatively compact analytic expression could be derived for that model's range CRLB. In Sec. 3.2, a model with two different LADAR signals was discussed. This model is used to describe the signal observed when a target is partially obscured by forest canopy or camouflage netting. It was shown that the presence of the second signal did not decrease the range CRLB to the target. Finally, in Sec. 3.3, the effect of unknown pulse width was examined. It was shown that lack of knowledge of the pulse width did not affect the range CRLB.

IV. Range Precision of LADAR Systems

The topic of this chapter is the precision of range estimates made by LADAR systems. In the previous chapter, it was assumed that the noise in a LADAR signal follows the Poisson distribution and that the shape of a received laser pulse was described by a truncated parabola. That model is discussed in this chapter, but other methods of signal modeling are also used. In some cases, the noise in the LADAR system is assumed to have a Gaussian distribution. The shape of the laser pulse can be modeled using functions other than the truncated parabola. In this chapter, the use of alternative pulse shape models is discussed.

In Sec. 4.1, the Poisson-distributed parabolic pulse model from Chapters II and III is employed to simulate shot-noise limited LADAR signals. The precision of range estimates made with shot-noise limited systems is discussed. The effect of pulse averaging is explored and the results are compared to systems with signals that have white Gaussian, rather than Poisson noise.

In Sec. 4.2, the effect of target surface orientation on range precision is quantified. It is shown that for typical LADAR systems this effect is only significant for targets that are many kilometers away. In order to simplify the analytics involved in this problem, the laser pulse is assumed to have a Gaussian shape and the noise is modeled as a white Gaussian process. Cramer-Rao lower bounds are calculated for range precision given a tilted target surface.

4.1 Target Range Estimation

A Cramer-Rao lower bound for range estimate variance was derived in Chapter III. Methods of range estimation were also developed and tested in that chapter. It was noted that for shot-noise limited (Poisson distributed) data, the maximum likelihood estimate could not be solved analytically. However, it was also shown that a combination of matched filtering and peak fitting produced reasonably precise range estimates in the sense that they were close to the CRLB. However, it was also demonstrated when the matched filter was replaced by a filter equal to the square

root of the laser pulse shape, the range precision improved in most cases. Range estimates produced by the square-root filter nearly achieved the CRLB when the signal amplitude was large compared to the background level (see Fig. 3.3).

In this section, the Poisson noise range estimation CRLB and simulation results are compared to range estimation for a signal mixed with additive white Gaussian noise (AWGN). It is shown that the Gaussian-distributed signal produces range estimates that are more precise than can be obtained from a Poisson-distributed signal with equal background noise variance and mean signal energy. This is proved through simulation and by comparing the Cramer-Rao lower bounds for these signals.

4.1.1 Comparison to Gaussian-Noise Signals. Noise in radar and communication systems is often assumed to have a Gaussian distribution. Gaussian noise has also been used to model LADAR signals [9, 31]. Gaussian noise models are common in the communication and signal processing literature and are well-understood. For purposes of comparison, the Poisson noise range CRLB derived in Chapter III is compared to a Gaussian noise range CRLB that is derived in this section. The comparison uses the parabolic pulse signal model from Eq. 3.112 for both Poisson and Gaussian noise.

The signal model is

$$I(t_k) = G \left[1 - \left(\frac{t_k - 2R/c}{p_w} \right)^2 \right] \text{rect} \left(\frac{t_k - 2R/c}{2p_w} \right) + B. \quad (4.1)$$

It is assumed that Gaussian-distributed samples $d_g(t_k)$ have been collected. The mean value of these samples is the mean photocurrent $I(t_k)$. The variance of the samples is B since that is the variance of the background in the Poisson-distributed case.

$$D_g(t_k) \sim \mathcal{N}[I(t_k), B]. \quad (4.2)$$

As in the Poisson case, it is assumed that all samples are statistically independent of each other. Note that in this case, it is possible for the signal to have negative values.

The range estimate CRLB for a signal mixed with AWGN was derived in *Fundamentals of Statistical Signal Processing: Estimation Theory* by Kay [23].

$$\text{Var} \left[\widehat{R}_g \right] \geq \frac{Bc^2}{4f_s \int_0^{t_d} \left[\frac{dI(t)}{dt} \right]^2 dt} \quad (4.3)$$

where \widehat{R}_g is any unbiased range estimate. This Gaussian-noise model CRLB derived in [23] was calculated assuming that, in the absence of signal, the noise is zero-mean. It is assumed here that there is a non-zero background mean of B . However, the Gaussian-noise range CRLB is unaffected by the presence of a bias (the background non-zero mean) in the data. For more detail on why the Gaussian-noise range CRLB is not dependent on bias, see [16].

The integral in Eq. 4.3 is

$$\int_0^{t_d} \left[\frac{dI(t)}{dt} \right]^2 dt = \int_{2R/c-p_w}^{2R/c+p_w} \left[-\frac{2G}{p_w^2} (t - 2R/c) \right]^2 dt = \frac{4G^2}{p_w^4} \int_{-p_w}^{p_w} v^2 dv = \frac{8G^2}{3p_w} \quad (4.4)$$

where the change of variable $v = t - 2R/c$ was used. Therefore, the Gaussian-noise range CRLB is

$$\text{Var} \left[\widehat{R}_g \right] \geq \frac{3Bc^2 p_w}{32G^2 f_s}. \quad (4.5)$$

For the purpose of comparison, a bound on the Poisson-noise range CRLB (Eq. 3.137) is desired. That CRLB is (see Eqs. 3.137 and 3.32)

$$\text{Var} \left[\widehat{R} \right] \geq \frac{c^2 p_w}{32G f_s \left[\sqrt{\frac{B+G}{G}} \text{atanh} \left(\sqrt{\frac{G}{B+G}} \right) - 1 \right]}. \quad (4.6)$$

The bound will be used to compare this CRLB to the Gaussian-noise CRLB from Eq. 4.5.

Inverse hyperbolic tangent can be written as an infinite series [1].

$$\operatorname{atanh}(x) = \sum_{n=0}^{\infty} \frac{x^{2n+1}}{2n+1} \quad (4.7)$$

where $|x| < 1$. If $\operatorname{atanh}(x)$ is divided by x , then one is subtracted, the geometric series can be used to find an upper bound. Consider the following series expansion.

$$\frac{\operatorname{atanh}(x)}{x} - 1 = \sum_{n=1}^{\infty} \frac{x^{2n}}{2n+1} = \frac{1}{3} \sum_{n=1}^{\infty} \frac{3x^{2n}}{2n+1}. \quad (4.8)$$

Using the fact that

$$\frac{3x^{2n}}{2n+1} < x^{2n} \quad \forall \quad n > 1, \quad (4.9)$$

Eq. 4.8 can be written

$$\frac{\operatorname{atanh}(x)}{x} - 1 < \frac{1}{3} \sum_{n=1}^{\infty} x^{2n} = \frac{x^2}{3} \sum_{n=0}^{\infty} x^{2n} = \frac{x^2}{3(1-x^2)}. \quad (4.10)$$

Therefore, the term from the denominator of the Poisson-noise CRLB (Eq. 4.6) is bounded by

$$\sqrt{\frac{B+G}{G}} \operatorname{atanh} \left(\sqrt{\frac{G}{B+G}} \right) - 1 < \frac{G}{3B}. \quad (4.11)$$

This implies that the Poisson-distribution CRLB is bounded by

$$\frac{c^2 p_w}{32Gf_s \left[\sqrt{\frac{B+G}{G}} \operatorname{atanh} \left(\sqrt{\frac{G}{B+G}} \right) - 1 \right]} > \frac{3Bc^2 p_w}{32G^2 f_s}. \quad (4.12)$$

This lower bound on the Poisson-distribution CRLB is equal to the Gaussian-noise CRLB from Eq. 4.5. If the CRLB can be achieved, then the variances of the estimators are related by

$$\operatorname{Var} \left[\widehat{R} \right] > \operatorname{Var} \left[\widehat{R}_g \right]. \quad (4.13)$$

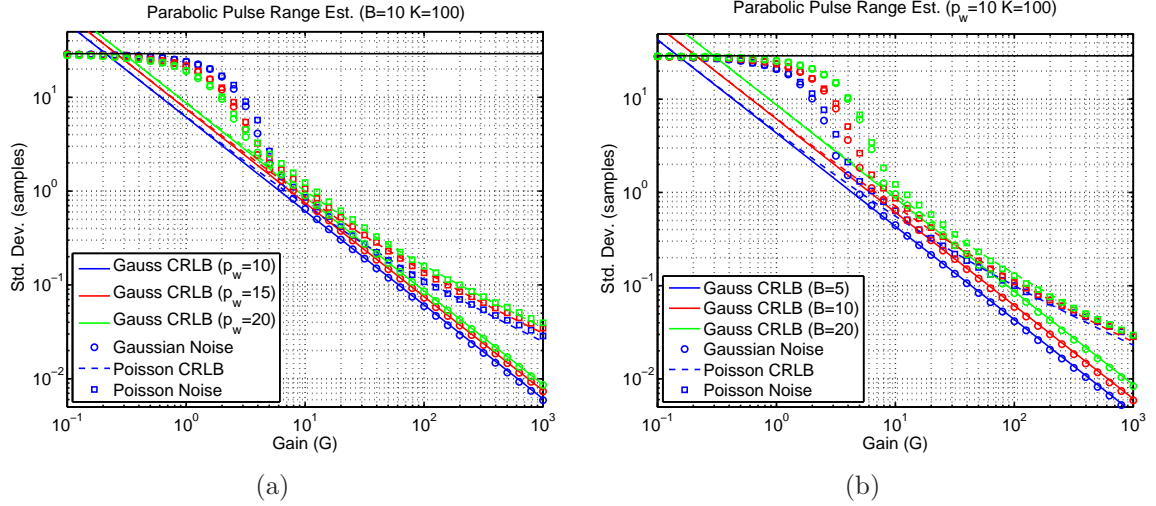


Figure 4.1: (a) Background is $B = 10$ and pulse width varies.
(b) Pulse width is $p_w = 10$ ns and background varies.

The CRLB is sometimes used to design LADAR systems. Eq. 4.12 shows that the Gaussian-noise CRLB is always less than the Poisson signal CRLB. The Poisson CRLB is therefore a more realistic representation of the range precision of a shot noise limited LADAR. Because the Gaussian CRLB is always less than the Poisson CRLB, Eq. 4.5 is a lower bound for shot noise limited range precision. However, the Poisson CRLB (Eq. 4.6) is a tighter bound on the range precision limit of a shot noise limited LADAR system. That is, real unbiased range estimates will have variances closer to the Poisson CRLB than to the Gaussian CRLB.

4.1.2 Simulations. Monte Carlo simulations of range estimation were completed and compared to the Poisson and Gaussian CRLBs. The results are shown in Fig. 4.1. In the simulations, a $p_w = 10$ ns parabolic pulse was sampled at frequency $f_s = 1$ GHz. One hundred samples were simulated ($K = 100$), so the sampling duration was $t_d = 100$ ns where $t_d = K/f_s$. The bias level in the simulation was $B = 10$. This value (B) is also the variance of the background samples in the Poisson and Gaussian distribution cases.

The pulse amplitude (G) was varied from 10^{-1} to 10^3 . For each pulse amplitude, 10,000 Poisson and 10,000 Gaussian signal realizations were generated. The mean value of these signals was the parabolic pulse from Eq. 4.1. Each of the signal realizations was match filtered. The simulated range estimates were calculated using three-point parabolic fits to the peaks of the match filter outputs. The parabolic fit equations used are shown in [20].

In Fig. 4.1, the CRLBs from Eqs. 4.5 and 4.6 are compared to the sample variances produced by the Monte Carlo simulations. At pulse amplitudes greater than the bias level ($G > B$), the bounds are tight for the Poisson and Gaussian distribution cases. As the pulse amplitude drops below the bias level, the simulation sample variances begin to deviate from the CRLBs. At very low signal amplitudes ($G \ll B$), the range estimation algorithm is reporting a random variable that is uniformly distributed over the sampling interval. In uniform distribution case, the range variance is Eq. 3.79.

At very low signal amplitudes, the sample variance is less than the CRLB. Cramer-Rao lower bounds are only valid for unbiased estimators. In the very low amplitude case, the range estimate is biased. Its mean value is near the center of the sampling interval regardless of the laser pulse's true position. It is this bias that allows the estimator's variance to surpass the bound. But in this case, the estimator's mean squared error (variance plus bias squared) can be very high. The fact that sample variance is below the CRLB should obviously not be mistaken for efficient performance.

The bias in low amplitude range estimates is illustrated in Fig. 4.2. The bias is shown using Monte Carlo simulations where one-hundred sample LADAR signals are simulated. A parabolic pulse is centered at sample 70 and the bias level is $B = 10$. In Fig. 4.2a, the gain is one ($G = 1$). The pulse is visible, but as the gain is so low that the distribution is nearly uniform over the sampling interval. The range estimates are biased toward the center of the sampling interval. The average range estimate is

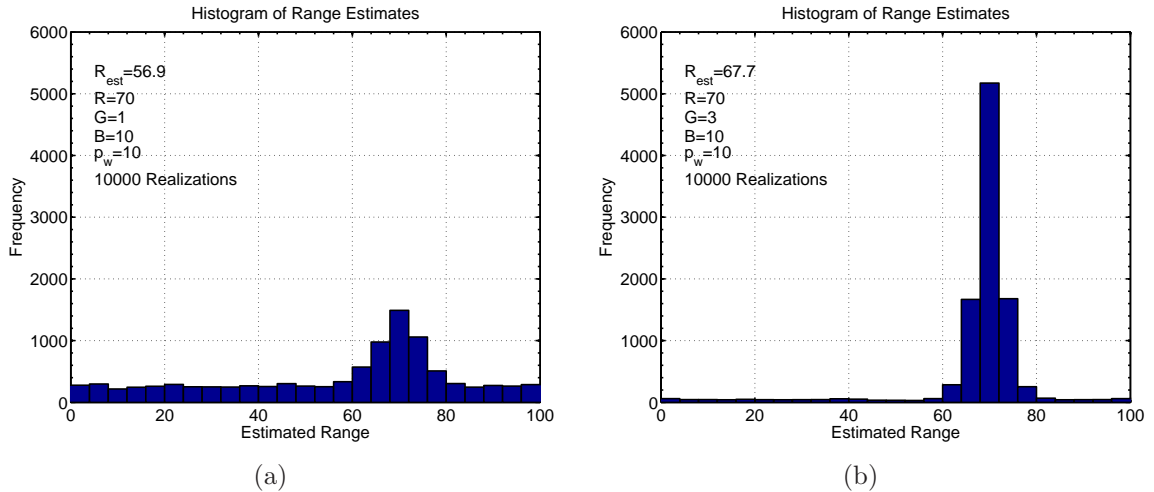


Figure 4.2: (a) Histogram of range estimates with gain $G = 1$.
 (b) Range estimates histogram with gain $G = 3$.

56.9. In Fig. 4.2b, the range gain has increased to three ($G = 3$). Outliers are visible throughout the sampling interval. However outliers are rare and do little to bias the range estimate. The average estimate of 67.7 is close to the true value.

4.1.3 Multiple Pulses and Range Precision. Range estimates from multiple LADAR signals can be combined to improve precision. Multiple range estimates could be averaged, or signals could be accumulated before one range estimate is computed. Regardless of the method of processing, (e.g. averaging of estimates or accumulation then estimation), the Cramer-Rao lower bound on range precision is valid for any unbiased range estimate.

Given N statistically independent signals, the variance CRLB for any parameter estimate decreases by a factor of N [5]. In that sense, having multiple pulses helps range precision. However, this assumes that the laser has transmitted N -times more energy than was transmitted in a single pulse.

If the amount of laser energy is fixed, but can be divided equally into N pulses, then the CRLB varies with N . In a photon counting system, mean pulse energy is proportional to the mean photocount gain G (see Eqs. 2.26 and 2.27). The range

CRLB, given that a total (accumulated) amplitude of G is divided equally into N pulses is

$$\text{Var} \left[\widehat{R} \right] \geq \frac{c^2 p_w}{32Gf_s \left[\sqrt{\frac{G+BN}{G}} \text{atanh} \left(\sqrt{\frac{G}{G+BN}} \right) - 1 \right]} \quad (4.14)$$

where \widehat{R} denotes any unbiased range estimate obtained from N Poisson-distributed pulses, each with amplitude G/N .

In order to compare this CRLB to the single pulse CRLB from Eq. 4.6, the infinite series for inverse hyperbolic tangent (see Eq. 4.10) is used.

$$\sqrt{\frac{G+BN}{G}} \text{atanh} \left(\sqrt{\frac{G}{G+BN}} \right) - 1 = \sum_{n=1}^{\infty} \frac{1}{2n+1} \left(\frac{G}{G+BN} \right)^n. \quad (4.15)$$

Gain G and background B are always positive. Therefore,

$$\frac{G}{G+BN} < \frac{G}{B+G} \quad \forall \quad N > 1. \quad (4.16)$$

This inequality implies that

$$\sum_{n=1}^{\infty} \frac{1}{2n+1} \left(\frac{G}{G+BN} \right)^n < \sum_{n=1}^{\infty} \frac{1}{2n+1} \left(\frac{G}{B+G} \right)^n. \quad (4.17)$$

Because the number of pulses N is a positive integer,

$$\sqrt{\frac{G+BN}{G}} \text{atanh} \left(\sqrt{\frac{G}{G+BN}} \right) - 1 \leq \sqrt{\frac{B+G}{G}} \text{atanh} \left(\sqrt{\frac{G}{B+G}} \right) - 1 \quad (4.18)$$

with equality if and only if $N = 1$. This equation means that the CRLBs from Eq. 4.6 and 4.14 are related by

$$\begin{aligned} & \frac{c^2 p_w}{32Gf_s \left[\sqrt{\frac{G+BN}{G}} \text{atanh} \left(\sqrt{\frac{G}{G+BN}} \right) - 1 \right]} \\ & \geq \frac{c^2 p_w}{32Gf_s \left[\sqrt{\frac{B+G}{G}} \text{atanh} \left(\sqrt{\frac{G}{B+G}} \right) - 1 \right]}. \end{aligned} \quad (4.19)$$

If range estimators can be found that achieve the Cramer-Rao lower bound, then the CRLB for a single Poisson-distributed laser pulse range measurement \widehat{R} and a range measurement made from a set of N Poisson-distributed pulses \widehat{R} are related by

$$\text{Var} \left[\widehat{R} \right] \geq \text{Var} \left[\widehat{R} \right] \quad (4.20)$$

with equality if and only if $N = 1$.

Eq. 4.20 proves that for a fixed total laser energy and Poisson-distributed signals, the range precision is maximized when all energy is transmitted in a single pulse. It is interesting to compare this fact to Poisson-distributed signal detection results from Gatt and Henderson [9]. In that paper, it was shown that for a fixed total energy, the detectability of Poisson signals is maximized by transmitting all energy in a single pulse. Thus, there is a relationship between the range precision and the detectability of a Poisson-distributed signal.

In [35], the CRLB for position estimates of a Gaussian pulse in Poisson noise was calculated. In that paper, it was assumed that there was no background noise ($B = 0$). The result in Eq. 4.20 stands in contrast to the zero background noise result (Eq. 18 of [35]). That CRLB is inversely proportional to amplitude. Thus, the range precision is independent of the number of averages in the zero-background noise case when the total laser energy is fixed.

The CRLB for a shot-noise limited system which divides a fixed total energy into N pulses (Eq. 4.14) is illustrated in Fig. 4.3. For the case considered in the illustration ($p_w = 10$ ns, $f_s = 1$ GHz, $B = 10$, and G varying between 10^{-1} and 10^3) the range precision decreases rapidly as laser energy is divided into multiple pulses. For example, when an accumulated gain of ten ($G \times N = 10$) is divided into three pulses, the range standard deviation CRLB is about twice as high as if all energy was transmitted in a single pulse over most accumulated gain values shown in the figure.

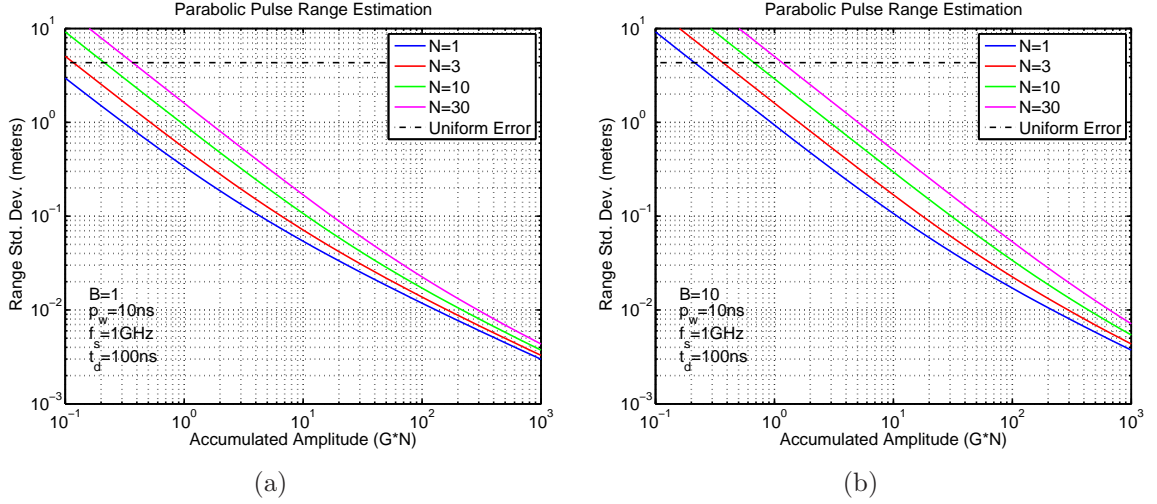


Figure 4.3: (a) Effect of pulse averaging on CRLB with $B = 1$.
(b) Effect of pulse averaging with $B = 10$.

4.2 Surface Orientation and Range Estimation

LADAR systems are capable of transmitting laser pulses with very short durations. Typical systems have pulses that are only a few nanoseconds in duration. Some future systems will employ pulses with even shorter durations. These short pulses provide excellent range resolution and precision. However, when a target has depth over the area illuminated by the beam, the reflection process causes the received laser signal to be wider than the transmitted signal. The widened received signal has less range precision than a signal that is not elongated due to target depth. Even when a flat surface is targeted, that surface has depth if it is tilted with respect to the LADAR line-of-sight.

In this section, the loss in range precision due to the tilt of a flat surface is quantified. Unlike in previous sections of this dissertation, the noise in the LADAR signal is assumed to be Gaussian. In practice, the Gaussian noise model does not completely capture the fluctuations in signal level due to laser speckle. However it is an accurate approximation for any system with a significant amount of electronic noise or for a LADAR that makes use of diversity to reduce speckle fluctuations. The temporal shape of the pulse is also modeled as a Gaussian function. These assumptions simplify

the analytic calculations need to analyze this problem and produce concise formulas describing the effect of tilt on the range CRLB.

The problem of target depth distorting the shape of received laser pulses has been addressed by other authors [15, 45, 46]. The novel material contained in this section is the analytic expression derived for a received laser pulse and the Cramer-Rao lower bound on range precision when the target is tilted.

4.2.1 Scenario and Assumptions. A TEM00 Gaussian beam is assumed to have been transmitted. A short pulse is used to achieve good range precision. Laser pulses are described by their duration and their size. The size is the beam's width transverse to the system's LOS. Propagated laser beam size is a function of beam size at the transmit aperture, laser wavelength, the focus distance, and distance of propagation. Beam size is dependent on the LADAR transmitter aperture. If the width of the transmit aperture is fixed, then as beam size increases more laser power is truncated by the opaque portions of the system. If the beam size is greater than the aperture radius, then a significant amount of laser energy is truncated. Thus, the beam size is almost always smaller than the aperture radius.

At ranges of less than a few kilometers, the effect of target tilt on range precision is negligible. However, LADAR systems are sometimes operated at long range. Systems are used to do three-dimensional imaging from the air. Airborne LADAR systems are used to image terrain and structures [43]. The three-dimensional data can be used for mapping and for automatic target recognition (ATR) [53]. Airborne systems have a wide field of regard and can operate at very long ranges. As range increases, the beam size gets large and the effect of target tilt on range precision becomes noticeable.

Because of size, weight, and power restrictions, transmit apertures in airborne LADAR systems are usually only several inches wide at most. These relatively small apertures keep the beam size small. Smaller transmitted beam size means larger beam

size in the far field. Increases in beam size at the target exacerbate the problem of range precision loss due to target tilt.

In military imaging scenarios the range to the target is often much greater than the platform's altitude. In this situation, even flat ground has a large tilt angle with respect to the LOS. The loss in range precision can be significant in this case.

It is assumed that the LADAR is either monostatic or that the transmitter and receiver apertures are located close together. Monostatic systems use transmit-receive (TR) switches to prevent the detector from being damaged by the relatively intense transmitted laser pulses. A TR switch enables the system to use a single aperture for the transmission and reception of laser energy. If the system is bistatic, then the transmit and receive apertures are almost always located so close together (they commonly share a gimballed turret in airborne systems) that they can be treated as monostatic for the purpose of this analysis.

4.2.2 Scenario Geometry. The scenario considered in this section is illustrated in Fig. 4.4. A short duration laser pulse is transmitted along the LADAR's line-of-sight. The temporal profile is assumed to be a Gaussian shape. The beam has an irradiance profile that is defined by the amount of power transmitted over time and the beam's size after propagating to the target.

The beam hits a surface that may be tilted with respect to the LADAR's LOS. The surface is assumed to be flat over the width of the irradiance profile. This assumption produces relatively simple analytic solutions for the received signal. If the surface is not flat, then shape of the reflected pulse could be complicated and would likely have to be calculated numerically. This sort of analysis has been done in [45, 46].

The reflected laser pulse is shown in Fig. 4.5. The target tilt, which is parameterized by angle ϕ (measured in radians), has elongated the reflected pulse as compared to the incident pulse shown in Fig. 4.4. Precision of a range measurement

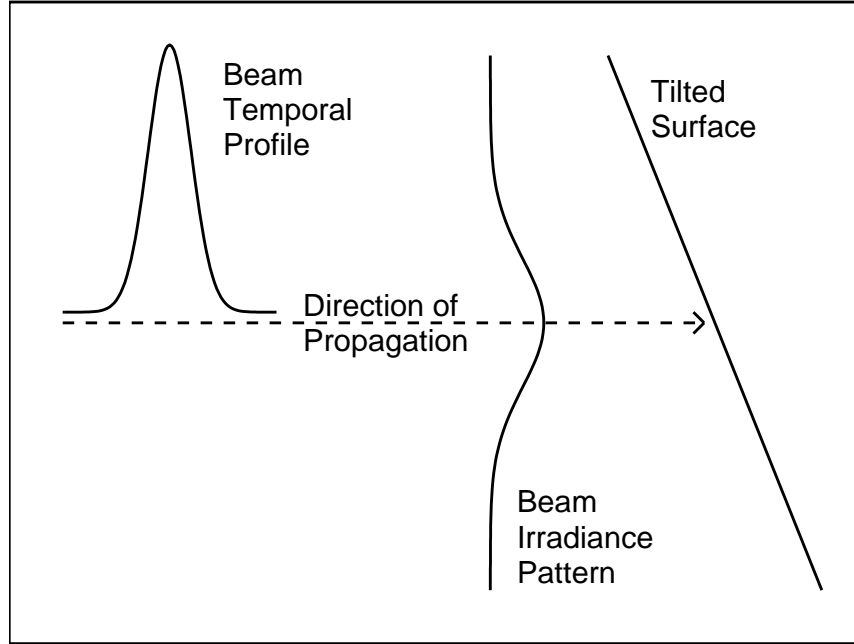


Figure 4.4: Illustration of a laser pulse, its irradiance pattern, and a tilted surface.

is dependent on the width of the received, not the transmitted pulse. Thus, the target tilt with respect to the LADAR LOS causes a drop in range precision.

4.2.3 Propagation and Reflection. The field at the transmit aperture is assumed to be Gaussian with beam size W_0 . The beam is focused at F_0 . The beam size is the radius where the field magnitude is below the peak magnitude by a factor of e^{-1} . This Gaussian field is given by Eq. 2.11 and is shown again here.

$$U_0(r, 0) = \left[\frac{2P_t(t)}{\pi W_0^2} \right]^{1/2} \exp \left(-\frac{1}{2} \alpha k r^2 \right) \quad (4.21)$$

where

$$\alpha = \frac{2}{kW_0^2} + \frac{i}{F_0}. \quad (4.22)$$

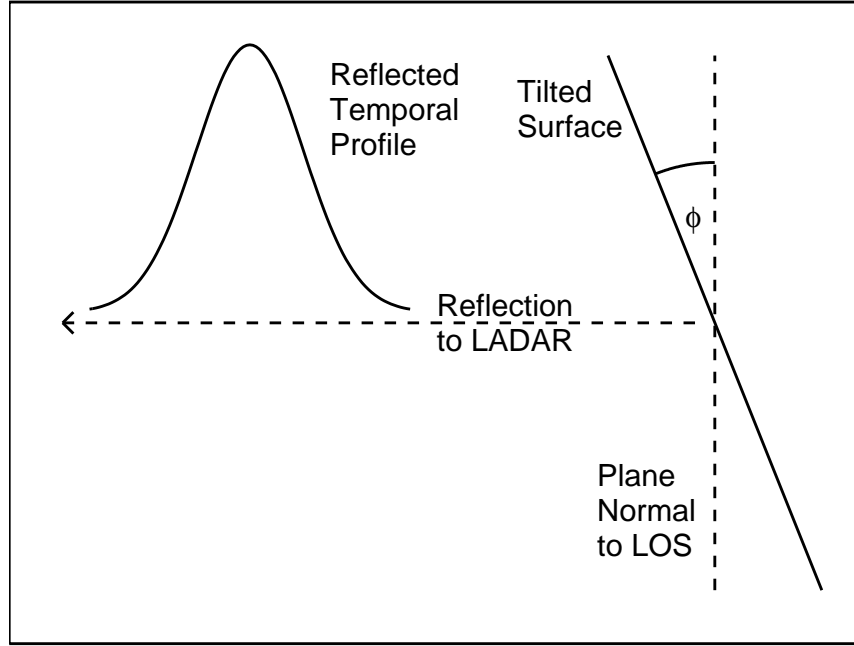


Figure 4.5: Reflected laser pulse from a surface tilted at angle ϕ with respect to the LADAR line-of-sight.

The function $P_t(t)$ is the instantaneous transmitted power in the laser beam. The Fresnel propagation of the field from Eq. 4.21 is

$$U_0(r, z) = \left[\frac{2P_t(t)}{\pi W_0^2} \right]^{1/2} \frac{1}{1 + i\alpha z} \exp \left[ikz - \frac{\alpha k r^2}{2(1 + i\alpha z)} \right]. \quad (4.23)$$

The variable z is the distance of propagation along the LADAR LOS. The propagated irradiance is

$$I_0(r, z) = |U_0(r, z)|^2 = \frac{2P_t(t)}{\pi W_z^2} \exp \left(-2 \frac{r^2}{W_z^2} \right) \quad (4.24)$$

where the beam size at range z is

$$W_z = W_0 \left[\left(1 - \frac{z}{F_0} \right)^2 + \left(\frac{\lambda z}{\pi W_0^2} \right)^2 \right]^{1/2}. \quad (4.25)$$

Eqs. 4.22 - 4.25 were also shown in Sec. 2.1.3, though the instantaneous power was not shown as a function of time in that section.

In a typical scenario, a LADAR receives only a tiny fraction of the laser energy that it transmits. If the laser beam reflects off of a flat surface that is oriented perpendicular to the line-of-sight, then the signal received by the LADAR, which is denoted $P_r(t)$, has the same shape as the transmitted pulse. Thus, the received signal is proportional to the transmitted signal.

$$P_r(t) \propto P_t(t). \quad (4.26)$$

Note that the delay due to the round-trip propagation time has not been introduced into $P_r(t)$. That delay is added later in this section when the effect of target tilt is analyzed.

Eq. 4.26 assumes that the propagated beam size is small compared to the distance of propagation. That is, $W_z \ll z$. If a wide beam is propagated a short distance, then the received signal $P_r(t)$ could have a shape different than the shape of the transmitted signal $P_t(t)$. This happens when the LOS distance between different parts of the illuminated target varies by an amount that is significant compared to the laser pulse duration.

It is assumed that the LADAR receiver aperture is located at the origin of a Cartesian coordinate system. The transmitted laser beam propagates in the positive z -direction. Referring to Figs. 4.4 and 4.5, the distance of propagation from the origin to target at coordinate (x, y) is approximately

$$z \approx R + \tan(\phi)y \quad (4.27)$$

where R is the range from the receiver to the target along the axis of propagation. The preceding approximation assumes that the vertical coordinate is small compared to the target range ($y \ll R$). In the figures, the y -axis has been defined as the vertical. However, the orientation is arbitrary because of the radial symmetry of the beam's irradiance pattern.

A tilt in the orientation of the target surface ($\phi \neq 0$), will distort the received laser pulse shape as compared to the transmitted shape. The signal received from a small rectangle with widths Δx and Δy located at (x, y) is

$$\begin{aligned} & \Delta x \Delta y I_0(x, y, r) P_r \left(t - \frac{2R}{c} \right) \\ &= \Delta x \Delta y \frac{2}{\pi W_z^2} \exp \left(-2 \frac{x^2 + y^2}{W_z^2} \right) P_r \left(t - \frac{2R}{c} \right) \\ &= \Delta x \Delta y \frac{2}{\pi W_z^2} \exp \left(-2 \frac{x^2 + y^2}{W_z^2} \right) P_r \left[t - \frac{2R}{c} - \frac{2 \tan(\phi)}{c} y \right] \end{aligned} \quad (4.28)$$

where c is the speed of light. The radial coordinate r in the propagated irradiance pattern (Eq. 4.24) has been replaced with the Cartesian coordinate (x, y) where $r^2 = x^2 + y^2$. The distance of propagation equation (Eq. 4.27) was also used to arrive at this result.

The total received signal from a tilted surface $P_{tilt}(t)$ can be derived by summing over all of the signals from the small rectangles (Eq. 4.28).

$$\begin{aligned} & P_{tilt}(t) \\ &= \sum_{m=-\infty}^{\infty} \sum_{n=-\infty}^{\infty} \Delta x \Delta y \frac{2}{\pi W_z^2} \exp \left(-2 \frac{x_m^2 + y_n^2}{W_z^2} \right) P_r \left[t - \frac{2R}{c} - \frac{2 \tan(\phi)}{c} y_n \right]. \end{aligned} \quad (4.29)$$

This result can be approximated by an integral.

$$P_{tilt}(t) = \int_{x=-\infty}^{\infty} \int_{y=-\infty}^{\infty} \frac{2}{\pi W_z^2} \exp \left(-2 \frac{x^2 + y^2}{W_z^2} \right) P_r \left[t - \frac{2R}{c} - \frac{2 \tan(\phi)}{c} y \right] dy dx. \quad (4.30)$$

Integrating over the x -axis yields

$$P_{tilt}(t) = \int_{y=-\infty}^{\infty} \left(\frac{2}{\pi W_z^2} \right)^{1/2} \exp \left(-2 \frac{y^2}{W_z^2} \right) P_r \left[t - \frac{2R}{c} - \frac{2 \tan(\phi)}{c} y \right] dy. \quad (4.31)$$

If the surface tilt is zero ($\phi = 0$), then the this equation is just $P_r(t)$, delayed by the round-trip propagation time. If the surface tilt is non-zero ($\phi \neq 0$), then the following two changes of variable are used to evaluate Eq. 4.31.

$$u = t - \frac{2R}{c}. \quad (4.32)$$

$$v = \frac{2 \tan(\phi)}{c} y. \quad (4.33)$$

Applying these changes of variable to Eq. 4.31 produces

$$\begin{aligned} P_{tilt}(t) &\approx \int_{v=-\infty}^{\infty} \left(\frac{2}{\pi W_z^2} \right)^{1/2} \exp \left[-2 \frac{c^2}{4 \tan^2(\phi) W_z^2} v^2 \right] P_r(u - v) dv \frac{c}{2 \tan(\phi)} \\ &= \frac{c}{\sqrt{2\pi} \tan(\phi) W_z} \exp \left[-\frac{c^2}{2 \tan^2(\phi) W_z^2} u^2 \right] * P_r(u) \end{aligned} \quad (4.34)$$

where $*$ denotes the convolution operation.

4.2.4 Gaussian Pulses. The equation describing the shape of a Gaussian pulse, which is denoted $p_g(t)$, is

$$p_g(t) = \exp \left(-\frac{1}{2w^2} t^2 \right) \quad (4.35)$$

where w is the pulse width. The full-width half-maximum (FWHM) is a commonly used metric to describe the width or duration of a pulse. The full-width half maximum for the Gaussian pulse, which is denoted τ_g , is

$$\tau_g = w [8 \log(2)]^{1/2}. \quad (4.36)$$

The variable E is the laser pulse energy that is intercepted by the LADAR's receiver aperture and focused onto the detector. The energy is

$$E = \int_{-\infty}^{\infty} P_r(t) dt. \quad (4.37)$$

This equation describes the amount of optical energy in the received signal. The signal $P_r(t)$ is not the usual voltage or current signal common in the electrical engineering literature. Thus, the signal is not squared to calculate its energy as is normally done when characterizing signals.

The equation for a received Gaussian pulse with energy E is

$$P_r(t) = \frac{E}{\sqrt{2\pi}w} p_g(t) = \frac{E}{\sqrt{2\pi}w} \exp\left(-\frac{1}{2w^2}t^2\right). \quad (4.38)$$

This is Eq. 4.35 after scaling so that its energy is E .

The received signal from a flat tilted surface, which is calculated by substituting Eq. 4.38 into Eq. 4.34, is

$$P_{tilt}(t) = \left\{ \frac{c}{\sqrt{2\pi} \tan(\phi) W_z} \exp\left[-\frac{c^2}{2 \tan^2(\phi) W_z^2} u^2\right] \right\} * \left[\frac{E}{\sqrt{2\pi}w} \exp\left(-\frac{1}{2w^2} u^2\right) \right]. \quad (4.39)$$

The convolution of two Gaussian waveforms with widths w_1 and w_2 and unity peak height is

$$\exp\left(-\frac{1}{2w_1^2}t^2\right) * \exp\left(-\frac{1}{2w_2^2}t^2\right) = \left(\frac{2\pi w_1^2 w_2^2}{w_1^2 + w_2^2}\right)^{1/2} \exp\left[-\frac{1}{2(w_1^2 + w_2^2)}t^2\right]. \quad (4.40)$$

Thus, the convolution of these two Gaussian functions is another Gaussian function with width $\sqrt{w_1^2 + w_2^2}$. Using Eq. 4.40, Eq. 4.39 becomes

$$P_{tilt}(t) = \frac{E}{\sqrt{2\pi} \left[w^2 + \frac{\tan^2(\phi)W_z^2}{c^2} \right]^{1/2}} \exp \left\{ -\frac{1}{2 \left[w^2 + \frac{\tan^2(\phi)W_z^2}{c^2} \right]} \left(t - \frac{2R}{c} \right)^2 \right\}. \quad (4.41)$$

The variable w_t is introduced to describe the width of a received Gaussian pulse that has reflected off a tilted surface. It is

$$w_t^2 = w^2 + \frac{\tan^2(\phi)W_z^2}{c^2}. \quad (4.42)$$

Using w_t , Eq. 4.41 becomes

$$P_{tilt}(t) = \frac{E}{\sqrt{2\pi}w_t} \exp \left[-\frac{1}{2w_t^2} \left(t - \frac{2R}{c} \right)^2 \right]. \quad (4.43)$$

Examples of received Gaussian pulses after reflection off a tilted surface are shown in Fig. 4.6. In this figure, a 2.5 cm beam propagates 10 km. The wavelength is 1.6 μm . The beam hits targets tilted at various angles with respect to the LADAR LOS.

In Fig. 4.6a, a $\tau_g = 1$ ns FWHM pulse is transmitted. For a 15 degree tilt angle, the received FWHM is only 1.09 ns. But with a 45 degree tilt, the pulse's FWHM nearly doubles. When the tilt reaches 75 degrees, the received FWHM is over six times greater than the transmitted FWHM. In Fig. 4.6b, the transmitted FWHM is 2 ns. This wider pulse is affected less by surface orientation than the 1 ns pulse. However, target tilt still affects the received signal. For a 45 degree tilt, the received FWHM increases about 28%. For the 75 degree tilt, the FWHM is over three times wider than the transmitted FWHM.

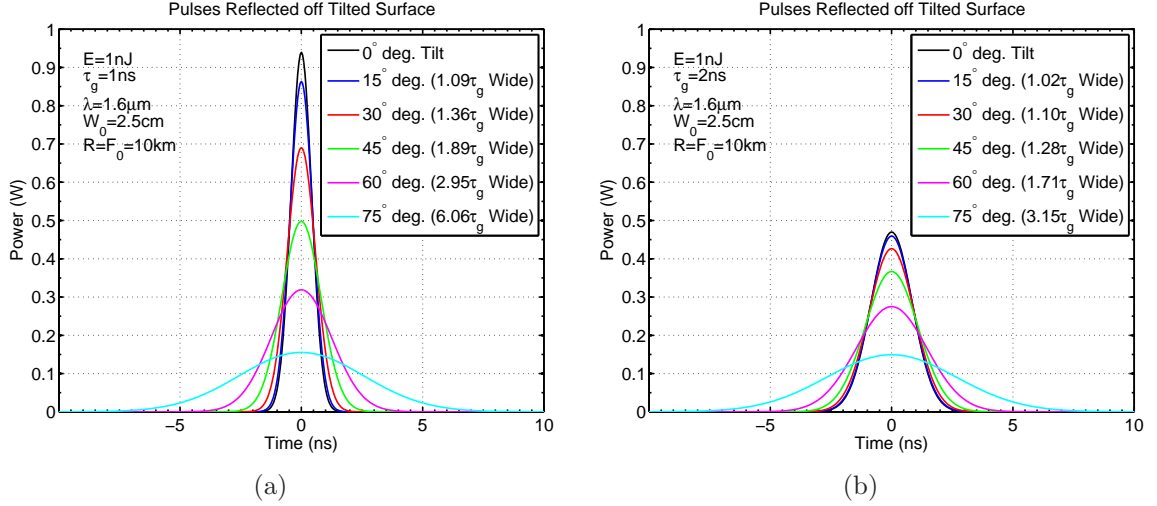


Figure 4.6: (a) Received signals for 1 ns FWHM pulse.
(b) Received signals for 2 ns FWHM pulse.

4.2.5 *Parabolic Pulses.* The equation for a received parabolic pulse with energy E is

$$P_r(t) = \frac{3E}{4p_w} p_p(t) = \frac{3E}{4p_w} \left(1 - \frac{t^2}{p_w^2}\right) \text{rect}\left(\frac{t}{2p_w}\right). \quad (4.44)$$

This is Eq. 3.74, scaled so that its energy is E . Also, Eq. 3.74 is being evaluated at range zero ($R_{rt} = 0$) in this case. For the parabolic pulse, the FWHM, which is denoted τ_p , is

$$\tau_p = \sqrt{2}p_w. \quad (4.45)$$

The received signal from a flat tilted surface, which is calculated by substituting Eq. 4.44 into Eq. 4.34, is

$$P_{\text{tilt}}(t) = \left\{ \frac{c}{\sqrt{2\pi} \tan(\phi) W_z} \exp\left[-\frac{c^2}{2 \tan^2(\phi) W_z^2} u^2\right] \right\} \quad (4.46) \\ * \left[\frac{3E}{4p_w} \left(1 - \frac{u^2}{p_w^2}\right) \text{rect}\left(\frac{u}{2p_w}\right) \right].$$

This equation is proportional to the convolution of a Gaussian (Eq. 4.35) and a parabolic (Eq. 3.74) pulse. The constants in Eq. 4.46 are ignored for the moment

and the convolution is denoted $y(t)$.

$$\begin{aligned}
y(t) &= p_p(t) * p_g(t) \\
&= \int_{-\infty}^{\infty} p_p(v)p_g(v-t)d\tau \\
&= \int_{-p_w}^{p_w} \left(1 - \frac{v^2}{p_w^2}\right) \exp\left[-\frac{(v-t)^2}{2w_{tilt}^2}\right] d\tau
\end{aligned} \tag{4.47}$$

where

$$w_{tilt}^2 = \frac{\tan^2(\phi)W_z^2}{c^2}. \tag{4.48}$$

After extensive algebra, it can be shown that this convolution is

$$\begin{aligned}
y(t) &= \frac{2w_{tilt}^2}{p_w^2} \exp\left(-\frac{p_w^2 + t^2}{2w_{tilt}^2}\right) \left[p_w \cosh\left(\frac{p_w t}{w_{tilt}^2}\right) + t \sinh\left(\frac{p_w t}{w_{tilt}^2}\right) \right] \\
&\quad + \frac{w_{tilt}\sqrt{\pi}}{\sqrt{2}} \left(1 - \frac{w_{tilt}^2 + t^2}{p_w^2}\right) \left[\operatorname{erf}\left(\frac{p_w - t}{\sqrt{2}w_{tilt}}\right) + \operatorname{erf}\left(\frac{p_w + t}{\sqrt{2}w_{tilt}}\right) \right].
\end{aligned} \tag{4.49}$$

Eq. 4.49 is illustrated and validated in Fig. 4.7. The Gaussian pulse width is fixed at $w = 2$ ns and the parabolic pulse width varies between 0.5 and 4 ns. The pulses are shown in Fig. 4.7a and the convolution in Fig. 4.7b. The analytic expression for the convolution is shown, along with a numeric calculation in order to validate the complicated expression from Fig. 4.7.

Eq. 4.49 can be used in Eq. 4.46 to calculate the received signal when a parabolic pulse reflects off of a tilted surface.

$$\begin{aligned}
P_{tilt}(t) &= \frac{c}{\sqrt{2\pi} \tan(\phi)W_z} \frac{3E}{4p_w} y\left(t - \frac{2R}{c}\right) \\
&= \frac{3E}{\sqrt{2\pi}4p_w w_{tilt}} y\left(t - \frac{2R}{c}\right)
\end{aligned} \tag{4.50}$$

where Eq. 4.48 was used. This equation is rather complicated. It would be difficult to derive CRLBs or parameter estimation techniques given the signal in Eq. 4.50.

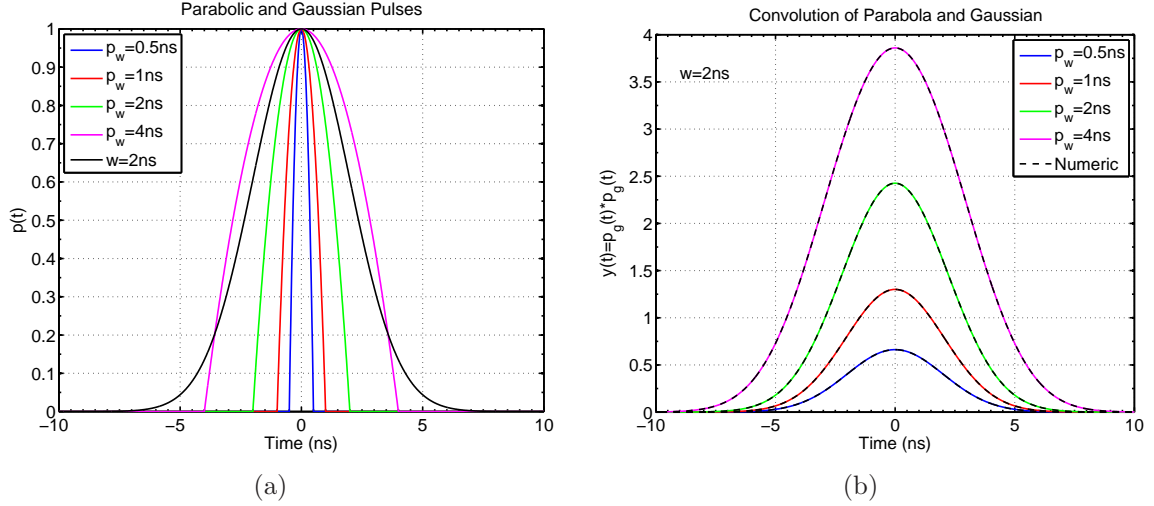


Figure 4.7: (a) Parabolic pulses with various widths and Gaussian pulse with $w = 2$. (b) Convolution of parabolic and Gaussian pulses.

Therefore, the remaining work in this chapter will focus on the Gaussian pulse model from Sec. 4.2.4 instead of the parabolic pulse model.

4.2.6 Range Precision and the CRLB. The signals in Eqs. 4.34, 4.43, and 4.50 describe the amount of optical power incident on the LADAR system's photodetector. The photodetector, typically a photodiode or photomultiplier tube, converts the optical power into an electrical signal. The relationship between the optical power and the photodetector's output current $i(t)$ is given by Eq. 2.26

$$i(t) = \frac{Gq\eta}{h\nu} P_{tilt}(t) = \Re P_{tilt}(t) \quad (4.51)$$

where G is the detector's gain, q is the electron charge, η is the fraction of photons converted to electrons or quantum efficiency, h is Planck's constant, and ν is the laser optical frequency. This relationship between the received optical power and the photocurrent is often written in terms of the detector's responsivity \Re (see Eq. 2.27). Responsivity has units of charge per energy, or equivalently, current per power.

The energy in the photocurrent signal (denoted E_e), normalized to unit resistance, is

$$E_e = \int_{-\infty}^{\infty} i^2(t) dt = \Re^2 \int_{-\infty}^{\infty} P_{\text{tilt}}^2(t) dt. \quad (4.52)$$

Notice that the optical energy E is the integral over $P_{\text{tilt}}(t)$ (see Eq. 4.37) while the electrical energy E_e is proportional to the integral over $P_{\text{tilt}}(t)$ squared. Thus, there is not a straightforward general relationship between the received optical energy E and the signal electrical energy E_e .

The signal that is recorded by the LADAR system is corrupted by noise sources. Noise sources include laser speckle, background light entering the LADAR's receiver aperture, dark current in the photodetector, and electronic noise in the analog-to-digital converter (ADC). Laser speckle and background light are usually modeled as Poisson processes [21, 31]. However, as the mean of a Poisson random variable increases, its distribution approaches the shape of a Gaussian distribution. Thus, Gaussian noise is sometimes an adequate approximation for the noise in LADAR systems. In this section, it is assumed that the noise in the received signal is additive white Gaussian.

The noisy received signal, denoted $r(t)$, is

$$r(t) = i(t) + w(t) \quad (4.53)$$

where $w(t)$ is white Gaussian noise with a power spectral density (PSD) that has height N_0 . This continuous-time signal is sampled at rate f_s . The variance of the Gaussian noise is denoted σ^2 . If an ideal anti-aliasing filter is used before the analog-to-digital conversion, then the per-sample noise variance is

$$\sigma^2 = f_s N_0. \quad (4.54)$$

The sampled signal is denoted $r[n]$.

$$r[n] = r(n/f_s) = i[n] + w[n]. \quad (4.55)$$

Because the noise is additive white Gaussian, the distribution of the samples is

$$r[n] \sim \mathcal{N} [i[n], \sigma^2]. \quad (4.56)$$

The anti-aliasing filter causes all of the noise realizations to be independent.

$$\text{E} [w[m]w[n]] = \sigma^2 \delta[m - n] \quad (4.57)$$

where

$$\delta [m] = \begin{cases} 1 & \text{if } m = 0 \\ 0 & \text{if } m \neq 0 \end{cases} \quad (4.58)$$

is the Kronecker delta function.

Given a signal mixed with AWGN, the Cramer-Rao lower bound for estimates of range is [23]

$$\text{Var} [\hat{R}] \geq \frac{c^2 N_0}{4 \int_{-\infty}^{\infty} \left[\frac{dP_{tit}(t)}{dt} \right]^2 dt} \quad (4.59)$$

where \hat{R} is any unbiased estimate of target range. Range estimation usually involves multiple steps. Combinations of matched filters and peak-fitting algorithms are common. One of the reasons that Cramer-Rao lower bounds are valuable is that they are valid regardless of the exact algorithm used to produce the range estimate. As long as the estimate produced by the algorithm is unbiased, the CRLB is valid.

The signal model from Eq. 4.43 differs from the model used in [23] in that the width of the received signal is unknown. However, the Gaussian pulse with AGWN model was also studied in [16]. In that reference, it was proved addition of an unknown

width parameter to the model does not change the range CRLB. Thus, the CRLB from Eq. 4.59 is valid in this case.

Using Fourier transform properties, the integral in Eq. 4.59 can be expressed

$$\int_{-\infty}^{\infty} \left[\frac{dP_{tilt}(t)}{dt} \right]^2 dt = \int_{-\infty}^{\infty} |2\pi f \mathcal{F}\{P_{tilt}(t)\}|^2 df = 4\pi^2 \int_{-\infty}^{\infty} f^2 |\mathcal{F}\{P_{tilt}(t)\}|^2 df \quad (4.60)$$

where $\mathcal{F}\{\}$ denotes the Fourier transform operation. The mean squared bandwidth of the signal, which is denoted σ_f^2 , is

$$\sigma_f^2 = \frac{\int_{-\infty}^{\infty} f^2 |\mathcal{F}\{P_{tilt}(t)\}|^2 df}{\int_{-\infty}^{\infty} |\mathcal{F}\{P_{tilt}(t)\}|^2 df}. \quad (4.61)$$

Using this result, the CRLB can be written

$$\text{Var}[\hat{R}] \geq \frac{1}{\text{SNR}} \left(\frac{c}{4\pi\sigma_f} \right)^2 \quad (4.62)$$

where the SNR is

$$\text{SNR} = \frac{E_e}{N_0}. \quad (4.63)$$

It is the ratio of the signal's electrical energy E_e to the height of the AWGN PSD (N_0).

4.2.7 Gaussian Pulse CRLB. Given the Gaussian pulse from Eq. 4.38, the noiseless electrical signal is

$$i(t) = \frac{\Re E}{\sqrt{2\pi w_t}} \exp \left[-\frac{1}{2w_t^2} \left(t - \frac{2R}{c} \right)^2 \right]. \quad (4.64)$$

The electrical energy in this signal is (see Eq. 4.52)

$$E_e = \frac{\Re^2 E^2}{2\sqrt{\pi} w_t}. \quad (4.65)$$

Eq. 4.43 is used to calculate the mean squared bandwidth. The Gaussian pulse mean square bandwidth is

$$\sigma_f^2 = \frac{1}{8\pi^2 w_t^2}. \quad (4.66)$$

Therefore, the CRLB for target range measurements made with a Gaussian pulse is

$$\text{Var} \left[\widehat{R} \right] \geq \frac{1}{\text{SNR}} \frac{c^2 w_t^2}{2}. \quad (4.67)$$

Examples of Gaussian pulse range CRLBs are shown in Fig. 4.8. In this figure, a 2.5 cm beam intercepts a target 10 km away from the LADAR. A 1.6 μm wavelength is assumed. In Fig. 4.8a, the transmitted pulse FWHM is 1 ns. The increase in the CRLB for a 15 degree tilt is small. However, once the tilt is 45 degree, the CRLB, which in standard deviation is proportional to the received pulse width w_t , has nearly doubled. For a 75 degree tilt, the CRLB is over six times greater than if the target was perpendicular to the LOS. In Fig. 4.8b, the transmitted pulse FWHM is 2 ns. This wider pulse is affected less by target tilt than the 1 ns pulse. For example, the 15 and 30 degree tilts are almost negligible in this case. However, for equal SNRs, the wider 2 ns pulse had a worse range precision in the absence of target surface tilt. Thus, given a fixed SNR, it is best to use the shortest pulse possible even though shorter pulses are more susceptible to distortion because of target tilt.

It was shown in Fig. 4.1 that if the noise in a signal is AWGN that the CRLB can be achieved unless the background noise dominates. However, the true received pulse width must be known in order to reach the bound. If the pulse width is unknown, then the filter used for range estimation will not be designed properly and the range estimates will be less precise than the CRLB predicts. This issue was studied for Poisson noise and is illustrated in Fig. 3.13.

The detrimental effect of target tilt on range precision can be mitigated by increasing the transmitted beam size. Larger transmitted beams make it possible to focus the beam into a smaller area at range. Thus, there is less spreading of the

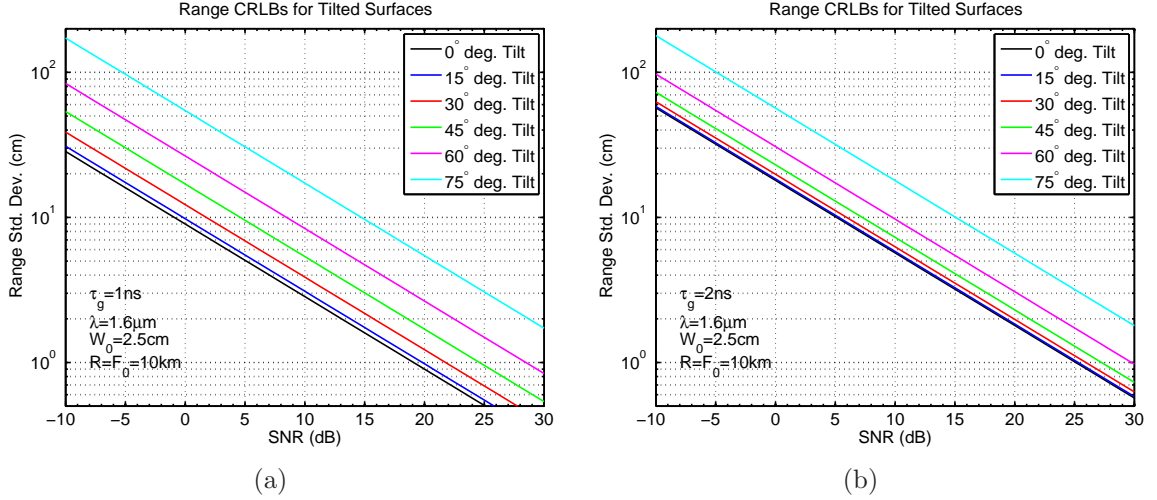


Figure 4.8: (a) Range CRLBs for 1 ns FWHM pulse.
(b) Range CRLBs for target tilted 45 degrees.

received pulse. The effect is illustrated in Fig. 4.9a. The target is assumed to have a 45 degree tilt. Doubling the beam size from 2.5 cm to 5 cm decreases the CRLB by about one-third. However, greater increases in beam size yield a diminishing return since the transmitted pulse’s 1 ns FWHM is not decreased. On the other hand, received optical energy is proportional to receiver aperture area. If the increase in beam size is accompanied by an increase in receiver aperture diameter, then the SNR will increase. It is necessary to focus the beam to gain this benefit. Increasing the size of a collimated beam will actually decrease the range precision since propagated beam size for collimated beams increases monotonically with increases in transmitted beam size.

In Fig. 4.9b, the effect of varying the transmitted pulse’s duration is studied. In the absence of target tilt, the range standard deviation is proportional to the FWHM. However, target tilt makes that relationship nonlinear. Given a target tilted at 45 degrees and a 2.5 cm beam propagating 10 km, there is a good increase in precision when the FWHM drops from 10 to 3 ns and again when it drops from 3 to 1 ns. However, decreasing the FWHM from 1 ns to 0.3 ns does little to improve the range precision for the 45 degree target. Without tilt, the range standard deviation would

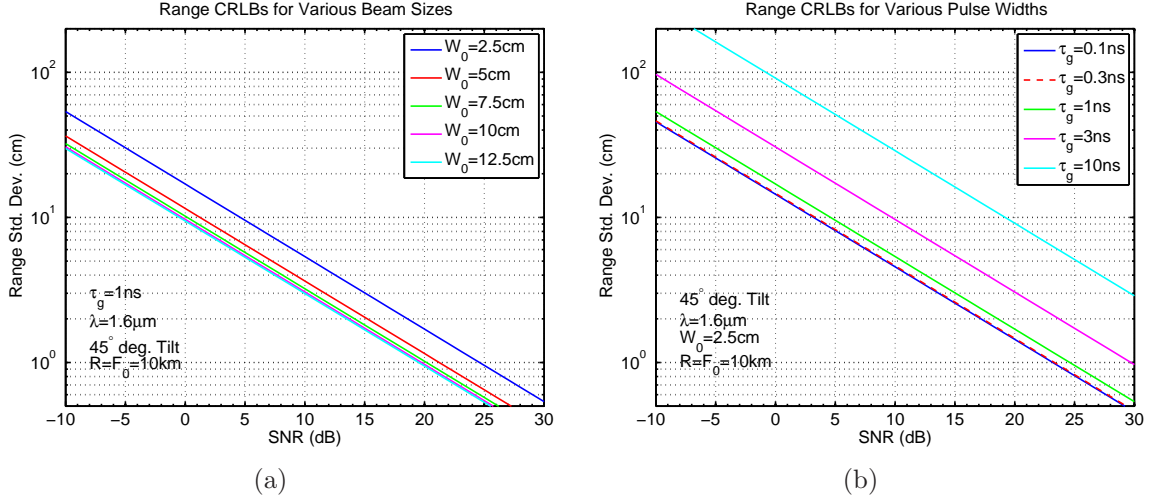


Figure 4.9: (a) Range CRLBs for 1 ns FWHM pulse.
(b) Range CRLBs for 2 ns FWHM pulse.

have dropped by a factor of 0.3. The performance difference between 0.3 and 0.1 ns FWHM pulses is almost not noticeable since in that case the width of the received pulse is dominated by the effect of target depth.

4.3 Chapter Summary

The range precision of LADAR systems was discussed in this chapter. Different signal and noise models were used to analyze range precision. In Sec. 4.1, the range CRLB derived in Chapter III for a truncated parabolic pulse in Poisson noise was compared to the bound for the same pulse shape and Gaussian noise. It was shown that the Poisson-noise CRLB was higher (worse range precision) than the Gaussian noise bound. The effect of pulse averaging was also discussed in Sec. 4.1. It was shown that if a fixed amount of laser energy is divided equally into multiple laser pulses, then the range precision for the accumulated or averaged signal drops as the number of pulses increases. Thus, transmitting laser energy in as few pulses as possible will maximize a LADAR's range precision.

In Sec. 4.2, it was noted that the reflection process can elongate a laser pulse. It was also shown that pulse elongation decreases range precision. Given a pulse with a

Gaussian shape mixed with AWGN noise, the range CRLB was calculated in terms of target surface orientation and other LADAR system parameters such as transmitter aperture size, range to target, and laser beam focus distance. Given an aperture that is a few inches in diameter and a laser pulse that is at least a nanosecond in duration, the effect of a target surface tilt on range precision is negligible at ranges less than a few kilometers. However, airborne LADAR systems can encounter scenarios where a target surface tilt can produce a significant drop in range precision. The amount of increase in the range CRLB due to target tilt was quantified in Sec. 4.2.

V. Gain Variation in APD Arrays

Some modern LADAR systems make use of compact arrays of avalanche photodiodes to produce high-resolution three-dimensional images of scenes. The arrays in those systems are often very compact. Systems with over ten thousand detector elements have been demonstrated. The sheer number of pixels present in modern photodetector arrays can eliminate the need for scanning equipment in LADAR systems. However, the miniaturization process used to make the compact detector arrays can introduce undesirable effects. An unwanted property that has been observed in arrays of APDs is gain variation.

Gain variation refers to fluctuation in the relationship between the number of electrons detected by the photodiode and the output current of that device. Ideally, this relationship would be fixed. In practice, it has been shown that gain can fluctuate over time. These fluctuations effect the entire array. The fluctuation can distort the shape of the received signal and can even create false signals on detector pixels that did not actually observe a laser signal.

In this chapter, mathematical models are proposed to represent gain variation in arrays of photodiodes. These models of signals observed by LADAR detector arrays are used to derive numeric methods of gain estimation. The numeric methods are tested using Monte Carlo simulations and LADAR data.

In Sec. 5.1, three-dimensional LADAR data collected during an experiment using a large target panel is displayed and the effect of gain variation on range-resolved signals is illustrated. In Sec. 5.2, a numeric method of gain estimation based on the Gauss-Newton iteration is derived and tested on simulated and real LADAR data. Finally, in Sec. 5.3, an alternative method of gain estimation using target-free LADAR data is derived and tested on LADAR data.

5.1 *FLASH LADAR Data*

Gain variation has been observed in the Advanced Scientific Concepts (ASC) LADAR system operated by AFRL Sensors Directorate. The likely cause of the gain

variation in this LADAR is the fact that the APD array was built around one common voltage regulator [37]. The voltage regulator attempts to keep the bias voltage V_{bias} constant. However, the bias voltage appears to fluctuate over time. Since the gain in a photodiode is a function of the bias voltage (Eq. 2.50), the gain varies with changes in that voltage.

The ASC LADAR is a flash system. Flash LADAR systems use a single laser pulse to image an entire scene. The imaging is accomplished using an array with many pixels. The ASC LADAR uses an 128×128 array of InGaAs photodiodes. The laser wavelength of this system is $1.54\mu\text{m}$. The detector array is bonded to a readout integrated circuit (ROIC). This ROIC samples the received LADAR signals at a rate of 420 MHz, corresponding to a round-trip range sampling resolution of 0.36 m.

The laser transmitter produces 1.7 mJ pulses with a full-width half-maximum of 4.7 ns. These pulses are diffused over an angle of 1.5 degrees. The LADAR data was collected using a 500 mm focal length lens with a 80 mm aperture. The laser is eye-safe at ranges more than a few inches from the aperture.

The APDs in the detector array are separated by $100\ \mu\text{m}$. They are approximately $10\ \mu\text{m}$ in width. An array of lenslets is used to improve the effective fill factor of the detector array. With the 500 mm lens, the instantaneous field of view (IFOV) of the pixels is 0.2 milliradians.

The ASC LADAR stores twenty samples per pixel. Therefore, the sampling depth for the system is only 7.2 m. The entire system operates at a 20 Hz rate, which provides three-dimensional image information at a rate compatible with typical video displays. Descriptions of LADAR systems built by ASC and examples of their imaging capabilities are shown in [47, 48].

A three-dimensional image of a target panel is shown in Fig. 5.1. The data was collected at Wright-Patterson Air Force Base. This image was collected using the Air Force Research Laboratory's ASC LADAR system. The LADAR system was located in a tower and was 23 m above the ground. The range to the target panel was 70

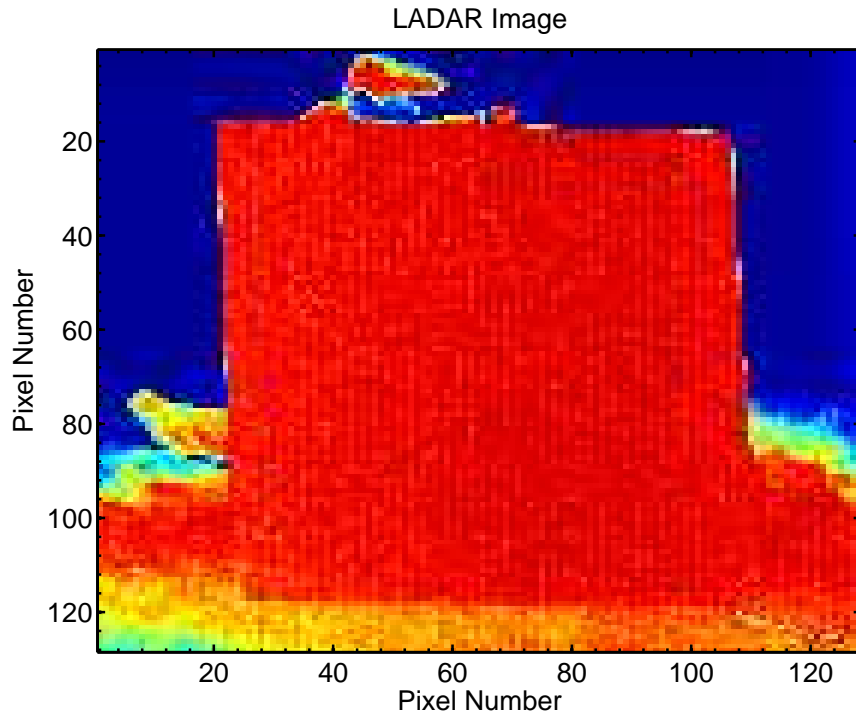


Figure 5.1: LADAR image of a target panel.

m. Thus, the downlook angle was 20 degrees. The target panel was made of plywood and was not painted or coated. That panel was 155 cm high and had a similar width.

In Fig. 5.1, the intensity from the tenth of the twenty range slices is shown. The target panel was supported manually. During the data collections, the target panel orientation with respect to the LOS was varied. There is significant fluctuation in the individual signals, so they are averaged over multiple image frames. In this case, 108 signals were averaged.

Range-resolved LADAR data collected by the ASC system is illustrated in Fig. 5.2. In Fig. 5.2a, four signals from the target panel are illustrated. In this experiment, the target panel was tilted. Data with lower row numbers corresponded to longer ranges to the panel. For all four signals, the first five or six samples are noise. In row one-hundred, the target appears in the six or seventh sample. The row forty target was not reached until sample ten. Near samples eight and nine, a drop in gain is visible in the row forty and row sixty data before the target panel is observed in those

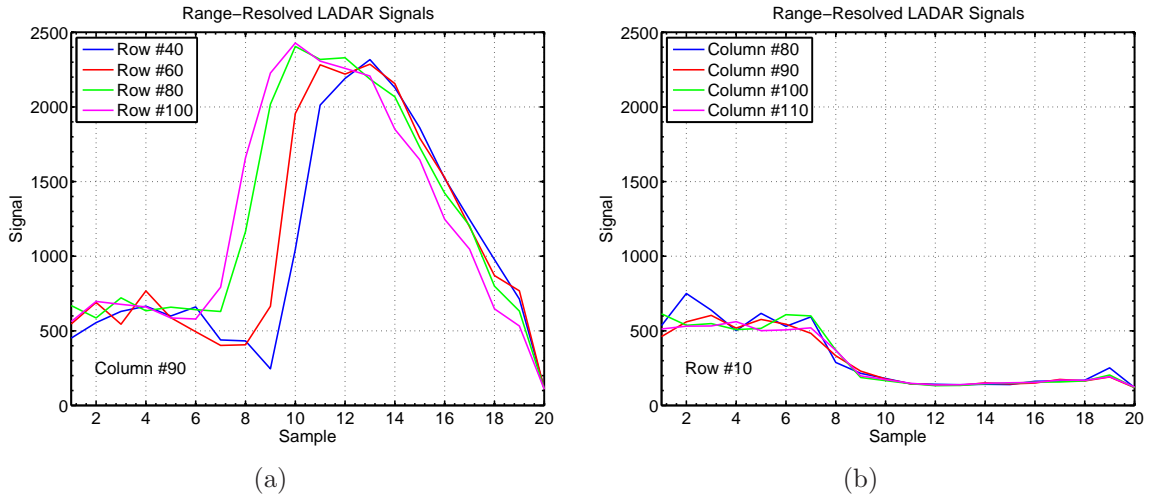


Figure 5.2: (a) LADAR signals from target panel.
(b) Background noise in LADAR image.

pixels. The variation in gain also altered the observed width of the laser pulse. The pulse is much wider in rows eighty and one-hundred than in rows twenty and forty.

Fig. 5.2b illustrates data from pixels where no target is present. In these pixels, the first seven samples contain only noise with mean level around five hundred. However, in samples eight and higher, the gain has dropped and the mean is around two hundred. This data is typical of what was observed throughout the experiment. A laser signal or signals affected the gain on all pixels in the array. The gain variation was observed whether or not there was actually a laser signal in the pixel.

5.2 Gauss-Newton Method for Gain Estimation

In this section, the Gauss-Newton method of parameter estimation is used to solve for the unknown gain in a LADAR detector array. This method requires that the probability density function of the data is known. Therefore, a signal model is developed to approximate the data observed by a LADAR system. This model assumes white Gaussian noise, but does not assume knowledge of the signal amplitudes or the target ranges. Those parameters are estimated along with the unknown gain values by the Gauss-Newton iteration.

5.2.1 *Detector Array Signal Model.* The model used to represent signals observed by the detector array is based on the LADAR signal model from [4]. However, some modifications have been made to that equation. The temporal pulse shape is assumed to be a Gaussian function, rather than the truncated parabola from Eq. 2.29. Also, it is assumed that the noise in all samples is modeled by independent and identically distributed (IID) Gaussian random variables. Some detector signal models used earlier in this dissertation assumed Poisson noise.

The detector array signal model is

$$\begin{aligned} I_{k,m} &= G_k i_{k,m} \\ &= G_k \left\{ A_m \exp \left[-\frac{(k - R_m)^2}{2w^2} \right] + B_m \right\} \end{aligned} \quad (5.1)$$

where

$$i_{k,m} = A_m \exp \left[-\frac{(k - R_m)^2}{2w^2} \right] + B_m \quad (5.2)$$

is the signal before the variable gain is applied. In Eq. 5.1, k denotes the temporal sample index and m denotes the detector pixel (spatial) index. Note that in this equation, the k , R_m , and w have units of samples. Each detector records K samples and there are M detectors in the array. The variable A_m is the peak amplitude of the received signal before gain. The range to the target, in samples, is denoted R_m . The bias level on the m -th detector element is B_m .

It is assumed that the gain values (the G_k 's) are unknown. It is also assumed that the signal amplitude and range values (the A_m 's and the R_m 's) are unknowns. However, the biases on each detector's signal (the B_m 's) are assumed to be known. In a real LADAR system, the bias is not known and must be estimated from the data. However, noise data, which can be used to measure the bias, is normally abundant. The large amount of available noise data can be used to produce precise bias estimates for each detector in the array.

The pulse width w is assumed known. There are LADAR imaging scenarios where this assumption is not realistic. However, during the data collection with the ASC system, the range to the target was short. Also, the system's instantaneous field of view is narrow. Under these circumstances (short range and narrow IFOV), target depth in individual pixels is normally shallow and the pulse width does not stretch significantly because of reflection.

The k -th sample recorded by the m -th detector in the array is the random variable $D_{k,m}$. This random variable has mean $I_{k,m}$ and additive noise. It has been assumed that the noise is Gaussian. The variance of each sample is σ^2 .

$$D_{k,m} \sim \mathcal{N} [I_{k,m}, \sigma^2]. \quad (5.3)$$

The probability density function is

$$p_{D_{k,m}}(d_{k,m}) = \frac{1}{\sqrt{2\pi\sigma^2}} \exp \left[-\frac{1}{2\sigma^2} (d_{k,m} - I_{k,m})^2 \right] \quad (5.4)$$

where $d_{k,m}$ is a realization of random variable $D_{k,m}$. Since the noise is IID, the joint distribution of the data is the product of the PDFs of the $d_{k,m}$'s. Let \mathbf{D} denote the set of random variables and \mathbf{d} denote the realization of the set of those random variables. The joint PDF of \mathbf{D} is

$$\begin{aligned} p_{\mathbf{D}}(\mathbf{d}) &= \prod_{k'=1}^K \prod_{m'=1}^M p_{D_{k',m'}}(d_{k',m'}) \\ &= \prod_{k'=1}^K \prod_{m'=1}^M \frac{1}{\sqrt{2\pi\sigma^2}} \exp \left[-\frac{1}{2\sigma^2} (d_{k',m'} - I_{k',m'})^2 \right] \\ &= \frac{1}{(2\pi\sigma^2)^{KM/2}} \exp \left[-\frac{1}{2\sigma^2} \sum_{k'=1}^K \sum_{m'=1}^M (d_{k',m'} - I_{k',m'})^2 \right]. \end{aligned} \quad (5.5)$$

Let \mathbf{g} denote the set of K unknown gain values, let \mathbf{a} be the set of M unknown amplitude values, and let \mathbf{r} be the set of M range values. The log-likelihood function

for random data set \mathbf{d} is

$$l(\mathbf{g}, \mathbf{a}, \mathbf{r}|\mathbf{d}) = -\frac{KM}{2} \log(2\pi\sigma^2) - \frac{1}{2\sigma^2} \sum_{k'=1}^K \sum_{m'=1}^M (d_{k',m'} - I_{k',m'})^2. \quad (5.6)$$

This log-likelihood function is relatively complicated. Its complexity will likely prevent efficient calculation of maximum likelihood estimates. However, in the next section, it is shown that it can be used in combination with the Gauss-Newton method to derive iterative estimates of the unknown parameters.

5.2.2 Iterative Gain Estimation. The unknown parameters in the detector array signal model from Eq. 5.1 can be estimated using the Gauss-Newton method. The Gauss-Newton method is an iterative technique for parameter estimation that is based on the log-likelihood function. The Gauss-Newton method is described in *Fundamentals of Statistical Signal Processing: Estimation Theory* by Kay [23]. Given a log-likelihood function with unknown parameter vector $\boldsymbol{\theta}$, the Gauss-Newton method relies on an initial estimate of the unknown parameters, $\widehat{\boldsymbol{\theta}}_0$. This estimate is not expected to be an optimal measurement of the unknown parameters. However, the Gauss-Newton method requires an precise initial estimate. If the initial estimate is not precise, the iteration could converge to a local maximum as opposed to the desired global maximum of the likelihood function. Given estimate $\widehat{\boldsymbol{\theta}}_n$, the Gauss-Newton iterative update is

$$\widehat{\boldsymbol{\theta}}_{n+1} = \widehat{\boldsymbol{\theta}}_n - \left[\mathbf{\Lambda}(\widehat{\boldsymbol{\theta}}_n) \right]^{-1} \boldsymbol{\lambda}(\widehat{\boldsymbol{\theta}}_n). \quad (5.7)$$

The matrix $\mathbf{\Lambda}$ and the vector $\boldsymbol{\lambda}$ in Eq. 5.7 are populated by derivatives of the log-likelihood function. The vector $\boldsymbol{\lambda}$ contains the first derivatives of the log-likelihood function. The i -th element of $\boldsymbol{\lambda}$ is the derivative of $l(\boldsymbol{\theta})$ with respect to the i -th unknown parameter.

$$[\boldsymbol{\lambda}]_i = \frac{\partial l(\boldsymbol{\theta})}{\partial \theta_i} \quad (5.8)$$

where θ_i is the i -th element of $\boldsymbol{\theta}$. The elements of matrix $\mathbf{\Lambda}$ are the second derivatives of the log-likelihood function. The element in the i -th row and j -th column of matrix

$\mathbf{\Lambda}$ is

$$[\mathbf{\Lambda}]_{ij} = \frac{\partial^2 l(\boldsymbol{\theta})}{\partial \theta_i \partial \theta_j}. \quad (5.9)$$

The likelihood function is parameterized by $\boldsymbol{\theta}$. That parameter vector is being updated iteratively. Within the iteration, $\mathbf{\Lambda}$ and $\boldsymbol{\lambda}$ are evaluated using the unknown parameter vector estimate from the previous step. This explains the notation $\boldsymbol{\lambda}(\widehat{\boldsymbol{\theta}}_n)$ and $\mathbf{\Lambda}(\widehat{\boldsymbol{\theta}}_n)$ in Eq. 5.7.

The first derivatives of the log-likelihood function are

$$\begin{aligned} \frac{\partial l(\boldsymbol{\theta})}{\partial \theta_i} &= \frac{\partial}{\partial \theta_i} \left[-\frac{1}{2\sigma^2} \sum_{k'=1}^K \sum_{m'=1}^M (d_{k',m'} - I_{k',m'})^2 \right] \\ &= \frac{1}{\sigma^2} \sum_{k'=1}^K \sum_{m'=1}^M (d_{k',m'} - I_{k',m'}) \frac{\partial I_{k',m'}}{\partial \theta_i}. \end{aligned} \quad (5.10)$$

The second derivative with respect to θ_i is

$$\frac{\partial^2 l(\boldsymbol{\theta})}{\partial \theta_i^2} = \frac{1}{\sigma^2} \sum_{k'=1}^K \sum_{m'=1}^M \left[(d_{k',m'} - I_{k',m'}) \frac{\partial^2 I_{k',m'}}{\partial \theta_i^2} - \left(\frac{\partial I_{k',m'}}{\partial \theta_i} \right)^2 \right]. \quad (5.11)$$

These second derivatives are the diagonal elements of $\mathbf{\Lambda}$. Matrix $\mathbf{\Lambda}$ also contains second derivatives with respect to θ_i and θ_j . These derivatives are the off-diagonal elements of $\mathbf{\Lambda}$. These derivatives are

$$\frac{\partial^2 l(\boldsymbol{\theta})}{\partial \theta_i \partial \theta_j} = \frac{1}{\sigma^2} \sum_{k'=1}^K \sum_{m'=1}^M \left[(d_{k',m'} - I_{k',m'}) \frac{\partial^2 I_{k',m'}}{\partial \theta_i \partial \theta_j} - \frac{\partial I_{k',m'}}{\partial \theta_i} \frac{\partial I_{k',m'}}{\partial \theta_j} \right]. \quad (5.12)$$

These log-likelihood derivative expressions with respect to general unknown parameters θ_i and θ_j , can be used to find elements of $\boldsymbol{\lambda}$ and $\mathbf{\Lambda}$ specific to the likelihood function associated with the joint density from Eq. 5.5.

The next step in the derivation of the Gauss-Newton iteration is evaluation of the derivatives of the signal from Eq. 5.1. The derivative of the signal with respect

to the k -th gain value is

$$\frac{\partial I_{k,m}}{\partial G_k} = i_{k,m}. \quad (5.13)$$

The signal $I_{k,m}$ does not depend on the gain on samples other than the k -th sample. Therefore,

$$\frac{\partial I_{k,m}}{\partial G_l} = 0 \quad \text{when } k \neq l. \quad (5.14)$$

The signal derivatives with respect to the amplitude and range for the m -th detector are

$$\frac{\partial I_{k,m}}{\partial A_m} = G_k \exp \left[-\frac{(k - R_m)^2}{2w^2} \right] \quad (5.15)$$

and

$$\frac{\partial I_{k,m}}{\partial R_m} = \frac{G_k A_m}{w^2} (k - R_m) \exp \left[-\frac{(k - R_m)^2}{2w^2} \right]. \quad (5.16)$$

The amplitude and range of signal $I_{k,m}$ do not depend on range and amplitude values of signals on other detectors. Therefore,

$$\frac{\partial I_{k,m}}{\partial A_n} = \frac{\partial I_{k,m}}{\partial R_n} = 0 \quad \text{when } m \neq n. \quad (5.17)$$

Second derivatives of $I_{k,m}$ are also needed to evaluate the terms in the Gauss-Newton iteration. Second derivatives with respect to gain and amplitude are zero.

$$\frac{\partial^2 I_{k,m}}{\partial G_k^2} = \frac{\partial^2 I_{k,m}}{\partial A_m^2} = 0. \quad (5.18)$$

The range second derivative is not zero.

$$\begin{aligned} \frac{\partial^2 I_{k,m}}{\partial R_m^2} &= -\frac{G_k A_m}{w^2} \exp \left[-\frac{(k - R_m)^2}{w^2} \right] + \frac{G_k A_m}{w^4} (k - R_m)^2 \exp \left[-\frac{(k - R_m)^2}{2w^2} \right] \\ &= \frac{G_k A_m}{w^2} \left[\frac{(k - R_m)^2}{w^2} - 1 \right] \exp \left[-\frac{(k - R_m)^2}{2w^2} \right]. \end{aligned} \quad (5.19)$$

Terms dependent on derivatives of different gain values are zero

$$\frac{\partial^2 I_{k,m}}{\partial G_k \partial G_l} = 0 \quad \text{when } k \neq l. \quad (5.20)$$

Similarly, derivatives dependent of different amplitude or different range values are zero.

$$\frac{\partial^2 I_{k,m}}{\partial A_m \partial A_n} = \frac{\partial^2 I_{k,m}}{\partial R_m \partial R_n} = \frac{\partial^2 I_{k,m}}{\partial A_m \partial R_n} = 0 \quad \text{when } m \neq n. \quad (5.21)$$

The derivatives corresponding to gain and amplitude values are

$$\frac{\partial^2 I_{k,m}}{\partial G_k \partial A_m} = \exp \left[-\frac{(k - R_m)^2}{2w^2} \right]. \quad (5.22)$$

The gain and range derivatives are

$$\frac{\partial^2 I_{k,m}}{\partial G_k \partial R_m} = \frac{A_m}{w^2} (k - R_m) \exp \left[-\frac{(k - R_m)^2}{2w^2} \right]. \quad (5.23)$$

The final derivative needed is

$$\frac{\partial^2 I_{k,m}}{\partial A_m \partial R_m} = \frac{G_k}{w^2} (k - R_m) \exp \left[-\frac{(k - R_m)^2}{2w^2} \right]. \quad (5.24)$$

The first derivatives of $l(\mathbf{g}, \mathbf{a}, \mathbf{r}|\mathbf{d})$ are needed to evaluate the elements of $\boldsymbol{\lambda}$. Eqs. 5.8 and 5.10 are combined to find the derivative with respect to unknown gain terms G_k .

$$\begin{aligned} \frac{\partial l(\mathbf{g}, \mathbf{a}, \mathbf{r}|\mathbf{d})}{\partial G_k} &= \frac{1}{\sigma^2} \sum_{k'=1}^K \sum_{m'=1}^M (d_{k',m'} - I_{k',m'}) \frac{\partial I_{k',m'}}{\partial G_k} \\ &= \frac{1}{\sigma^2} \sum_{m'=1}^M (d_{k,m'} - I_{k,m'}) i_{k,m'} \end{aligned} \quad (5.25)$$

where Eqs. 5.13 and 5.14 were used. The other elements of $\boldsymbol{\lambda}$ are

$$\frac{\partial l(\mathbf{g}, \mathbf{a}, \mathbf{r}|\mathbf{d})}{\partial A_m} = \frac{1}{\sigma^2} \sum_{k'=1}^K (d_{k',m} - I_{k',m}) G_{k'} \exp \left[-\frac{(k' - R_m)^2}{2w^2} \right] \quad (5.26)$$

and

$$\begin{aligned} \frac{\partial l(\mathbf{g}, \mathbf{a}, \mathbf{r}|\mathbf{d})}{\partial R_m} & \quad (5.27) \\ &= \frac{1}{\sigma^2} \sum_{k'=1}^K (d_{k',m} - I_{k',m}) G_{k'} A_m \frac{k' - R_m}{w^2} \exp \left[-\frac{(k' - R_m)^2}{2w^2} \right]. \end{aligned}$$

The first and second derivatives of $l(\mathbf{g}, \mathbf{a}, \mathbf{r}|\mathbf{d})$ are needed to evaluate the elements of $\boldsymbol{\Lambda}$. The diagonal elements of $\boldsymbol{\Lambda}$ are evaluated first, beginning with the gain terms. Using Eq. 5.11

$$\frac{\partial^2 l(\mathbf{g}, \mathbf{a}, \mathbf{r}|\mathbf{d})}{\partial G_k^2} = -\frac{1}{\sigma^2} \sum_{m'=1}^M i_{k,m'}^2. \quad (5.28)$$

The terms associated with the unknown signal amplitudes (the A_m 's) are

$$\frac{\partial^2 l(\mathbf{g}, \mathbf{a}, \mathbf{r}|\mathbf{d})}{\partial A_m^2} = -\frac{1}{\sigma^2} \sum_{k'=1}^K \left\{ G_{k'} \exp \left[-\frac{(k' - R_m)^2}{2w^2} \right] \right\}^2. \quad (5.29)$$

The range terms are

$$\begin{aligned} \frac{\partial^2 l(\mathbf{g}, \mathbf{a}, \mathbf{r}|\mathbf{d})}{\partial R_m^2} & \quad (5.30) \\ &= -\frac{1}{\sigma^2} \sum_{k'=1}^K (d_{k',m} - I_{k',m}) \frac{G_{k'} A_m}{w^2} \left[1 - \frac{(k' - R_m)^2}{w^2} \right] \exp \left[-\frac{(k' - R_m)^2}{2w^2} \right] \\ &\quad - \frac{1}{\sigma^2} \sum_{k'=1}^K \left\{ G_{k'} A_m \frac{k' - R_m}{w^2} \exp \left[-\frac{(k' - R_m)^2}{2w^2} \right] \right\}^2. \end{aligned}$$

Now the off-diagonal elements of $\mathbf{\Lambda}$ are calculated. Terms corresponding to derivatives to different gain values are zero.

$$\frac{\partial^2 l(\mathbf{g}, \mathbf{a}, \mathbf{r}|\mathbf{d})}{\partial G_k \partial G_l} = 0 \quad \text{when } k \neq l. \quad (5.31)$$

Several other off-diagonal elements of $\mathbf{\Lambda}$ are zero.

$$\frac{\partial^2 l(\mathbf{g}, \mathbf{a}, \mathbf{r}|\mathbf{d})}{\partial A_m \partial A_n} = \frac{\partial^2 l(\mathbf{g}, \mathbf{a}, \mathbf{r}|\mathbf{d})}{\partial R_m \partial R_n} = \frac{\partial^2 l(\mathbf{g}, \mathbf{a}, \mathbf{r}|\mathbf{d})}{\partial A_m \partial R_n} = 0 \quad \text{when } m \neq n. \quad (5.32)$$

However, terms derived using derivatives of gain and amplitude are not zero. These terms are

$$\frac{\partial^2 l(\mathbf{g}, \mathbf{a}, \mathbf{r}|\mathbf{d})}{\partial G_k \partial A_m} = \frac{1}{\sigma^2} (d_{k,m} - 2I_{k,m}) \exp \left[-\frac{(k - R_m)^2}{2w^2} \right]. \quad (5.33)$$

The gain and range terms are

$$\frac{\partial^2 l(\mathbf{g}, \mathbf{a}, \mathbf{r}|\mathbf{d})}{\partial G_k \partial R_m} = \frac{1}{\sigma^2} (d_{k,m} - 2I_{k,m}) A_m \frac{k - R_m}{w^2} \exp \left[-\frac{(k - R_m)^2}{2w^2} \right]. \quad (5.34)$$

The final terms from $\mathbf{\Lambda}$ are

$$\begin{aligned} & \frac{\partial^2 l(\mathbf{g}, \mathbf{a}, \mathbf{r}|\mathbf{d})}{\partial A_m \partial R_m} \\ &= \frac{1}{\sigma^2} \sum_{k'=1}^K (d_{k',m} - I_{k',m}) G_{k'} \frac{k' - R_m}{w^2} \exp \left[-\frac{(k' - R_m)^2}{2w^2} \right] \\ & \quad - \frac{1}{\sigma^2} \sum_{k'=1}^K A_m \frac{k' - R_m}{w^2} \left\{ G_{k'} \exp \left[-\frac{(k' - R_m)^2}{2w^2} \right] \right\}^2. \end{aligned} \quad (5.35)$$

All terms necessary to evaluate $\boldsymbol{\lambda}$ and $\mathbf{\Lambda}$ have been derived. The elements of $\boldsymbol{\lambda}$ are shown in Eqs. 5.25-5.27. The elements on the diagonal of $\mathbf{\Lambda}$ are found in Eqs. 5.28-5.30. The off-diagonal elements $\mathbf{\Lambda}$ are listed in Eqs. 5.31-5.35. In the next section, the Gauss-Newton iterative solution to the array signal model is tested via simulation.

5.2.3 Simulations. In this section, the Gauss-Newton iterative gain estimation process derived in Sec. 5.2.2 is tested using Monte Carlo simulations. The simulated signals are illustrated in Fig. 5.3. Four signals were generated ($M = 4$). Each of those signals had thirty-two samples ($K = 32$). The range and amplitudes of the signals were generated randomly. The range values, measured in samples, were between eight and twenty-four. The amplitude values were between ten and twenty.

The width of the Gaussian pulse was set at three samples ($w = 3$). This value was assumed to be known in the Gauss-Newton iteration. The bias level on each signal was generated randomly. The bias values were between five and ten. These values were assumed to be known for the iteration. In a real LADAR system, the background or bias level must be estimated. However, noise data is abundant and precise background level measurements are usually available.

The additive IID Gaussian noise in each sample had unit variance ($\sigma^2 = 1$). Knowledge of this value is not needed by the Gauss-Newton iteration. All elements of vector $\boldsymbol{\lambda}$ and $\mathbf{\Lambda}$ are inversely proportional to σ^2 . Therefore $\boldsymbol{\lambda}$ and $\mathbf{\Lambda}$ are also inversely proportional to σ^2 . The Gauss-Newton iteration (Eq. 5.7) contains the term $\mathbf{\Lambda}^{-1}\boldsymbol{\lambda}$. The variance in that term cancels since $\mathbf{\Lambda}^{-1}$ is proportional to σ^2 . Thus, the variance is not needed in the Gauss-Newton iteration equations.

A series of gain values, common to all four signals, was generated. The sequence of gain values in the Monte Carlo was a sinusoid with values between 0.8 and 1.2. The phase of this sinusoid was generated randomly and the frequency was selected so that there were about two complete oscillations over the thirty-two samples.

In Fig. 5.3a, the simulated signals before the gain is applied are illustrated by solid lines. The signals after the multiplicative gain values are applied are shown as broken lines. The signals before and after gain are related according to Eq. 5.1. There is also a random realization of simulated LADAR data in Fig. 5.3b. The signals with gain (broken lines) are shown for comparison. The unit variance additive noise is

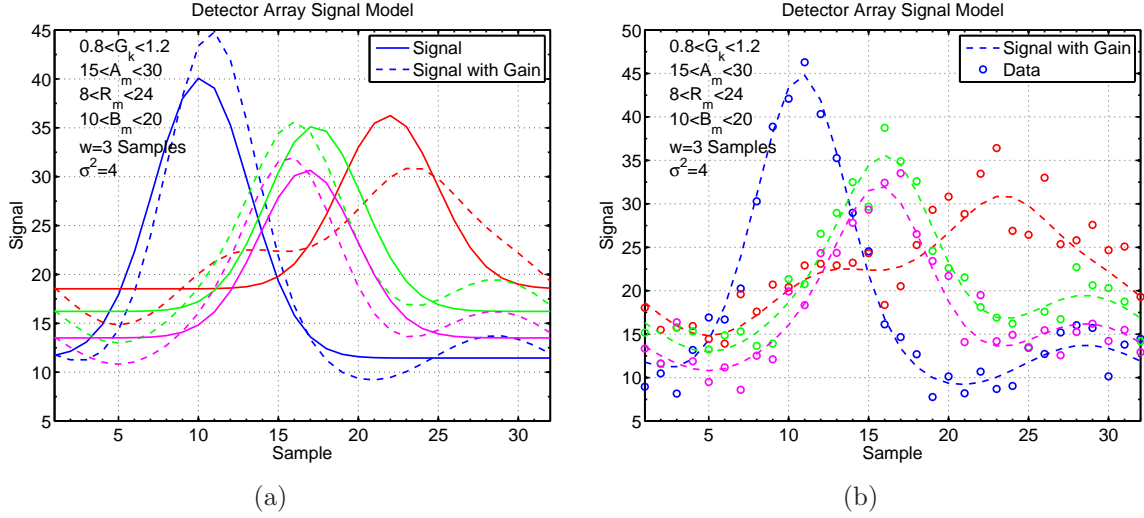


Figure 5.3: (a) Simulated signals before and after variable gain. (b) Noisy data with variance $\sigma^2 = 1$.

distributed according to Eq. 5.5. The noise is noticeable, but is not very powerful compared to the signal energy.

The simulated LADAR data shown in Fig. 5.3 was processed using the Gauss-Newton iteration from Eq. 5.7. That equation required an initial estimate of the unknown parameter vector $\hat{\theta}_0$. The actual order in which the gain, amplitude, and range estimates are arranged in θ is arbitrary. The convention adopted in this dissertation is to order the gain estimates first, then the amplitude estimates, and finally the range estimates.

The initial K gain estimates are all assumed to be one.

$$\left[\hat{\theta}_0 \right]_k = 1 \quad \forall \quad k. \quad (5.36)$$

The M initial amplitude estimates are determined from the data. These estimates are the peak value on each detector minus the known bias B_m on that detector.

$$\left[\hat{\theta}_0 \right]_{m+K} = \max_k \{ d_{k,m} - B_m : k = 1, 2, \dots, K \} \quad (5.37)$$

The initial range estimate, in samples, is the argument k corresponding to the maximum recorded value on the m -th detector.

$$\left[\hat{\theta}_0\right]_{m+2K} = \arg \max_R \{d_{k,m} : k = 1, 2, \dots, K\}. \quad (5.38)$$

The initial estimates from Eqs. 5.36, 5.37, and 5.38 are used to initialize the Gauss-Newton iteration. Those initial estimates are also needed to evaluate λ and Λ in the Gauss-Newton iteration. The initial iteration is

$$\hat{\theta}_1 = \hat{\theta}_0 - \left[\Lambda(\hat{\theta}_0)\right]^{-1} \lambda(\hat{\theta}_0). \quad (5.39)$$

After this initial calculation is made, the process is repeated using Eq. 5.7. In theory, this Gauss-Newton iteration always converges. However, it is possible for it to converge to a local maximum rather than the desired global maximum of the likelihood function. In practice, numeric errors in the calculations can make the iteration unstable. In that case, the parameter estimates may fail to converge to finite values.

It is straightforward to tell when the iteration is not converging. In that case, the magnitudes of at least some of the estimates approach infinity. Also, the condition number of matrix Λ becomes very large. The condition number is defined to be the ratio of the largest to the smallest singular value of a matrix [18]. If the Gauss-Newton iteration does not converge it can be tried again using different initial estimates. In a LADAR system with multiple detectors, it is also possible to omit data from certain detectors when implementing the iteration. It is possible that omitting data from some detectors could cause the iteration to converge even though it did not when data from all detectors was used.

Using the simulated LADAR data shown in Fig. 5.3, the Gauss-Newton derived in Sec. 5.2.2 iteration was tested. The initial estimate of θ was calculated using Eqs. 5.36, 5.37, and 5.38. Twenty iterations of the algorithm were computed. The

amplitude and range estimates for each of the four simulated detectors are shown in Fig. 5.4.

Range estimation was straightforward since the initial estimates were precise. All initial estimates were within two samples of the true value (see Fig. 5.4a). The algorithm converged to stable and precise range estimates with a few steps. Amplitude estimation was more challenging because of the unknown gain values in the simulated LADAR data. Initial amplitude estimates were off by over one-quarter of the true value. However, after about ten steps, the Gauss-Newton iteration converged to stable and relatively precise estimates of the true amplitude values (see Fig. 5.4b).

The iteration also yielded estimates of the unknown gain values in the simulated LADAR data. The final gain estimates after twenty iterations of the Gauss-Newton algorithm are shown in Fig. 5.5a. Most of the estimates are within ten percent of the true gain value even though only four detectors were simulated. If there had been data from more than four detectors, then these gain estimates would have been even more precise.

Using the final estimates of gain, amplitude, and range, the original LADAR signals can be estimated. These estimates are plotted in Fig. 5.5b. The true signals are shown for comparison. There is good agreement between the true signals and the estimated signals that are defined by the output parameter estimates from the Gauss-Newton iteration.

5.2.4 Gain Estimation with LADAR Data. The Gauss-Newton iteration derived in Sec. 5.2.2 was tested on LADAR data collected by the ASC camera. Data from the target panel shown in Fig. 5.1 was used. The algorithm was seeded using the initialization equations from Sec. 5.2.3.

The Gauss-Newton iteration was tested on many different combinations of pixels from the target panel. The performance of the algorithm using real LADAR data was bad. In the vast majority of cases, the iteration diverged immediately. In those cases, estimates of range, amplitude, and gain immediately trended toward unreasonable

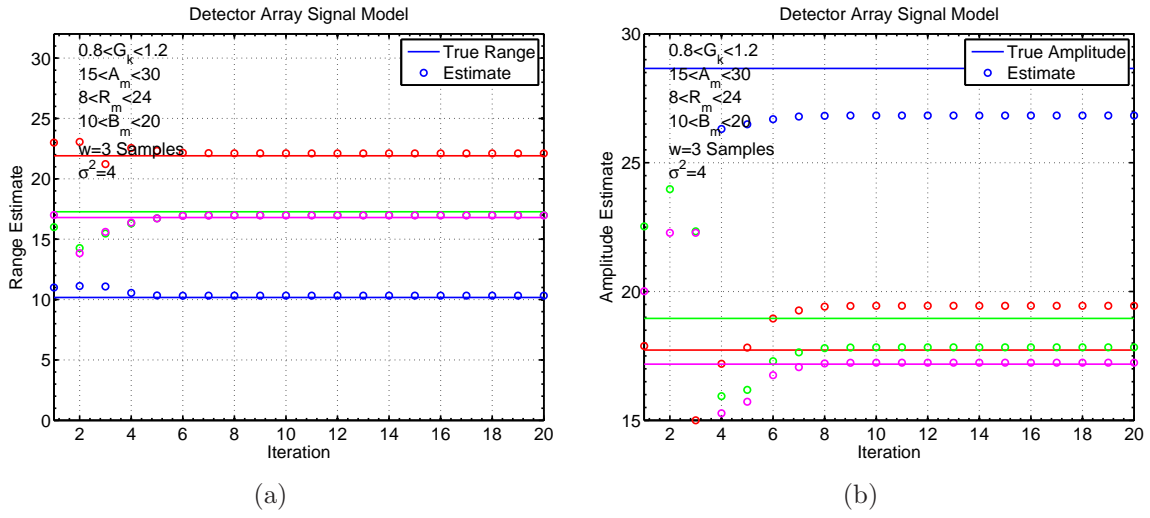


Figure 5.4: (a) Iterative estimation of the unknown range values. (b) Iterative estimation of the unknown amplitude values.

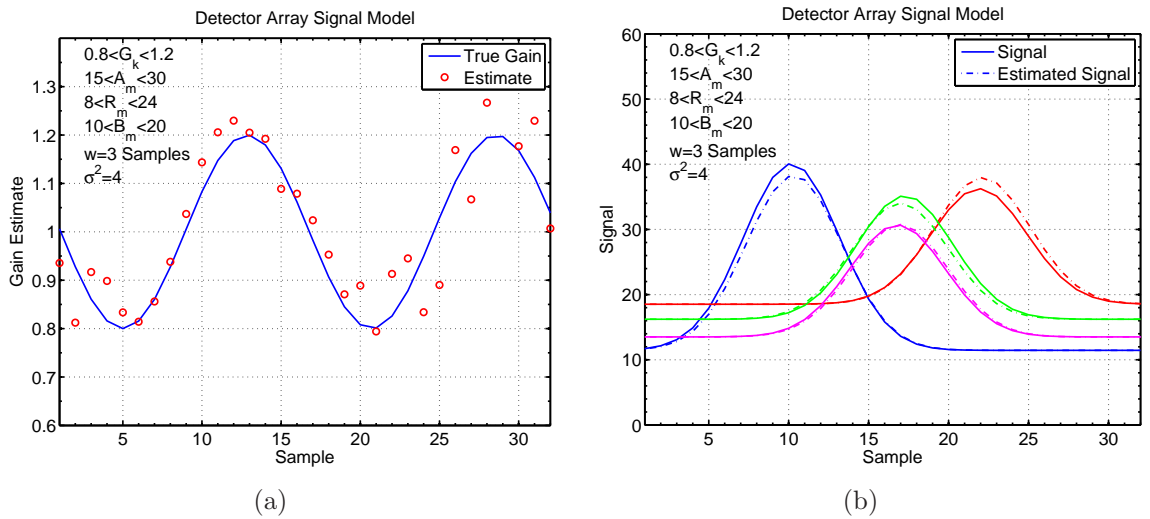


Figure 5.5: (a) Estimation of unknown gain values. (b) Estimated signals.

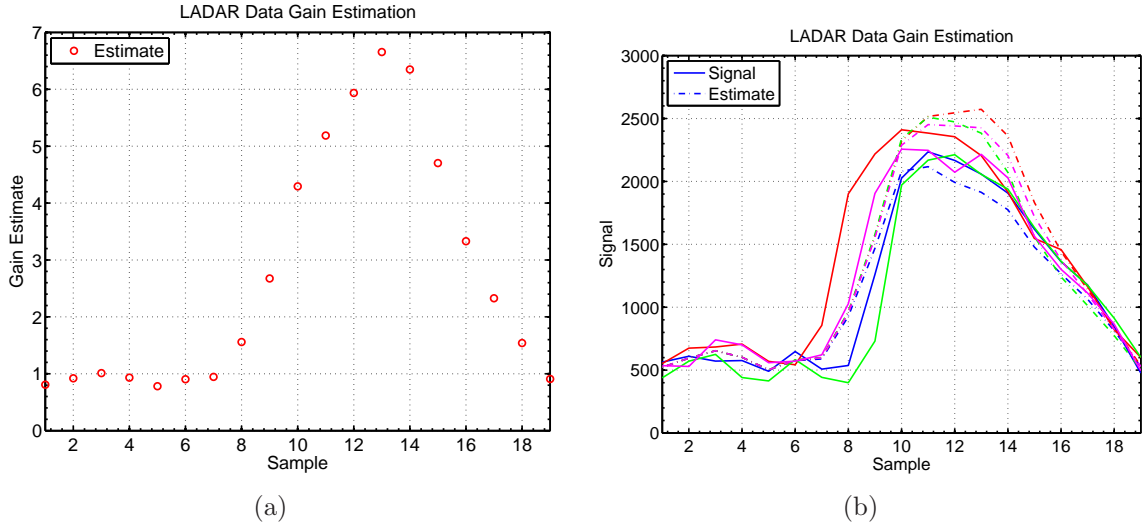


Figure 5.6: (a) Gain estimates after ten iterations.(b) Signal estimates.

values. When the iteration diverged, the condition number of $\mathbf{\Lambda}$ became very large within a few steps and that matrix became impossible to accurately invert.

In some tests of the Gauss-Newton iteration, the gain estimates started to look similar to the shape of the range-resolved LADAR data. One of these cases is illustrated in Fig. 5.6a. The four pixels of LADAR data used in this case are shown in Fig. 5.6b. The algorithm was allowed to iterate ten times. The gain estimates corresponding to background (noise) data were approximately one. However, the gain estimates when laser pulses were present in the data were several times greater than one and took on the shape of the pulses. In this case, the modeled LADAR signals using the algorithm's estimates were reasonably accurate. However, the modeled signals did not accurately capture the range variations in the signals. The closest and farthest LADAR signals are about two samples apart. But the range estimates provided by the Gauss-Newton iteration are all within a fraction of a sample.

Inspection of the range and amplitude values during iteration shows a problem in the process. The iteration consistently drove the signal amplitude estimates toward zero (see Fig. 5.7b). In some cases, the amplitude estimates took negative values. Negative amplitudes are physically meaningless. As illustrated in Fig. 5.6, the Gauss-

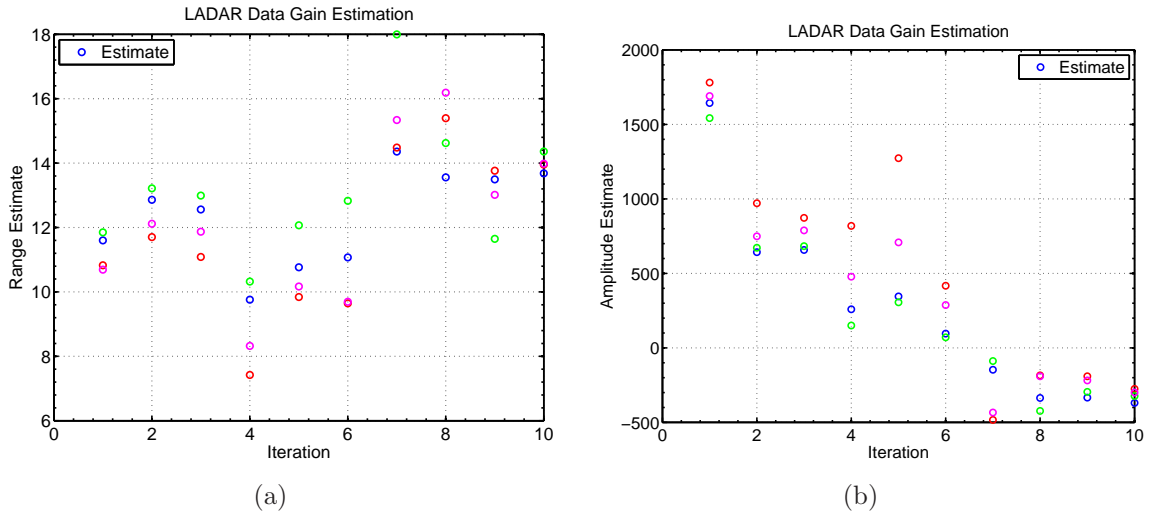


Figure 5.7: (a) Iterative estimation of the unknown range values.
(b) Iterative estimation of the unknown amplitude values.

Newton iteration preferred to model the laser pulses using the gain values rather than the Gaussian pulse shape embedded in the signal model. As the amplitude values dropped, the range estimates became unstable. The range estimates started to vary quickly between steps of the iteration. Eventually, the range estimates always moved outside the range of meaningful values and the condition number of $\mathbf{\Lambda}$ became very large.

The Gauss-Newton iteration for gain estimation was tested on many thousands of combinations of pixels of LADAR data. The gain estimates should have observed a drop over time. This drop in gain is obvious in the background data shown in Fig. 5.2. However, good algorithm performance was never observed. The algorithm occasionally modeled the LADAR signals accurately. However, that only happened when the iteration used the gain values to approximate the pulse shape. The Gauss-Newton iteration algorithm never successfully measured the gain variation in the LADAR data.

5.3 Gain Equalization using Background Data

In this section, a second method of gain estimation is proposed and tested. This method uses data from target-free (background light and electronic noise only) pixels to observe the gain variation. The observed variation in APD gain is used to equalize LADAR data that has targets. It is shown that this method improves the precision of range estimates made with the LADAR system.

A modification of the photocurrent from Eq. 4.51 is used in this section. The modified version includes a term for the background or noise power observed. It is assumed that the background power is constant in the signal. The photocurrent is related to the received optical power by

$$i(t) = \frac{Gq\eta}{h\nu} [P_r(t) + P_b] \quad (5.40)$$

where G is the detector's gain, q is the charge of an electron, η is the detector's quantum efficiency, h is Planck's constant, and ν is the laser's optical frequency. The term P_b is the power from background light in the scene and other noise sources in the system. This power level is measured before amplification (gain). Background power is assumed constant and is amplified in the same way that the received laser signal power is increased.

Ideally, the gain of the detector would be constant. However, it has been shown in this dissertation and in [37] that gain fluctuates in APD arrays. Gain variation distorts the shape of received laser pulses. In imaging LADAR systems using focal planes, the gain variations can affect the entire array. Background light is amplified by APDs in the same way that received laser signals are. Because the entire array is affected by the gain variation, it is possible for pixels with no target present to appear as though they have observed one because the signal level is fluctuating.

A relatively simple gain equalization algorithm is proposed and tested. This algorithm uses data from target-free pixels to estimate the avalanche photodiode gain over time. It is shown that the equalization algorithm can decrease range error in

LADAR data. It is possible that this method could be applied to design of APD arrays. A single or a few pixels could be isolated and used for measurement of gain variation. That data would be available to the ROIC for gain equalization.

5.3.1 Gain Variation in Flash LADAR Data. The same LADAR data that was shown in Sec. 5.1 and processed in Sec. 5.2.4 is used in this section. All of the three-dimensional LADAR images are of a large target panel that was supported manually. In image of the panel is shown in Fig. 5.1 and examples of range resolved LADAR signals are shown in Fig. 5.8.

The data displayed in Fig. 5.8a is from a three-dimensional LADAR image where the target panel was tilted -20 degrees with respect to the LOS. The tilt angle was defined so that a negative tilt corresponded to the top of the target moving toward the LADAR. Thus, a positive tilt implies that the panel's top has moved away from the sensor. In the case shown in Fig. 5.8a, the target panel was oriented perpendicular to the ground. Because the LADAR viewed the panel from a tower, the top of the panel is the part that is closest to the system. Range resolved signals are shown in Fig. 5.8a. As the row number of these signals increases, the leading edge of the recorded laser pulses moves to the right. The trailing edge is also shifted to the right with increasing row number. However, the trailing edge does not shift as quickly as the leading edge does.

The leading edges of pulses reflected off of the top and bottom of the target panel are separated by about 2.5 samples. However, the trailing edges are only separated by about 1.5 samples. The received laser pulses should have the same shape. However, the gain on those pulses from the avalanche photodiode array varies over time. Thus, the width of the recorded signals decreases as the target range increases.

In Fig. 5.8b, the panel was tilted so that its bottom is the part closest to the LADAR. In this case, the signals shift to the left as the row number increases. The tilt was 32 degrees. Because of the target panel tilt, the leading edges of the

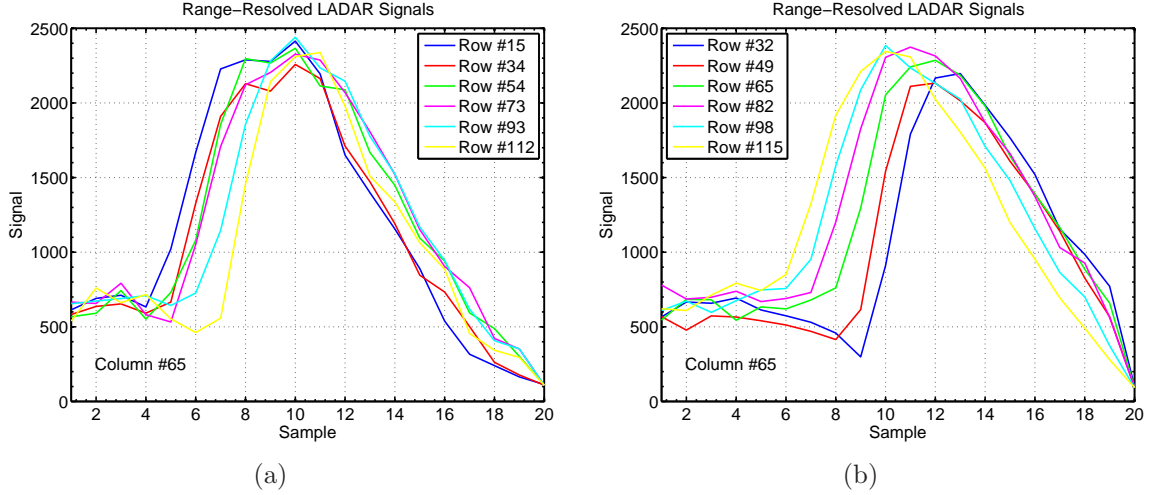


Figure 5.8: (a) Target panel tilt is -20 degrees. (b) Target panel tilt is 32 degrees.

recorded pulses are separated by about 3.5 samples. However, the trailing edges are only separated by about 2 samples.

Inspection of the data displayed in Figs. 5.8a and 5.8b shows that the LADAR signals recorded by the APD array are distorted in a predictable manner. The signals in pixels closest to the LADAR are have the longest duration. Signals recorded in pixels farther from the LADAR are narrower regardless of the orientation of the panel with respect to the system. The cause of the distortion in laser pulse shape is gain variation in the array of APDs.

5.3.2 Gain Variation Equalization. It is hypothesized that the gain of the entire avalanche photodiode array drops when laser signals are detected. The relationship between background photocurrent level $i_b(t)$ and gain is given by Eq. 5.40 with signal power $P_r(t) = 0$.

$$i_b(t) = \frac{Gq\eta}{h\nu} P_b. \quad (5.41)$$

Data from target-free pixels is shown in Fig. 5.9. There is significant fluctuation in the background data. Thus, it is averaged over 108 frames and over multiple (thirty)

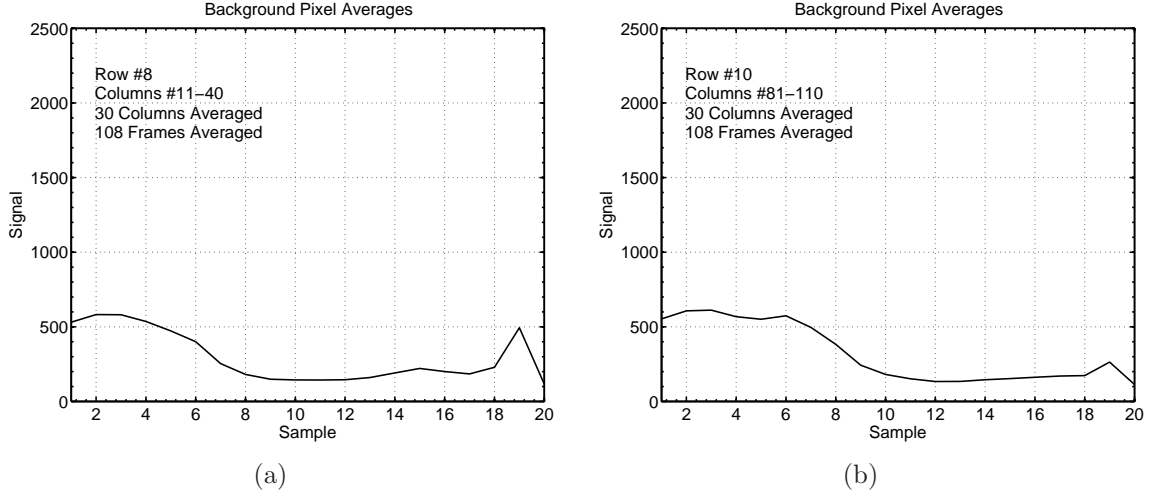


Figure 5.9: (a) Background data with panel tilted -20 degrees. (b) Background data with panel tilted 32 degrees.

pixels. The background signal level is steady for the first six samples. After that, the background level drops by a factor of more than two. This drop in gain occurs at the point where the target panel is located (see Fig. 5.8).

Averaged background data is used to estimate the time-varying gain. The gain estimate \hat{G} , which is written here as a function of time, is calculated using Eq. 5.41.

$$\hat{G}(t) \propto \overline{i_B(t)} \quad (5.42)$$

where $\overline{i_B(t)}$ is the average of background signals. This estimate of the gain is used to correct the variation in the LADAR signals shown in Fig. 5.8. The data from those plots, divided by the average background (that is, $i(t)/\overline{i_B(t)}$) is shown in Fig. 5.10.

The equalized data in Fig. 5.10a is from images with the panel tilted at -20 degrees (the raw data is shown in Fig. 5.8a). Gain equalization removed most of the width variation in the pulses. However, the trailing edge of the row 112 pulse is out of position compared to the pulses from rows 54, 73, and 93. But overall, the gain equalization process has improved the quality of the data in spite of the row 112 outlier.

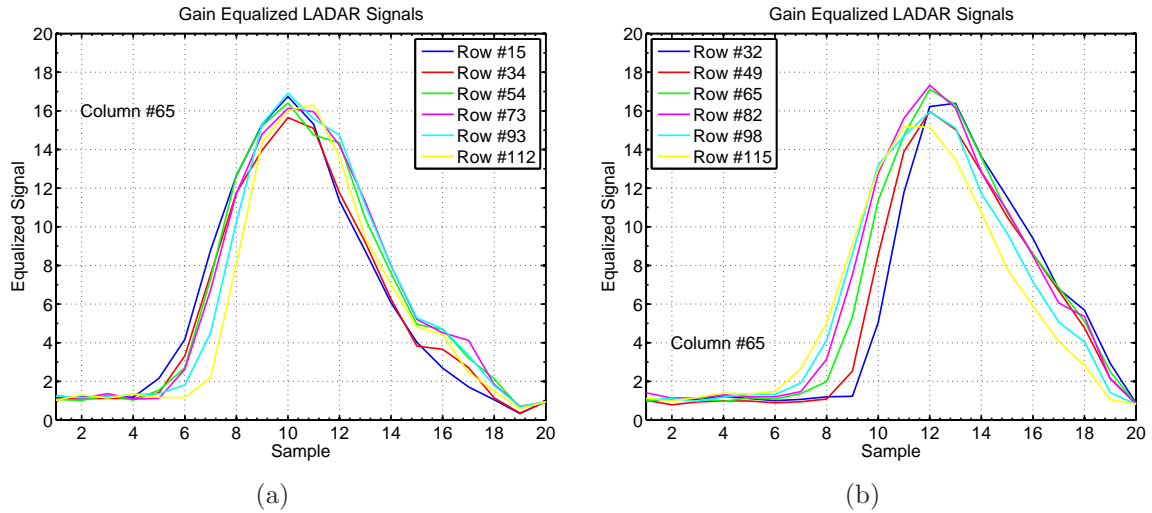


Figure 5.10: (a) Target panel tilt is -20 degrees. (b) Target panel tilt is 32 degrees.

In Fig. 5.10b, the data from panel tilted 32 degrees from LOS is shown after equalization. (The raw data is shown in Fig. 5.8b.) In this case, equalization worked very well. The gain equalized laser pulses all have the same width regardless of their position on the panel. Equivalently, the pulse width no longer depends on the range to the target.

5.3.3 Range Measurements. In this section, raw and equalized LADAR signals are used to make measurements of range to the target panel. The range estimates were calculated by computing a threshold crossing. Specifically, the point where the leading edge of the pulse is one-half the maximum height of the pulse is considered to be the target range. The range estimate was determined using a linear fit to the pulse's leading edge. The fit used the points that were just above and below the threshold.

The range estimation algorithm is illustrated in Fig. 5.11. The peak value of the signal is located and a parabolic fit (shown in red) is calculated to the points around the peak. For range estimation, the threshold is set at one-half of the peak fit value

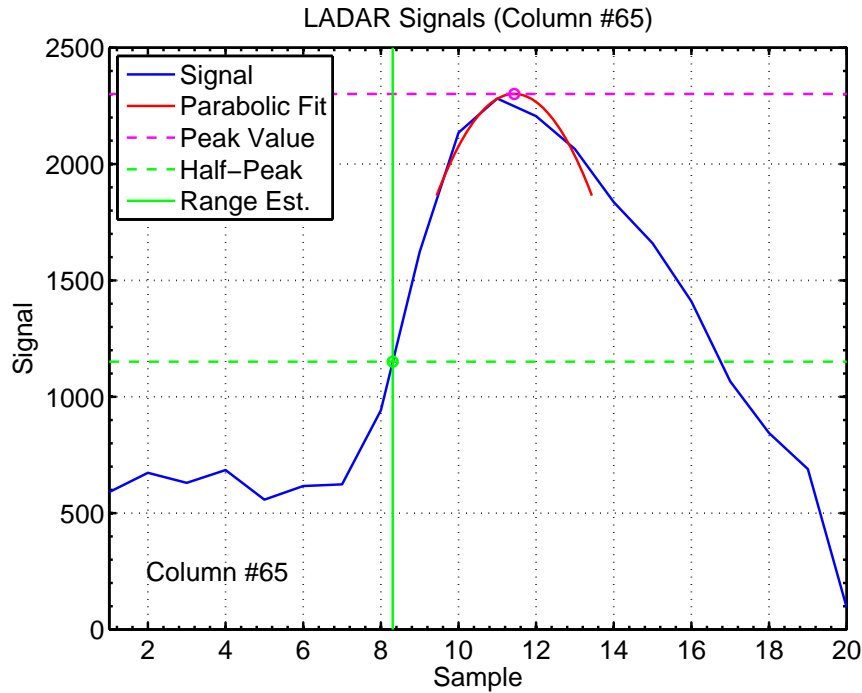


Figure 5.11: Illustration of range estimation algorithm.

(shown as a broken green line). The range estimate is the location where the data first crosses the threshold (shown as a solid green line).

It is common to use a matched filter when processing range-resolved data. However, the use of matched filters assumes that the shape of the received pulse is known. Matched filters also assume that the background level is not changing. The gain variation is obviously distorting the pulse shape, making the use of a true matched filter impossible.

It has also been shown that three-dimensional imaging LADARs with short range sampling intervals such as this one sometimes fail to sample the received signal completely [4]. The pulses shown in Fig. 5.8 take up most of the range record. If the trigger had been off by a few nanoseconds, these pulses would not have been sampled completely. When the pulse is sampled incompletely, correlation-based operations such as matched filtering do not function as intended.

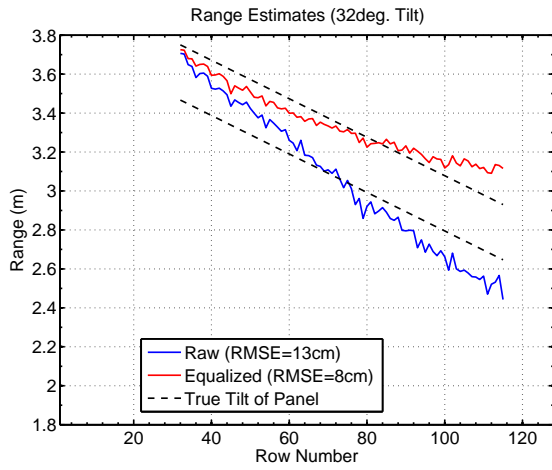
Because of the gain variation, the distortion of the received laser pulses, and the fact that pulses are sometimes sampled incompletely, an alternative to matched filtering is desired. The threshold crossing technique described earlier and illustrated in Fig. 5.11 is an acceptable alternative to the matched filter for this LADAR data set. It is simple and performs well at range estimation.

The first range estimation result is shown in Fig. 5.12a. This data was collected when the panel was tilted 32 degrees from the LADAR LOS. Examples of the raw and equalized data used in these range calculations are shown in Figs. 5.8b and 5.10b, respectively.

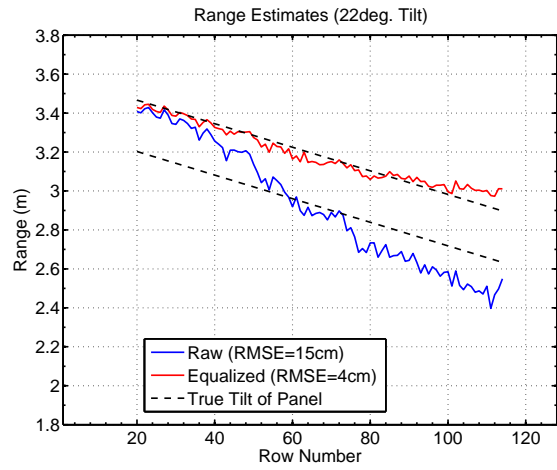
The raw range data in Fig. 5.12a does not match the true tilt of the target panel. The 155 cm high panel, when tilted 32 degrees, has a depth of 82 cm. However, the gain variation makes the target depth, as measured before equalization (shown in blue), appear to be about 1.2 m. The range estimates made with the equalized data (shown in red in Fig. 5.12a) do not match the target panel's tilt exactly. However, they are much more precise than the raw range measurements. The root mean squared error (RMSE) for the gain equalized range estimates was 8 cm. The RMSE for the raw data was 13 cm.

In Fig. 5.12b, the target panel was tilted 22 degrees from LADAR LOS. In this case, gain variation in the raw data still causes a dramatic overestimate of the panel's tilt. The RMSE is 15 cm. The equalized data matched the slope of the panel almost exactly. The gain equalized range measurements have an RMSE of only 4 cm. This error is mostly due to noise in the laser signals themselves rather than gain variation distortions.

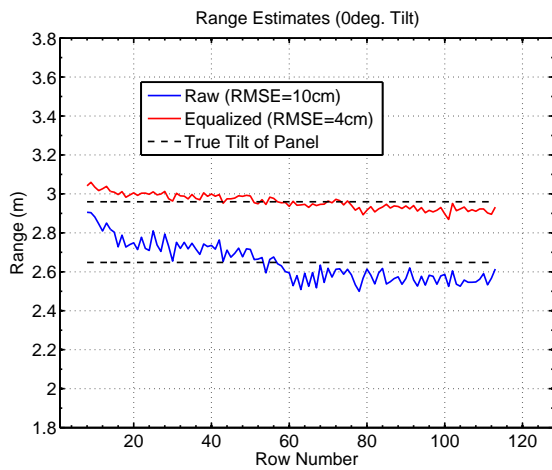
In Fig. 5.12c, the target panel was oriented perpendicular to the LADAR's line-of-sight. The range error for the raw data was 10 cm. However, when the gain equalized data was processed, the RMSE dropped to 4 cm. Because the target is at basically the same range in all target pixels, the laser pulse distortion due to gain variation should be roughly equal on all signals. However, there is still more



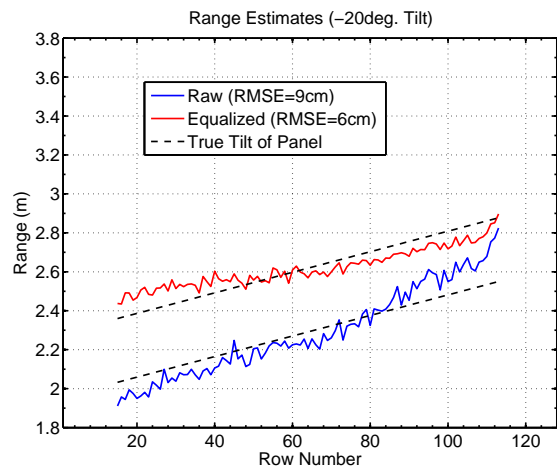
(a)



(b)



(c)



(d)

Figure 5.12: (a) Target panel tilt is 32 degrees. (b) Target panel tilt is 22 degrees. (c) Target panel tilt is 0 degrees. (d) Target panel tilt is -20 degrees.

Table 5.1: Range Error in APD Array LADAR Data.

Panel Tilt	Raw Data RMSE	Equalized Data RMSE
-20 deg.	9 cm	6 cm
0 deg.	10 cm	4 cm
9 deg.	14 cm	3 cm
15 deg.	15 cm	2 cm
22 deg.	15 cm	4 cm
27 deg.	14 cm	6 cm
32 deg.	13 cm	8 cm

fluctuation in the range estimates made with the raw data than with the equalized data.

The final example of range estimation is illustrated in Fig. 5.12d. In this case the target panel is -20 degrees from LOS. Raw and gain equalized data for this test are illustrated in Figs. 5.8a and 5.10a. The sign change of the panel tilt causes the range errors to occur opposite of how they appear in Figs. 5.12a-c where the tilt angle was nonnegative. However, the gain variation technique still helped. For range estimates made with raw data, the RMSE is 9 cm. Using gain equalization, the range error drops to 6 cm.

The range RMSEs for the entire data collection are listed in Table 5.1. For target panel tilt angles between 0 and 27 degrees, the raw data RMSE is at least double the RMSE for range measurements made with the equalized data. For the large magnitude tilt angles of -20 and 32 degrees, the raw data range RMSE is higher than for the equalized data, but only by about 50%. Thus, there appears to be a limit on the amount target tilt that the gain equalization algorithm can tolerate before its performance degrades significantly.

5.4 *Chapter Summary*

Avalanche photodiodes are used in LADAR systems to detect laser light reflected from targets. Arrays of APDs can be very dense and compact, but can be challenging to work with because of variations in the relationship between their input and output signals. In Sec. 5.1, LADAR images collected by a system using an APD array as a photodetector were shown. The effect of gain variation on the recorded signals was illustrated in that section.

In Secs. 5.2 and 5.3, methods of gain equalization were proposed and tested. In Sec. 5.2 a multidimensional Gauss-Newton method was used successfully on simulated LADAR data. However, this technique did not work well on real LADAR data. In Sec. 5.3, an equalization method that used target-free pixels was successfully demonstrated. Through the use of a target panel in LADAR images, it was shown that gain variation could introduce significant bias into range measurements. The gain equalization method tested in Sec. 5.3 decreased, but did not eliminate, the range bias in the three-dimensional LADAR images.

VI. Conclusion

All of the research in this dissertation applies to the problem of making measurements of range to a target using a LADAR system. However, range measurements are affected by many different factors. Noise models, signal shapes, and detector electronics all influence the precision of LADAR range estimates. Thus, a wide variety of subjects were discussed in the dissertation.

6.1 Poisson-Distributed LADAR Signal Models

In Chapter III, three different LADAR signal models were examined. These models are all variations of work previously published in [4]. That paper assumes that laser pulses received by LADAR systems can be modeled as a truncated parabola plus a background noise level. It is also assumed that the LADAR system is shot-noise limited, which means that the signal and noise follow the Poisson distribution.

In Sec. 3.1, the laser pulse model from [4] was revisited. The Cramer-Rao lower bounds for range and other signal parameters derived in that paper were expressed in terms of summations. In this dissertation, analytic approximations to those summations were derived.

LADAR systems are sometimes used to image targets beneath tree canopies. In Sec. 3.2, the signal model is generalized to include two signal pulses. The first signal represents the tree canopy and the second is the target on the ground. CRLBs were derived for this model. It was shown that the presence of obscuration did not affect the range CRLB for the obscured target.

Some targets observed by LADAR systems are extended. That is, their depth is significant compared to the length of the transmitted laser pulse. In this case, the reflection process varies the length of the received pulse. It had been assumed that the pulse width in the received signal was known. But in Sec. 3.3, the width was treated as an unknown for the purpose of CRLB derivations in order to model variations in target depth. It was shown that the range CRLB is the same regardless of whether

the pulse width was known or unknown. However, the CRLB is still dependent on the pulse width in this case.

It was shown in Chapter III that the Poisson noise model used to simulated shot-noise limited signals made calculation of maximum likelihood estimates difficult. However, in most cases it was straightforward to create a relatively simple, though suboptimal estimator which nearly achieved the CRLB. This fact was verified through the use of Monte Carlo simulations.

6.2 Range Precision of LADAR Systems

Chapter IV of this dissertation focused on the topic of the precision of LADAR range measurements. Some of the work in this chapter used the Poisson-distributed signal models developed in Chapter III. Other analysis relied on signal models that assumed additive white Gaussian, rather than Poisson noise. The use of laser pulse shapes other than the truncated parabola was also discussed.

In Sec. 4.1, the range CRLB derived in Chapter III was discussed. The range CRLB for a truncated parabolic pulse mixed with Gaussian rather than Poisson noise was derived. It was shown that the Gaussian-noise CRLB is always less than the Poisson-noise CRLB. Thus, range measurements are more precise in the presence of Gaussian noise than when the signal is mixed with shot (Poisson) noise.

The topic of pulse averaging was also discussed in Sec. 4.1. It was also shown that for a system that can divide a fixed amount of laser energy into multiple pulses, that that range precision of a shot-noise limited system is maximized when all energy is transmitted in a single pulse. That is, averaging decreases range precision unless the total amount of pulse energy is increased.

In Sec. 4.2, it was noted that some LADAR systems operate at ranges of several kilometers. Airborne systems in particular tend to operate at long ranges. Airborne LADAR system often observe a scene from an oblique angle. Unless a target is oriented normal to the LADAR line-of-sight, the laser pulse reflection process will

distort the shape of the received laser signal. It was shown that if a nanosecond-class duration beam that is a few inches in diameter at the transmitter propagates more than a few kilometers, the effect of target orientation on range precision can not be neglected.

In Sec. 4.2, the shape of the received laser signal was derived as a function of target surface orientation and other system parameters. The CRLB was calculated as a function of target tilt. The effect of mitigation strategies such as increasing the transmitted beam size and decreasing the pulse duration was studied and the limitations of those method were quantified. This analysis assumed a laser pulse with a Gaussian shape and a received signal mixed with AWGN.

6.3 Gain Variation in APD Arrays

The topic of gain variation was studied in Chapter VI. Compact avalanche photodiode arrays are being used to create three-dimensional LADAR images with large numbers of pixels. Ideally, the amount of amplification, or gain, in an APD would be constant. However, it has been shown in this dissertation and elsewhere than gain in APD arrays varies over time. Gain variation distorts the recorded laser signals and introduces bias into measurements of target range.

In the course of this dissertation research, a LADAR data collection experiment was done to examine the effect of gain variation (see Sec. 5.1). Three-dimensional images were collected using an Air Force Research Laboratory LADAR system. The images were of a large target panel. The panel was tilted at various orientations with respect to the LADAR line-of-sight. Examination of the effect of target tilt clearly illustrated the effect of gain variation on range-resolved LADAR data. It was shown that gain variation introduced bias into range measurements.

Gain variation degraded the ability of LADAR systems to make range measurements. Therefore, a method of gain equalization that corrects for variations in the

array of APDs was desired. In this dissertation, two methods of gain equalization were proposed and tested.

The first method of gain equalization was developed in Sec. 5.2. This method was based on the Gauss-Newton method of parameter estimation. A model was developed for range-resolved LADAR signals observed by an array of avalanche photodiodes in the presence of gain variation. This model assumed Gaussian-shaped laser pulses and white Gaussian noise. The method was tested successfully on simulated data. However, the Gauss-Newton method did not work well with real LADAR data collected from the target panel. This relatively sophisticated approach relied on too many assumptions, such as exact knowledge of the shape of the signals embedded in the noisy data.

The second method of gain equalization was derived and tested in Sec. 5.3. This method used averaged signals from target-free pixels to measure the change in gain over time in the APD array. This background-averaging method was tested using data collected from the target panel tilt tests. It was shown that the gain equalization method based on background data reduced, though did not eliminate, the bias in the range measurements to the target panel. Though this method did not eliminate the problems introduced by gain variation in APD arrays, it had the advantage of being quite simple. This method could potentially be implemented in near real-time in a LADAR receiver's ROIC.

6.4 Summary

Measurement of range to a target is one of the most fundamental problems in the field of remote sensing. Short duration laser pulses make LADAR systems ideal instruments for precise range measurement. This dissertation discussed limits on range precision of LADAR measurements due to stochastic noise sources, the laser pulse reflection process, and characteristics of current photodetectors. The work can be used to model the performance of current LADARs and could help design future LADAR systems.

Appendix A. Photoelectron Statistics

Much of the analysis in this dissertation relies on the Poisson approximation. That is, it is frequently assumed that probability distribution describing number of photoelectrons observed in an imaging LADAR has a Poisson distribution. In this appendix, the origin of and justification for this assumption is discussed. Some of the derivations used in the Poisson approximation are reviewed.

A.1 Integration of Intensity

One of the early references on photon statistics is “*Some Effects of Target-Induced Scintillation on Optical Radar Performance*” by Goodman [11]. That paper notes that the total energy W incident on an optical system’s receiving aperture is

$$W = \int_{-\infty}^{\infty} \int_{-\infty}^{\infty} A_r(x, y)w(x, y)dxdy \quad (\text{A.1})$$

where x and y are the aperture coordinates, $w(x, y)$ is the energy density in the aperture plane, and $A_r(x, y)$ is the binary receiver aperture function. For a circular aperture with diameter D_a , this function is

$$A_r(x, y) = \begin{cases} 1 & \text{when } \sqrt{x^2 + y^2} \leq D_a/2 \\ 0 & \text{when } \sqrt{x^2 + y^2} > D_a/2 \end{cases} . \quad (\text{A.2})$$

Using results from earlier works [33, 34] Goodman notes in Eq. 15 of [11] that the total energy is approximately a gamma random variable. Therefore, the PDF of W is

$$p(W) = \begin{cases} \frac{1}{\Gamma(\mathcal{M})} a^{\mathcal{M}} W^{\mathcal{M}-1} e^{-aW} & \text{when } W > 0 \\ 0 & \text{when } W \leq 0 \end{cases} \quad (\text{A.3})$$

where a and \mathcal{M} are related so that the mean energy, which is denoted \bar{W} , is

$$\bar{W} = \frac{\mathcal{M}}{a}. \quad (\text{A.4})$$

The variance of the energy is

$$\overline{W^2} - \bar{W}^2 = \frac{\mathcal{M}}{a^2}. \quad (\text{A.5})$$

Goodman shows that

$$a = \frac{\mathcal{M}}{\bar{W}} \quad (\text{A.6})$$

and that \mathcal{M} is the diversity or the number of spatial correlation cells subtended by the aperture.

The second moment of the energy can be evaluated by integrating the autocorrelation of the energy density function

$$\overline{W^2} = \int_{-\infty}^{\infty} \int_{-\infty}^{\infty} \int_{-\infty}^{\infty} \int_{-\infty}^{\infty} A_r(x_1, y_1) A_r(x_2, y_2) R_w(x_1, y_1; x_2, y_2) dx_1 dy_1 dx_2 dy_2. \quad (\text{A.7})$$

This integral requires the energy density autocorrelation $R_w(x_1, y_1; x_2, y_2)$, which is (Eq. 12 of [11])

$$R_w(x_1, y_1; x_2, y_2) = E[w(x_1, y_1)w(x_2, y_2)]. \quad (\text{A.8})$$

The diversity parameter is (Eq. 18 of [11])

$$\mathcal{M} = \frac{A_r^2}{\int_{-\infty}^{\infty} \int_{-\infty}^{\infty} \int_{-\infty}^{\infty} \int_{-\infty}^{\infty} A_r(x_1, y_1) A_r(x_2, y_2) |\gamma(x_1, y_1; x_2, y_2)|^2 dx_1 dy_1 dx_2 dy_2} \quad (\text{A.9})$$

where $\gamma(x_1, y_1; x_2, y_2)$ is the complex degree of coherence (see Eq. 5.2-11 of [12]).

A.2 Photon Arrival Statistics

It is assumed that arrival of photons is a Poisson process [25]. Given incident energy W , the distribution of the number of photons arriving in some time interval

is a Poisson random variable.

$$\begin{aligned}
 p(k|W) &= \frac{1}{k!} \bar{N}^k e^{-\bar{N}} \\
 &\text{where} \\
 &k = 0, 1, 2, \dots
 \end{aligned}
 \tag{A.10}$$

where k is the number of photons arriving and \bar{N} is the average number of photons observed. The mean and the energy W are related by

$$\bar{N} = \frac{W}{h\nu}.
 \tag{A.11}$$

In the above equation, h is Planck's constant and ν is the optical frequency.

The distribution of photons arriving conditioned on the energy is given by Eq. A.10. However, the energy W is itself an random variable. The joint distribution of k and W is just the product of the energy density from Eq. A.3 and the conditional density from Eq. A.10. The joint density is

$$\begin{aligned}
 p(k, W) &= p(k|W)P(W) \\
 &= \frac{1}{k!} \bar{N}^k e^{-\bar{N}} \frac{1}{\Gamma(\mathcal{M})} a^{\mathcal{M}} W^{\mathcal{M}-1} e^{-aW}.
 \end{aligned}
 \tag{A.12}$$

The marginal density of k is obtained by integrating over joint density $p(k, W)$.

$$p(k) = \int_0^{\infty} p(k, W) dW.
 \tag{A.13}$$

It was shown in Eqs. 28-30 of [11] that this is

$$\begin{aligned}
 p(k) &= \frac{\Gamma(k+\mathcal{M})}{k!\Gamma(\mathcal{M})} \left(1 + \frac{\mathcal{M}}{\bar{N}}\right)^{-k} \left(1 + \frac{\bar{N}}{\mathcal{M}}\right)^{-\mathcal{M}} \\
 &\text{where} \\
 &k = 0, 1, 2, \dots
 \end{aligned}
 \tag{A.14}$$

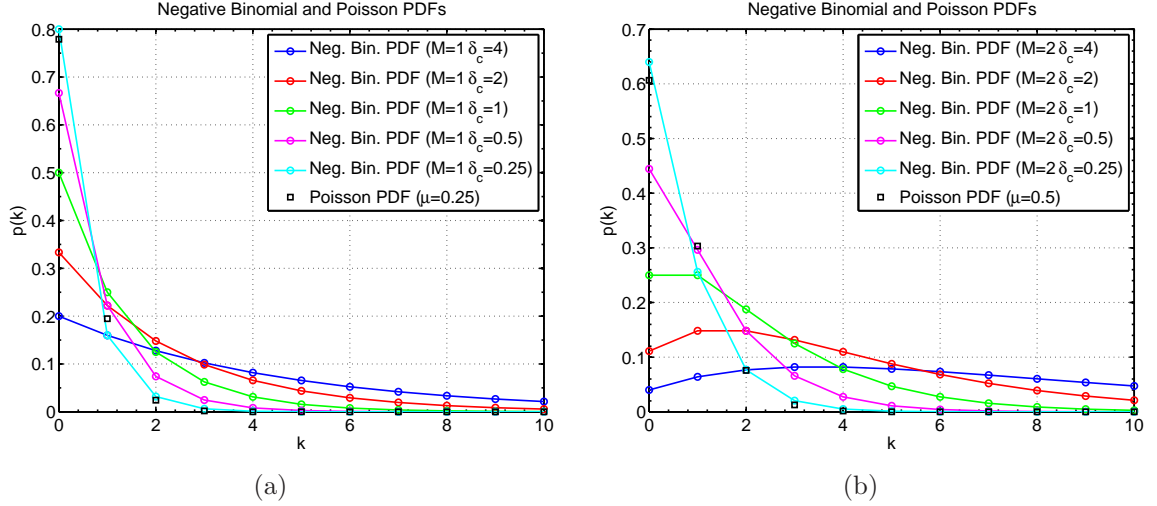


Figure A.1: (a) Negative binomial densities with $\mathcal{M} = 1$ and Poisson density. (b) Negative binomial densities with $\mathcal{M} = 2$ and Poisson density.

This is a negative binomial density with mean \bar{N} and diversity parameter \mathcal{M} . The diversity is given in Eq. A.9.

A.3 Poisson Approximation to Negative Binomial Distribution

The mean number of photons per speckle correlation cell is called the count degeneracy parameter [13]. It is denoted δ_c .

$$\delta_c = \frac{\bar{N}}{\mathcal{M}}. \quad (\text{A.15})$$

It was noted in [11] that when the count degeneracy parameter becomes small

$$\delta_c \ll 1 \quad (\text{A.16})$$

that the negative binomial density converges to the Poisson distribution with mean \bar{N} . This characteristic is illustrated in the Fig. A.1. The plots in Fig. A.1 show that as the mean number of photons per speckle cell approaches zero, the negative binomial density approaches the Poisson density.

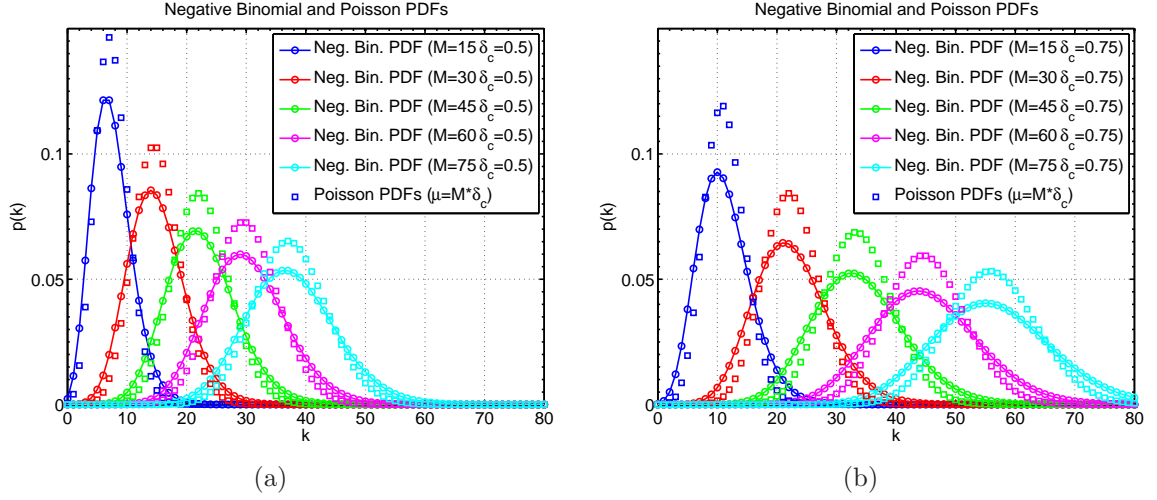


Figure A.2: (a) Negative binomial densities with $\delta_c = 0.5$ and Poisson densities. (b) Negative binomial densities with $\delta_c = 0.75$ and Poisson densities.

The negative binomial density also converges to the Poisson density as the diversity goes to infinity [5]. In this case the convergence is very slow and is difficult to illustrate. In Fig. A.2, the ratio of the mean number of photons to the diversity $\delta_c = \bar{N}/\mathcal{M}$ is not near zero. Therefore, the condition required by Eq. A.16 is not satisfied. However, as \mathcal{M} gets large, the negative binomial density is slowly converging to the Poisson density.

A.4 Photon Arrivals and Quantum Efficiency

LADAR systems rely on photodetectors to convert photons to a measurable signal. The process of converting photons to electrons (typically called photoelectrons) is imperfect. That is, some photons incident on the detector will fail to convert to signal. The fraction of photons converted to photoelectrons is called the quantum efficiency and is denoted η .

The statistics describing photon arrival densities were derived using mathematics that model optical propagation. Those derivations tell how many photons are incident on a detector in some time interval. However, only some of the incident

photons are successfully converted to photoelectrons by that detector. Undetected photons are not of interest. It is the photoelectron density that is desired.

In “*Effect of random deletion and additive noise on bunched and antibunched photon-counting statistics*”, Teich and Saleh [50] considered several different photon arrival densities. They assumed that the probability of each photon being converted to a photoelectron was fixed and statistically independent of the conversion process for all other arriving photons. They proved that if photon arrivals are Poisson distributed with mean \bar{N} , that the photoelectron density is $\eta\bar{N}$. For a negative binomial density with mean \bar{N} and diversity \mathcal{M} , the photoelectron density is also negative binomial with mean $\eta\bar{N}$. They also showed that the diversity of the photoelectron density is the same as the diversity of the photon density.

Appendix B. Parabolic and Gaussian Pulse Properties

This appendix contains a discussion of the duration and bandwidth of the temporal LADAR signal models used in this dissertation. The parabolic pulse shapes that are used in Chapters II and III are discussed. The Gaussian pulse models from Chapters IV and V are also reviewed. The full-width half-maxima of these pulses are calculated. The energy spectral densities are derived using the Fourier transforms of the pulses. The durations and bandwidths of parabolic and Gaussian pulses are compared.

The signals described in this appendix are the photodetector output signals. The energy or power in these signals is generally not equal to the optical energy or power in the received laser pulse. The photocurrent signals are measured in units of normalized current or normalized voltage. These normalized units are proportional to the received optical power observed by the LADAR photodetector. These relationships are explained in more detail in Sec. B.1.

B.1 Parabolic Pulse Properties

The parabolic pulse equation centered at time zero is

$$p_p(t) = G \left(1 - \frac{t^2}{p_w^2} \right) \text{rect} \left(\frac{t}{2p_w} \right). \quad (\text{B.1})$$

The parabolic pulse's FWHM is given by Eq. 4.45. The Fourier transform of the parabolic pulse is

$$\begin{aligned} P_p(f) &= \int_{-p_w}^{p_w} p_p(t) e^{-i2\pi ft} dt \\ &= G \int_{-p_w}^{p_w} e^{-i2\pi ft} dt - \frac{G}{p_w^2} \int_{-p_w}^{p_w} t^2 e^{-i2\pi ft} dt \\ &= 4p_w G \left[\frac{\sin(2\pi p_w f) - (2\pi p_w f) \cos(2\pi p_w f)}{(2\pi p_w f)^3} \right]. \end{aligned} \quad (\text{B.2})$$

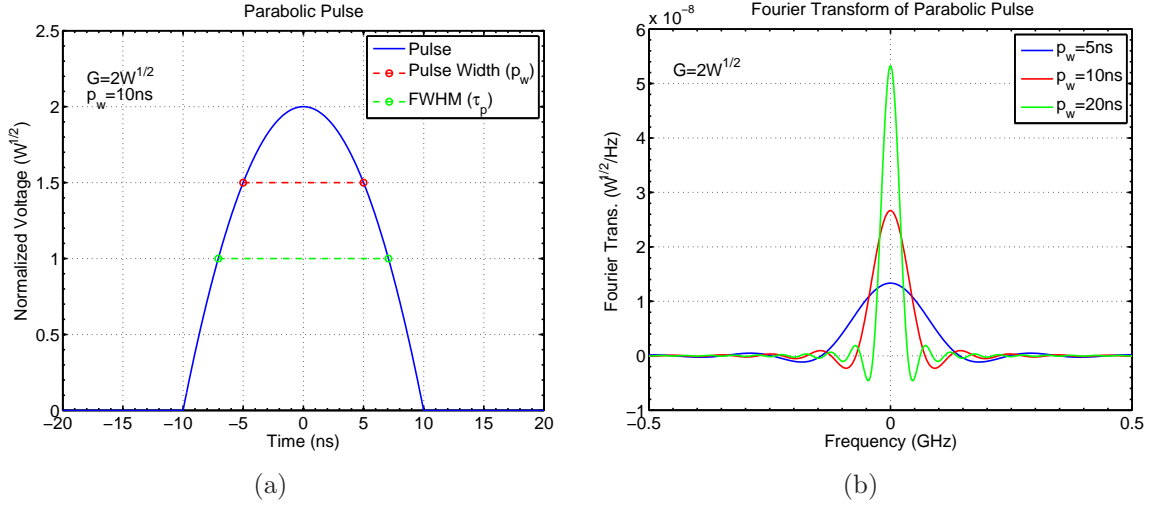


Figure B.1: (a) Parabolic pulse with width $p_w = 10$ ns and peak normalized voltage $G = 2 W^{1/2}$.
 (b) Pulse Fourier transforms for widths $p_w = 5, 10,$ and 20 ns.

A 10 ns parabolic pulse is illustrated in Fig. B.1a. Fourier transforms for 5, 10, and 20 ns pulses are shown in Fig. B.1b. The pulses's units are normalized voltage, which is the voltage divided by the square root of the resistance (e.g. Volts per root Ohm). The units of normalized voltage are equal to the square root of the power (e.g. Watts).

$$\begin{aligned}
 \sqrt{\text{Power}} &= \sqrt{\text{Voltage} \times \text{Current}} \\
 &= \sqrt{\text{Voltage} \times \frac{\text{Voltage}}{\text{Resistance}}} \\
 &= \frac{\text{Voltage}}{\sqrt{\text{Resistance}}}.
 \end{aligned}
 \tag{B.3}$$

The reason for using normalized voltage in place of regular voltage is that normalized voltage produces energy and power spectra with the correct units of energy times time and power times time, respectively.

Alternately, the photocurrent could be analyzed in terms of normalized current. Normalized current is current times the square root of resistance (e.g. Amps times

root Ohms).

$$\begin{aligned}
\sqrt{\text{Power}} &= \sqrt{\text{Voltage} \times \text{Current}} \\
&= \sqrt{\text{Current} \times \text{Current} \times \text{Resistance}} \\
&= \text{Current} \times \sqrt{\text{Resistance}}.
\end{aligned} \tag{B.4}$$

As with normalized voltage, normalized current will produce energy and power spectra with the correct units of energy times time and power times time.

A signal's energy spectral density (ESD) is the magnitude squared of its Fourier transform [32]. The ESD of the parabolic pulse from Eq. B.1, which is denoted $G_p(f)$, is

$$G_p(f) = |P_p(f)|^2 = 16p_w^2 G^2 \left[\frac{\sin(2\pi p_w f) - (2\pi p_w f) \cos(2\pi p_w f)}{(2\pi p_w f)^3} \right]^2. \tag{B.5}$$

The ESDs for parabolic pulses with various widths are illustrated in Fig. B.2a.

In most LADAR systems, the received signal is digitally sampled. In a sampled signal, pulse energy inside the Nyquist frequency, which is half the sampling frequency ($f_n = f_s/2$), is sampled properly. However, energy outside than the Nyquist frequency is aliased [30]. Aliasing will cause interference and will degrade the performance of parameter estimation techniques. The fraction of pulse energy that is aliased can be calculated by integrating the ESD over frequencies with magnitudes greater than f_n , then dividing by the total energy. Since the ESD has even symmetry, the fraction of energy outside the Nyquist frequency is

$$A_p(f_n) = \frac{\int_0^{f_n} G_p(f) df}{\int_0^{\infty} G_p(f) df} = \frac{\int_0^{\infty} G_p(f) df - \int_0^{f_n} G_p(f) df}{\int_0^{\infty} G_p(f) df} = 1 - \frac{2}{E_p} \int_0^{f_n} G_p(f) df \tag{B.6}$$

where the energy in the parabolic pulse E_p is

$$E_p = \int_{-\infty}^{\infty} G_p(f)df = \int_{-\infty}^{\infty} |P_p(f)|^2 df. \quad (\text{B.7})$$

An efficient way to calculate the pulse energy is through the use of Parseval's theorem, which states that

$$\int_{-\infty}^{\infty} |P_p(f)|^2 df = \int_{-\infty}^{\infty} |p_p(t)|^2 dt. \quad (\text{B.8})$$

Combining Eqs. B.1, B.7, and B.8 yields

$$E_p = \int_{-p_w}^{p_w} \left[G \left(1 - \frac{t^2}{p_w^2} \right) \right]^2 dt = \frac{16}{15} G^2 p_w. \quad (\text{B.9})$$

Using this result in Eq. B.6 shows that the fraction of energy that is greater than the Nyquist frequency can be written

$$A_p(f_n) = 1 - 30p_w \int_0^{f_n} \left[\frac{\sin(2\pi p_w f) - (2\pi p_w f) \cos(2\pi p_w f)}{(2\pi p_w f)^3} \right]^2 df. \quad (\text{B.10})$$

The fraction of a parabolic pulse's energy outside the Nyquist frequency is illustrated in Fig. B.2b. For the 20 ns pulse, about $3 \times 10^{-4}\%$ of the pulse energy is aliased when the sampling rate is one Gigahertz ($f_n = 500$ MHz). However, for the 5 ns pulse, about $2 \times 10^{-2}\%$ of the energy is aliased.

B.2 Gaussian Pulse Properties

Let the Gaussian pulse equation is

$$p_g(t) = G \exp\left(-\frac{t^2}{2w^2}\right) \quad (\text{B.11})$$

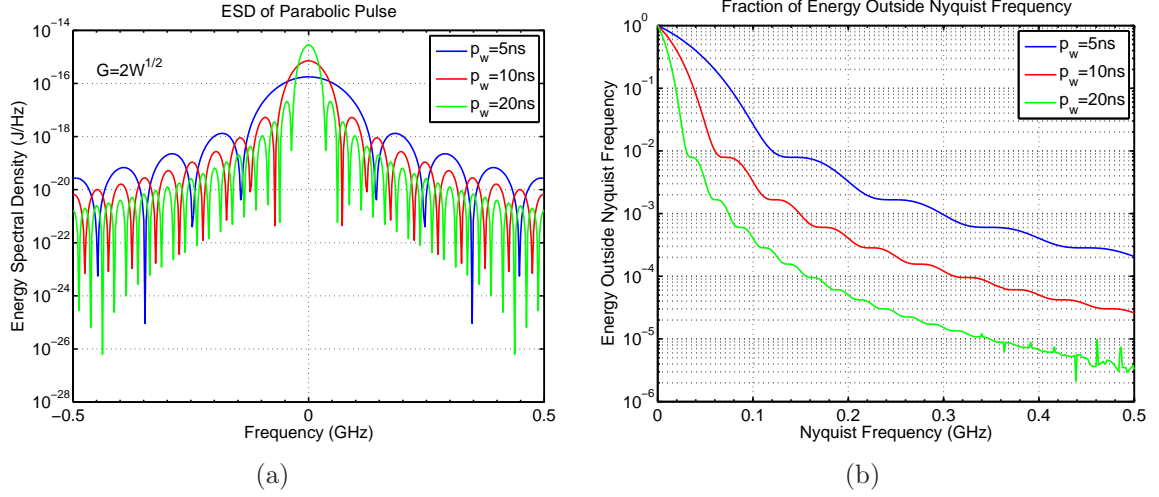


Figure B.2: (a) Parabolic pulse energy spectrum for pulse widths $p_w = 5, 10,$ and 20 ns. (b) Fraction of pulse energy outside Nyquist frequency.

where G is the gain and w is the variable describing the width of the pulse. At distance w from the pulse center, the Gaussian pulses's amplitude is $e^{-1/2}$ times its peak height. The full-width half-maximum of this pulse is given by Eq. 4.36.

The Fourier transform of the parabolic pulse is

$$P_g(f) = \int_{-\infty}^{\infty} p_g(t) e^{-i2\pi ft} dt = \sqrt{2\pi w} G e^{-2(\pi w f)^2}. \quad (\text{B.12})$$

The Gaussian pulse and its Fourier transform are illustrated in Fig. B.3. The ESD of the Gaussian pulse, which is denoted $G_g(f)$, is

$$G_g(f) = |P_g(f)|^2 = 2\pi w^2 G^2 e^{-2(\pi w f)^2}. \quad (\text{B.13})$$

The energy in the Gaussian pulse, denoted E_g , is

$$E_g = \int_{-\infty}^{\infty} G_g(f) dt = \sqrt{\pi} w G^2. \quad (\text{B.14})$$

The fraction of energy that is outside the Nyquist frequency, denoted $A_g(f_n)$, is

$$\begin{aligned}
A_g(f_n) &= \frac{\int_{f_n}^{\infty} G_g(f) df}{\int_0^{\infty} G_g(f) df} \\
&= 1 - \frac{2}{E_g} \int_0^{f_n} G_g(f) df \\
&= 1 - \frac{4\pi w^2 G^2}{\sqrt{\pi} w G^2} \int_0^{f_n} e^{-(2\pi w f)^2} df \\
&= 1 - \frac{2}{\sqrt{\pi}} \int_0^{2\pi w f_n} e^{-u^2} du \\
&= 1 - \text{erf}(2\pi w f_n)
\end{aligned} \tag{B.15}$$

where the change of variable $u = 2\pi w f$ was used and

$$\text{erf}(x) = \frac{2}{\sqrt{\pi}} \int_0^x e^{-u^2} du \tag{B.16}$$

is the error function (see Eq. 7.1.1 of [1]). The ESD of the Gaussian pulse and energy fraction are illustrated in Fig. B.4. The ESD of the Gaussian pulse decays much faster than the ESD for the parabolic pulse (shown in Fig. B.2a). Similarly, the function describing the fraction of Gaussian pulse energy $A_g(f_n)$ decays very quickly compared to the same function for the Gaussian pulse.

B.3 Parabolic and Gaussian Pulse Comparison

The parabolic and Gaussian pulses are compared in Fig. B.5. Both pulses have a 10 ns FWHM and 1 μ J of energy. The gain for the pulses and the FWHM are almost identical. However, the parabolic pulse is narrower (see Fig. B.5a) and its energy fraction that falls outside a Nyquist frequency is much higher (see Fig. B.5b).

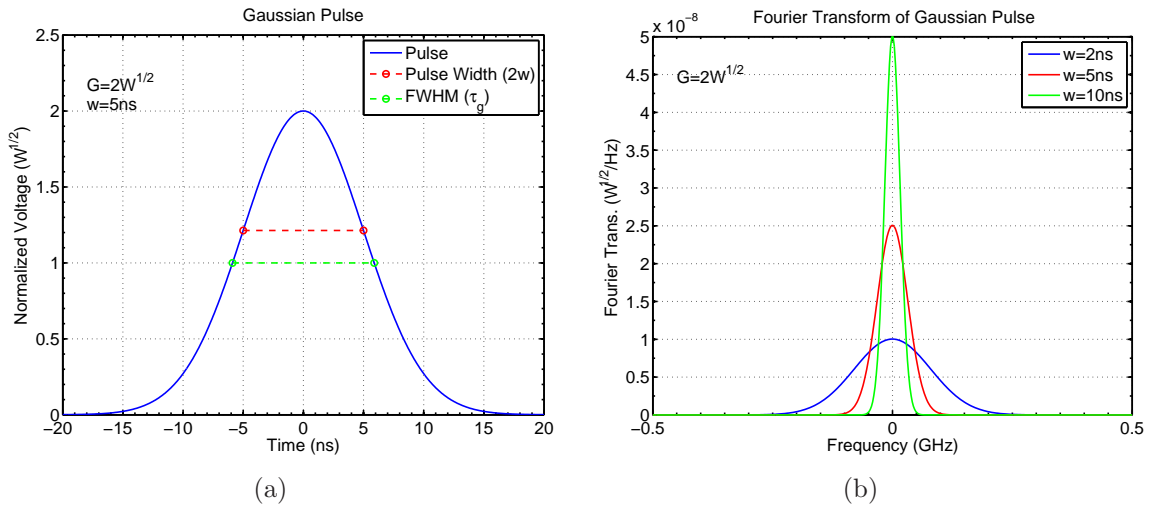


Figure B.3: (a) Gaussian pulse with width $w = 5$ ns and peak normalized voltage $G = 2 W^{1/2}$.
 (b) Pulse Fourier transforms for widths $w = 2, 5,$ and 10 ns.

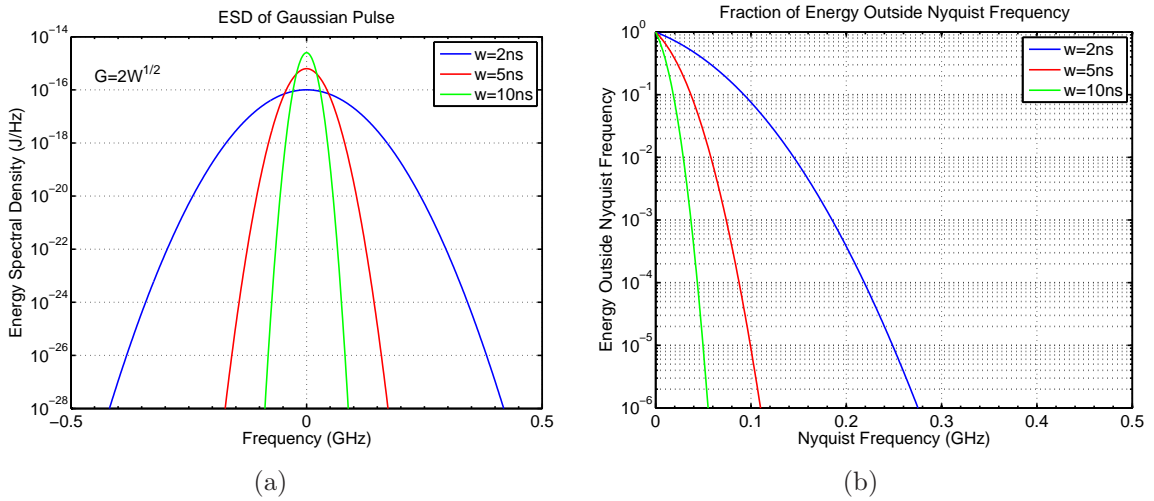


Figure B.4: (a) Gaussian pulse energy spectrum for pulse widths $w = 2, 5,$ and 10 ns.
 (b) Fraction of pulse energy outside Nyquist frequency.

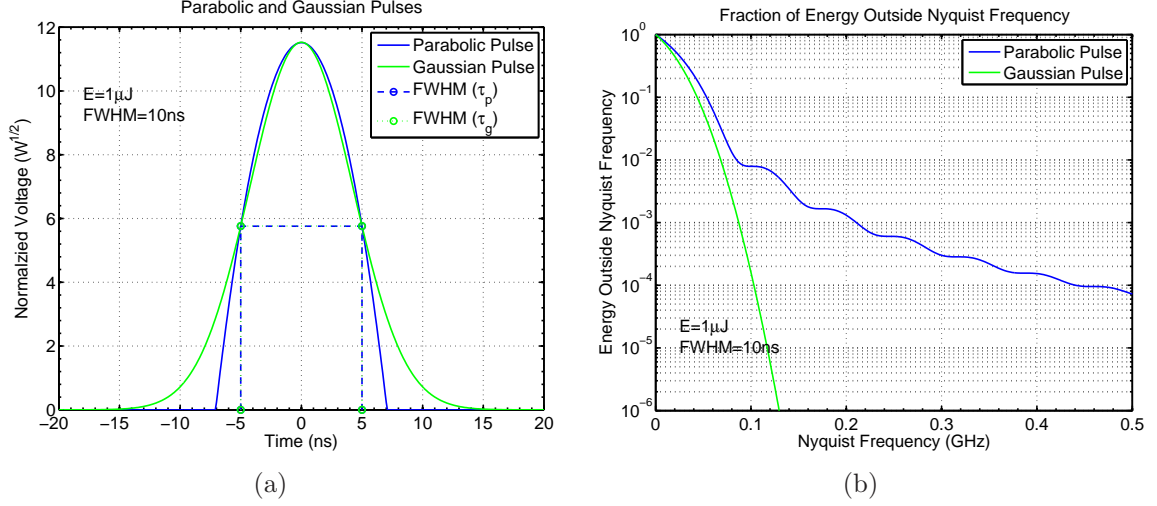


Figure B.5: (a) Parabolic and Gaussian pulses with 10 ns FWHM and $1\mu\text{J}$ energy. (b) Fraction of pulse energy outside Nyquist frequency.

B.4 Power Full-Width Half-Maximum

The FWHM can be measured from the pulse's power instead of the pulse's normalized voltage. The power is the normalized voltage squared. The power FWHM for a parabolic pulse is

$$\delta_p = 2p_w \left(1 - \frac{1}{\sqrt{2}}\right)^{1/2}. \quad (\text{B.17})$$

The power FWHM for a Gaussian pulse is

$$\delta_g = 2w [\log(2)]^{1/2}. \quad (\text{B.18})$$

The power FWHMs for parabolic and Gaussian pulses are illustrated in Fig. B.6.

B.5 Time-Bandwidth Products

The time-bandwidth product (TBP) of a waveform is used as a measure of its quality. It is a measure of the compactness of a waveform in both time and frequency. The TBP is computed in the same way as beam quality was calculated in Chapter II. It is the product of the mean square duration σ_t and the mean square bandwidth σ_f

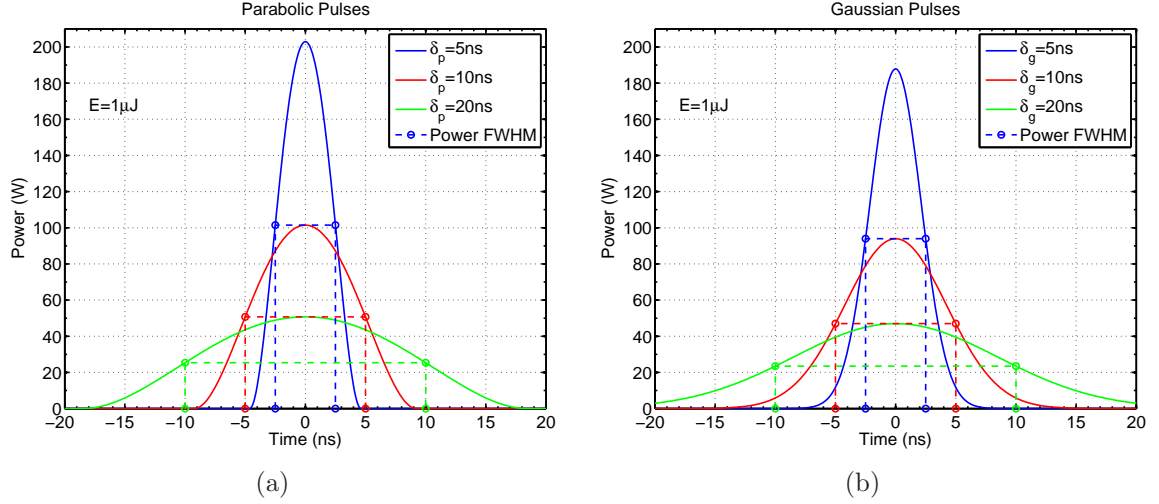


Figure B.6: (a) Power FWHM for parabolic pulses.
(b) Power FWHM for Gaussian pulses.

of a waveform [52].

$$\text{TBP} = \sigma_t \sigma_f. \quad (\text{B.19})$$

Given arbitrary waveform $p(t)$, the quantities needed to calculate the time-bandwidth product are

$$\sigma_t^2 = \frac{\int_{-\infty}^{\infty} t^2 p^2(t) dt}{\int_{-\infty}^{\infty} p^2(t) dt} \quad (\text{B.20})$$

and

$$\sigma_f^2 = \frac{\int_{-\infty}^{\infty} f^2 |P(f)|^2 df}{\int_{-\infty}^{\infty} |P(f)|^2 df} \quad (\text{B.21})$$

where $P(f)$ is the Fourier transform of the waveform.

The waveform uncertainty relation is a lower bound on the time-bandwidth product of any waveform (see p. 600 of [52]). The waveform uncertainty relation is

$$\sigma_t \sigma_f \geq \frac{1}{4\pi}. \quad (\text{B.22})$$

For the Gaussian pulse from Eq. B.11, the mean square duration squared is

$$\sigma_{t-gaussian}^2 = \frac{w^2}{2} \quad (\text{B.23})$$

and the mean square bandwidth squared is

$$\sigma_{f-gaussian}^2 = \frac{1}{8\pi^2 w^2}. \quad (\text{B.24})$$

Thus, the time-bandwidth product for a Gaussian pulse is

$$\text{TBP}_{gaussian} = \frac{1}{4\pi} \approx 0.0796. \quad (\text{B.25})$$

Comparison of this result with the waveform uncertainty relation (Eq. B.22) shows that the Gaussian waveform achieves the bound. It is the only waveform that achieves this bound.

Given the parabolic pulse from Eq. B.1, the mean square duration squared is

$$\sigma_{t-parabolic}^2 = \frac{p_w^2}{7} \quad (\text{B.26})$$

and the mean square bandwidth squared is

$$\sigma_{f-parabolic}^2 = \frac{5}{8\pi^2 p_w^2}. \quad (\text{B.27})$$

Thus, the time-bandwidth product for a parabolic pulse is

$$\text{TBP}_{parabolic} = \frac{1}{2\pi} \left(\frac{5}{14} \right)^{1/2} \approx 0.0951. \quad (\text{B.28})$$

Comparison of the time-bandwidth products of the Gaussian pulse (Eq. B.25) and the parabolic pulse (Eq. B.28) shows that, as expected, the parabolic pulse's time-bandwidth product is greater. However, the difference is not that great. The

ratio is

$$\frac{\text{TBP}_{\text{parabolic}}}{\text{TBP}_{\text{gaussian}}} = \left(\frac{10}{7}\right)^{1/2} \approx 1.195. \quad (\text{B.29})$$

Thus, the parabolic pulse's TBP is less than 20% higher than for the Gaussian pulse. Therefore, the truncated parabolic pulse is a relatively compact waveform.

The mean squared duration of the Gaussian pulse in terms of the FWHM is (see Eqs. 4.36 and B.23)

$$\sigma_{t\text{-gaussian}} = \frac{\tau_g}{4 [\log(2)]^{1/2}} \approx 0.300\tau_g. \quad (\text{B.30})$$

For the parabolic pulse, the mean squared duration is (see Eqs. 4.45 and B.26)

$$\sigma_{t\text{-parabolic}} = \frac{\tau_p}{\sqrt{14}} \approx 0.267\tau_p. \quad (\text{B.31})$$

The duration of the parabolic pulse is shorter than the duration of the Gaussian pulse by over 10%. The parabolic pulse is an example of a pulse that is a compact in the time domain. It is the relatively wide bandwidth of the parabolic pulse, which is illustrated in Fig. B.5, that makes its TBP greater than the Gaussian pulse's time-bandwidth product.

Appendix C. Lower Bound on Estimator Variance

In this appendix, it is demonstrated that the reciprocal of any diagonal element of a Fisher information matrix is a lower bound for the Cramer-Rao lower bound associated with that parameter. In other words, the FIM diagonal element's reciprocal is a lower bound on the variance of unbiased parameter estimates. However, it is generally a looser lower bound than the CRLB.

The fact FIM diagonal element reciprocals are lower bounds for the CRLB has already been noted by Van Trees for the special case of 2×2 Fisher information matrices [52]. However, that reference does not discuss cases where the Fisher information matrix is larger than 2×2 . In this appendix it is shown that the property is true for any nonsingular FIM, regardless of its size.

C.1 Decomposition of the Fisher Information Matrix

Fisher information matrices are nonnegative definite. This follows from the fact that they can be defined as covariance matrices [23]. It is possible for the FIM to be singular. In that case, the FIM inverse does not exist and there are no unbiased finite variance estimators of the unknown parameters [49].

If the FIM is also nonsingular, then it is positive definite. Any positive definite matrix has the following eigenvalue decomposition [36].

$$\mathbf{J} = \mathbf{U}\mathbf{\Sigma}\mathbf{U}^H \quad (\text{C.1})$$

where \mathbf{U} is a unitary matrix and $\mathbf{\Sigma}$ is diagonal. The notation H denotes Hermitian (conjugate) transpose. By exploiting the fact that \mathbf{U} is unitary and $\mathbf{\Sigma}$ is diagonal, Eq. C.1 can be written

$$\mathbf{J} = \sum_{m=1}^M \lambda_m \mathbf{u}_m \mathbf{u}_m^H \quad (\text{C.2})$$

where M is number of rows and columns in the FIM. The vector \mathbf{u}_m is the m -th column of \mathbf{U} .

$$\mathbf{U} = [\mathbf{u}_1 \quad \mathbf{u}_2 \quad \dots \quad \mathbf{u}_M]. \quad (\text{C.3})$$

The diagonal elements of $\mathbf{\Sigma}$ are denoted λ_m . Since it has been assumed that the FIM is positive definite, all of its eigenvalues are positive [18].

$$\lambda_m > 0 \quad \forall \quad m. \quad (\text{C.4})$$

The inverse of the Fisher information matrix is

$$\mathbf{J}^{-1} = \sum_{m=1}^M \frac{1}{\lambda_m} \mathbf{u}_m \mathbf{u}_m^H. \quad (\text{C.5})$$

The Cramer-Rao lower bound for estimates of the n -th parameter is the reciprocal of the n -th diagonal element of the inverse of the FIM. That is,

$$\text{Var} [\hat{\theta}_n] \geq [\mathbf{J}^{-1}]_{nn}. \quad (\text{C.6})$$

Combining Eqs. C.5 and C.6 produces

$$\begin{aligned} \text{Var} [\hat{\theta}_n] &\geq \left[\sum_{m=1}^M \frac{1}{\lambda_m} \mathbf{u}_m \mathbf{u}_m^H \right]_{nn} \\ &= \sum_{m=1}^M \frac{1}{\lambda_m} [\mathbf{u}_m]_n ([\mathbf{u}_m]_n)^* \\ &= \sum_{m=1}^M \frac{1}{\lambda_m} |[\mathbf{U}]_{n,m}|^2. \end{aligned} \quad (\text{C.7})$$

C.2 Relationship Between CRLB and FIM Diagonal Elements

In this section, the relationship between the Cramer-Rao lower bound and the diagonal elements of the Fisher information matrix is studied. Using Eq. C.2, the n -th diagonal element of the FIM can be written

$$[\mathbf{J}]_{nn} = \sum_{m=1}^M \lambda_m |[\mathbf{U}]_{n,m}|^2. \quad (\text{C.8})$$

Let

$$a_{n,m} = \sqrt{\lambda_m} \left| [\mathbf{U}]_{n,m} \right| \quad (\text{C.9})$$

and

$$b_{n,m} = \frac{1}{\sqrt{\lambda_m}} \left| [\mathbf{U}]_{n,m} \right|. \quad (\text{C.10})$$

Eqs. C.8 and C.9 combine to form

$$[\mathbf{J}]_{nn} = \sum_{m=1}^M a_{n,m}^2. \quad (\text{C.11})$$

Eqs. C.6, C.7, and C.10 combine to produce

$$[\mathbf{J}^{-1}]_{nn} = \sum_{m=1}^M b_{n,m}^2. \quad (\text{C.12})$$

The Cauchy-Schwarz-Buniakowsky inequality is (p. 1049 of [14])

$$\left(\sum_{m=1}^M a_{n,m}^2 \right) \left(\sum_{m=1}^M b_{n,m}^2 \right) \geq \left(\sum_{m=1}^M a_{n,m} b_{n,m} \right)^2. \quad (\text{C.13})$$

All real unitary matrices are orthogonal. Because \mathbf{U} is orthogonal, its rows and columns are each orthonormal bases [23]. Using this fact, along with Eqs. C.9 and C.10, shows that

$$\sum_{m=1}^M a_{n,m} b_{n,m} = \sum_{m=1}^M \left| [\mathbf{U}]_{n,m} \right|^2 = 1 \quad (\text{C.14})$$

Therefore,

$$\sum_{m=1}^M b_{n,m}^2 \geq \frac{1}{\sum_{m=1}^M a_{n,m}^2}. \quad (\text{C.15})$$

When Eq. C.15 is combined with Eqs. C.11 and C.12, the following inequality is produced.

$$[\mathbf{J}^{-1}]_{nn} \geq \frac{1}{[\mathbf{J}]_{nn}}. \quad (\text{C.16})$$

Combining this result with the CRLB from Eq. C.7 produces a lower bound for the variance of unbiased estimates of parameter θ_n .

$$\text{Var} [\hat{\theta}_n] \geq \frac{1}{[\mathbf{J}]_{nn}}. \quad (\text{C.17})$$

This bound is generally looser than the CRLB. However it is of value when there is a complicated Fisher information matrix that is cumbersome to invert. In that case, a simple lower bound can be obtained by simply taking the reciprocal of the appropriate FIM diagonal element.

Bibliography

1. Abramowitz M. and Stegun I. *Handbook of Mathematical Functions*. New York: Dover, 1965.
2. Albota M., Aull B., Fouche D., Heinrichs R., Kocher D., Marino R., Mooney J., Newbury N., O'Brien M., Player B., Willard B., and Zayhowski J. "Three-Dimensional Imaging Laser Radars with Geiger-Mode Avalanche Photodiode Arrays," *Lincoln Laboratory Journal*, 13(2):351–370 (2002).
3. Andrews L. and Phillips R. *Laser Beam Propagation through Random Media*. Bellingham: SPIE Optical Engineering Press, 1998.
4. Cain S., Richmond R., and Armstrong E. "Flash light detection and ranging accuracy limits for returns from single opaque surfaces via Cramer-rao bounds," *Applied Optics*, 45(24):6154–6162 (August 2006).
5. Casella G. and Berger R. *Statistical Inference*. California: Duxbury, 2002.
6. Chazan D., Zakai M., and Ziv J. "Improved Lower Bounds on Signal Parameter Estimation," *IEEE Transactions on Information Theory*, 21(1):90–93 (January 1975).
7. Fano U. "Ionization Yield of Radiations. II. The Fluctuations of the Number of Ions," *Physical Review*, 72(1):26–29 (July 1947).
8. Frehlich R. and Kavaya M. "Coherent laser radar performance for general atmospheric refractive turbulence," *Applied Optics*, 30(36):5325–5352 (December 1991).
9. Gatt P. and Henderson S. "Laser Radar Detection Statistics: A Comparison of Coherent and Direct Detection Intensity Receivers," *Proc. SPIE Vol. 4377, Laser Radar Technology and Applications VI*, 251–262 (2001).
10. Gini F., Greco M., and Farina A. "Clairvoyant and adaptive signal detection in non-Gaussian clutter:a data-dependent threshold interpretation," *IEEE Transactions on Signal Processing*, 47(6):1522–1531 (June 1999).
11. Goodman J. "Some Effects of Target-Induced Scintillation on Optical Radar Performance," *Proceedings of the IEEE*, 53(11):1688–1700 (November 1965).
12. Goodman J. *Statistical Optics*. New York: Wiley-Interscience, 1985.
13. Goodman J. *Introduction to Fourier Optics*. New York: McGraw-Hill, 1996.
14. Gradshteyn I. and Ryzhik I. *Table of Integrals, Series, and Products*. San Diego: Academic Press, 2000.
15. Gronwall C., Steinvall O., Gustafsson F., and Chevalier T. "Influence of laser radar sensor parameters on range-measurement and shape-fitting uncertainties," *Optical Engineering*, 46(10):106201 (October 2007).

16. Hagen N., Kupinski M., and Dereniak E. "Gaussian profile estimation in one dimension," *Applied Optics*, 46(22):5374–5383 (August 2007).
17. Hill C., Harris M., and Ridley K. "Fiber-based 1.5 um lidar vibrometer in pulsed and continuous modes," *Applied Optics*, 46(20):4376–4385 (July 2007).
18. Horn R. and Johnson C. *Matrix Analysis*. Cambridge: Cambridge University Press, 1985.
19. Huffaker M. and Hardesty R. "Remote sensing of atmospheric wind velocities using solid-state and CO₂ coherent laser systems," *Proceedings of the IEEE*, 84(2):181–204 (February 1996).
20. Jacobsen E. and Kootsookos P. "Fast, Accurate Frequency Estimators," *IEEE Signal Processing Magazine*, 24(3):123–125 (May 2007).
21. Jelalian A. *Laser Radar Systems*. Massachusetts: Artech House, 1992.
22. Johnson S., Nichols T., Gatt P., and Klausutis T. "Range Precision of Direct Detection Laser Radar Systems," *Proc. SPIE Vol. 5412, Laser Radar Technology and Applications IX*, 72–86 (2004).
23. Kay S. *Fundamentals of Statistical Signal Processing: Estimation Theory*. New Jersey: Prentice Hall, 1993.
24. Kozick J. and Sadler B. "Bounds and algorithms for time delay estimation on parallel, flat fading channels," *IEEE International Conference on Acoustics, Speech and Signal Processing*, 2413–2416 (2008).
25. Mandel L. "Fluctuations of Photon Beams: The Distribution of the Photo-Electrons," *Proceedings of the Royal Society of London*, 74:233–243 (1959).
26. Marino R. and Davis W. "Jigsaw: A Foliage-Penetrating 3D Imaging Laser Radar System," *Lincoln Laboratory Journal*, 15(1):23–36 (2005).
27. Marino R., Stephens T., Hatch R., McLaughlin J., Mooney J., OBrien M., Rowe G., Adams J., Skelly L., Knowlton R., Forman S., and Davis W. "A compact 3D imaging laser radar system using Geiger-mode APD arrays: system and measurements," *Proc. SPIE Vol. 5086, Laser Radar Technology and Applications VIII*, 1–15 (August 2003).
28. Measures R. *Laser Remote Sensing*. Florida: Krieger, 1984.
29. Miller S. "Ionization Rates for Holes and Electrons in Silicon," *Physics Review*, 105(4):1246–1249 (February 1957).
30. Oppenheim A. and Schaffer R. *Discrete-Time Signal Processing*. New Jersey: Prentice Hall, 1989.
31. Osche G. *Optical Detection Theory*. New Jersey: Wiley-Interscience, 2002.
32. Proakis J. and Salehi M. *Communication Systems Engineering*. New Jersey: Prentice Hall, 1994.

33. Rice S. "Mathematical Analysis of Random Noise (Parts I, II)," *Bell System Technical Journal*, 23:282–333 (1944).
34. Rice S. "Mathematical Analysis of Random Noise (Part III)," *Bell System Technical Journal*, 24:46–108 (1945).
35. Rye B. and Hardesty R. "Discrete spectral peak estimation in incoherent backscatter-heterodyne lidar. I. Spectral accumulation and the Cramer-Rao lowerbound," *IEEE Transactions on Geoscience and Remote Sensing*, 31(1):16–27 (January 1993).
36. Scharf L. *Statistical Signal Processing*. Massachusetts: Addison-Wesley, 1991.
37. Seal M. *Nonlinear Time-Variant Response in an Avalanche Photodiode Array Based Laser Detection and Ranging System*. MS thesis, Air Force Institute of Technology, 2007.
38. Siegman A. *Lasers*. California: University Science Books, 1986.
39. Siegman A. "New developments in laser resonators," *Proc. SPIE Vol. 1224, Optical Resonators*, 2–14 (1990).
40. Siegman A. "Defining, measuring, and optimizing laser beam quality," *Proc. SPIE Vol. 1868, Laser Resonators and Coherent Optics: Modeling, Technology, and Applications*, 2–12 (1993).
41. Siegman A. "High-power laser beams: defining, measuring and optimizing transverse beam quality," *Proc. SPIE Vol. 1810, 9th International Symposium on Gas Flow and Chemical Lasers*, 758–765 (1993).
42. Siegman A. and Sziklas E. "Mode calculations in unstable resonators with flowing saturable gain. 1: Hermite-Gaussian expansion," *Applied Optics*, 13(12):2775–2792 (December 1974).
43. Soderman U., Ahlberg S., and Elmqvist, M. and Persson A. "Three-dimensional environment models from airborne laser radar data," *Proc. SPIE Vol. 5412, Laser Radar Technology and Applications IX*, 333–344 (2004).
44. Stann B., Redman B., Lawler W., Giza M., Dammann J., and Krapels K. "Chirped amplitude modulation lidar for range and Doppler measurements and 3-D imaging," *Proc. SPIE Vol. 6550, Laser Radar Technology and Applications XII*, 655005 (2007).
45. Steinvall O. "Effects of Target Shape and Reflection on Laser Radar Cross Sections," *Applied Optics*, 39(24):4381–4391 (August 2000).
46. Steinvall O. and Chevalier T. "Range accuracy and resolution for laser radars," *Proc. SPIE Vol. 5988, Electro-Optical Remote Sensing*, 598808 (2005).
47. Stettner R., Bailey H., and Richmond R. "Eye-safe laser radar 3D imaging," *Proc. SPIE Vol. 5412, Laser Radar Technology and Applications IX*, 111–116 (2004).

48. Stettner R., Bailey H., and Silverman S. “Large format time-of-flight focal plane detector development,” *Proc. SPIE Vol. 5791, Laser Radar Technology and Applications X*, 288–292 (2005).
49. Stoica P. and Marzetta T. “Parameter estimation problems with singular information matrices,” *IEEE Transactions on Signal Processing*, 49(1):87–90 (January 2001).
50. Teich M. and Saleh B. “Effects of random deletion and additive noise on bunched and antibunched photon-counting statistics,” *Optics Letters*, 7(8):365–367 (August 1982).
51. Van Trees H. *Detection, Estimation, and Modulation Theory Part I. Detection, Estimation, and Linear Modulation Theory*. New York: Wiley-Interscience, 2001.
52. Van Trees H. *Detection, Estimation, and Modulation Theory Part III. Radar-Sonar Processing and Gaussian Signals in Noise*. New York: Wiley-Interscience, 2001.
53. Vasile A. and Marino R. “Pose-Independent Automatic Target Detection and Recognition Using 3D Laser Radar Imagery,” *Lincoln Laboratory Journal*, 15(1):61–78 (2005).
54. Wackerly D., Mendenhall W., and Scheaffer R. *Mathematical Statistics with Applications*. California: Duxbury, 2002.
55. Winick K. “Cramer-Rao lower bounds on the performance of charge-coupled device optical position estimators,” *Journal of the Optical Society of America A*, 3(11):1809–1815 (November 1986).
56. Wolfe W. *Introduction to Imaging Spectrometers*. Washington: SPIE Optical Engineering Press, 1997.
57. Ziv J. and Zakai M. “Some lower bounds on signal parameter estimation,” *IEEE Transactions on Information Theory*, 15(3):386–391 (May 1969).

REPORT DOCUMENTATION PAGE

Form Approved
OMB No. 0704-0188

The public reporting burden for this collection of information is estimated to average 1 hour per response, including the time for reviewing instructions, searching existing data sources, gathering and maintaining the data needed, and completing and reviewing the collection of information. Send comments regarding this burden estimate or any other aspect of this collection of information, including suggestions for reducing this burden to Department of Defense, Washington Headquarters Services, Directorate for Information Operations and Reports (0704-0188), 1215 Jefferson Davis Highway, Suite 1204, Arlington, VA 22202-4302. Respondents should be aware that notwithstanding any other provision of law, no person shall be subject to any penalty for failing to comply with a collection of information if it does not display a currently valid OMB control number. **PLEASE DO NOT RETURN YOUR FORM TO THE ABOVE ADDRESS.**

1. REPORT DATE (DD-MM-YYYY) 29-07-2008		2. REPORT TYPE Doctoral Dissertation		3. DATES COVERED (From — To) Oct 2005 — Sept 2008	
4. TITLE AND SUBTITLE Range Precision of LADAR Systems				5a. CONTRACT NUMBER DACA99-99-C-9999	
				5b. GRANT NUMBER	
				5c. PROGRAM ELEMENT NUMBER	
6. AUTHOR(S) Steven Johnson				5d. PROJECT NUMBER	
				5e. TASK NUMBER	
				5f. WORK UNIT NUMBER	
7. PERFORMING ORGANIZATION NAME(S) AND ADDRESS(ES) Air Force Institute of Technology Graduate School of Engineering and Management (AFIT/EN) 2950 Hobson Way WPAFB OH 45433-7765				8. PERFORMING ORGANIZATION REPORT NUMBER AFIT/DEE/ENG/08-15	
9. SPONSORING / MONITORING AGENCY NAME(S) AND ADDRESS(ES)				10. SPONSOR/MONITOR'S ACRONYM(S)	
				11. SPONSOR/MONITOR'S REPORT NUMBER(S)	
12. DISTRIBUTION / AVAILABILITY STATEMENT Approval for public release; distribution is unlimited.					
13. SUPPLEMENTARY NOTES					
14. ABSTRACT A key application of Laser Detection and Ranging (LADAR) systems is measurement of range to a target. Many modern LADAR systems are capable of transmitting laser pulses that are less than a few nanoseconds in duration. These short-duration pulses provide excellent range precision. However, randomness in the detected laser signals places limits on the precision. The goal of this dissertation is to quantify the range precision limits of LADAR systems. The randomness in the time between photon arrivals, which is called shot noise, is discussed in depth. System-dependent noise sources such as dark current and detector gain variation are considered. The effect of scene-dependent parameters including background light, target obscuration, and target orientation is also discussed. Finally, noise mitigation strategies such as pulse averaging and gain equalization are described and tested on simulated and real LADAR data.					
15. SUBJECT TERMS ladar					
16. SECURITY CLASSIFICATION OF:			17. LIMITATION OF ABSTRACT	18. NUMBER OF PAGES	19a. NAME OF RESPONSIBLE PERSON
a. REPORT	b. ABSTRACT	c. THIS PAGE			Prof. Stephen Cain
U	U	U	UU	198	19b. TELEPHONE NUMBER (include area code) (937) 255-3636, ext 4625; stephen.cain@afit.edu